



UNIVERSITY OF
BIRMINGHAM

NOVEL ROUTES TO NANO-METAMATERIALS USING
A SYNTHETIC BIOLOGY APPROACH

by

RACHAEL CULLINAN

A thesis submitted to

The University of Birmingham

for the degree of

DOCTOR OF PHILOSOPHY

Dept. Biochemical Engineering
School of Chemical Engineering
College of Engineering and Physical Sciences
The University of Birmingham
August 2019

UNIVERSITY OF
BIRMINGHAM

University of Birmingham Research Archive

e-theses repository

This unpublished thesis/dissertation is copyright of the author and/or third parties. The intellectual property rights of the author or third parties in respect of this work are as defined by The Copyright Designs and Patents Act 1988 or as modified by any successor legislation.

Any use made of information contained in this thesis/dissertation must be in accordance with that legislation and must be properly acknowledged. Further distribution or reproduction in any format is prohibited without the permission of the copyright holder.

ABSTRACT

Here a report shows a new class of biological three-dimensional (3D) metamaterials (MM) architected from M13 bacteriophage, using a facile and scalable evaporative front deposition methodology (EFD). The highly anisotropic structures achieved tuneable negative refraction from the visible to the mid-infrared (MIR) ranges of the electromagnetic spectrum.

Optical MM are considered composite materials in which sub-wavelength features, engineered from constituent materials, can control the macroscopic electromagnetic properties of the material. EFD afforded architecture of one-dimensional (1D) arrays of 3D ridges on substrate surfaces, whereby transmission, reflection, optical imaging and modelling were utilised to further characterise topography, and also demonstrate their activity as optical MM, in particular as negative index materials (NIM). Therefore, a new class of biological MM with exciting potential for defence systems and wave guiding over a tuneable wavelength range has been proposed.

The high surface area and loading capacity, provided by the hierarchical internal structure, allowed for pre-templating surface modifications of M13 to display functional nanomaterials. This extra functionality of the 3D architecture to act as a colorimetric detection system, highlights the flexibility of the dynamic system to be tailored towards a multitude of research areas, from cloaking to diagnostics and drug delivery.

DEDICATION

I would like to dedicate this thesis to Marcus Cullinan for his continued support and funding my Starbucks™ addiction throughout the process.

Without him none of this would have been possible.

x

ACKNOWLEDGEMENTS

First and foremost, I would like to thank my supervisor's Dr Pola. Oppenheimer, and Prof. Tim Dafforn for trusting me to carry out this research within their research groups and for their continued support throughout the process.

I would also like to thank Dr J Rickcard for his mentoring in creating a rig for the evaporative front deposition process.

I would also like to thank Prof. Shuang Zhang and Dr. Changxu Liu of The University of Birmingham's Metamaterials group for allowing me to use their dark room, alongside their aid in creating an in-house rig for the measurements of circular dichroism and negative refraction.

Other thanks go to the ANMSA research group at The University of Birmingham for providing me with guidance over the 3 years.

Finally, I would like to thank my sponsors DSTL who without their continued support and funding this PhD would never have been explored. I hope they continue to fund blue sky projects such as mine to create materials that are truly fascinating.

Table of Contents

LIST OF FIGURES	IX
LIST OF TABLES	XX
LIST OF UNITS	XXI
LIST OF ABBREVIATIONS AND COMMON TERMS	XXVI
CHAPTER 1 THE SCOPE OF BIOLOGICAL METAMATERIALS	1
1.1 Biological Building Blocks and Synthetic Biology	3
1.1.1 M13 Bacteriophage	4
1.2 Self-Assembly and Functional Nanoporous Networks	8
1.3 Liquid Crystals	10
1.4 Bio-inspired Metamaterials, Photonic Crystals and Chirality	11
1.5 The Route to Optical Metamaterials and Negative Index Materials	14
1.6 Outline of the Thesis	16
CHAPTER 2 M13: A SELF-ASSEMBLING BUILDING BLOCK	17
2.1 Methodology	18
2.1.1 Materials and Reagents	18
2.1.2 Instruments	18
2.1.3 Analysis Techniques	19
2.1.3.1 Ultra Violet-Visible Spectrophotometry	19
2.1.3.2 Polarised Light Microscopy	20
2.1.3.3 Atomic Force Microscopy	21
2.1.3.4 Scanning Electron Microscopy	23
2.1.4 Propagation and Isolation of M13 ssDNA	25
2.1.4.1 M13 Structure	25
2.1.5 Thiol modification of M13	28
2.1.6 PVIII Thiol Modification	29

2.1.7	Surface Modification of Substrates Prior to Deposition Techniques	30
2.1.8	Sessile Drop Casting	31
2.1.9	Spin Coating	31
2.1.10	Shearing Force and Channelled Deposition	32
2.1.11	Evaporative Front Deposition	34
2.1.12	Statistical Analysis using MATLAB	37
2.2	Problems Encountered During Experimental Methods	37
2.3	Results and Discussion	38
2.3.1	Propagation and Isolation of M13 ssDNA	38
2.3.2	Sessile Drop Casting	40
2.3.3	Spin Coating	42
2.3.4	Evaporative Front Deposition	46
2.3.4.1	Analysis of M13 Evaporative Front Deposition on BSi	53
2.3.4.2	Analysis of M13 Evaporative Front Deposition on AuSi	75
2.3.4.3	Analysis of M13 Evaporative Front Deposition on AuGMS	91
2.3.4.4	Analysis of Ridge Diameter	102
2.3.4.5	Analysis of Ridge Height	104
2.3.4.6	Analysis of Bundle Sizes	105
2.3.5	Compiled Data Tables for Each Substrate	107
2.4	Conclusions	109
CHAPTER 3	M13: A CHIRAL ROUTE TO NEGATIVE REFRACTION	111
3.1	The Chiroptical Response	112
3.2	Negative Index Materials (NIM)	115
3.3	Reflectance and Transmittance of Linear Light	117
3.4	Methodology	119
3.4.1	Linear Reflectance	119
3.4.2	Circular Dichroism (ΔCD) and Dissymmetry Factor (g)	122
3.4.3	Negative Refraction ($\theta_{t,\perp}$)	125
3.4.4	Mesh grids created using MATLAB	130
3.5	Problems Encountered During Phase II	130
3.6	Results and Discussion	131

3.6.1	Linear Reflectance	131
3.6.1.1	Linear Reflection; A Function of Wavelength and Periodicity	133
3.6.1.2	Linear Reflection; A Function of Wavelength and Incident Angle	136
3.6.2	Circular Dichroism and Degree of Anisotropy	140
3.6.2.1	Intrinsic Circular Dichroism and Degree of Anisotropy; A Function of Wavelength and Periodicity	141
3.6.2.2	Intrinsic-Extrinsic Circular Dichroism and Degree of Anisotropy; A Function of Wavelength and Incident Angle	145
3.6.3	Negative Index Material activity	150
3.6.3.1	Theoretical Models for Negative Index Material Activity in the Visible to Mid-Infrared Range	151
3.6.3.2	MATLAB Simulations of Negative Index Material Behaviour for 1D Arrays of M13 onto BSi, AuSi and PtSi	155
3.6.3.3	MATLAB Simulation and Practical Demonstration of Negative Index Material Behaviour for 1D Arrays of M13 onto AuGMS	159
3.7	Conclusions	165
CHAPTER 4	M13: FURTHER APPLICATIONS OF THE 3D SCAFFOLD	168
4.1	Heavy Metal Detection Systems	169
4.2	Methodology and Results	171
4.2.1	Materials and Reagents	171
4.2.2	Instruments	172
4.2.3	Synthesis of AuNP	172
4.2.4	Synthesis of AuNP-GA	173
4.2.5	Synthesis of M13-AuNP and Mechanism of Action Towards Pb ²⁺	174
4.3	Results and Discussion	177
4.3.1	Synthesis of AuNPs	177
4.3.2	Evaporative Front Deposition of Active Material bound M13	180
4.3.3	Projections of M13-AuNP loading of the substrate	181
4.3.3.1	Projections using average AuNP-GA size	182
4.3.3.2	Projections using maximum AuNP-GA size	184
4.4	Conclusions	185
CHAPTER 5	CONCLUDING REMARKS AND GOING FORWARD	187

REFERENCES

191

APPENDICES

I

LIST OF FIGURES

Figure 1.1	p1	Projection of areas suitable to be expanded by MM.
Figure 1.2	p2	Current projections of the MM research.
Figure 1.3	p5	The protein structure of M13 bacteriophage.
Figure 1.4	p6	Image of the <i>Morpho didius</i> butterfly.
Figure 1.5	p7	Rig set-up used to template M13 onto various substrates.
Figure 1.6	p10	Degrees of hierarchical ordering.
Figure 2.1	p19	Schematic of UV-vis spectrophotometer.
Figure 2.2	p21	Schematic of POM reflectance technique.
Figure 2.3	p22	Schematic of AFM scanning technique.
Figure 2.4	p24	Schematic of SEM scanning technique.
Figure 2.5	p28	Schematic of stages 2-4 of the phage propagation process
Figure 2.6	p30	Mechanism of PVIII protein modification to display thiol functionality
Figure 2.7	p34	Schematic of 'in-house' rig used to achieve EFD on a substrate.
Figure 2.8	p38	A characteristic UV-vis spectrum obtained from M13.
Figure 2.9	p39	A characteristic CD spectrum obtained from M13.

Figure 2.10	p41	Optical images of SSD deposition technique.
Figure 2.11	p42	POM imaging of M13 SC onto BSi.
Figure 2.12	p43	Increased magnification POM images of SC M13 onto BSi.
Figure 2.13	p45	AFM images of SC M13 onto BSi.
Figure 2.14	p47	Bungee cord suspension system used to template M13 onto substrates.
Figure 2.15	p48	Schematic of the EFD process
Figure 2.16	p55	a) POM image of M13 templated at $14.9 \mu\text{m}.\text{min}^{-1}$ on BSi b) AFM image of M13 templated at $14.9 \mu\text{m}.\text{min}^{-1}$ on BSi.
Figure 2.17	p56	a) POM image of M13 templated at $52.0 \mu\text{m}.\text{min}^{-1}$ on BSi b) AFM image of M13 templated at $52.0 \mu\text{m}.\text{min}^{-1}$ on BSi.
Figure 2.18	p58	a) POM image of M13 templated at $74.3 \mu\text{m}.\text{min}^{-1}$ on BSi b) AFM image of M13 templated at $74.3 \mu\text{m}.\text{min}^{-1}$ on BSi.
Figure 2.19	p60	a) POM image of M13 templated at $96.5 \mu\text{m}.\text{min}^{-1}$ on BSi b) AFM image of M13 templated at $96.5 \mu\text{m}.\text{min}^{-1}$ on BSi.
Figure 2.20	p61	a) POM image of M13 templated at $148.5 \mu\text{m}.\text{min}^{-1}$ on BSi b) AFM image of M13 templated at $148.5 \mu\text{m}.\text{min}^{-1}$ on BSi.

Figure 2.21	p62	Graphical comparison of ridge width within the 1D arrays, constructed via varying ridge widths using AFM and POM analysis.
Figure 2.22	p64	Boxplot to demonstrate the effect of templating speed on ridge diameter during the EFD process on BSi from POM.
Figure 2.23	p65	Two-way ANOVA analysis for the ridge diameter taken from POM imaging.
Figure 2.24	p66	Boxplot to demonstrate the effect of templating speed on ridge diameter during the EFD process on BSi from AFM.
Figure 2.25	p66	Two-way ANOVA analysis for the ridge diameter taken from AFM imaging.
Figure 2.26	p68	Boxplot to demonstrate the effect of templating speed on bundle diameter during the EFD process on BSi.
Figure 2.27	p68	Two-way ANOVA analysis for the bundle diameter taken from AFM imaging.
Figure 2.28	p69	Boxplot to demonstrate the effect of templating speed on bundle diameter during the EFD process on BSi.
Figure 2.29	p70	Two-way ANOVA analysis for the bundle diameter taken from AFM imaging.
Figure 2.30	p71	Colormap key to indicate the colour representation of the FFT images used here for spatial frequency.

Figure 2.31	p72	Phase-scan profiles of M13 templated onto BSi at varying speeds and the corresponding histogram plots
Figure 2.32	p73	Phase-scan profiles of M13 templated onto BSi at varying speeds and the corresponding histogram plots
Figure 2.33	p74	FFT of height scan profiles of M13 templated onto BSi at varying speeds.
Figure 2.34	p75	FFT of height scan profiles of M13 templated onto BSi at varying speeds.
Figure 2.35	p77	a) POM image of M13 templated at 52.0 $\mu\text{m}.\text{min}^{-1}$ on AuSi b and c) AFM images of M13 templated at 52.0 $\mu\text{m}.\text{min}^{-1}$ on AuSi.
Figure 2.36	p78	a) POM image of M13 templated at 74.3 $\mu\text{m}.\text{min}^{-1}$ on AuSi b and c) AFM images of M13 templated at 74.3 $\mu\text{m}.\text{min}^{-1}$ on AuSi.
Figure 2.37	p80	a) POM image of M13 templated at 96.5 $\mu\text{m}.\text{min}^{-1}$ on AuSi b and c) AFM images of M13 templated at 96.5 $\mu\text{m}.\text{min}^{-1}$ on AuSi.
Figure 2.38	p81	a) POM image of M13 templated at 111.4 $\mu\text{m}.\text{min}^{-1}$ on AuSi b and c) AFM images of M13 templated at 111.4 $\mu\text{m}.\text{min}^{-1}$ on AuSi.
Figure 2.39	p83	Boxplot to demonstrate the effect of templating speed on ridge diameter during the EFD process on AuSi.

Figure 2.40	p83	Two-way ANOVA analysis for the ridge diameter taken from AFM imaging.
Figure 2.41	p84	Boxplot to demonstrate the effect of templating speed on bundle diameter during the EFD process on AuSi.
Figure 2.42	p85	Two-way ANOVA analysis for the bundle diameter taken from AFM imaging.
Figure 2.43	p86	Boxplot to demonstrate the effect of templating speed on bundle diameter during the EFD process on AuSi.
Figure 2.44	p87	Two-way ANOVA analysis for the bundle diameter taken from AFM imaging.
Figure 2.45	p89	Phase-scan profiles of M13 templated onto AuSi at varying speeds and the corresponding histogram plots.
Figure 2.46	p90	FFT of height scan profiles of M13 templated onto AuSi at varying speeds.
Figure 2.47	p92	AFM image of M13 templated at 52.0 $\mu\text{m}.\text{min}^{-1}$ on AuGMS.
Figure 2.48	p93	AFM image of M13 templated at 74.3 $\mu\text{m}.\text{min}^{-1}$ on AuGMS.
Figure 2.49	p94	AFM image of M13 templated at 96.5 $\mu\text{m}.\text{min}^{-1}$ on AuGMS
Figure 2.50	p94	AFM image of M13 templated at 96.5 $\mu\text{m}.\text{min}^{-1}$ on AuGMS - increased resolution.

Figure 2.51	p95	AFM image of M13 templated at 111.4 $\mu\text{m}.\text{min}^{-1}$ on AuGMS
Figure 2.52	p96	AFM image of M13 templated at 148.5 $\mu\text{m}.\text{min}^{-1}$ on AuGMS.
Figure 2.53	p97	AFM image of M13 templated at 148.5 $\mu\text{m}.\text{min}^{-1}$ on AuGMS – increased resolution.
Figure 2.54	p98	Phase-scan profiles of M13 templated onto AuGMS at varying speeds and the corresponding histogram plots.
Figure 2.55	p99	Phase-scan profiles of M13 templated onto AuGMS at varying speeds and the corresponding histogram plots
Figure 2.56	p100	FFT of height scan profiles of M13 templated onto AuGMS at varying speeds.
Figure 2.57	p101	FFT of height scan profiles of M13 templated onto AuGMS at varying speeds.
Figure 2.58	p105	Schematic displaying the effect of pore size on the incident light beam.
Figure 3.1	p114	Interaction of CPL with an inherently chiral structure.
Figure 3.2	p116	Schematic representation of negative phase velocity leading to negative refraction.
Figure 3.3	p118	Schematic representation of reflectivity and refractivity of light through a medium.

Figure 3.4	p119	Schematic representation for linear reflectance characterisation of 1D arrays of M13 templated via EFD onto BSi and AuSi.
Figure 3.5	p121	Schematic representation for linear refraction characterisation of 1D arrays of M13 templated via EFD onto AuGMS.
Figure 3.6	p123	Schematic representation for DCD and (<i>g</i>) characterisation of 1D arrays of M13 templated via EFD onto BSi and AuSi.
Figure 3.7	p124	Experimental rig set up for DCD and (<i>g</i>) characterisation of 1D arrays of M13 templated via EFD onto BSi and AuSi.
Figure 3.8	p128	Schematic representation for DCD, (<i>g</i>) and negative refraction characterisation of 1D arrays of M13 templated via EFD onto AuGMS.
Figure 3.9	p129	Trigonometric calculation of the laser displacement of the refracted light beam.
Figure 3.10	p132	Visual representation of the colour change observed by M13 1D arrays templated onto BSi ($G=55\text{ }\mu\text{m}$).
Figure 3.11	p134	Graphical representation of normalized reflection, as a function of wavelength and periodicity for M13 templated via EFD onto BSi wafers at varying templating speeds.
Figure 3.12	p135	Graphical representation of normalized reflection, as a function of wavelength and

periodicity for M13 templated via EFD onto AuSi wafers at varying templating speeds.

- Figure 3.13 p138 **Graphical representation of normalized reflection, as a function of wavelength and F for M13 templated via EFD onto BSi wafers at 74.3 $\mu\text{m}.\text{min}^{-1}$.**
- Figure 3.14 p139 **Graphical representation of normalized reflection, as a function of wavelength and F for M13 templated via EFD onto BSi wafers at 74.3 $\mu\text{m}.\text{min}^{-1}$.**
- Figure 3.15 p142 **Graphical representation of g , as a function of wavelength and periodicity for M13 templated via EFD onto BSi wafers at varying templating speeds.**
- Figure 3.16 p144 **Graphical representation of g , as a function of wavelength and periodicity for M13 templated via EFD onto AuSi wafers at varying templating speeds.**
- Figure 3.17 p145 **Graphical representation of broadening and narrowing of I_{osc} , as a function of periodicity (G) for M13 templated via EFD.**
- Figure 3.18 p147 **Graphical representation of g , as a function of wavelength and F for M13 templated via EFD onto BSi wafers at 74.3 $\mu\text{m}.\text{min}^{-1}$.**
- Figure 3.19 p149 **Graphical representation of g , as a function of wavelength and ϕ for M13 templated via EFD onto AuSi wafers at 96.5 $\mu\text{m}.\text{min}^{-1}$.**

Figure 3.20	p151	Representation of θ_t and θ_i values able to produce negative refraction.
Figure 3.21	p152	Graphical simulation for FOM as a function of λ and Γ.
Figure 3.22	p154	Simulation of the gradient value as a function of Γ and λ_0, for M13 templated onto BSi.
Figure 3.23	p155	Simulation of the gradient value as a function of Γ and λ_0 for M13 templated onto AuSi.
Figure 3.24	p157	MATLAB simulation observing the intrinsic and extrinsic chirality of the 1D arrays of varying ridge diameter (G) for M13 templated onto BSi.
Figure 3.25	p158	MATLAB simulation observing the intrinsic and extrinsic chirality of the 1D arrays of varying ridge diameter (G) for M13 templated onto AuSi.
Figure 3.26	p159	MATLAB simulation observing the intrinsic and extrinsic chirality of the 1D arrays of varying ridge diameter (G) for M13 templated onto AuSi at a reduced range of wavelengths.
Figure 3.27	p160	MATLAB simulation observing the intrinsic and extrinsic chirality of the 1D arrays of varying ridge diameter (G) for M13 templated onto PtSi.
Figure 3.28	p162	MATLAB plot using a, simulated and b, practical data to observe how small angles of F impacted the refractive index of the 1D arrays, of varying ridge diameter (G) for M13 templated onto AuGMS.

Figure 3.29	p163	MATLAB plot using practical data to observe how small angles of F impacted the refractive angle of the 1D arrays, of varying ridge diameter (G) for M13 templated onto AuGMS.
Figure 3.30	p164	MATLAB plot using a, practical data to observe how small angles of F impacted the refractive index of the 1D arrays, of varying ridge diameter (G) for M13 templated onto AuGMS.
Figure 3.31	p165	MATLAB plot using theoretical data to observe how small angles of F impacted the refractive index of the 1D arrays, of varying ridge diameter (G) for M13 templated onto AuGMS.
Figure 4.1	p175	Surface attraction between GA and the nanomaterial surface.
Figure 4.2	p177	Schematic of the phage-based detection system for Pb²⁺.
Figure 4.3	p179	Observational colour change during successful AuNP synthesis.
Figure 4.4	p179	Absorbance of prepared AuNP.
Figure 4.5	p180	DLS size distribution by volume.
Figure 4.6	p180	UV-Vis spectra for the formation of M13-AuNP.
Figure 4.7	p181	AFM image of M13-AuNP onto BSi.
Figure 4.8	p182	AFM image of M13-AuNP templated onto AuSi via EFD. M13
Figure 4.9	p184	Projection for the number of AuNP-GA per area.

Figure 4.10 p185 **Projection for the number of AuNP-GA per area.**

LIST OF TABLES

Table 2.1	Bond energies for Au coupled molecules.
Table 2.2	SC experimental conditions for templating of M13 onto BSi and AuSi.
Table 2.3	Templating speeds utilised during EFD for M13 templating of a 1D array on varying substrates.
Table 2.4	Optical techniques utilised for characterisation of the topographical characteristics of the 1D arrays.
Table 2.5	Frictional forces per substrate taken from literature values.
Table 2.6	Experimental data gained for M13 templated onto BSi at varying speeds.
Table 2.7	Experimental data gained for M13 templated onto AuSi at varying speeds.
Table 2.8	Experimental data gained for M13 templated onto AuGMS at varying speeds.
Table 3.1	The effect of wavelength of the incident light beam to the sample surface in generating a refractive index.
Table 4.1	Characterisation data for synthesised AuNP.

LIST OF UNITS

Å	Angstroms
:	Ratio
(g)	Anisotropic Factor
%	Percent
%T	Percentage Transmittance
%v/v	Percentage as volume per volume
°	Degrees
°C	Degrees Centigrade
<	Less than
>	More than
≈	Around
≤	Less than or equal to
≥	More than or equal to
A	Absorbance
arcsin	Anti-sine
cm	Centimetre
d	Diameter
d.nm	Nanometre Diameter
F	Frequency

g	Grams
h	Hours
I	Intensity of light reaching detector
I ₀	Intensity of incident light
kV	Kilo Volts
M	Molar
M .cm	Moles per Centimetre Cubed
mdeg	milliidegrees
mA	milli Amps
mg.cm-2	milligrams per centimetre squared
mg.mL-1	milligrams per millilitre
min	Minute
mm	Millimetre
mM	Millimolar
mm.min-1	Millimetre per minute
mW	Milli Watts
N/m	Newtons per metre
nm	Nanometre
nM	Nanomolar
sec	Seconds

THz	Tetrahertz
V	Volts
W	Watts
Γ	Gamma, Periodicity
Δ	Delta, Change in
ϵ M.cm	Molar absorptivity
n	Refractive Index
θ	Theta, angle
θ_i	Incident Angle of Light Beam
$\theta_{t,\perp}$	Negatively Refracted Light Beam Angle
λ	Wavelength
μm	Micrometre
μM	Micromolar
$\mu\text{m.min}^{-1}$	Micrometre per minute
μW	Microwatts
Φ	Phi, Incident Angle of Light Beam Incident to Outer Surface

LIST OF EQUATIONS

EQUATION NUMBER	EQUATION
Eqn.1.1	Intrinsic = function of λ Extrinsic = function of Φ
Eqn.1.2	$\Delta CD = \frac{RCP-LCP}{RCP+LCP}$
Eqn.1.3	$g = \frac{2(RCP-LCP)}{RCP+LCP}$
Eqn.2.1	$\%T = \frac{I}{I_0}$
Eqn.2.2	$A = -\log \left(\frac{\%T}{100\%} \right)$
Eqn.2.3	$\frac{0.1}{\text{Stock Phage Concentration}} = X \text{ mL to each NB}_2 \text{ beaker}$
Eqn.2.4	$\frac{\text{Absorbance} \times \text{dilution factor}}{3.84} = \text{Conc. (mg.mL}^{-1}\text{)}$
Eqn.3.1	$\eta_1 \sin \theta_1 = \eta_2 \sin \theta_2$

Eqn.3.2	$\theta_{t,\perp} = \arcsin[\eta_{sub}\sin(\theta_i) - (\lambda_0/\Gamma)]$
Eqn.3.3	$\%R = \frac{I}{I_0} \times 100$
Eqn.3.4	$\tan(\theta_{t,\perp}) * 7 = AB$
Eqn.3.5	$\theta_{t,\perp} = \tan^{-1}\left(\frac{AB}{7}\right)$

LIST OF ABBREVIATIONS AND COMMON TERMS

λ	(lambda) wavelength
θ	(theta) angle (degrees)
Φ	(phi) incident angle of light
Δ	(delta) change in...
Γ	Periodicity
n	Refractive Index
-SH	Sulphydryl Bond
1D	One-Dimensional
2D	Two-Dimensional
3D	Three-Dimensional
AAS	Atomic Absorption Spectrometry
AFM	Atomic Force Microscopy
ALD	Atomic Layer Deposition
AuGMS	Gold coated Silica Fused Glass Microscope Slides
AuNP	Gold Nanoparticle
AuSi	Gold Coated Silicon Wafers
BSi	Bare Silicon Wafers
CA	Contact Angle

ca.	Around
Cc	Critical Contact Angle
CD	Circular Dichroism
CPL	Circularly Polarised Light
dd	Double Distilled
DLS	Dynamic Light Scattering
DNA	Deoxyribonucleic acid
DSTL	Defence Science for Technology Laboratory
<i>E.coli</i>	Escherichia coli
EFD	Evaporative Front Deposition
Eqn.	Equation
FIR	Far Infrared Range
fN	Frictional forces
FOM	Figure of Merit
GMS	Silica Fused Glass Microscope Slides
HMI	Heavy Metal Ions
ICP-AES	Inductively Coupled Atomic Emission Spectrometry
ICP-MS	Inductively Coupled Mass Spectrometry
ICP-OES	Inductively Coupled Optical Emission Spectrometry

IR	Infrared Spectrophotometry
LC	Liquid Crystal
LCP	Left-handed Circularly Polarized Light
LOD	Limit of Detection
M13	M13 Bacteriophage
M13-AuNP	M13 Bound Gold Nanoparticles (see M13)
MIR	Mid Infrared Range
MM	Metamaterials
MS	Mass Spectrometry
NIM	Negative Index of Refraction Material
NIR	Near Infrared Range
NP	Nanoparticle
PC	Photonic Crystal
POM	Polarized Light Microscopy
ppt.	Precipitate
PtSi	Platinum Coated Silicon Wafers
PtNP	Platinum Nanoparticle
PVIII	Major Coat Protein p8 of M13 (see M13)
RCP	Right-handed Circularly Polarized Light
rpm	Rotations Per Minute

SC	Spin Coating
SDC	Sessile Drop Casting
SEM	Scanning Electron Microscopy
SERS	Surface Enhanced Raman Scattering
SPR	Surface Plasmon Resonance
ssDNA	Single Stranded DNA (see DNA)
UV-vis	Ultra-violet Visible Spectrophotometry

CHAPTER 1 THE SCOPE OF BIOLOGICAL METAMATERIALS

Metamaterials (MM) are defined as artificially engineered materials that do not exist in nature. The development of MM was a rapidly expanding field that continues to redefine the boundaries of materials science. The versatility in which their functionality can be predetermined allowed highly tuneable structures and materials with significant advantages over their conventional counterparts. The exotic properties exhibited by MM will contribute to advances in an expanse of fields including imaging, sensing, data storage, defence, quantum image processing and light harvesting (Figure 1.1).¹⁻⁵

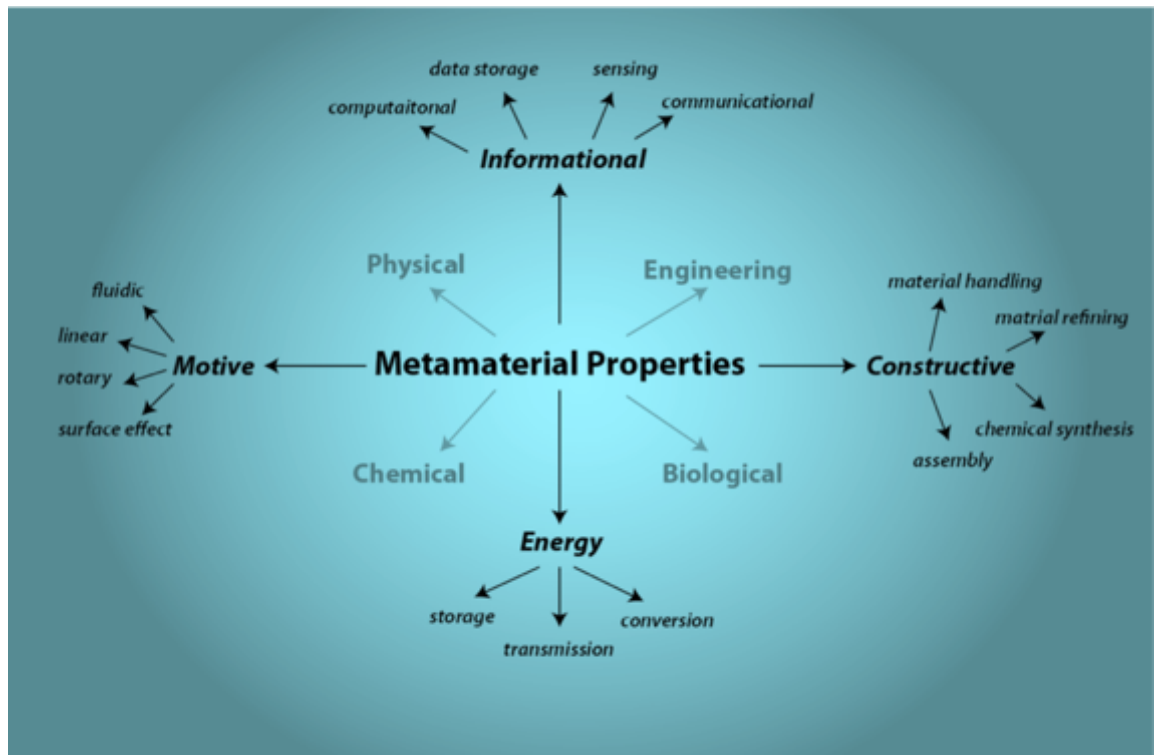


Figure 1.1 | Projection of areas suitable to be expanded by MM. MM are of an interdisciplinary nature and so have the potential to be exploited in a wide range of fields attributing to their broad range of characteristics.

Whilst Sir John Pendry was not the first to propose the field of MM, it was his research on cloaking and light manipulation in early 2000 which spearheaded the

exponential increase of worldwide MM research.⁶ Whilst a relatively young field, MM quickly gained traction within aerospace and the defence sector. This was due to their extraordinary capabilities, ranging from super-strength to lightweight composition and invisibility.⁵ MM have the ability to demonstrate properties that go beyond classical science, rendering them highly desirable. The use of the MM research has been predicted to surge between the 2016 – 2020. It was expected that the \$45 million invested around the globe in 2016 will rise to around \$250 million by 2020 and \$1.35 billion by 2025 for the aerospace and defence sector alone (Figure 1.2).⁷

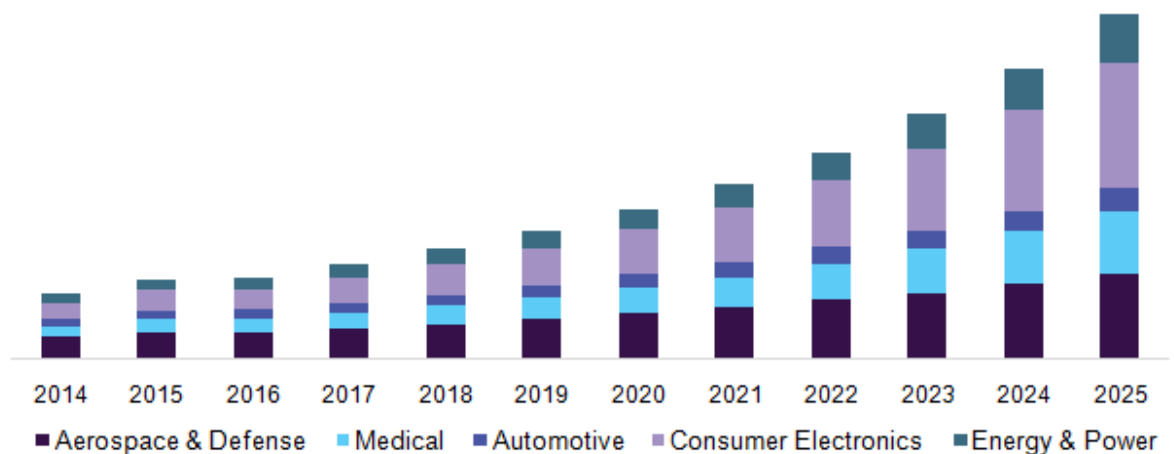


Figure 1.2 | Current projections of the MM research. Research projections from 2014 through to 2025 for aerospace and defence, medical, automotive, consumer electronics and energy and power. Reproduced with permission from Grand View Research.⁷

MM are created *via* ‘top-down’ systems incorporating metallic components through the use of both nano- and photolithographic techniques. However, these processes are costly with the creation of potential hazardous by-products during the fabrication process.⁸ Furthermore the processes are very labour intensive, often encompassing multiple complex stages. ‘Top-down’ systems encompass the fabrication of materials with a predesigned functionality. While they are readily reproducible, they are of a small scale with limited resolution with scalability restrictions. ‘Bottom-up’ systems use molecular building components to achieve structures and networks using chemical components and self-assembly

techniques.^{8–11} A gap has therefore been identified, whereby one can exploit the properties of molecules found in nature to achieve MM in a more economic and environmentally friendly manner. Exploiting nature's building blocks allowed major drawbacks of current MM production: scalability to be overcome.¹²

To date the majority of MM have been constructed from inorganic materials such as silicon (Si) and gold (Au). These materials, well known for their extraordinary electromagnetic properties, have been the driving force behind applications in cloaking and super-lenses.¹³ An alternative biological building block, namely M13 bacteriophage (M13), can be exploited for its intrinsically chiral structure to produce novel MM.^{9,14} The flexibility and high aspect ratio for functionality of M13, combined with its availability for large scale production within a short time frame reaching titres of up to 10^3 per mL in small scale cultures, make it ideal from both a fundamental science and application standpoint.¹⁵ Together these characteristics make it superlative for translation into industrial applications.¹⁶

Herein, innovative synthetic biology based nanoporous 3D networks, functioning as MM, through their liquid crystal (LC) and hierarchical structural properties has been produced. These networks displayed a negative refractive index and high chirality for the architected networks; these particular characteristics have demonstrated cloaking abilities in literature.

1.1 Biological Building Blocks and Synthetic Biology

Interdisciplinary research has led to new fields of research such as synthetic biology, in which a biological and engineering approach was combined to construct novel biomolecular components, networks and pathways.^{9,17} These constructs then have the possibility to reprogram and rewire organisms, and to yield innovative characteristics that would not usually be possible by the constituent components alone.⁹

Biological molecular organisms and assemblies pose as excellent models for the development of nano-engineered systems with desired chiroptical properties. Biological systems in particular are driven towards energetically favourable structures that have increased molecular sensitivity and recognition. This makes them ideal building blocks for nanoscale based molecular assembly.^{18–20}

1.1.1 M13 Bacteriophage

M13 was a robust filamentous bacteriophage that retains the ability to be easily functionalised through its protein rich high aspect ratio exterior (800 nm × 6 d.nm, Figure 1.3). M13 itself was made up of a major and minor coat proteins. The 50-residue major coat protein (PVIII) comprises 98% by mass of the M13 bacteriophage and contains 3 distinct areas:

- 1. A negatively charged hydrophilic N-terminal domain consisting of amino groups of lysine residues (residues 1-20)**
- 2. An intermediate hydrophobic domain consisting of carboxylic acid groups of aspartic acid or glutamic acid residues (residues 21-39)**
- 3. A positively charged domain that interacts electrostatically with phage genomic DNA due to the phenol group of tyrosine residues (residues 40-50)**

The N-terminal domain represents the only region that would be exposed to any media; thus, it was the only area available for genetic or chemical functionalization. M13 was able to withstand adverse conditions such as high salt concentration, acidic and basic pH environments ($2 < \text{pH} < 12$), prolonged storage and high temperatures ($< 100\text{ }^{\circ}\text{C}$).^{15,21–24} These physical characteristics make M13 advantageous for use in the extreme conditions required for 'bottom-up' assembly techniques.^{15,24}

M13 has previously been shown to demonstrate a great ability to produce intricate structures such as stars, cubes and letters through synthetic biology techniques such as genetic modification and insertion, DNA origami and self-assembly, and chemical modification.^{25–28} However, translation of these processes to create a 3D network at macro or industrial scale was relatively unexplored. In addition the construction of such networks and structures for use in aerospace and defence systems was even sparser.²⁹ Therefore, efforts were focused into creating systems that are directly translational into defence sectors.

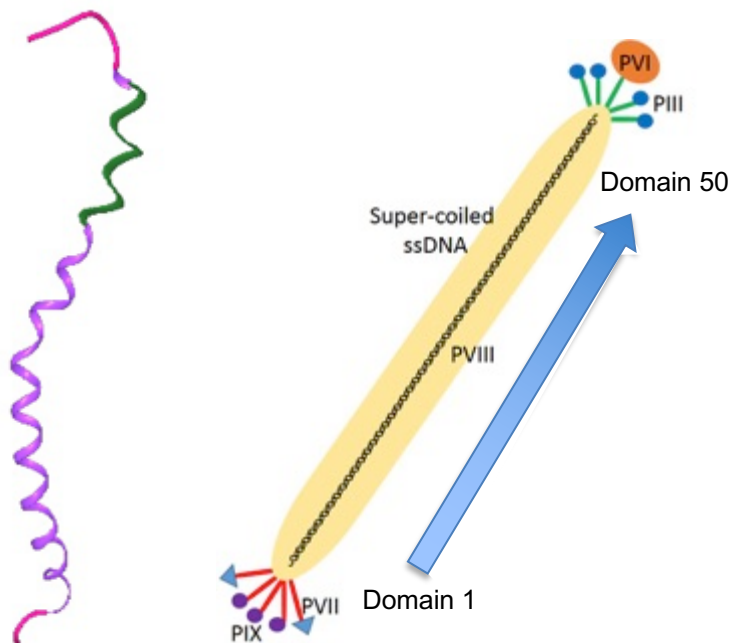


Figure 1.3 | The protein structure of M13 bacteriophage. The major (PVIII) coat protein alongside the minor coat proteins (PIII, PVI, PVII and PIX) and the super-coiled ssDNA on the interior of the PVIII are indicated above.

Chung et al. confirmed the capability of M13 to show LC characteristics. They were able to achieve molecular alignment of M13 on a substrate by withdrawing the substrate through a solution of phage molecules *via* syringe pump. This allowed for control over the observed colour of the templated surface through modulation of the speed at which the substrate was withdrawn and concentration of M13 within the solvent (PBS).³⁰ Whilst the method by *Chung et al.* was not

particularly expensive, using a syringe pump introduced limitations into the system for scaling up to industry. Expanding on their initial set-up a more cost-efficient in-house rig set-up capable of evaporative front deposition (EFD), was engineered with the added ability to be scaled-up for industry.



Figure 1.4 | Image of the *Morpho didius* butterfly. The structural colour was due to the hierarchical nature of the wing scales. The hierarchical nature allowed the butterfly to yield a different observational colour dependant on the angle of viewing.³¹ Reproduced with permission from the Tropical Andean Butterfly Diversity Project.

A similar effect of angular colour change was observed in the blue/green colour of the *Morpho didius* butterfly (Figure 1.4). Its structural colour was generated by topography of the wings and their photonic crystal (PC) structure. Naturally occurring PC structures such as this are typically 3D, however they can also be quasi-ordered (ordered but not periodic) led to difficulties in complete structural replication.^{12,32–34} The filamentous nature of M13 allowed it to behave as a LC, a property that can give rise to similar properties of PC. It was this ability that subsequently allowed M13 to be self-assembled into a hierarchical structure using facile techniques such as EFD.^{9,35–37} The set-up proposed by *Chung et al.* was modified to construct an in-house rig consisting of an automated micrometer

withdrawal system controlled through a Raspberry Pi 2 configured with a Gertbot GUI. The in-house rig (Figure 1.5) allowed for the very slow withdrawal speeds required for ordering of M13 on a substrate ($1.48 \mu\text{m}.\text{min}^{-1}$ to $14.86 \text{ mm}.\text{min}^{-1}$).

The rig developed here, differed significantly from *Chung et al.* in that their process consisted of a syringe driver retracting the substrate from the solution, to yield a receding meniscus in a downward motion.

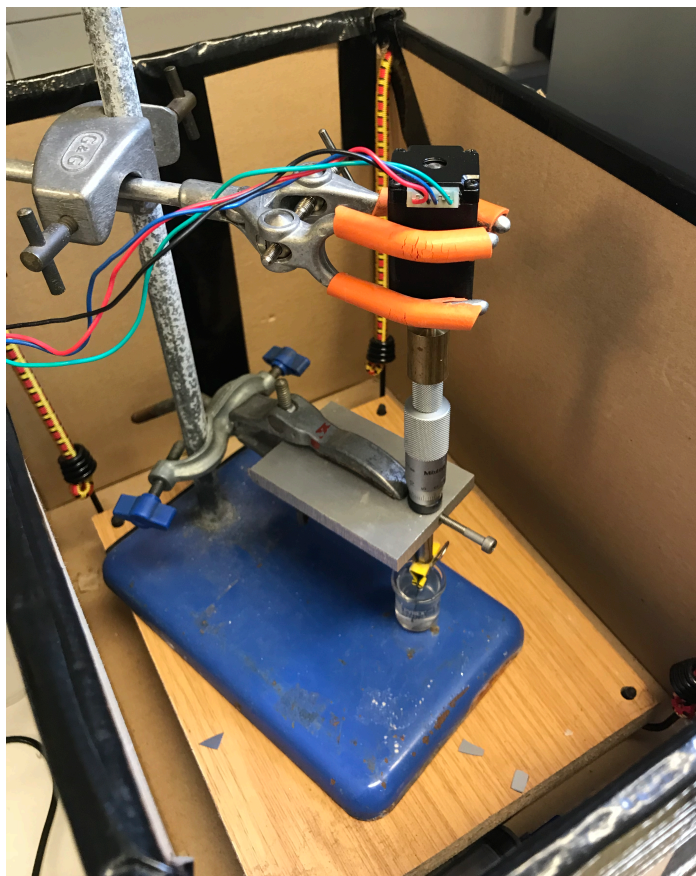


Figure 1.5 | Rig set-up used to template M13 onto various substrates. The rig set up allowed slow templating of M13 onto substrates at speeds between $1.48 \mu\text{m}.\text{min}^{-1}$ and $14.86 \text{ mm}.\text{min}^{-1}$

The rig provided a tuneable and facile approach to ordering M13 and subsequently other desired nanomaterials onto a substrate surface through EFD. EFD allowed the production of 1D and 2D arrays, which demonstrate internal 3D hierarchical structures.^{38,39} Initial experiments and simulations conducted within this project have indicated interesting properties, such as strong chirality (section;

3.1.3) and negative refraction (section; 3.1.4). Such extraordinary capabilities demonstrated by the fabricated structures presents them as viable options for further development and transition into potential defence applications.

1.2 Self-Assembly and Functional Nanoporous Networks

As previously described, the focus of this research was towards developing a self-assembled approach to functional and 3D MM structures. In particular, methods surrounding drying-mediated self-assembly of non-volatile solutes through irreversible solvent evaporation were explored. The ease in production of large and complex 3D structures *via* this approach makes it an attractive fabrication method for translation into a broad scale of industries.^{15,40,41}

Self-assembly allowed control over the dimensionality of the evolving nanostructures, whereby individual constituent components of a material do not have the capacity to self-assemble *via* conventional manufacturing methods, or generic wet chemistry techniques.⁴² Guided self-assembly has proved to be both cost and production efficient through combining the advantages from both ‘top-down’ and ‘bottom-up’ assembly systems.^{9,10,43} Both the physical and experimental parameters can be fine-tuned and manipulated to yield a highly tuneable fabrication method.

In solution, M13 was able to interact with a range of components, such as nanomaterials, quantum dots and fluorescent dyes to generate complex ordered structures at the evaporation line.^{26,44–47} These components can be pre-fabricated to have specific functionality, which can be transferred into the 3D network. The high aspect ratio of M13 and availability of the protein exterior for functionalization allowed for an even distribution of the desired components.⁴⁸ Incorporation of functional materials to interconnect with a 3D scaffold with uniform distribution was still a significant challenge using ‘top-down’ lithographic methods.⁴⁹ Creating such functional networks could provide increased

performance for a range of fields, including photovoltaics, optical imaging and electrochemical devices due to the high aspect ratio for charge transport and nanoscale features that M13 provides.^{9,50–53}

Nanoporous networks offer advantages over bulk, macro, meso or micro-porous structures, due to the higher surface area per unit area for the material.^{1,54–57} Generally, nanopore arrays are fabricated with energy intensive approaches that are neither cost nor environmentally friendly. Approaches include electron beam etching, nano-imprinting, nano-lithography and atomic layer deposition (ALD).^{54,58} Methods involving nucleating of materials and/or metals onto a previously formed biological scaffold typically generate pores of meso/micro-scale opposed to nanopores.^{55,59,60} These methods were therefore not explored for the architecture of the 3D structures described in this work.

Recently, *Courchesne et al.* used a ‘one-pot’ approach to develop a high porosity gel. It consisted of an M13 fibre biomolecular scaffold throughout the system for electrochemical and catalytic applications.⁴⁴ However, the fabrication methodology led to a highly aggregated network of bundled structures that consisted of large pore sizes, thereby lowering its functionality for catalysis and electrochemical applications.^{44,61} Furthermore the distribution of functional nanomaterials proceeded to be irregular over the entire surface.⁴⁴ Functionalization of M13 prior to templating would provide well-dispersed arrays of nanomaterials throughout the scaffold. Inclusion of noble metal nanomaterials, such as gold (Au) and platinum (Pt) within the structure could lead to the production of plasmonic structures within the material.^{59,62,63} Enhanced performance of light absorbance, light trapping and transmitting devices could, therefore, be readily achieved.

1.3 Liquid Crystals

Materials found in nature can be divided into different phases known as states of matter. These individual states are dependent on the mobility of the individual atoms or molecules within the structure.⁶⁴ Whilst solids, liquids and gases are the most commonly described states, there are other intermediate phases that can be observed. The majority of these intermediate states are witnessed between the solid and liquid phases. These states resemble solids yet are capable of free flow, much like a liquid.^{64,65} These fluidic states allow molecules to demonstrate ordered alignment, a phenomenon referred to as 'phase ordering'.^{1,30}

Ordinary liquids by nature are isotropic *i.e.* they are optically and magnetically the same from all directions, and therefore are equally disordered in all directions. LCs are anisotropic, in which the opposite effect was observed.^{35,56,66,67} Weak intermolecular forces between molecules plague LC, and so they can be easily perturbed by an electric field. Electric fields can manipulate and orientate the alignment of the molecules due to their polarity.⁶⁸ Electric field stimulation therefore highlights how LC are capable of demonstrating hierarchical ordering throughout the system. Subsequent classifications of LC are then defined by their molecular alignment (Figure 1.6).⁶⁸

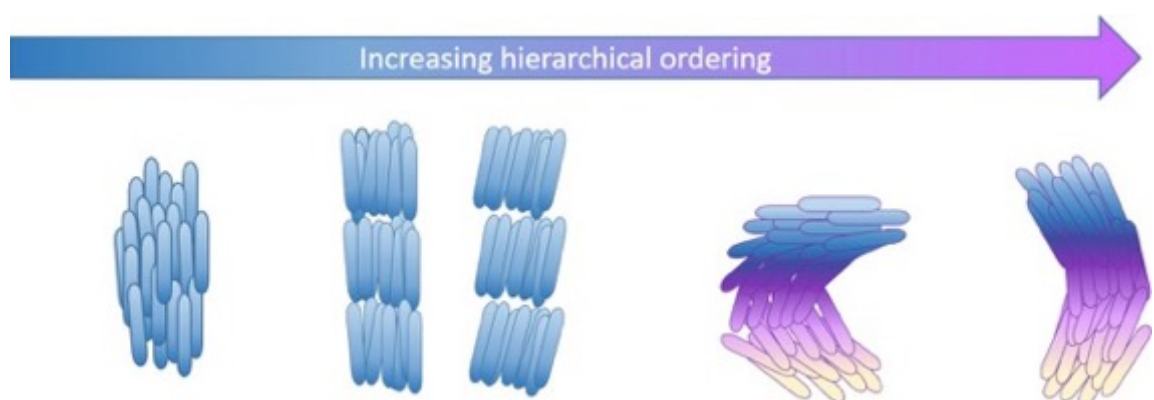


Figure 1.6 | Degrees of hierarchical ordering. From left to right: the degree of hierarchical ordering increases within liquids from nematic to smectic phase and finally to the cholesteric (chiral nematic) phase.

Nematic phase ordering was directional ordering along the longitudinal director axis (y-axis), however there was no further orientation in the horizontal x-axis. The nematic phase therefore mostly resembles the isotropic phase.^{56,64} An increase in molecular alignment including x-directional order was termed smectic. It presents orientation and some periodicity. The chiral smectic phase closest resembles the phase ordering witnessed in a solid crystal, whereby orientation and full periodicity was observed.⁶⁴ A final cholesteric phase was an amalgamation of chiral smectic and nematic ordering, in which there was director axis ordering (nematic phase), however, the axis was not fixed in space and so was free to rotate throughout the sample.⁶⁴ The intermolecular forces between molecules in the cholesteric phase are such that they favour alignment at a slight angle to each other.³⁰ Therefore for a molecule to be considered as a LC the following conditions must be met:

- **The molecule must have an aspect ratio that was >1:1 to yield an elongated shape**
- **It must have some degree of rigidity**
- **It must have ends or a point which was somewhat flexible for allowance of a liquid crystal to be formed**

1.4 Bio-inspired Metamaterials, Photonic Crystals and Chirality

PC represent a broad class of crystal molecules that contain spatial periodicity within their dielectric constant.²⁹ Under specific conditions, PC have the ability to create a photonic band gap - a frequency window in which the propagation of light was inhibited.^{69,70} This inhibition at defined frequencies allowed for a periodically changing dielectric constant, which in turn alters the propagation of electromagnetic radiation.^{71,72} PC yields structures in which the movement of energy through the system progresses at such a slow rate, that the stationary modes act as resonators reflecting light in anomalous and unexpected directions.¹³

This phenomenon was the basic principle relating to negative refraction, one of the most highly desired MM behaviours for the defence sector.⁷³

MM have similar properties to PC. However, they have one distinct difference. Each part of the MM has the ability to respond independently and uniquely to the radiated spectrum.^{5,74} One of most desirable conditions that a MM can therefore display was invisibility, whereby the MM can create electromagnetic blind spots.^{75–78} These blind spots are then able to ‘cloak’ objects from view. *Wang et al.* successfully managed to develop an organic-inorganic composite material with PC structure *via* Atomic Layer Deposition (ALD).⁷³ A mask layer was used to mimic the shape of the scale on the wings of *Papilio blumei*. Whilst being able to create intricate mimics of the upper surface layer, ALD produces inaccurate internal replication. Further, ALD also lacks scalability, as the process was limited to the dimensionality of the original structure, in this case the wing dimension.^{12,69,79} The problems associated with simple masking methods probed consideration of methods of fabrication that can produce unique properties similar to that achieved by *Wang et al.* without the limits of dimensionality and poor internal replication.⁸⁰

Nature has produced a large variety of objects that possess chiral morphology, ranging from macroscopic seashells to nanoscopic DNA.^{30,81} Transfer of chiral information through biomolecular components has facilitated the formation of chiral macroscopic shapes in living organisms. Chirality in molecular systems and assemblies was attributed to the dissymmetry of the environment and the chiroptical properties of such systems.³³ Due to the complex nature of chirality transfer, the research surrounding biomimetics and replication was still very active.

Circular dichroism (CD) has long been established and extensively used to demonstrate the ground state chiroptical properties of a system. The process considers the difference in response to either reflected or transmitted circularly

polarised light (CPL) taken at 45° and 135° (Left-handed Circularly Polarised light (LPC) and Right-handed Circularly Polarised light (RCP), respectively). The differential emission of LCP vs. RCP was correlated to the excited state properties of the chiral system. On manipulation of the incident polarization angle the response of the sample changes accordingly to the incident field. When biomolecules, such as M13, inherently chiral itself, interact with CPL, a CD effect or optical rotary dispersion can be observed.^{9,82,83}

The chirality of the bulk system as a non-molecular system must be considered when developing macro-scale 3D architectures to allow them to be scalable to industrial level. For chirality to be observed in a macro-scale object the upper limit of the size and scale of the optical cavities must be an order of magnitude smaller than the wavelength of light. This was so that light can perturb the optical cavities.³⁴ In the case that would mean the inter-bundle spacing within the 3D structure would need to be smaller than the incident wavelength of light used to observe such chirality. (See Chapter 2 for more information regarding the physical parameters of the 3D scaffold). It was therefore expected that the near infrared (NIR) range and above will generate the highest degree of chirality due to the dimensionality of the ridges and inter-bundle distance of the 3D scaffold.⁸⁴ Chirality was divided into two sub categories: extrinsic and intrinsic. The former was concerned with chiroptical activity observed due to a change in angle of the sample to the incident light beam, whereas the latter was a result of a change in the wavelength of light used to perturb the sample.^{82,85}

$$\begin{aligned} \text{Intrinsic} &= \text{function } (\lambda) \\ \text{Extrinsic} &= \text{function } (\Phi) \end{aligned} \quad (\text{Eqn.1.1})$$

Since Watson and Crick first discovered DNA double helix in the early 1950's, there has been a great interest in mimicking chiral activity in other forms.⁸⁶ On the nanoscale these chiral structures are termed chiral nanostructures or chiral nanoarchitectures. The fabricated structures can serve as a bridge between

intrinsically chiral building blocks such as DNA and M13, and macroscopic functional entities.^{23,38}

M13 fibres act as nanoscopic monomeric chiral units that can be assembled into higher order meso- or macroscopic aggregates or architectures. The chirality of the system can then be expressed at a range of length scales *via* cooperative effects resulting from inter and intra-molecular chirality interactions among the primary chiral units.^{57,84} Through performing systematic differential emission CD measurements (ΔCD) on samples with an array of different experimental conditions the cooperative chirality as a function of changing geometric shape and hierarchical ordering can be examined.⁸⁴

$$\Delta CD = \frac{RCP - LCP}{RCP + LCP} \quad (\text{Eqn.1.2})$$

1.5 The Route to Optical Metamaterials and Negative Index Materials

An optical MM was a composite in which sub-wavelength features, along with the constituent materials, control the macroscopic electromagnetic properties of the material. Newly invented MM open new opportunities to the optical engineer to design novel properties for optical materials, demonstrating unique optical phenomena and applications. Negative index materials (NIM) represent one of the most desired fields of MM as they present possibilities in extensive applications such as cloaking, super-lenses, perfect-lenses and infinite resolution detectors.^{87,88}

Traditional examples of NIM have played upon the material simultaneously displaying negative values for both permittivity (ϵ) and permeability (μ), achieved through intricate nanofabrication of structures.^{89–91} Whilst these designs have been expanded into the Near Infra-Red (NIR) and optical wavelengths, the NIM produced loses a great deal of energy within the system and require complex and

expensive production methodology. More recent developments, such as that by *Hoffmann et al.* exploit anisotropic behaviour to achieve NIM activity in the NIR range using a simple fabrication method of layering doped/undoped heterostructures and quantum well super-lattices.⁸⁷

Using an inherently chiral biomolecule such as M13 as the foundation for a 3D MM, it was believed possible to achieve anisotropic hierarchical devices with expected unique characteristics as described by *Hoffmann et al.* Templating a crystalline layer of M13 on top of a crystalline substrate, such as Si or Au coated Si (AuSi) affords an epitaxial crystalline structure, that eliminates the need for further nano-fabrication.⁵⁹ Furthermore, the structures are inherently 3D and planar, where the operational NIM wavelength range was determined by the free carrier charge density, the dimensionality and the periodicity of the structure. In the case the dimensionality and periodicity refers to the ridge height and ridge diameter.^{87,92} Chirality plays a prominent role in this work as it was known to have a distinct influence on the spin of photons. In conventional materials LCP and RCP propagate at the same phase velocity. However, in chiral materials one polarization was more dominant than the other, propagating at a faster phase velocity. The inferior phase velocity slows down and in the case of sufficiently strong chirality can become negative. It was this negative phase velocity that can produce NIM, irrespective of whether the material has simultaneously negative values for the permittivity of the medium (ϵ) and the permeability of the medium (μ).^{85,91} *Zhang et al.* reported this extraordinary effect to be attributed to the negative refractive index observed by their micrometre (μm) array of gold resonators at terahertz wavelengths (1.06 – 1.27 THz).⁹¹ It was therefore expected that the 3D constructs produced by the EFD at a given wavelength and/or angle of incidence could potentially show activity as NIM, due to their strong chirality towards one polarization *i.e.* a distinct shift from (LCP- ΔCD =0 (Eqn.1.2) or (g)=0 (Eqn.1.3).^{76,93,94}

$$(g) = \frac{2(RCP-LCP)}{RCP+LCP} \quad (\text{Eqn. 1.3})$$

1.6 Outline of the Thesis

The aim of the research within this thesis was to bridge the traditional sciences, forming an interdisciplinary approach of using synthetic biology to achieve MM. Advanced deposition processes were facilitated to achieve highly ordered, hierarchical and tuneable structures, through the combination of both ‘Top-down’ and ‘Bottom-up’ assembly techniques.

In the first instance, M13 was used as a biological building block to architect 3D scaffolds onto an array of substrates. This will be achieved *via* controlled deposition processes, whereby the physical, chemical and mechanical parameters of the fabrication process will be considered. Characterization followed for the robustness of the fabrication process for reproducibility and tunability through topographical imaging techniques (Chapter 2). The scaffolds will also be tested for activity as functional optical MM alongside the topographical imaging. The experimental data collected related to the activity of an optical MM will then be compared to a theoretical model (Chapter 3).

In addition to the fabrication of an optical MM, the efficiency of the produced M13 structure to act as a scaffold to display functional nanoparticles were explored briefly (Chapter 4). In considering the 3D scaffold for further functionalities it was shown that the scaffold was not limited to an optical MM but could also be used for a broad range of industrial applications. Therefore, it was anticipated that the findings described here will pave the way for further developments towards functional smart materials.

CHAPTER 2 M13: A SELF-ASSEMBLING BUILDING BLOCK

The physical properties of M13 make it an exceptional candidate in acting as a biological building block in assembling the 3D scaffold. To achieve isolation of M13 ssDNA a short propagation period of 16 hours incubation, followed by 8 hours of post incubational stages, made it a quick process, and fosters its use for large-scale production.^{15,24} Initial stages of the project surrounded the architecting of M13 bundles atop of a suitable substrate and in a periodic fashion. Achieving periodicity within the sample was deemed crucial in developing a tuneable MM with properties as described in section 1.

Self-assembled MM remains a relatively young field of research, however it has shown great promise in its short career in producing structures with properties not witnessed in nature.^{1,9,11} The engineered structures utilise a range of architectural methods with nanolithography being amongst the most widely used.^{10,49} Whilst nanolithography can produce intricate and reproducible structures at the nanoscale it was an exceptionally expensive and cumbersome technique that would be challenging to employ in creating bulk 3D metamaterials.^{92,95} Utilising facile techniques influenced by the intrinsic self-templating ability of M13, the aim was to achieve bulk 3D MM at large scales with techniques that are much more economically viable by using low-cost elements and environmentally friendly due to the lack of harmful chemicals used during nanolithography.

The aims of this chapter are:

- **Successful propagation of M13 and modification of the PVIII**
- **Explore deposition methods to create periodic ordering**
- **Explore the transferability of the optimal deposition method to other substrates**
- **Determine the tunability of the periodic array on the substrates**
- **Select 3D nanoarchitectures suitable for characterisation of MM activity**

2.1 Methodology

2.1.1 Materials and Reagents

Phosphate buffered saline (PBS) pellets were purchased from Sigma-Aldrich and made up according to specification, the PBS solution was further autoclaved to prevent contamination of M13 stock solutions. Si wafers and glass microscope slides (GMS) were used as supplied with no further cleaning required.

2.1.2 Instruments

Heating and magnetic stirring during experiments was conducted on a Camlab MS-H280-Pro. An Avanti J-26S Series ultracentrifuge and a SciSpin SS-6010 desktop centrifuge were used for the propagation technique alongside a Stuart SA8 vortex mixer and a Brunswick Innova 4330 Refrigerated Floor Incubator Shaker. A Rodwell ambassador autoclave set a 121 °C, 1 bar pressure for 15 minutes, was used to promote sterile conditions for the propagation of M13. UV-Vis spectroscopy was carried out using a Cary 6000i UV-Vis-NIR combined with Cary WinUV software

2.1.3 Analysis Techniques

2.1.3.1 Ultra Violet-Visible Spectrophotometry

Ultra-violet-visible spectrophotometry (UV-Vis) was carried out using a Cary 6000i UV-Vis-NIR combined with Cary WinUV software. UV-Vis was an instrument used to determine the transparency of a sample (Figure 2.1). The intensity of light reaching the detector (I) was compared to the initial intensity of the incident light beam (I_0). The ratio of transmitted light to incident light was then given as a percentage of transmittance (%T). (Eqn.2.1)

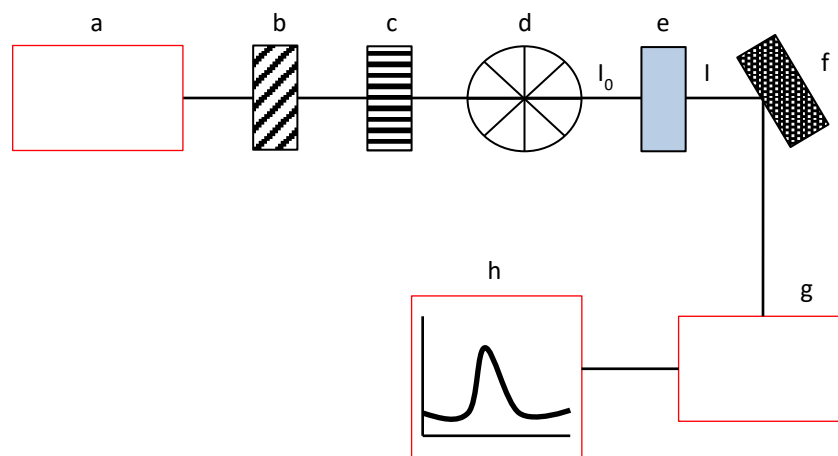


Figure 2.1 | Schematic of UV-vis spectrophotometer. **a)** the initial light source emits a beam that passes through **b)** a diffraction grating followed by **c)** a slit. **d)** A monochromator emits the specific wavelength of light required by the system yielding the incident wavelength of light (I_0), which passes through **e)** the sample to afford the transmitted wavelength of light (I). **f)** A mirror reflects the light onto **g)** a detector which transfers the information to **h)** a computer display system.

$$\%T = \frac{I}{I_0} \quad (\text{Eqn. 2.1})$$

The percentage transmittance can then be converted to absorbance (A) using the antilog functionality. (Eqn.2.2).

$$A = -\log \left(\frac{\%T}{100\%} \right) \quad (\text{Eqn. 2.2})$$

A baseline of the solvent in which the solute was dispersed will be taken and removed from the absorbance signal of the sample. For the measurements concerned with this research UV-vis data will be noted in terms of absorbance.

2.1.3.2 Polarised Light Microscopy

Polarised light microscopy (POM) was carried out using a Leica DM 2700M polarised light microscope fitted with a Leica LH 113 LED lamp (U;12V, DC; Pramx: 15W). A Leica DFC295 (12V/170 mA) camera system was used to observe samples (Figure 2.2) under linearly polarised light (LPL).

A range of objectives were utilised to observe the sample topography (5×, 10×, 20×, 50×, and 100×) after which the images were processed with ImageJ imaging software. A linear polarizer allowed the user to manipulate the plane of polarisation (0°– 90°) in respect to the sample.

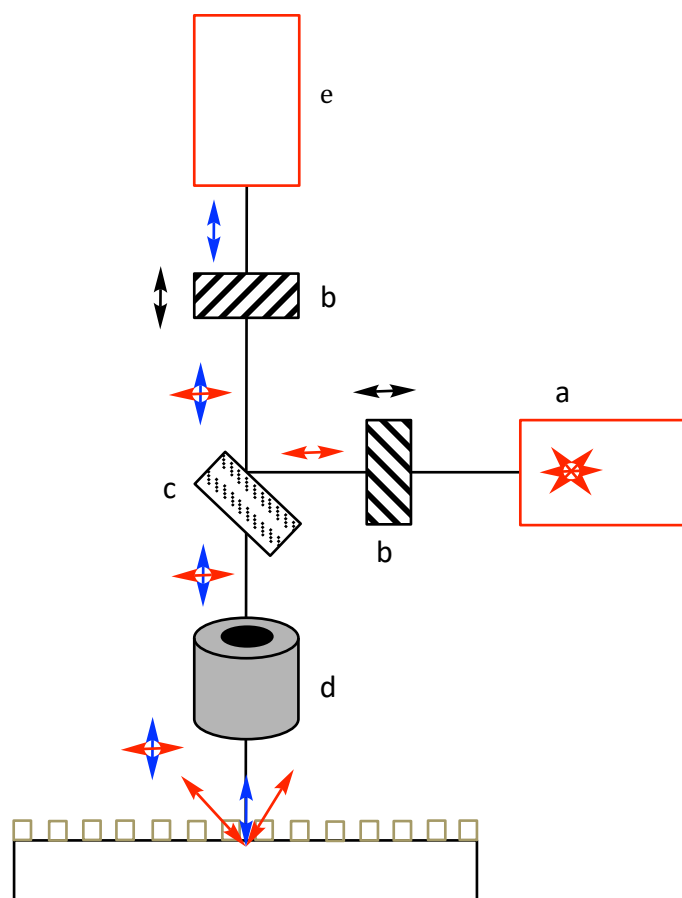


Figure 2.2 | Schematic of POM reflectance technique. a) light from a lamp was emitted through b) an initial polarizer to c) a beam splitter through d) an objective lens and onto the sample surface. The reflected beam was then reflected back up towards e) a camera or spectroscopic detector connected to a visual display.

2.1.3.3 Atomic Force Microscopy

Atomic force microscopy (AFM) is a form of scanning probe microscopy with resolution on the order of a fractions of a nanometre making it the highest resolution scan used in this thesis. A sharp tip is raster-scanned over a surface using a feedback loop (Figure 2.3) to adjust parameters needed to image a surface, whereby the sample is not required to be conducting.¹²²

Atomic forces are used to map the tip-sample interaction. A laser beam detection system is created by a laser being reflected from the back of the reflective AFM cantilever (opposite side to the tip) and back to the position-sensitive detector. As the tip interacts with the surface, the laser position on the photodetector is used within the feedback loop to track the surface for imaging and measuring.¹²²

AFM measurements were made using a Nanowizard II AFM (JPK Instruments AG, Berlin, Germany), using height profile modulation. The tip height was 10 – 15 μm , with a cantilever force constant of 10 – 130 N/m. Scans were processed using JPK Data Processing software (JPK Instruments AG, Berlin, Germany).

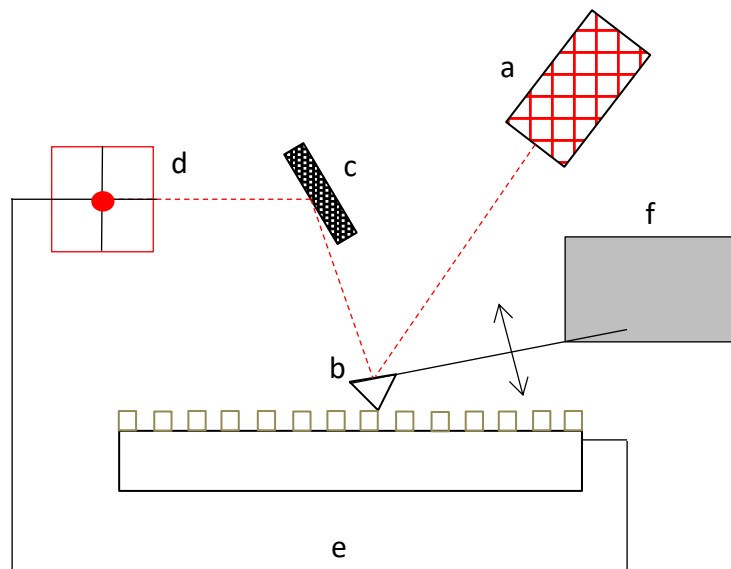


Figure 2.3 | Schematic of AFM scanning technique. **a)** the laser projects on the **b)** tip of the cantilever, before being reflected onto **c)** a mirror and **d)** the photodiode detector. **e)** The feedback loop returns topographical information about the surface to **f)** the piezoelectric driver to apply more or less force to the cantilever to create a topographical scan on a display.

As the tip of the probe scans the surface of the sample, van der Waals forces (VDW) are detected between the sample and tip through deflection of the probe, which was calculated from the reflected laser deflection. PointProbe Plus (PPP-NCR) non-contact high resonance frequency silicon scanning mode microscopy

sensors were used, with tip radius <10 nm (Nanosensors TM., Switzerland). Tapping mode was chosen due to sample deformation associated with contact mode AFM, and also removes artefacts created via the stick-slip phenomenon (tip sticking to the sample). The use of tapping mode also allowed for a more accurate representation of the topographical area when processed into a 3D surface profile.

2.1.3.4 Scanning Electron Microscopy

Scanning electron microscopy (SEM) consists of five main components:

- **Source of electrons (Figure 2.4a)**
- **Column down which electrons travel with electromagnetic lenses (Figure 2.4b, 2.4c and 2.4d)**
- **Electron chamber (Figure 2.4g)**
- **Sample chamber (Figure 2.4e and 2.4f)**
- **Computer and display to view image (Figure 2.4h and 2.4j)**

During SEM, electrons are produced at the top of the column and are accelerated down and pass through a combination of lenses and apertures to produce a focused beam of electrons. This focused beam of electrons then hits the surface of a sample which must be conductive. The sample is mounted onto a stage in the chamber area, and both the chamber and column are evacuated by a combination of pumps to create a vacuum. The position of the electron beam on the sample is controlled by scan coils. The scan coils are situated above the objective lens and allow the beam to be scanned over the surface of the sample. As electrons interact with the sample, they produce secondary electrons, backscattered electrons and characteristic X-rays which produced signals that are collected by detectors.¹²²

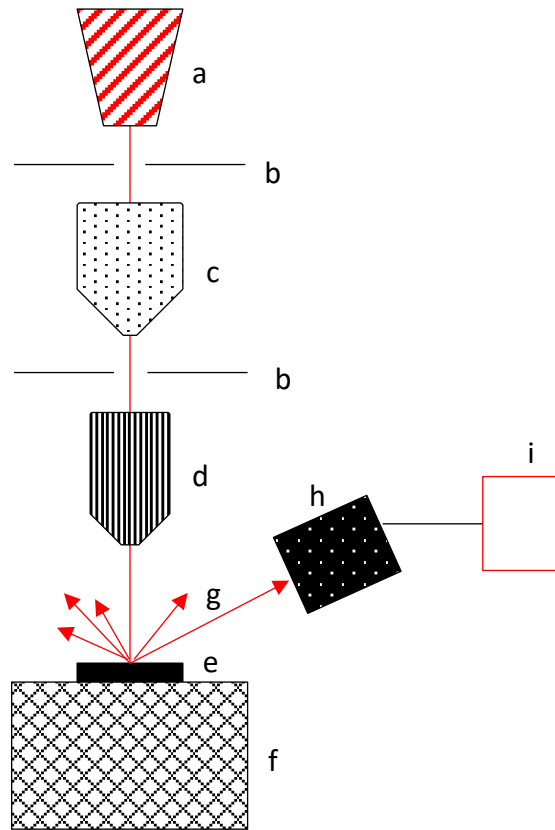


Figure 2.4 | Schematic of SEM scanning technique. a) the electron source emits a steady beam of electrons, the beam passes through b) a limiting aperture, before c) a condenser lens and a secondary limiting aperture. The beam finally passes through d) an objective lens prior to hitting e) the sample mounted on top of f) a conductive stub. g) Secondary electrons are refracted off of the sample, with some reaching h) the detector. The data was relayed from the detector to i) a computer interface for analysis.

SEM allowed higher magnification investigation of a specimen when compared to POM. Under vacuum conditions, an electron beam was fired at the surface of the sample. Prior to SEM analysis samples underwent sputter coating. Sputter coating provided grounding *via* a thin, conductive coating for specimens. Thus, prior to imaging samples using SEM, specimens were mounted on an SEM stub with conductive double-sided tape and were sputter coated with gold at 2.5kV using an Agar automatic sputter coater (Agar Scientific, Elektron, Technology UK

Ltd, Essex, UK) for 30 s at 20 mA, followed by a further 30 s at 30 mA, to ensure an even covering of 150 – 200 Å.⁹⁶

Samples were imaged using a Hitachi TM3030 SEM (Hitachi Ltd., Tokyo, Japan) at 15 kV.

2.1.4 Propagation and Isolation of M13 ssDNA

2.1.4.1 M13 Structure

M13 bacteriophage contains major and minor coat proteins as described earlier (Figure 1.3), with the 50-residue PVIII major coat protein making up 98% by mass of the entire bacteriophage. PVIII contains three domains:

- 1. Negatively charged hydrophilic N-terminal domain (residues 1 – 20)**
- 2. Intermediate hydrophobic chain (residues 21 – 39)**
- 3. Positively charged domain (residues 40 – 50) that interacts electrostatically with phage genomic DNA**

Only the N-terminal domain is exposed to media during any modifications.

Initially, incubation of inoculated media for growth of M13 was carried out. Isolation of the ssDNA from M13 followed through separating the phage from the cellular components of the *E.coli* Top 'F host cells by centrifugal force. This was sufficient to remove the phage particles from the media and cells in which they were contained. The small size of M13 allowed it to remain within the supernatant, whilst cells and cellular debris are pelleted. M13 was then removed from the supernatant *via* the use of polyethylene glycol (PEG) and sodium chloride (NaCl), this process was termed PEGylation. PEG acts to absorb the water from the centrifuged sample, thus allowing the phage to aggregate and precipitate into a pellet for further use in analyses.⁹⁷

Preparation of NB₂ broth and PEG - Stage 1:

NB₂ powder (60 g) was dissolved in ddH₂O (2.4 L). The resulting NB₂ solution was separated into 6 × 2L conical flasks (400 mL to each) and a sponge seal was added and topped with foil. PEG (6000 Da, 250 g) and NaCl (146 g) were added to a beaker (1 L) and made up to 1 L with ddH₂O under magnetic stirring (15 min, or until reagents are dissolved). The PEG/NaCl solution was separated into 2 × 1 L autoclave bottles. Both the NB₂ and PEG solutions were autoclaved prior to further stages.¹⁵ (Figure 2.5)

Amplification of M13 using *E.coli* top 10 'F host cells - Stage 2:

Tetracycline (0.01g) was added to ethanol (2 mL, to yield a 5 mg.mL⁻¹ solution). Inoculation of NB₂ broth was carried out using aseptic technique, by adding the prepared tetracycline solution (400 µL) and *E.coli* top 10 'F cells (500 µL) to each beaker of NB₂ (6 × 400 mL) alongside a calculated volume of stock M13 phage solution (Eqn. 2.3). The beakers were then left to incubate (37 °C, 200 rpm, 16 hours).¹⁵ (Figure 2.5)

$$\frac{0.1}{\text{Stock Phage Concentration}} = X \text{ mL to each NB}_2 \text{ beaker} \quad (\text{Eqn.2.3})$$

Purification of M13 phage - Stage 3:

The amplified M13 was separated into 6 × 500 mL ultracentrifuge tubes and centrifuged (4 °C, 8500 rpm, 30 min). The supernatant was then removed, and the solution centrifuged again (4 °C, 8500 rpm, 30 min). The supernatant (80% ≈ 300 µL) was collected from each beaker and combined into a conical flask with a magnetic stirrer bar. The PEG/NaCl solution (1:5 %v/v, ≈ 360 µL) was added to the beaker and the solution was left on ice with stirring (90 min).¹⁵ (Figure 2.5)

Collection of M13 precipitate - Stage 4:

The solution was then separated into 6 × 500 mL ultracentrifuge tubes and centrifuged (4 °C, 10000 rpm, 25 min). The supernatant was discarded, and the pellet re-suspended in minimal amount PBS buffer (50 mM, ≈ 1 mL, pH 8.0). The suspensions were then centrifuged (using a desktop centrifuge, 15000 rpm, 5 min) and the supernatants collected in fresh Eppendorf tubes.

PEG/NaCl solution was again added (1:5 %v/v, ≈ 200 µL) to each tube and left on ice (60 min). The resulting suspensions were centrifuged (using a desktop centrifuge, 14000 rpm, 15 min) with the supernatant discarded. The pellets were then suspended in PBS buffer (50 mM, ≈ 200 µL, pH 8.0) and subsequently combined in a falcon tube.^{15,97} (Figure 2.5)

$$\frac{\text{Absorbance} \times \text{dilution factor}}{3.84} = \text{Conc. (mg.mL}^{-1}\text{)} \quad (\text{Eqn. 2.4})$$

During initial propagation of M13 difficulties were experienced due to the fluctuation of the freestanding incubator not reaching desired temperatures adequately. The incubator was therefore set at 40°C for stage 2 of M13 propagation to allow for optimal growth of M13 within the given 16-hour incubation period. Confirmation of successful M13 propagation was confirmed *via* UV-vis analysis. A characteristic absorption peak was expected at 269 nm. To calculate the concentration of the produced stock solution, the phage was diluted by a factor of 100 in PBS buffer and the absorbance read at 269 nm. The ϵ of M13 phage was 3.84 mg.cm⁻² at 269 nm and so the concentration could be calculated using Eqn. 2.4. For accurate calculation of the concentration of the propagated solution a maximum accepted relative absorbance of 1.5 was considered. If the value of absorbance fell above 1.5 the sample was further diluted by a factor of 10 using PBS solution until a suitable absorbance was observed.

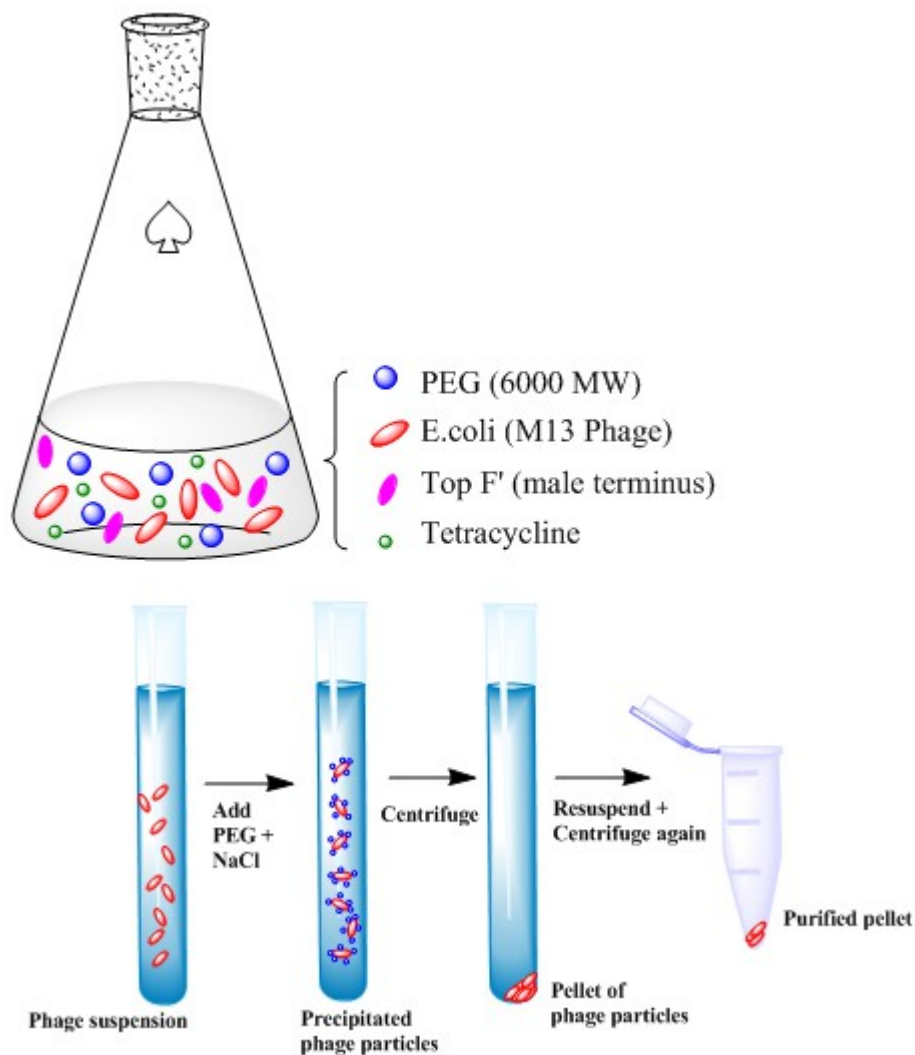


Figure 2.5 | Schematic of stages 2-4 of the phage propagation process.¹⁵

2.1.5 Thiol modification of M13

M13 viral solution (1 mL, 2 mg.mL⁻¹, in PBS) was added to N-succinimidyl-S-acetylthiopropionate (SATP), (10 µL, ≈ 55 mM in dimethyl sulfoxide (DMSO) and left to equilibrate (room temperature (RT), 1.5h). The modified phage was then purified *via* PEG precipitation (ppt.) (×2) and resuspended in PBS (1 mL). The modified single stranded DNA (ssDNA) can then be kept at 4 °C.⁹⁸

Deacetylation to generate direct -SH groups was achieved by adding modified ssDNA (200 μ L) to PBS (800 μ L) and hydroxylamine (100 μ L, 0.5 M in PBS + 25 mM ethylenediaminetetraacetic acid (EDTA)). The reaction was left to proceed (RT, 2h) prior to purification by PEG ppt. ($\times 2$). The resulting ppt. was dissolved in PBS (1 mL) and stored at 4 $^{\circ}$ C.⁹⁸

2.1.6 PVIII Thiol Modification

Functionalising the PVIII with -SH groups provided a more stable bond between M13 bundles and the gold coated silicon substrates (AuSi). SATP modification of the Nitrogen (N)-termini of PVIII was modified to present an acetyl-protected sulphur (S) group along the exterior. Hydroxylamine ($\text{NH}_2\text{OH}\cdot\text{HCl}$) was then able to remove the protecting acetyl group. The higher donor strength of sulphur, compared to nitrogen, allowed for direct bonding of –sulphur-hydrogen (-SH) functional groups to the PVIII *via* short (Table 2.1), strong and stable covalent bonds between the biomolecule and AuNPs (Figure 2.6).⁹⁸

Table 2.1 | Bond energies for Au coupled molecules. Bond energies are highlighted for the range of bonds that are formed during the wet-chemistry techniques and M13 propagation and modification^{99,100}.

Bond	Bond Energy (kJ/mol)	Bond length (\AA)
Au-Si	312	2.251
Au-Au	221.3	2.868
Au-H	314	2.620
Au-S	418	2.314
HS-SH	272	1.490

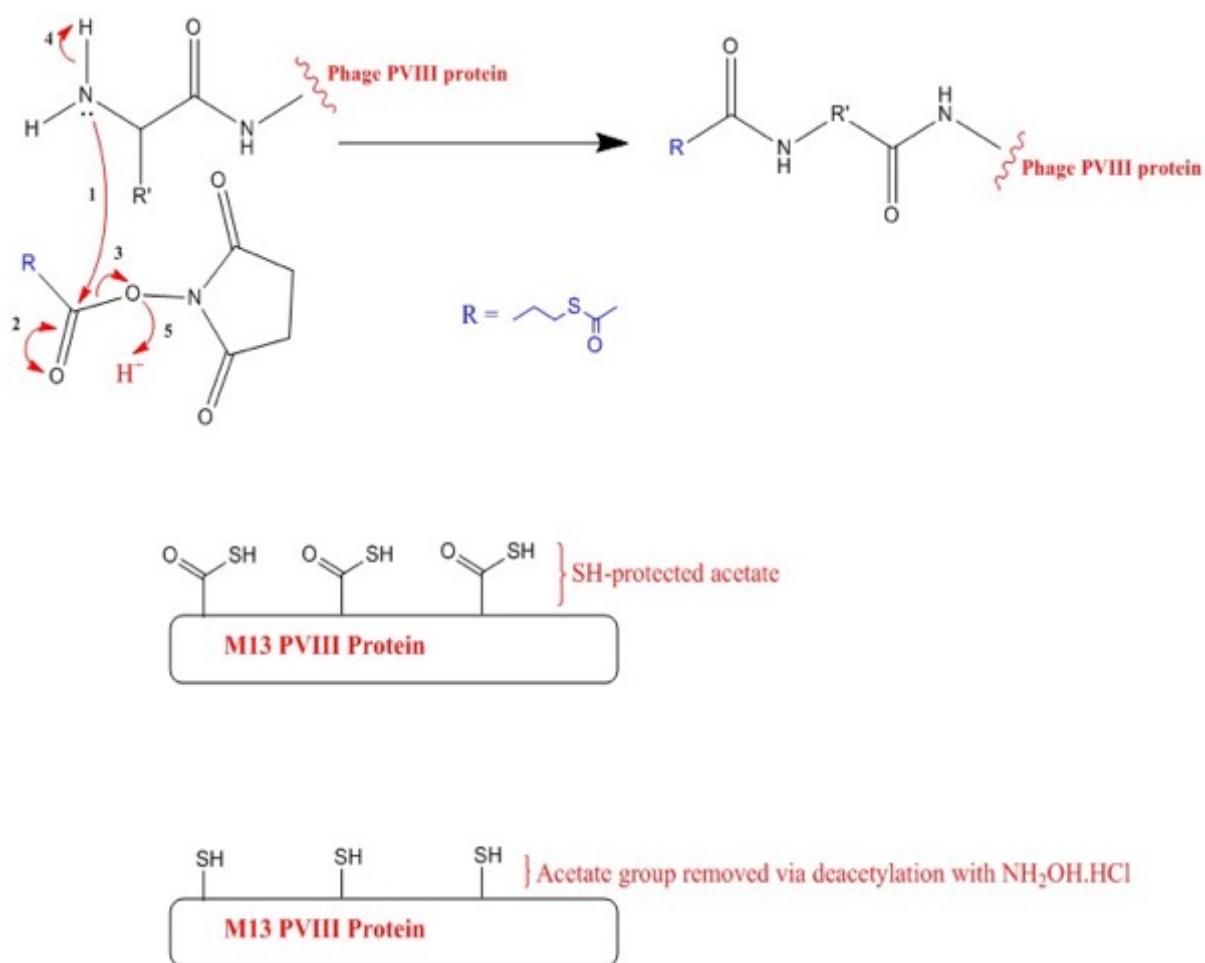


Figure 2.6 | Mechanism of PVIII protein modification to display thiol functionality.

2.1.7 Surface Modification of Substrates Prior to Deposition Techniques

To achieve Au coated substrate surfaces sputter coating of the surfaces was carried out using an Agar Automatic Sputter Coater B7341 (Agar Scientific, Elektron, Technology UK Ltd, Essex, UK).

BSi (polished side) wafers were used as the initial substrate material for analysis of deposition techniques. Where coating of BSi with Au was required, a sputter coating technique was utilised to create a homogeneous layer of Au on the polished side of BSi.

Portions of BSi were initially cut from the purchased BSi wafer and cleaned with acetone and dd H₂O prior to coating. The cut BSi wafers were then placed into the vacuum chamber of the sputter coater fitted with an Au target. To generate a thin layer of Au on the surface (10 nm), a current of 20 mA for 30 seconds was used in the presence of an Argon (Ar) stream. Subsequently the substrate was baked for 1 hour at 250°C to adhere the Au layer to the BSi wafer. The height of the Au layer was established using atomic force microscopy (AFM). This was achieved by placing a BSi wafer over one half of BSi wafer to be coated. Upon removal of the wafer it was possible to see the area of Au deposition due to a clear colour change on the surface. A range of currents and times for deposition of Au were explored to reach a desired homogenous layer of Au using the minimum amounts of energy, the corresponding data are found in Appendix I

The same methodology was further used to coat glass microscope slides with thin layers of Au (10 nm).

2.1.8 Sessile Drop Casting

Sessile Drop Casting (SCD) was performed by pipetting 10 µL of a desired solution onto the substrate and allowed to air dry for 15 minutes. After 15 minutes the sample was dried with a constant flow of N₂ gas. The dried solutes were then suitable for imaging *via* POM and AFM.

To prevent saturation of the substrate with solute after drying, a reduced concentration of solute within the media was required. In the case of M13 dispersed within a PBS solution, concentration of 0.01 mg.mL⁻¹ was used.

2.1.9 Spin Coating

A Laurell Model WS-650MZ-23NPPB spin coater was utilized for this methodology.

Spin coating (SC) was carried out on both BSi and AuSi wafers produced as per section 2.1.7. Portions (1 cm²) of the substrates were cut prior to the SC deposition, during SC a constant air flow of N₂ was used, and a standard time setting of 10 minutes. M13 was used at a concentration of 0.01 mg.mL⁻¹ for all samples. The samples were then subjected to topographical analysis using POM and AFM. Through the introduction of energy into the deposition process *via* SC methodology, it was expected that a more ordered system could be achieved than simple observed with SDC.¹⁰¹

The conditions trialed during SC are detailed below in Table 2.2. The conditions were repeated for both BSi and AuSi.

Table 2.2 | SC experimental conditions for templating of M13 onto BSi and AuSi. Sample conditions that were tested are indicated by an X and those not trialed indicated by a –.

Rpm of SC →				
Volume M13 soln./ μL ↓	2,000	3,000	4,000	10,000
5	–	–	–	X
10	X	X	X	–
25	X	X	X	–

2.1.10 Shearing Force and Channelled Deposition

Moving on from the efforts towards SDC of M13 onto a surface, other facile methods of deposition were explored. Work achieved by Merzlyak *et al.* demonstrated the ability to control the directionality of M13 fibres on a substrate surface. This was through genetic modification of the M13 PVIII protein with iodoacetamide and maleimido compounds, to generate phage-encoded peptides

with three cysteines combined with application of shear force to a droplet of M13 solution atop of a glass microscope slide.^{23,102} The success by Merzlyak *et al.* prompted considerations to modifications that could be applied to the experimental methodology, to achieve hierarchically ordered 3D structures of increasing intricacy, over the nematic ordering they had achieved.

When considering other literature, it was observed that one way to achieve increased hierarchical ordering through using techniques such as shear force, would be to embed narrow channels within the substrate surface. The target material, such as M13, could be probed to self-assemble into hierarchical materials along the narrow channels.^{103–105} As it was desired to use a simple and inexpensive route to induce micro channels within the substrate surface, it was chosen to pursue a facile method of stretching strips of PDMS to 1.5× of its' original length. This was followed with subsequent UV light curing to achieve regular ridges and grooves throughout the surface.^{42,106,107} After subjecting the substrate surface to stretching and curing, the shearing force methodology described by Merzlyak *et al.* was used.¹⁰⁸

It was expected that the grooves within the surface topography would be sufficient to allow the M13 fibres to bundle over one another as they accumulated more heavily within the narrow channels. This combined with the parallel orientation of the grooves to the directionality of which the shear was applied to the surface would achieve a hierarchical ordered system. However, when attempting to create regular grooves within the surface topography of PDMS, only irregular structures were constructed within the PDMS including multiple cracks within the topography. Therefore, it was decided to move to other methods of deposition that could be templated onto reproducible surfaces.

2.1.11 Evaporative Front Deposition

An 'in-house' rig set up was built to carry out electronic front deposition (EFD) onto BSi, AuSi and gold coated microscope slides (AuGMS). The rig set up was detailed in Figure 2.7, the calculations regarding the movement of the stepper motor are detailed in APPENDIX II.

For all EFD, 8 mL of the templating media was contained within a 10 mL beaker to maintain the same basal conditions of meniscus drying at the three-phase contact line. A range of sample solutions of M13 (in PBS, filtered through a 0.45 μm mesh) were prepared of concentrations 0.5 – 5 $\text{mg}\cdot\text{mL}^{-1}$.

All sample solutions were then subjected to EFD on BSi wafers at a selected speed of 74.3 $\mu\text{m}\cdot\text{min}^{-1}$ to observe effectiveness of each sample concentration to achieve a distinctive 1D array visible *via* the naked eye. Those which were deemed suitable were then subjected to POM and AFM topographical analysis.

Following initial characterisation into effects that the M13 concentration M13 could have on the EFD system, effects of the templating speed *i.e.* the mechanical force through the system were explored. For this characterisation concentration of M13 at 1 $\text{mg}\cdot\text{mL}^{-1}$ in PBS (Section 3.4.6) was maintained. The templating speeds it was decided to analyse are documented below (Table 2.3), the changing templating speeds were analysed are a result of the characterisation results from each previous sample. BSi was initially examined as the substrate for EFD, followed by AuSi and finally AuGMS. Following on from the EFD templating of M13 onto the varying substrates the samples were subjected to the characterisation techniques described in Table 2.4.

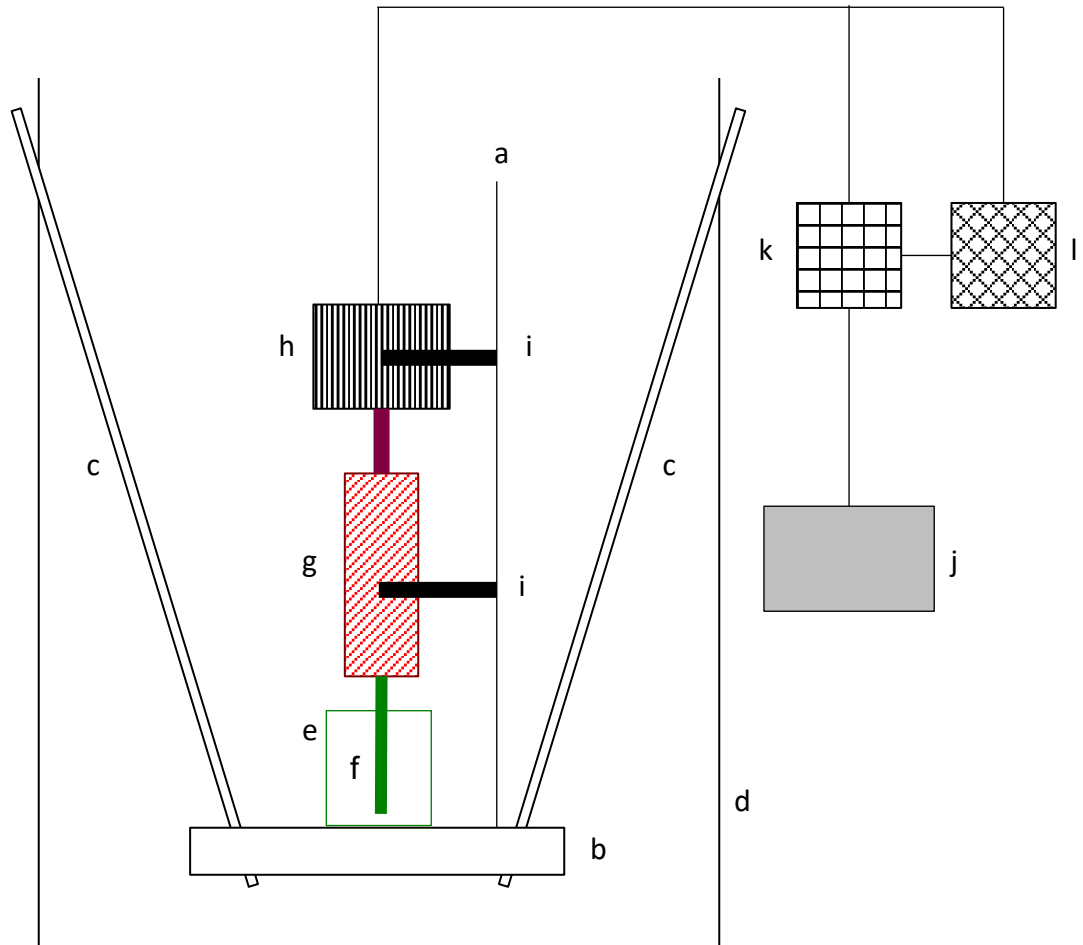


Figure 2.7 | Schematic of ‘in-house’ rig used to achieve EFD on a substrate. a) A clamp stand was placed atop of b) a wooden block that was suspended by c, bungee cords within d) a cardboard box. e) The templating solution contained within a small beaker was then placed on top of b). f) The substrate surface was fixed to the non-rotating head of g) the micrometer, which was fixated to h) a stepper motor. i) A Gertbot GUI interface coded by k) a Raspberry Pi 2 combined with a Gertbot hat, was used to control the speed h). i), A Voltmeter was used connected to both k) and h) to drive the motion of g). As power was supplied to g), the spindle within g) allowed the non-rotating head to withdraw the fixated substrate surface through e), along the y-axis (director axis).

Table 2.3 | Templating speeds utilised during EFD for M13 templating of a 1D array on varying substrates. The changing speeds of EFD per sample surface were changed due to results observed on prior substrate surfaces (Section 3.4.6). BSi was analysed first, followed by AuSi and finally AuGMS.

Substrate Material →	BSi	AuSi	AuGMS
Templating Speed / $\mu\text{m}.\text{min}^{-1}$ ↓			
14.9	X	-	-
52.0	X	X	X
74.3	X	X	X
96.5	X	X	X
111.4	-	X	-
148.5	X	-	-

Table 2.4 | Optical techniques utilised for characterisation of the topographical characteristics of the 1D arrays. Naked-eye detection was a primitive characterisation tool used for confirmation of a horizontal 1D array on the sample surface for observations related to the concentration of M13 required for successful EFD. The bundle distances column represents bundle diameters measured from the central point of the ridge and on the outer region of the ridge.

	Ridge Width / W_R	Ridge Height / H_R	Bundle Distances
Naked-eye detection	-	-	-
POM	X	-	-
SEM	X	-	-
AFM	X	X	X

2.1.12 Statistical Analysis using MATLAB

To carry out statistical analysis of data a two way-ANOVA was utilised to calculate between sample and within sample variance for Section 3.4. The coding used to carry out this analysis was supplied in APPENDIX III.

2.2 Problems Encountered During Experimental Methods

Throughout the formation of samples and collection of data for Chapter 2 there were multiple hurdles which needed to be overcome to enable the progression of the project.

Initial problems in finding a suitable methodology for the deposition of M13 to generate hierarchical ordering of M13 at the surface interface hindered the progress of this project. Multiple other avenues were explored prior to highlighting EFD as a subsequent method in architecting a potentially hierarchical structure. Once EFD was selected as a suitable option for templating 1D arrays, building a suitable rig to generate very slow rates of withdrawal was required due to the lack of capability of commercially available systems. Due to the slow nature of being able to manufacture a workable rig, it was decided to pursue some parts of Chapter 4. This included using wet chemistry techniques to further modify the PVIII of M13 to display functional nanomaterials that could have potential applications in sought after industries for DSTL.

Whilst building the rig, it was clear that a method of motorization would be required, and so it was chosen to use a Raspberry Pi interface and a Gertbot GUI to facilitate the motorization of the rig. Again, critical time delays were faced as unfortunately at the time of this project the manufacturers had ceased to make the initial Raspberry Pi model and had released a Raspberry Pi 2 model. This was rife with problems when using the provided Gertbot GUI code for the previous model.

Another problem faced during this Chapter was the imaging of samples generated once the EFD rig was established. Around the time of the EFD rig being finished, the AFM being used to analyse the samples at the University of Birmingham was unusable. Therefore, it was only possible to use POM analysis to guide sample assembly. AFM was used towards the last few months of the PhD to gain more insight to the sample surface topography, phase of the bundles, inter-bundle distance and Fast-Fourier Transformations to generate spatial domain profiles.,

2.3 Results and Discussion

2.3.1 Propagation and Isolation of M13 ssDNA

A typical UV-vis spectrum of M13 for reference was shown below (Figure 2.8). Due to the changing nature of the concentration of each stock solution a recalculation of each propagated solution must be conducted to achieve accurate concentrations of M13 in subsequent experiments.

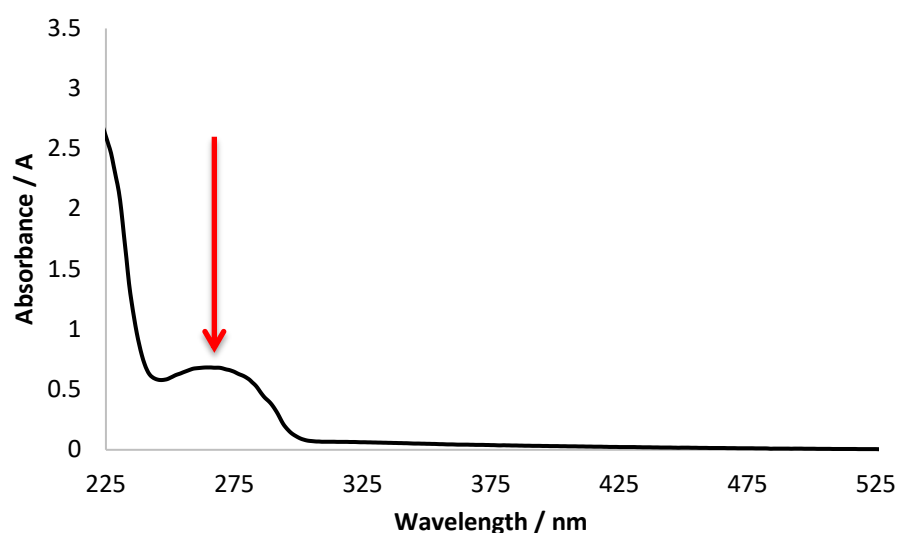


Figure 2.8 | A characteristic UV-vis spectrum obtained from M13. The sample was diluted in PBS (further diluted by a factor of 100 in PBS buffer). Absorption maximum (indicated by the arrow) was observed at 269 nm, with a relative absorbance of 0.682.

CD spectral analysis of the M13 solutions were also used to confirm viability of the M13 solutions prior to further use for SSD, SC or EFD (Figure 2.9). CD allowed confirmation that the protein structure of the individual M13 fibres remained intact. Due to the phage being exploited for its high aspect ratio and flexible structure, it was pertinent that M13 retained its protein structure whilst being stored for long periods of time.

Thiol modification was initially explored as a way to increase the strength of attachment between M13 and the Si and/or Au-Si wafer due to the increased bond strengths (Table 1). However, it was observed that by modifying the PVIII to contain –SH functional groups that the attractive force between S and Si and/or Au, disrupted the mechanism of EFD. Therefore, the thiol modified M13 samples were only used to nucleate gold nanoparticles onto the PVIII surface later on in this thesis (Chapter 4).

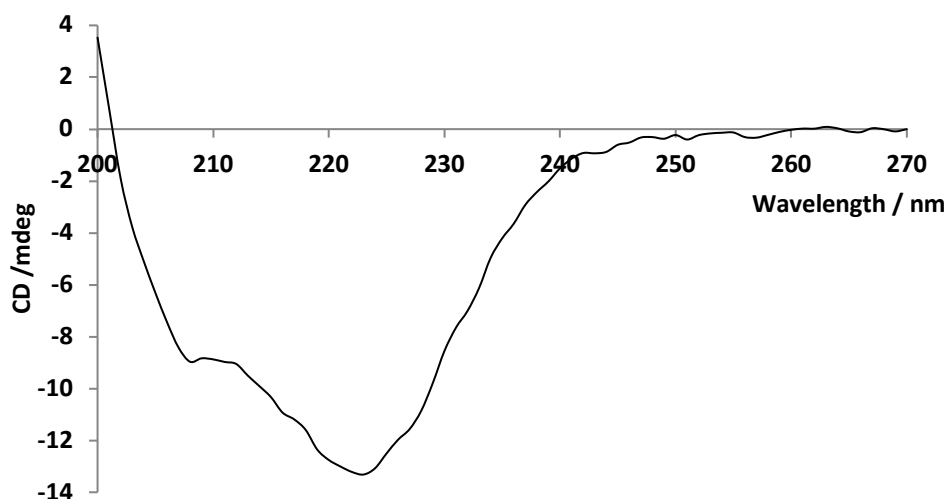


Figure 2.9 | A characteristic CD spectrum obtained from M13. The sample was diluted to 0.045 mg/mL prior to analysis, as the process requires absorption levels of the solution to remain low over the wavelength range being analysed. A typical absorption spectra is detailed in APPENDIX IVI.

2.3.2 Sessile Drop Casting

Sessile drop casting (SDC) represented the most facile method explored in the deposition of M13 onto a substrate. A small volume of solution (10 μL) containing M13 was pipetted onto the substrate of interest. However, the drop could contain very inconsistent concentrations of M13 due to the relatively small sample size applied to the substrate.

As the sample drop only succumbs to weak drying mediated forces, it was not expected that SDC would exhibit any ordering on the surface, but instead display an isotropic ordered system.¹⁰⁹

As expected M13 phage molecules were not visible at 100 \times magnification-using POM due to the nanoscale dimensions of M13. As a result, only, salt crystals present from the M13 solution were visible on the substrate surface. Subsequently AFM was utilised to observe the nanostructures (Figure 2.10).

Initial deposition of PBS onto a BSi wafer highlighted the phase change that occurs within the drying droplet, whereby a liquid to solid transition was exhibited. During the solvent evaporation, the salts crystallize and grow during the drying NaCl within the PBS solution, generally was known to form cubic anhydrous crystals.¹¹⁰ After subsequent washing of the sample with H_2O post drying, the larger salt molecules were washed away, with only those less aggregated salt molecules remaining (Figure 2.10a). M13 remained bound to the surface due to the electrostatic interaction between the viral capsid molecules (NH_2) and the BSi. This interaction was the most prominent due to the 50 residue PVIII major coat protein makes up 98% by mass of the M13 bacteriophage, with the N-terminal domain containing NH_2 being exposed at the outer most surface.¹⁰⁰

In the first instance, SDC of M13 was conducted on BSi. Analysis *via* AFM confirmed that, as expected, M13 fibres acted as discrete entities (Figure 2.10b).

The fibres showed no self-assembling properties and instead flow instabilities within the drying droplet were observed. This was demonstrated by random organised convection patterns *i.e.* non-equilibrium and irregular dissipative structures.³⁸ Due to the lack of competitive advection and diffusion forces no pinning of the M13 fibres to the BSi was observed *i.e.* there was a lack of a visible 'coffee ring'.¹¹¹

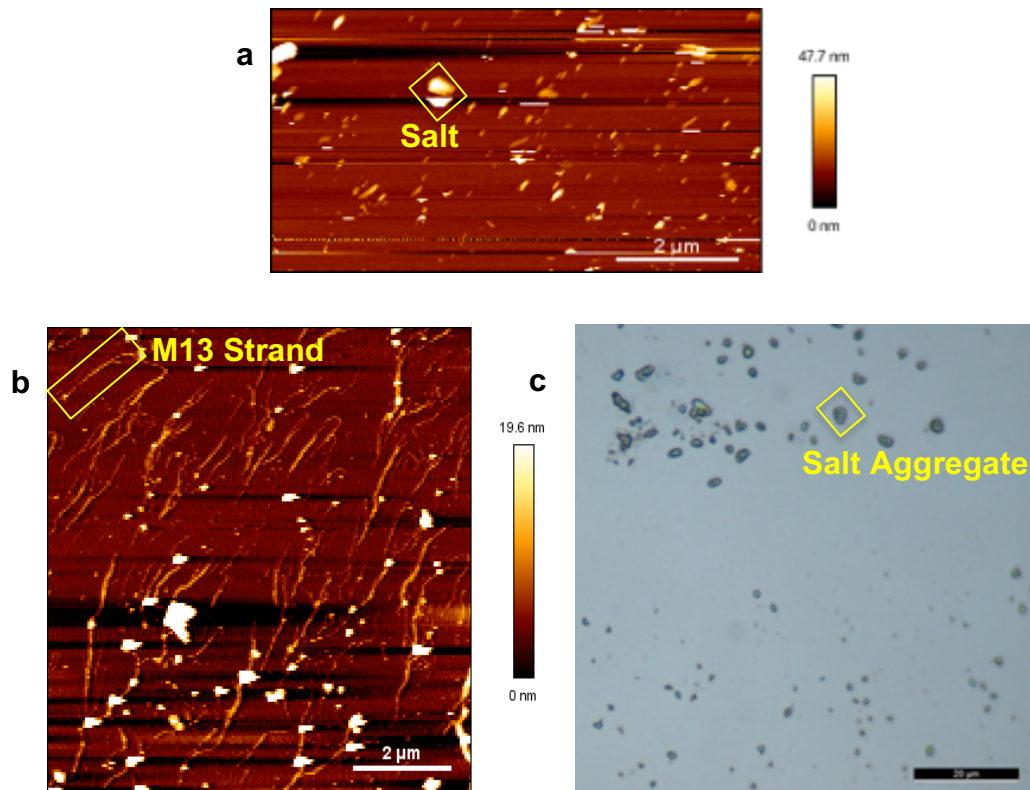


Figure 2.1 | images of SSD deposition technique. a) AFM topographical height-scan profile of SSD of PBS onto a BSi wafer **b)** AFM topographical height-scan profile of SSD of M13 onto a BSi wafer **c)** POM (×100 zoom) of SSD M13 onto a BSi wafer.

The central portion of the ring, however, showed a high presence of NaCl molecules, this was due to the effects of the increasing crystal size during the crystallization process becoming confined between the free liquid surface and solid substrate. This resulted in the deformation of the liquid-air interface and therefore, the geometrical constraint caused capillary forces to push the NaCl

crystals towards the centre of the droplet.^{110–112} Shahidzadeh *et al.* have documented this phenomena whereby the combined effects of NaCl crystal size increase and decreased contact angle of the three-phase contact line quantitatively explain the inward motion of NaCl crystals towards the epicentre of the drying droplet.^{110,111}

2.3.3 Spin Coating

Upon applying centrifugal force to the evaporation system *via* an SC method the spatial variation of evaporation and unexpected convection lead to the formation of irregular structures, such as coffee rings, fingering patterns and polygonal networks.¹⁰⁹ AFM and POM characterisation (Figures 2.11 and 2.13) yielded the conclusion that a more precise and reproducible evaporation method was required to achieve a periodic pattern of M13.

POM images allowed observation of large areas of the SC wafers (Figure 2.11 and 2.12), however, to visualise the micro- and/or nanostructure of the surface topography, AFM was carried out. When using AFM, the morphological changes in the SC layer of M13 fibres at different points within the ‘coffee ring’ were observed.¹⁰⁹ In the central region (Figure 2.11) it can be seen that there were minimal M13 bundles present and no ordering within the system, *i.e.* it was of isotropic nature.^{35,56}

Moving outward from the epicentre of the sample, whereby centrifugal force was highest towards the edge of the ‘coffee ring’ (Figure 2.12) it was clear that the M13 fibres began to interact with each other, through the demonstration of bundling and twisting within the AFM height scan profile (Figure 2.13).

As SC was a relatively turbulent and hard to control process, the bundling remained very inconsistent, resembling more of a webbing effect rather than

discrete periodicity.⁹⁶ The peripheral region of the ‘coffee ring’ (Figure 2.12) showed a distinct change in the way in which M13 fibres were interacting. This was observed as a conformational change in direction of M13 bundling to a perpendicular angle, from the webbing observed in Figure 2.13.

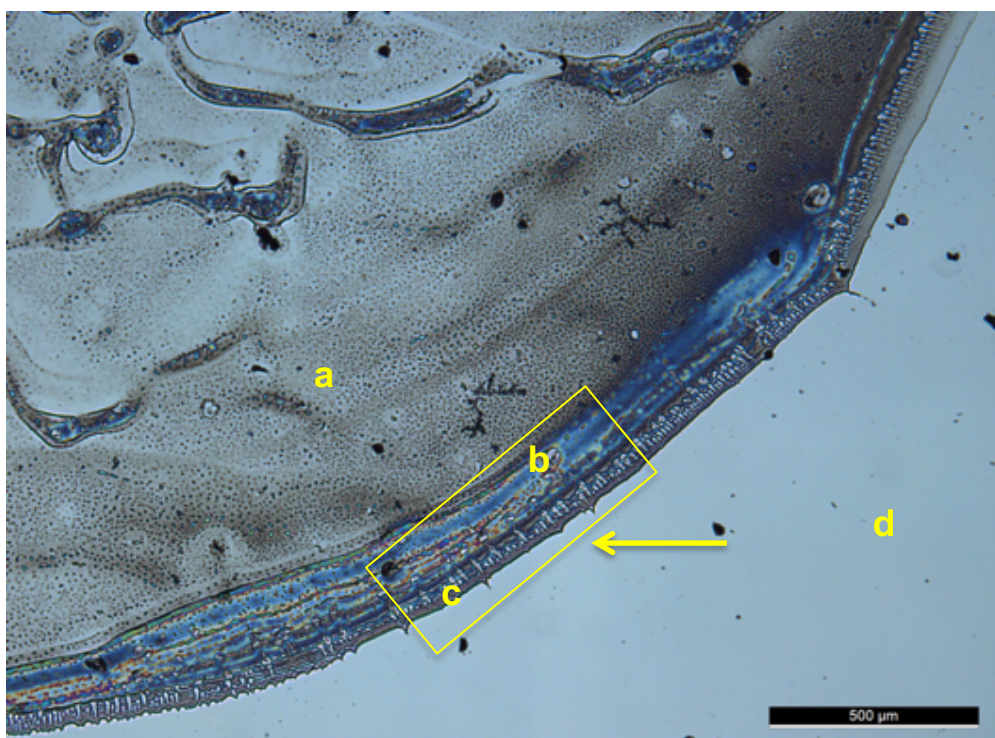


Figure 2.11 | POM imaging of M13 SC onto BSi. POM image taken at $\times 5$ magnification. SC produced the classical coffee ring effect, consisting of **a)** a thin, almost homogeneous central region, contained by **b)** a thicker outer ridge of heavily accumulated M13 fibres. The peripheral edge **c)** contains the most hierarchically ordered region of the ‘coffee ring’. **d)** exterior region of the ‘coffee ring’ showing an absence of M13 phase.

The manifestation of this change resides in the mechanical forces observed during SC. The initial application of centrifugal force pulled the individual light M13 fibres away from the epicentre, as the outward force increases proportionally to the distance from the epicentre the light M13 fibres were dragged towards the edges of the solvent film.⁹⁶ This allowed them to become bundled over each other, creating a mesh (Figure 2.14). M13 accumulated at the highest density at the most outer region of the ‘coffee ring’, whereby they not only bundled together,

but created a ridge of much higher height proportion to the rest of the ‘coffee ring’, thus trapping any further M13 fibres from being carried further outward from this position (Figure 2.11).^{96,113,114}

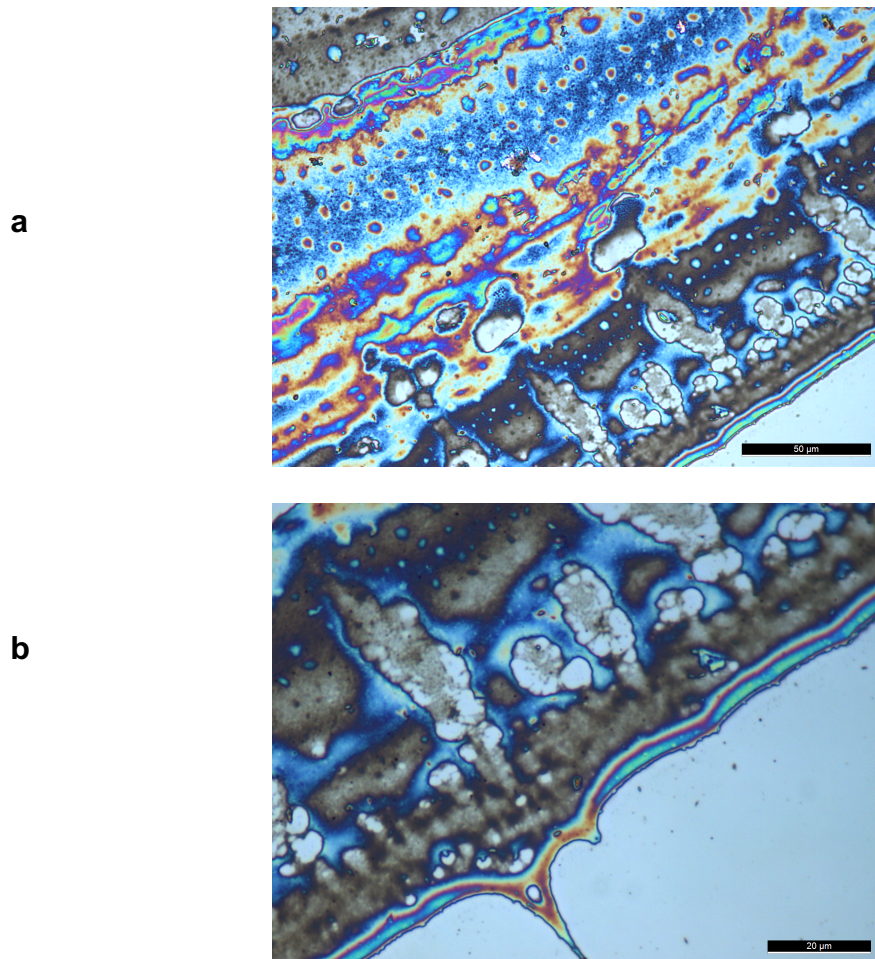


Figure 2.12 | Increased magnification POM images of SC M13 onto BSi. The outer edges of the coffee ring were viewed at increased magnification using POM to observe the effect in more detail, **a)** $\times 50$ magnification and **b)** $\times 100$ magnification.

The success of beginning to achieve a degree of hierarchical ordering upon a substrate using SC of a simple wild type M13 phage and PBS solution without genetic modification of the virus, led to the consideration of other mechanical force application methods for 3D hierarchical ordering of M13.

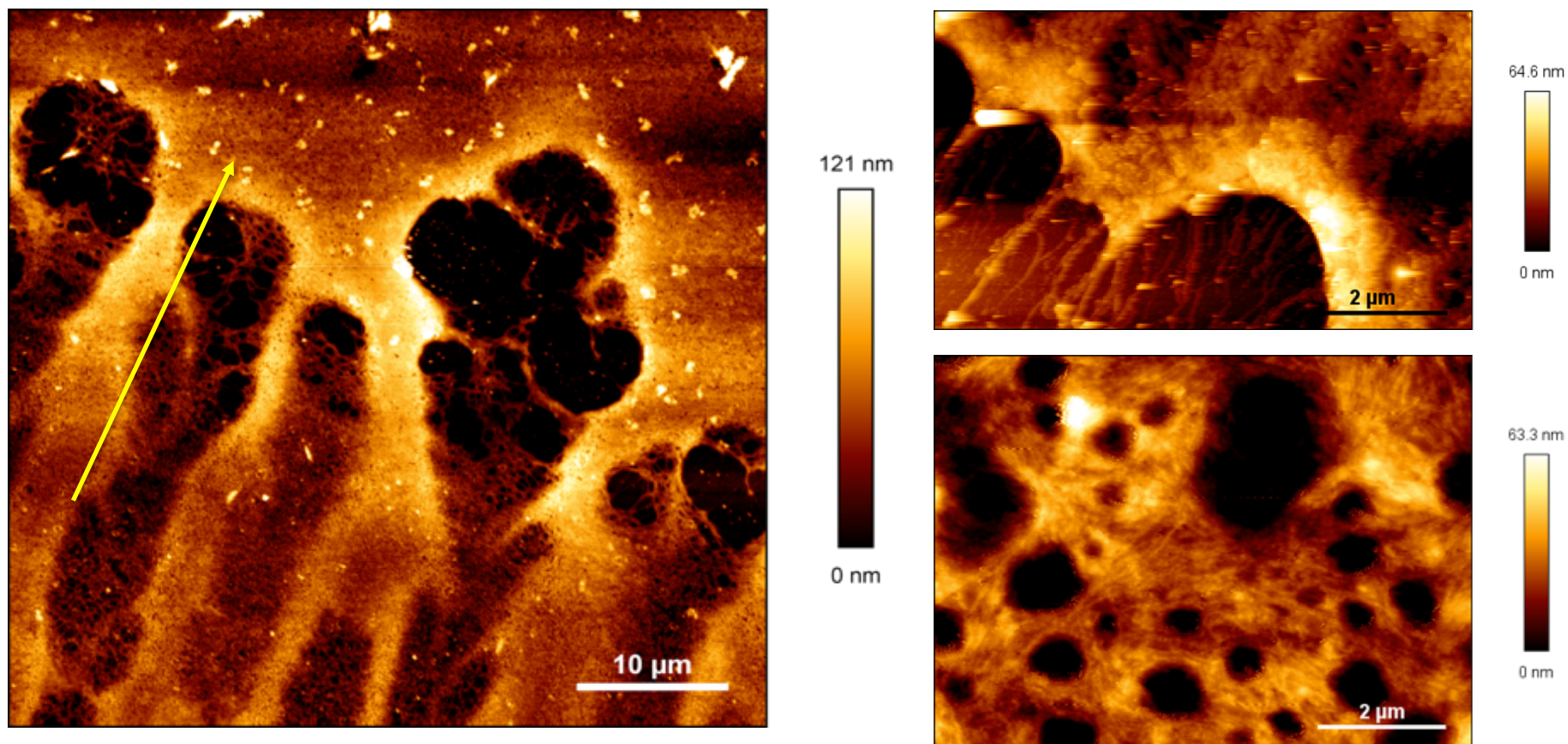


Figure 2.13 | AFM images of SC M13 onto BSi. The AFM height-scan profile of M13 (PBS in H₂O) deposited via SC onto BSi shown here, highlights the irregular deposition of M13 onto the substrate. The arrow highlights the direction of travel of M13 from the epicentre of the droplet to the outer edge of the 'coffee ring'. Higher resolution images are included for reference.

2.3.4 Evaporative Front Deposition

Considering the data obtained by the SC methodology it was clear that an electronically driven process was required to achieve hierarchically structured materials. However, a more controlled system, capable of creating a less destructive templating force was desired due to the fragile nature of M13. EFD and Langmuir Blodgett deposition methods were initially highlighted as additional mechanical deposition methods to SC, which could achieve hierarchical ordering of M13 on a substrate surface. Due to the flexible nature of M13 fibres and the struggle that could be faced in bringing M13 to the surface of a solution for the Langmuir Blodgett style deposition process, it was opted to pursue the EFD process.¹¹⁵

Chung et al. successfully demonstrated the possibility of subjecting M13 to an EFD process to achieve a periodic 1D array of horizontal bands.³⁰ The periodic nature of these arrays was deemed a critical property that was desired due to the influence periodicity could have on the interaction of electromagnetic waves with the substrate surface. Further still, it was opted to keep with the principles laid out by the funding body, DSTL, to create a low-cost, facile and green methodology towards the production of MM. The developed 'in-house' rig (Figures 2.14 and 2.15) was deemed capable in adhering to these principles, whilst also having the added capacity of 1D periodic array production.

Building upon the experimental technique set out by *Chung et al.*, superior structures were achieved, fine-tuned to architect exotic properties for functionality in the defence sector.³⁰ Initially experimental conditions proposed by *Chung et al.* were mimicked to observe the chiral arrangements they had demonstrated in their research. These conditions consisted of initial phage concentrations of 4 – 6 mg/mL templated at pulling speeds of 50 – 80 $\mu\text{m} \cdot \text{min}^{-1}$.³⁰ However, it soon became clear that the conditions they had set out for their analysis would not meet the criteria desired for the periodic banding needed to create a negative index material. For example, much thicker (greater height) horizontal bands of M13 were required with a narrower ridge

dimensionality (ridge diameter), further it was also required that ridges displayed 3D hierarchical structure opposed to that achieved by *Chung et al.*

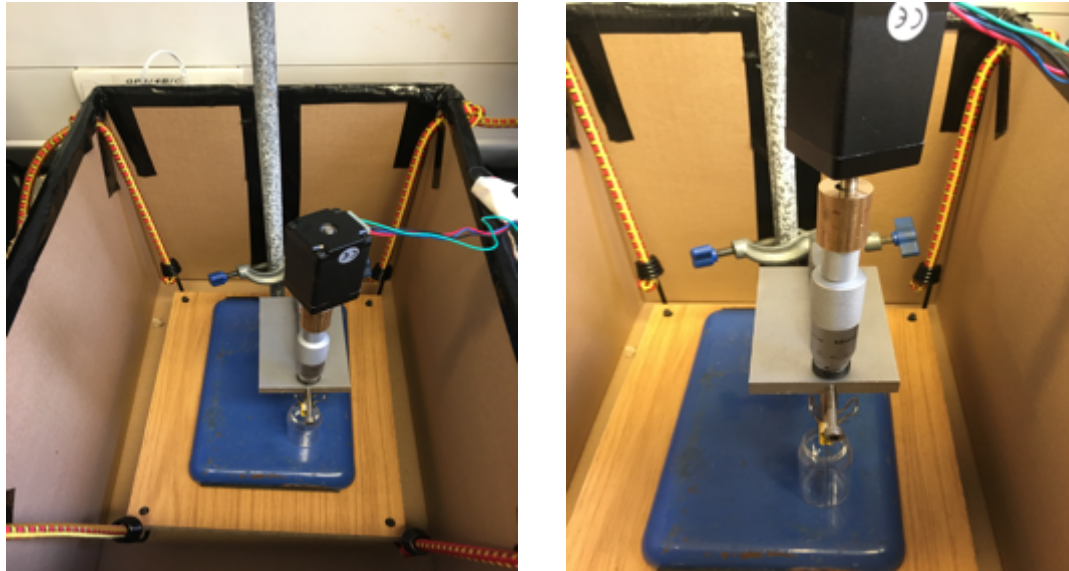


Figure 2.14 | Bungee cord suspension system used to template M13 onto substrates. The suspension system was utilised to minimise vibrational effect on the three-phase contact line of the templating solution, within the laboratory.

The EFD process utilised competing forces; surface tension and frictional adhesion, allow for the successful templating of M13 fibres onto a substrate surface as a 1D array (Figure 2.15). The increasing surface tension, achieved through withdrawal of the substrate along the y-axis, drew M13 fibres (and salt within the solution) to three-phase contact line. The kinetic sliding friction, associated with the substrate surface (Table 2.5), promoted pinning of M13 fibres to the surface. Thus, resulting in effective bundling and hierarchical ordering at the meniscus. When the surface tension reached a critical energy, surpassing that of the kinetic sliding friction, the surface tension broke and slipped to a new point on the substrate move downwards along the y-axis, termed de-pinning. This pinning and de-pinning of M13 (and salt) to the substrate surface refers to the ridges and grooves respectively.^{30,38,39,116} The ease of operation, alongside the ability to fine-tune a multitude of characteristics within the assembly process, make it an optimal process for the hierarchical ordering of M13.

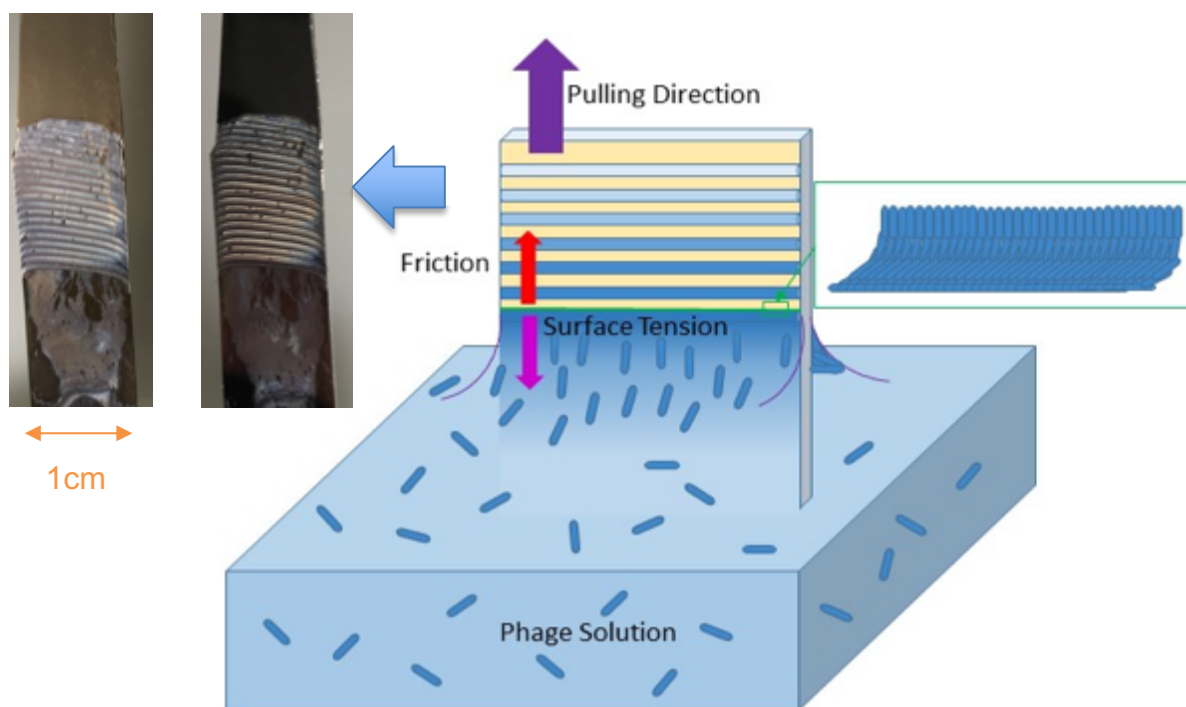


Figure 2.15 | Schematic of the EFD process. Competitional forces allow for a 1D array of ridges on the substrate containing a combination of M13 fibres and salt molecules. Example slides visualised *via* naked eye detection of ridges produced *via* EFD of M13 onto BSi are visualised on the left. The image on the left it taken with the slide tilted to *ca.* 30° and the image on the right was taken of the same slide under no tilting. Utilising just naked eye detection the influence of tilting the sample shows iridescence of the sample.

EFD as previously described allowed for a more controllable system in templating of M13 onto substrates surfaces. The wide-spread use of EFD to organise molecules, such as; carbon nano-tubes and DNA, allowed the prediction of a range of suitable templating speeds that could achieve a 1D array of ridges and grooves at a perpendicular angle to that of the director axis.^{116–118} Producing 1D arrays of ridges and groove introduced a degree of periodicity to the system. This introduction of periodicity in turn could aid in modulating the way light interacted with the templated sample.^{12,69,119} Therefore, to create an optically active synthetic bio-nano-metamaterial achieving a 1D array that displayed consistency in its dimensionality was paramount.

Modulation of the speed at which the substrate was extracted from the solution along the y-axis, and the concentration of M13 within the templating solution, afforded a tuneable 1D array of M13 bundles arranged in ridges and grooves. During EFD initial samples demonstrated clear deformations visible *via* naked eye detection of the ridges. It was decided to move from a freestanding EFD rig on a laboratory bench to an elevated rig system. This was achieved through placing the rig onto a wooden block, this was then suspended within a cardboard box *via* bungee cords. The bungee cord suspension system was used to minimize the environmental effects such as vibrations on the three-phase contact line, with the aim to produce adequate ridges and grooves (Figure 2.13). The ability of this system to create distinct ridges and grooves on the substrate was shown in Figure 2.14. This factor was introduced to limit the error that vibrations could introduce to the system. This factor had not previously been considered by other groups such as Chung et al.^{14,30,38}

POM and AFM analysis of the samples produced under the same experimental conditions, aside from the implementation of the bungee cord suspension system, showed a distinct difference in surface topography. Those produced *via* the suspension system showed a much more consistent appearance, in that they demonstrated discreet and periodic horizontal bands of M13 arranged in 1D arrays formed at speeds 52.0 – 148.5 $\mu\text{m}.\text{min}^{-1}$.

Initially, the concentration of M13 within the templating solution was considered as the most prominent experimental condition. The primary range of concentrations of M13 within the templating solution was set at 0.5 – 5 $\text{mg}.\text{ml}^{-1}$ based on a number of literature values.^{30,34,38,39,116,120} A constant templating speed of 74.3 $\mu\text{m}.\text{min}^{-1}$ was used to observe the effects of a changing templating solution concentration. This speed was chosen due to literature values set out by *Chung et al.*, where they successfully induced a degree of hierarchical ordering of M13 on substrates surfaces using EFD.³⁰

After this concentrations in the range 1 – 3 $\text{mg}.\text{ml}^{-1}$ were taken forward for analysis as a hierarchical 3D structure. This range was selected as samples <1 $\text{mg}.\text{ml}^{-1}$ showed a lack of ability in pinning of the phage at the three-phase contact line to the substrate.

This was attributed to the low concentration of phage within the templating solution not being capable of creating a sufficient frictional force.¹²¹ The opposite was true of templating solutions containing $>3 \text{ mg.ml}^{-1}$, whereby the high concentration of M13 within the templating solution led to saturation of M13 on the substrate. Images of these samples that lacked a clear 1D array arrangement are included in APPENDIX V. The frictional force adhesion was inflated due to the constant flow of large volumes of M13 fibres to the three-phase contact line. The surface tension was not able to overcome the frictional force, which led to a constant residual meniscus down the vertical plane of the substrate surface. Hence no clear 1D array of ridges and grooves were observed at the sample surface.

Upon further analysis of the $1 - 3 \text{ mg.ml}^{-1}$ samples it was deemed that no significant difference in ability to produce a successful 1D array was observed. The conclusion that 1 mg.ml^{-1} was sufficient for the production of a periodic 1D array was taken forward as it presented higher economic viability, due to reduced quantities of reagents used within the propagation stage.

Phage solutions of 1 mg.ml^{-1} in PBS were then used for all subsequent EFD experiments unless otherwise stated.

After the selection of the optimal concentration for EFD, the effects of templating speed used to produce 1D arrays on a range of substrates were explored. The substrates which were explored were:

- **Bare Si wafers (BSi)**
- **Au coated (10 nm) Si wafers (AuSi)**
- **Au coated (10 nm) silica fused glass microscope slides (AuGMS)**

AuGMS was utilised particularly due to its transparent optical properties, making it a more versatile substrate for application in the defence sector.

The range of templating speeds considered was 14.9 – 148.5 $\mu\text{m}.\text{min}^{-1}$. Again, visual analysis *via* the naked eye was used to initially inspect the samples, however it was deemed necessary to analyse all samples further using POM, AFM and SEM. POM was used in the first instance due to the convenience and cost of running analysis on the samples.¹²²

On analysis using POM it was clear that, although the ridges initially looked 2D on the substrate surface, sufficiently high templating speeds ($>52.5 \mu\text{m}.\text{min}^{-1}$) in-fact demonstrated 3D hierarchical structure when observed under AFM (Figures 2.16 to 2.20). Further still, ridges that had similar appearance *via* naked eye detection, showed inherently different structures once observed under increased magnification when using POM and AFM (Figures 2.16 to 2.20). AFM allowed characterisation of the inter-bundle distances between the M13 bundles within the ridges and also the height of the ridges, both characteristics that were not possible through either POM or SEM. Further still a phase image of the M13 3D topography could be determined through AFM, which highlighted the clear hierarchical structuring within the ridges.

Initially SEM was considered as a method of characterisation for the surface topography of the EFD samples, however the insulating nature of M13 required the structures to be coated with a thin conductive layer of Pt, as the BSI M13 was templated atop of was coated with Au. This coating of the surface led to a reduced resolution of the topographical representation of the sample as the SEM analysis showed significantly different values for the ridge ($P<0.05$) and bundle widths ($P<0.05$) to that observed by POM and AFM (APPENDIX VI). Further still, the nano-scale height of the ridges created issues when conducting SEM, leading the images to be of low contrast, making it hard to see the structures. As SEM, like POM, was a 2D topographical profiling tool in the x-y planes, it failed to offer much more information about the topographical characteristics than POM, other than being able to achieve significantly higher magnifications.

Access to an AFM provided a much more advanced analysis of the surface topography in 3D, *i.e.* the x-y-z planes, alongside producing multiple surface profiles, including phase and amplitude surface plots. As all profile scans during AFM are recorded simultaneously, there was no need for multiple scans of the same area, making it a very time efficient and economical analysis tool for high resolution topographical images. It was therefore chosen to omit using SEM as a characterisation technique. APPENDIX VI includes the SEM images for a sample of M13 templated via EFD onto an AuSi wafer and subsequently coated with Pt (50 nm).

When concerning the EFD process, the motion of the three-phase contact line was a fundamental, yet complex phenomenon. As the substrate was withdrawn from the solution at a controlled rate, the meniscus recedes in a downward motion synergistically with the adsorption of molecules at the three-phase contact line to the substrate. Thus, molecular kinetics and fluid dynamics are involved in the dissipation of energy. One key factor at play within the system was the ability of the substrate to allow pinning of the substances to the surface. The kinetic sliding friction of the substrate material plays a key role in this factor (Table 2.5). Here, a lower kinetic sliding friction would indicate the decreased ability of the substrate to promote successful binding of the sample. The minor fluctuations in the edges of the horizontal ridges of the M13 structure reflect this as the contact line becomes distorted.^{43,123}

Table 2.5 | Frictional forces per substrate taken from literature values.^{121,124,125}

Substrate	Kinetic Sliding Friction μ_k
GMS	0.4
BSi	0.5
AuSi	2.5
AuGMS	2.5
PtSi	3.0

2.3.4.1 Analysis of M13 Evaporative Front Deposition on BSi

Primary analysis into the effects of templating speed during the EFD templating technique were observed on BSi. This allowed observation of effects that were produced due to the mechanical force imposed on the system by EFD in comparison to that achieved through SSD and SC deposition processes. Further, the use of BSi allowed disregard of any surface modification variances that could have arisen from coating techniques.

2.3.4.1.1 imaging of M13 EFD on BSi

For all POM images displayed here a $\times 100$ objective lens was used to capture the images.

Low speeds such as $14.9 \mu\text{m}.\text{min}^{-1}$, produced inconsistent structures that failed to achieve discreet ridges and grooves upon the sample (Figure 2.16). This was highlighted by the dense presence of M13 within the 'groove region'. This ineffectiveness to produce periodic horizontal banding across the surface has been previously highlighted (Section; 2.2.4) to be a critical factor for successful production of MM behaviour in a material.

The irregular structure and merging of the ridges were attributed to rayleigh instabilities that did not allow for the definitive difference in the frictional adhesion force achieved at the pinning or de-pinning stages of the EFD process. The extended length of time left in-between the pinning and depinning jerking motions *i.e.* the length of time taken for the micrometer to move from one step to the next, allowed M13 to accumulate within the groove area.

Further still M13 within the ridge sections of the templated structures remained inconsistent with only nematic hierarchical ordering witnessed *i.e.* ordering along the

y-axis of the M13 fibres. Figure 2.16 indicates the areas of ridges and grooves within the templated structure.

As the rate of withdrawal of the substrate vertically through the templating solution was increased to $52.0 \mu\text{m}.\text{min}^{-1}$, discrete horizontal ridges of M13 that were dimensionally consistent ($P>0.95$) were generated. (Figure 2.17) Through increasing the templating speed to $52 \mu\text{m}.\text{min}^{-1}$ a new hierarchical layer was introduced above the initial y-axis templated direction. This new hierarchical level included both x and y-axis directionality (Figure 2.17b). The primitive nematic ordered layer as witnessed in Figure 23 remained to be of consistent optical blue and yellow colour in Figure 23a. However, the subsequent layer with added x-axis directionality can be seen in purple/blue (Figure 2.17a). The second hierarchical layer, having both x- and y-axis directionality therefore showed movement towards a chiral-smectic system.

This increase in hierarchy was fundamental for creating 3D MM. The optical traps created between the hierarchically ordered bundles of M13 to slow down propagations of light enough to induce CD effects and more importantly NIM behaviour. These characteristics could be extensively useful in the fields of defence and wave-guiding for light avoidance systems.

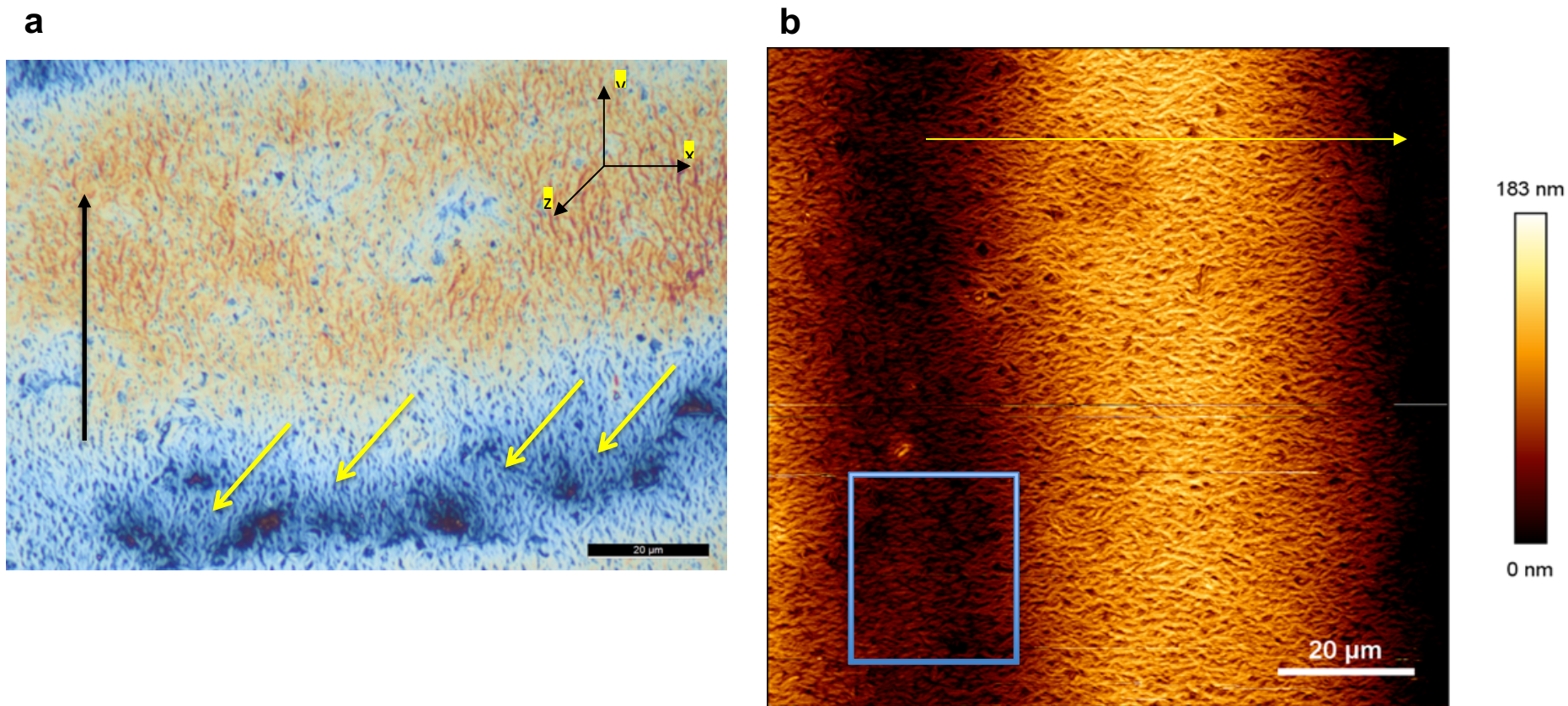


Figure 2.16 | a) POM image of M13 templated at $14.9 \mu\text{m}.\text{min}^{-1}$ on BSi. Rayleigh instabilities witnessed at low templating speeds to yield templating in a vertical manner, within the ridge in the same direction as the director axis. The high surface pressure yielded a positive meniscal curvature, whereby the cylindrical liquid ridge broke up into fingers, indicated by yellow arrows.¹²³ The black arrows represent the director axis *i.e.* direction of substrate withdrawal during EFD. **b) AFM image of M13 templated at $14.9 \mu\text{m}.\text{min}^{-1}$ on BSi.** The yellow arrow represents the director axis *i.e.* direction of substrate withdrawal during EFD. The box indicates the groove region.

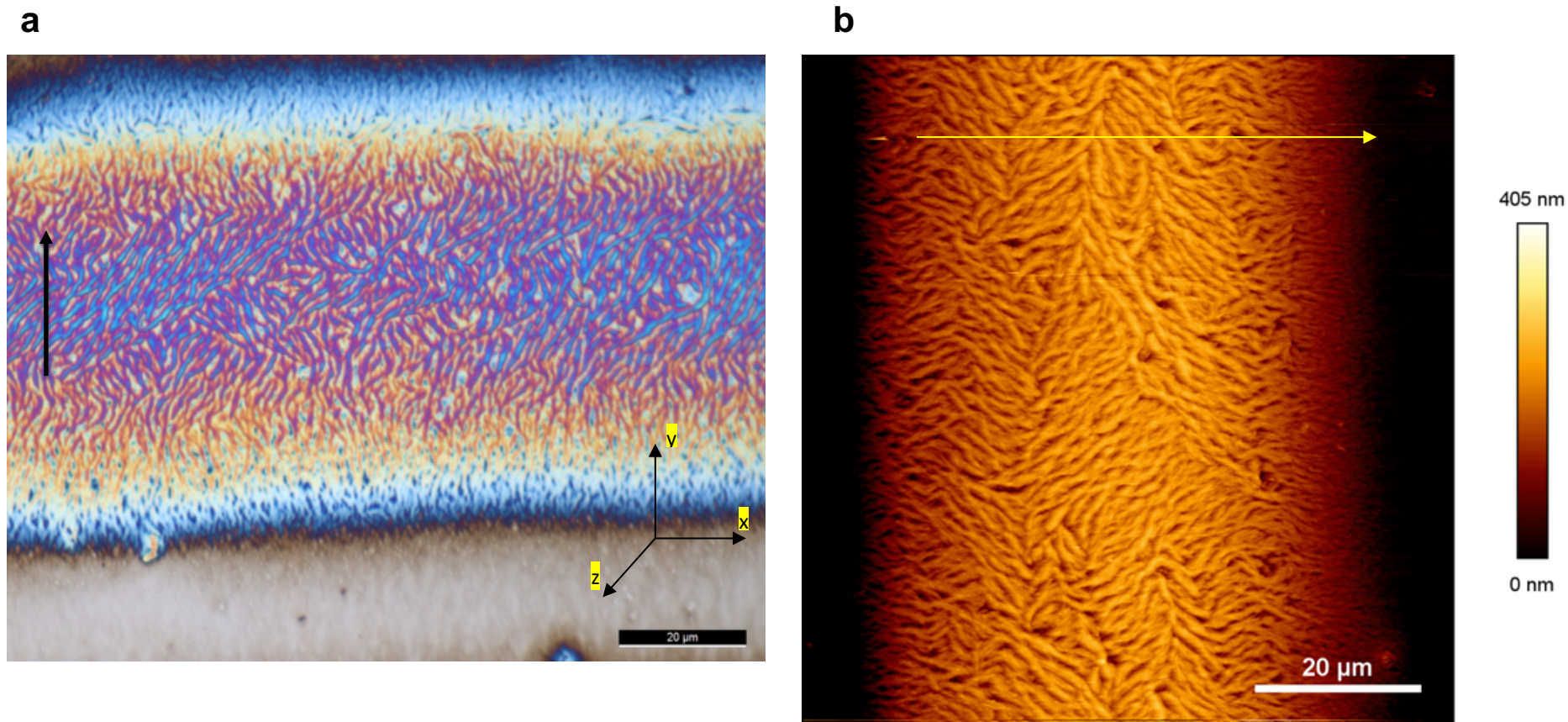


Figure 2.17 | a) POM image of M13 templated at $52.0 \mu\text{m}.\text{min}^{-1}$ on BSi. Increasing the templating speed caused a shift in meniscal curvature to a negative angle, creating a lower surface pressure at the dynamic contact angle. The oscillation of the dynamic contact line afforded a slip-stick motion at the surface to yield distinct templated bands of solute horizontally to the director axis.¹²³ The black arrows represent the director axis *i.e.* direction of substrate withdrawal during EFD. **b) AFM image of M13 templated at $52.0 \mu\text{m}.\text{min}^{-1}$ on BSi.** The yellow arrow represents the director axis *i.e.* direction of substrate withdrawal during EFD.

When observing the M13 bundles themselves it was clear that they were becoming denser, whereby the bundle diameter was significantly larger than those observed at slower templating speeds ($P < 0.05$). This can be observed from Figure 2.17a, in that the POM indicated a range of different polarisations highlighted by the intense rainbow colorization with the images. Whilst POM was not a 3D imaging technique it was possible to deduce a rough guide to the areas which are closer to or further from the objective lens. The AFM imaging of corresponding areas (Figure 2.17b) provided further quantitative detail regarding the height of the ridges, opposed to the qualitative analysis using POM. However, it should be noted that the maximum height observed was not the average for the ridge, but rather the absolute maximum z-value recorded for the entire sample. The colour-bar allowed for a qualitative interpretation of the height over the entire image. AFM does, however, does allowed specific information to be gained regarding each pixel which could provide a more quantitative analysis for the pixels contained within the image. However, for the analysis within this thesis this was not necessary in determining the effectiveness of the sample as a NIM and/or MM. The focus was kept particularly to the ridge diameter and the ability of the EFD process to produce consistent dimensionality of the ridge to induce periodicity and surface effects that can manipulate incoming electromagnetic waves. Hence, the z-max was considered as the 'ridge height'. Further still, the ridge height showed significant increase from that witnessed at slower templating speeds ($P < 0.05$), however the ridge height remained consistent throughout the sample ($P > 0.95$).

Further increase of the templating speed to $74.3 \mu\text{m} \cdot \text{min}^{-1}$ afforded supplementary hierarchical levels, of x-, y- and z-axis directionality. A secondary z-axis band can be seen to be 'above' the initial ridge structure (highlighted by the box on Figure 2.18b), differing from that observed at lower speeds (Figure 2.18). However, this increase in templating speed did not produce consistent z-axis directionality throughout the sample. Furthermore, the z-band was neither centralised within the ridge, nor was it of consistent width throughout the ridge ($P > 0.05$). Therefore, the speed was again increased marginally higher to $96.5 \mu\text{m} \cdot \text{min}^{-1}$ to afford more consistent areas of cholesteric ordering (xyz-plane ordering) upon the ridges throughout the sample.

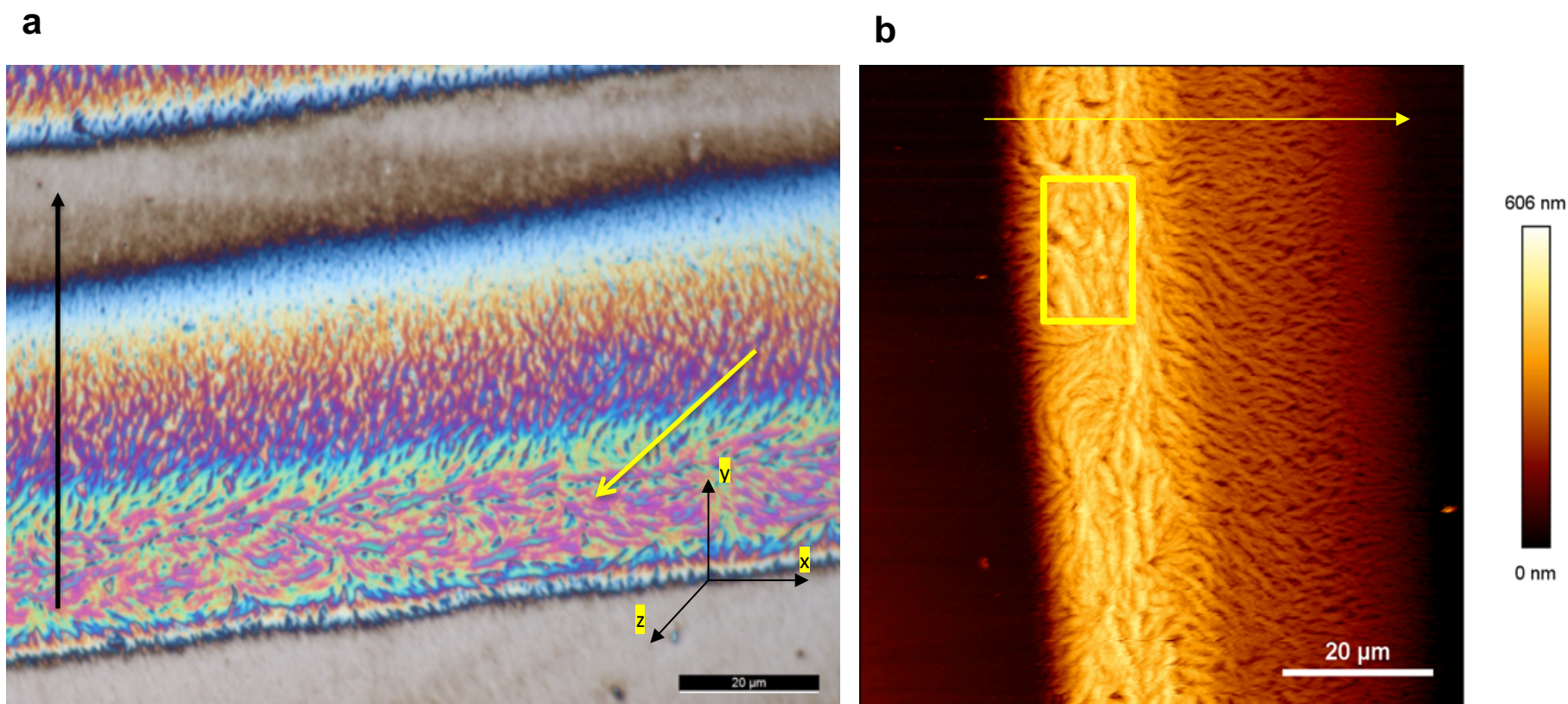


Figure 2.18 | a) POM image of M13 templated at $74.3 \mu\text{m}\cdot\text{min}^{-1}$ on BSi. On increasing the speed slightly further hierarchical ordering within the templated bands began to emerge, highlighted in yellow. The black arrows represent the director axis *i.e.* direction of substrate withdrawal during EFD. **b) AFM image of M13 templated at $74.3 \mu\text{m}\cdot\text{min}^{-1}$ on BSi.** The yellow arrow represents the director axis *i.e.* direction of substrate withdrawal during EFD.

As expected, a marginal increase in the templating speed (Figure 2.19) afforded more consistent cholesteric bands that were centralised upon the horizontal ridges. They also showed a consistent diameter of the centralised cholesteric region ($P>0.95$).

Although the ridge appeared to be saturated *i.e.* a dense area of thick M13 bundles using POM analysis (Figure 2.19a), when conducting AFM (2.19b) on top of the ridges it was clear that gaps remained within the hierarchical layers, through which the Si wafer could be observed. This was easily visible when using SEM analysis of the samples (APPENDIX VI). Total saturation of M13 on the ridges would prevent light perturbing the system, leading to inability of the 1D arrays to create optical cavities. Hence, negative phase velocity of the incoming light beam would not be possible to be observed as a negative refraction angle.

The increased speed of templating to $148.5 \mu\text{m}.\text{min}^{-1}$ produced an adequately turbulent flow, such that M13 fibres were no longer able to produce sufficient bundles at the three-phase contact line (Figure 2.20). The bundles produced showed to be of a much lower density. Further still, the bundles appeared to act more independently of one another, when compared to the lower speeds of $52 - 96 \mu\text{m}.\text{min}^{-1}$ (Figures 2.16 to 2.19). Instead of the bundles intertwining over one-another they have appeared to of accumulated into a ridge structure with no distinct order on the substrate surface past that of a nematic system. This could be due to the lack of time within the pinning stage of the EFD process, combined with the increased turbulence at the meniscus, preventing adequate bundle formation.

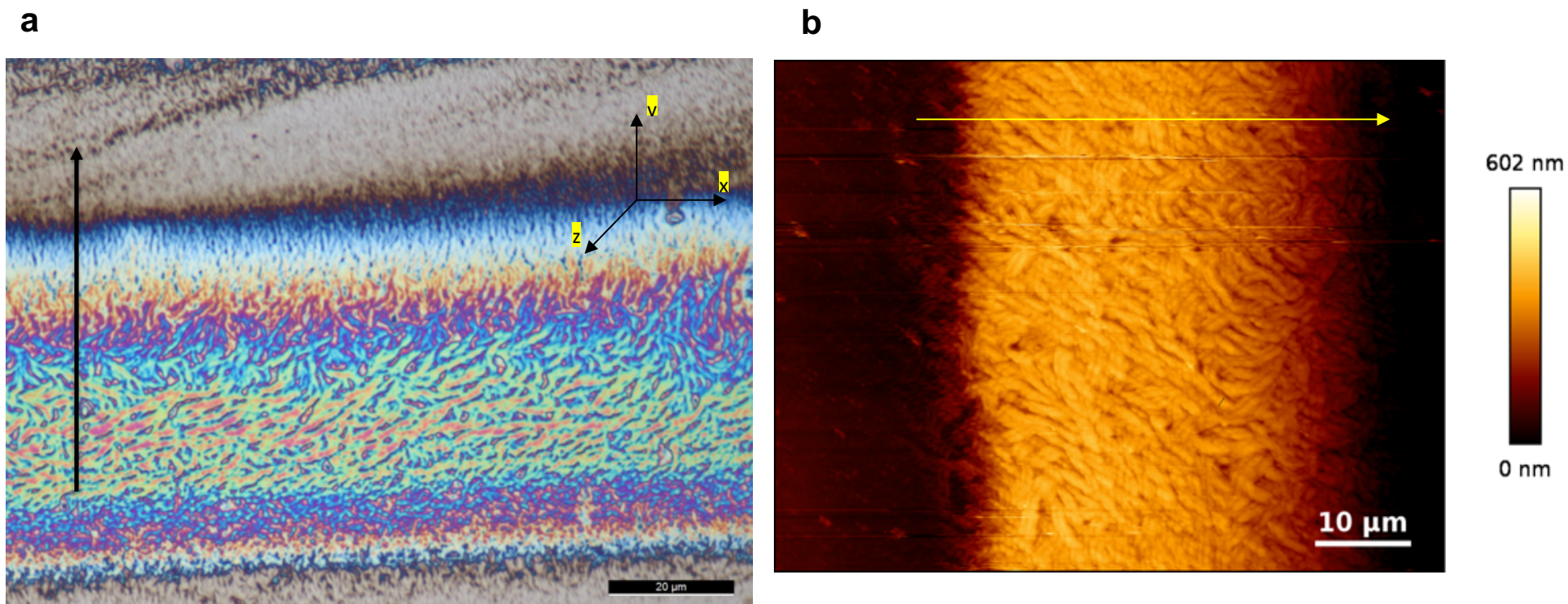


Figure 2.19 | a) POM image of M13 templated at $96.5 \mu\text{m}\cdot\text{min}^{-1}$ on BSi. The black arrows represent the director axis *i.e.* direction of substrate withdrawal during EFD. **b) AFM image of M13 templated at $96.5 \mu\text{m}\cdot\text{min}^{-1}$ on BSi.** The yellow arrow represents the director axis *i.e.* direction of substrate withdrawal during EFD.

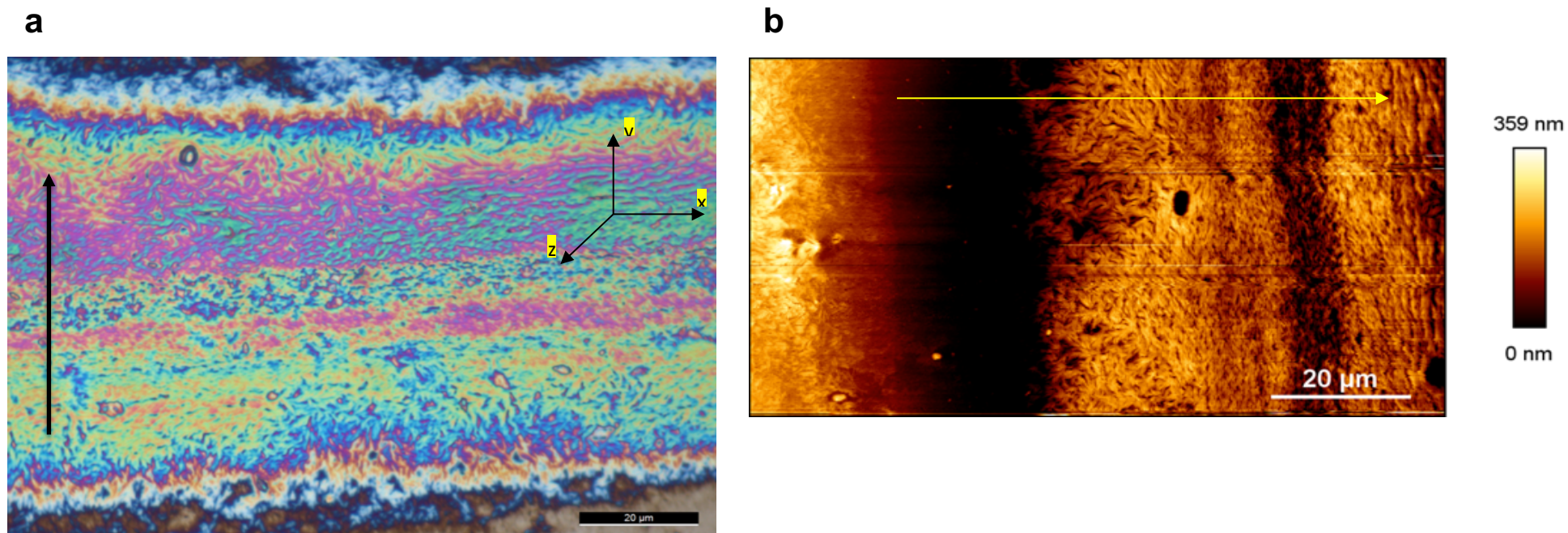


Figure 2.20 | a) POM image of M13 templated at $148.5 \mu\text{m}.\text{min}^{-1}$ on BSi. The increased in speed to $148.5 \mu\text{m}.\text{min}^{-1}$ appeared to have caused extensive deformations of the ridges, leading to total breakdown of the hierarchical levels, heterogeneous ridge structures and fraying of the ridge edges. The black arrows represent the director axis *i.e.* direction of substrate withdrawal during EFD. **b) AFM image of M13 templated at $148.5 \mu\text{m}.\text{min}^{-1}$ on BSi.** The yellow arrow represents the director axis *i.e.* direction of substrate withdrawal during EFD.

2.3.4.1.2 Analysis of ridge diameter vs. templating speed

As observed in Figure 2.21, an increase of templating speed yielded a decrease in the diameter of the ridge until speeds of $96.5 \mu\text{m}.\text{min}^{-1}$, whereby an increase in diameter of the ridge occurs again at $148.5 \mu\text{m}.\text{min}^{-1}$.

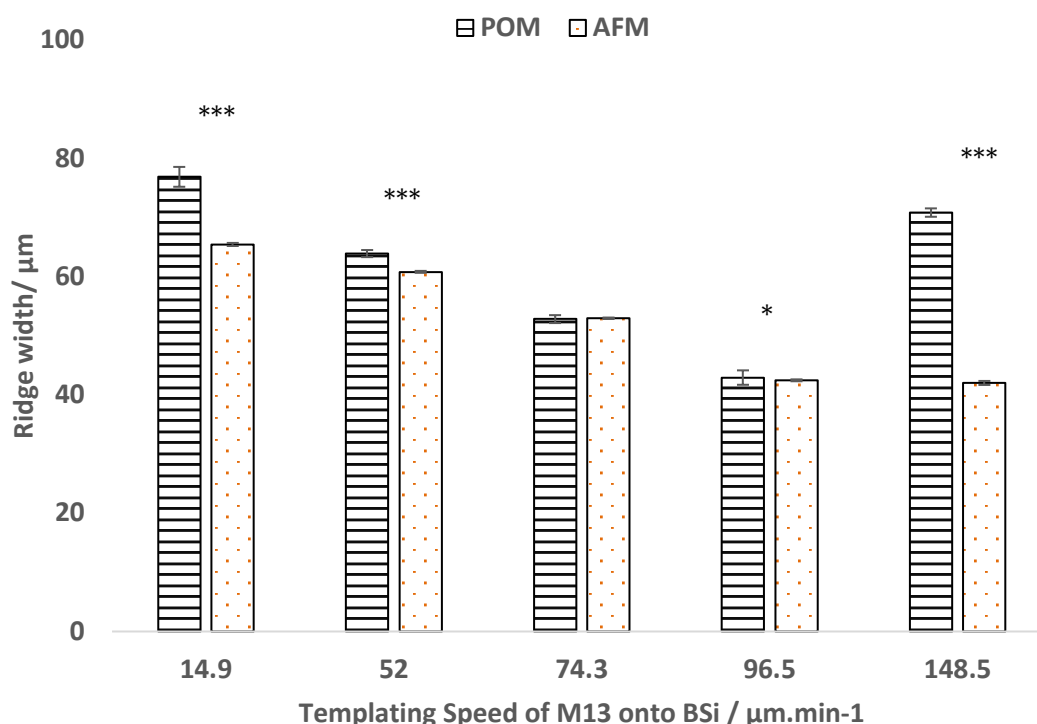


Figure 2.21 | Graphical comparison of ridge width within the 1D arrays, constructed via varying ridge widths using AFM and POM analysis. Graphical analysis allowed visualization of the differences that can be collected for the width of the ridges within the 1D array through analysis of POM or AFM topographical images in ImageJ. * indicates a significant difference ($P < 0.05$) and *** indicates a highly significant difference ($P < 0.001$)

This could be explained through the theory of pinning and depinning of the three-phase contact meniscus. As the speed was increased the moving meniscal motion of the substrate through the templating solution increases the turbulent flow of M13 fibres within the solution, to bring the fibres to the surface. This increase in M13 fibres at the

three-phase interface allowed M13 fibres to accumulate and bundle over one another in a twisting motion to achieve bundles of M13 along the horizontal band *i.e.* the pinning motion. The pinning motion proceeded to occur until the stepper motor jerked to its next position. As the templating speed was increased, the frequency of the stepper motor to take each step also increased, affording a reduced time between each step (APPENDIX III). Hence, the accumulation of M13 fibres at the three-phase contact line bundles together over a shorter distance of the substrate *i.e.* they produced a narrower ridge diameter. However, at higher templating speeds such as $148.5 \mu\text{m}.\text{min}^{-1}$, the increased turbulence within the templating solution, caused by the quicker removal of the substrate through the solution, disrupted the accumulation and bundling of M13 at the three-phase contact line. This combined within the fast stepping motion of the motor brought a high enough concentration of M13 to the surface in the depinning motion, affording M13 fibres to attach on the substrate between the horizontal bands of pinned M13 fibres. This combination of factors caused an increase in the ridge diameter of the 1D array.

The EFD templating speeds of 14.9, 52.0, 74.3, 96.5 and $148.5 \mu\text{m}.\text{min}^{-1}$ are represented by templating speeds 1, 2, 3, 4 and 5 respectively in the figures shown below. ANOVA two-way analysis was ran in MATLAB to determine whether there was both:

- 1. Significant difference between the ridge diameters of varying template speeds**
- 2. Significant difference between values obtained within each sample *i.e.* variance in the ridge diameters obtained for each templating speed**

It was expected that there should be significant difference regarding varying templating speeds. However, a significant difference posed within each sample would indicate that the templating method was un-reliable in producing reproducible 1D arrays of specified ridge diameter. For reference $P < 0.05$ was deemed significant and $P < 0.001$ was deemed highly significant.

Boxplots and two-way ANOVA were generated separately for images taken using POM and AFM due to the significantly different ridge diameters computed from each imaging technique (Figure 2.21).

The lack of overlap between the boxes within the plot (Figure 2.22) indicate that there was a degree of significance of ridge diameter between the templating speeds. This was confirmed by two-way ANOVA (Figure 2.23) to $P < 0.001$.

The red crosses above and below the box plot for M13 templated at $148.5 \mu\text{m} \cdot \text{min}^{-1}$ onto BSi indicate that there was within sample variance at $P > 0.05$. However, this was expected due to the turbulent templating at such high speeds producing un-reliable results.

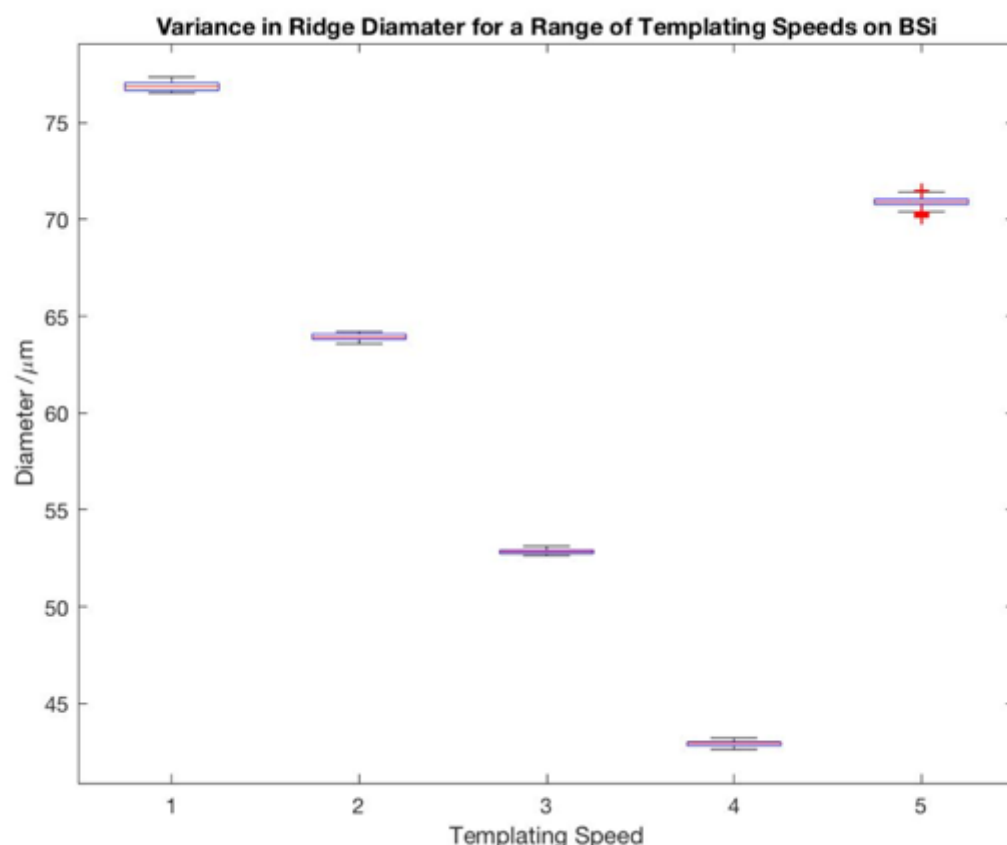


Figure 2.22 | Boxplot to demonstrate the effect of templating speed on ridge diameter during the EFD process on BSi from POM. The EFD templating speeds of 14.9, 52.0, 74.3, 96.5 and $148.5 \mu\text{m} \cdot \text{min}^{-1}$ are represented by templating speeds 1, 2, 3, 4 and 5 respectively in the figure.

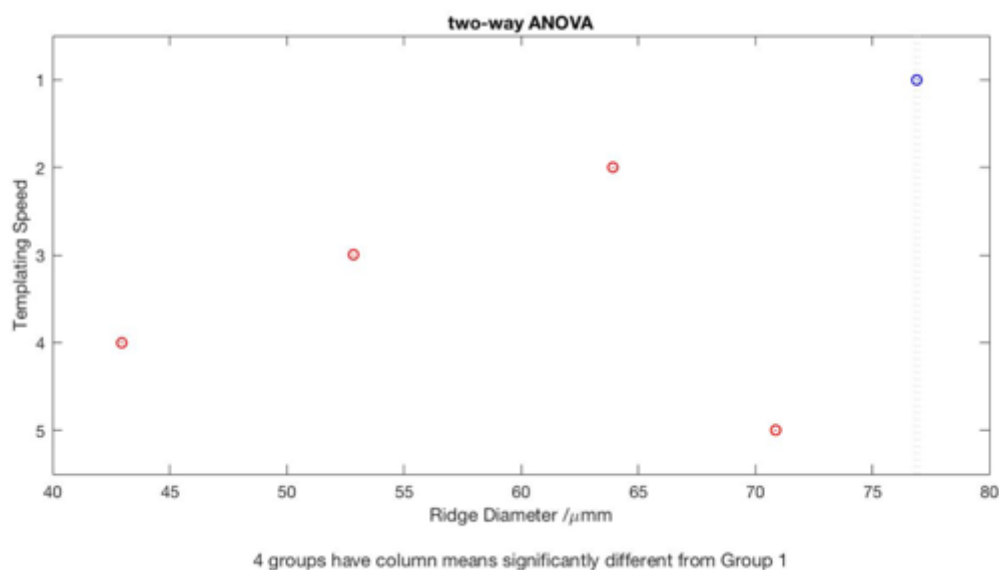


Figure 2.23 | Two-way ANOVA analysis for the ridge diameter taken from POM imaging. The two-way ANOVA for the samples conducted in MATLAB. The EFD templating speeds of 14.9, 52.0, 74.3, 96.5 and 148.5 $\mu\text{m}.\text{min}^{-1}$ are represented by templating speeds 1, 2, 3, 4 and 5 respectively in the figure.

When considering the AFM data for ridge diameter (Figure 2.24), a similar trend was observed to that of the POM data analysis, in that increasing templating speed generally correlated with a narrower ridge diameter. However, using the AFM analysis there showed significant between sample variance at 52.0 $\mu\text{m}.\text{min}^{-1}$, highlighted by a red cross above the boxplot, but no significant difference at 148.5 $\mu\text{m}.\text{min}^{-1}$. As the AFM image for 148.5 $\mu\text{m}.\text{min}^{-1}$ was taken un-centralsed upon the ridge (Figure 2.20b) the value has been reduced by some volume, in which it would have been increased from the value observed for 96.5 $\mu\text{m}.\text{min}^{-1}$.

The lack of overlap of all boxplots within the range 14.9 to 96.5 $\mu\text{m}.\text{min}^{-1}$ highlights there was a degree of significance of ridge diameter between the templating speeds, this was confirmed by two-way ANOVA (Figure 2.25) to $P < 0.001$. There was no significant difference between 96.5 and 148.5 $\mu\text{m}.\text{min}^{-1}$ at $P > 0.05$.

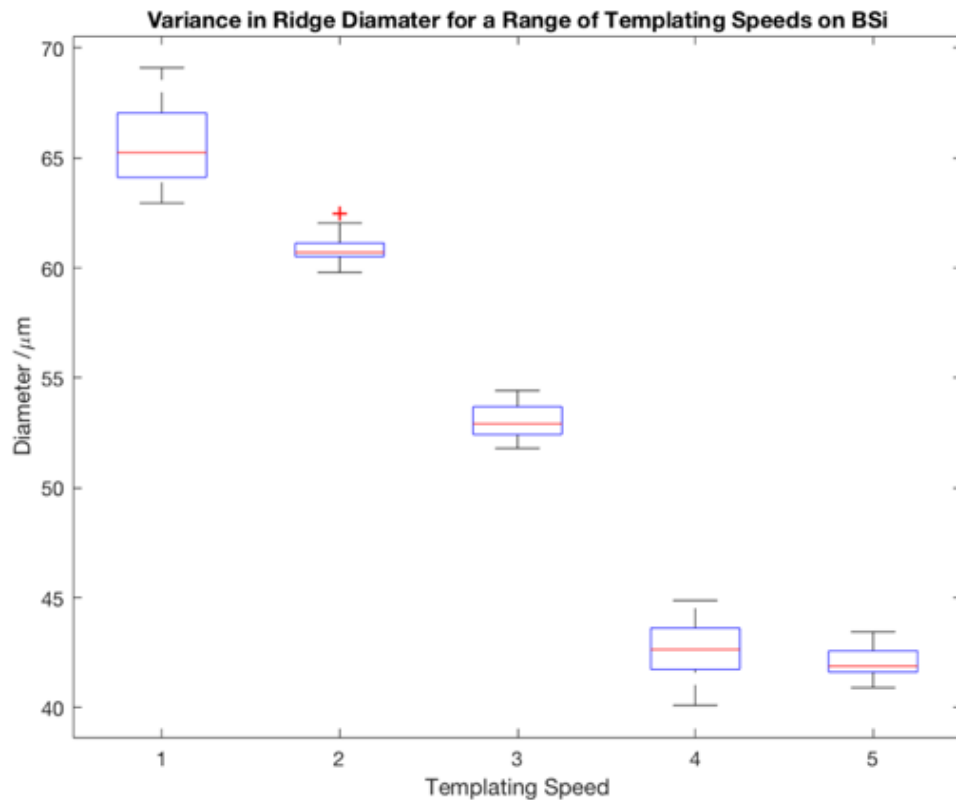


Figure 2.24 | Boxplot to demonstrate the effect of templating speed on ridge diameter during the EFD process on BSi from AFM. The EFD templating speeds of 14.9, 52.0, 74.3, 96.5 and 148.5 $\mu\text{m}.\text{min}^{-1}$ are represented by templating speeds 1, 2, 3, 4 and 5 respectively in the figure.

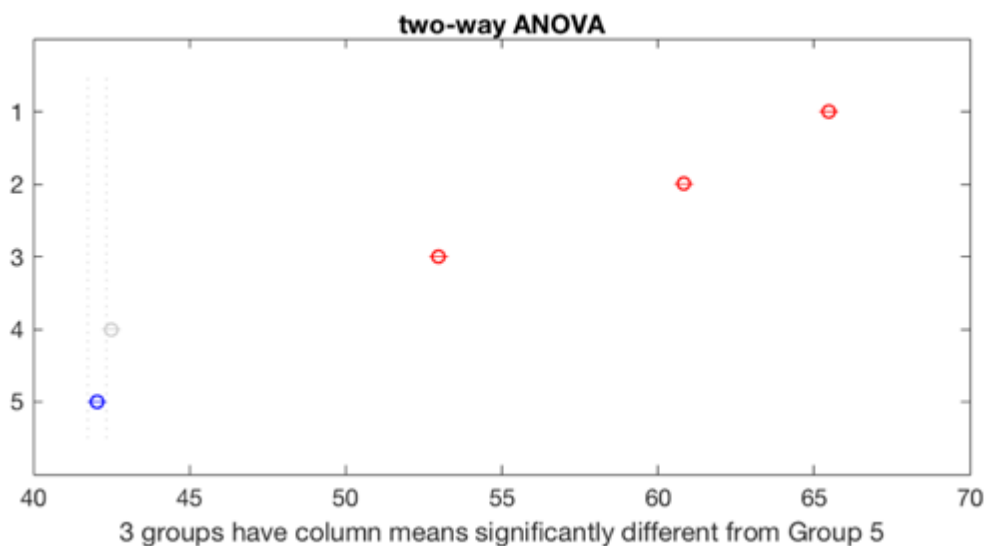


Figure 2.25 | Two-way ANOVA analysis for the ridge diameter taken from AFM imaging. The two-way ANOVA for the samples conducted in MATLAB. The EFD templating speeds of 14.9, 52.0, 74.3, 96.5 and 148.5 $\mu\text{m}.\text{min}^{-1}$ are represented by templating speeds 1, 2, 3, 4 and 5 respectively in the figure.

There are several possible reasons why the variance between AFM and POM data collection could have occurred. One being that POM analysis yielded a lower resolution to that of AFM, this made the ridges appear larger on the topographical POM images due to the decreased precision. However, the AFM height-scan profiles do present their own problems, in that the height of the ridges could force the tip of the cantilever towards a rounded motion over the ridge, losing some z-directional data in the process from the most outer regions of the ridges. This was especially present when ridges are of high z-dimensionality. This lack of z-directional data can lead to areas shown as 0 nm on the height-scan profile during AFM, potentially leading to miscalculation of the ridge diameter appearing narrower than it is.

When considering these points together it was most likely an amalgamation of all introductions of variance within the analysis techniques that has led to significant differences within the data. Going further, it was chosen to accept the ridge dimensionality determined through characterisation of the AFM images, due to its superior resolution and decreased within sample variance. Further still, the characterisation of AFM images allowed the comparison of bundle diameters to be collected.

2.3.4.1.3 Analysis of bundle diameter ridge vs. templating speed

It was chosen to analyse the bundle diameter on the ridge using AFM analysis due to the ability to produce a higher pixel count for the height scan profile, which in turn could increase the accuracy of the analysis of the optically small diameters. The variance in bundle diameter was analysed both on the central point of the ridge and at the edge of the ridge. This was due to the increased bundling of M13 observed on the ridge earlier (Figures 2.15 to 2.20).

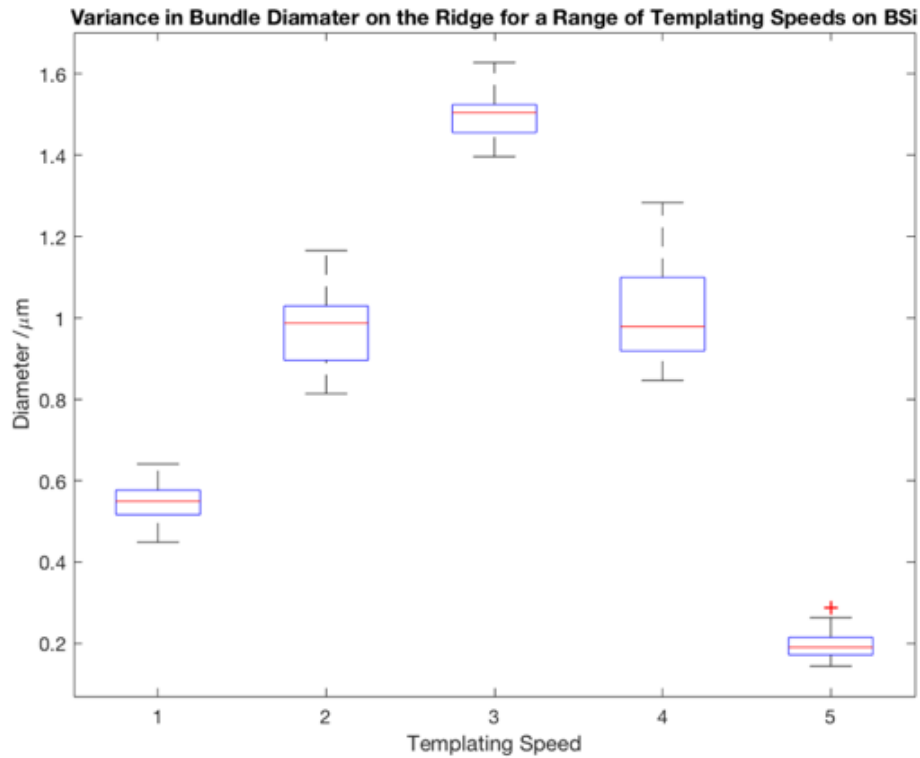


Figure 2.26 | Boxplot to demonstrate the effect of templating speed on bundle diameter during the EFD process on BSi. The EFD templating speeds of 14.9, 52.0, 74.3, 96.5 and 148.5 $\mu\text{m}\cdot\text{min}^{-1}$ are represented by templating speeds 1, 2, 3, 4 and 5 respectively in the figure.

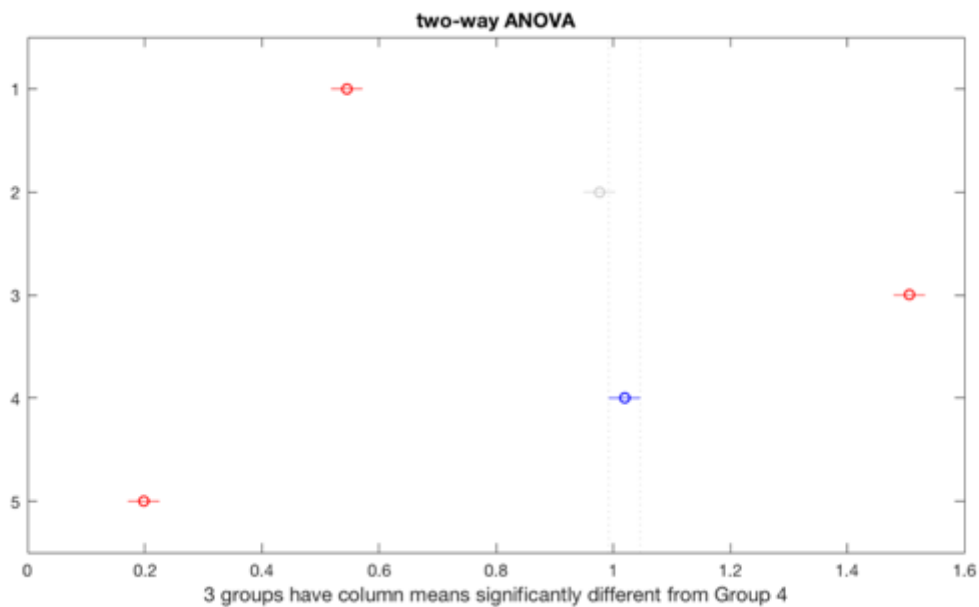


Figure 2.27 | Two-way ANOVA analysis for the bundle diameter taken from AFM imaging. The two-way ANOVA for the samples conducted in MATLAB. The EFD templating speeds of 14.9, 52.0, 74.3, 96.5 and 148.5 $\mu\text{m}\cdot\text{min}^{-1}$ are represented by templating speeds 1, 2, 3, 4 and 5 respectively in the figure.

The boxplot (Figure 2.26) shows that there was significance between all templating speeds in the bundle diameter on the central point on the ridge, other than between 52.0 and 96.5 $\mu\text{m}.\text{min}^{-1}$. This was confirmed *via* two-way ANOVA (Figure 2.27).

The turbulent flow of M13 to the contact line during fast templating speeds caused M13 fibres to bundle more tightly with each other, shown by the sharp decrease of bundle diameter observed during the AFM at speeds above 74.3 $\mu\text{m}.\text{min}^{-1}$. The tight bundling of the M13 phage could also be attributed to the decrease in ridge height observed at the higher templating speeds (Figure 2.24).

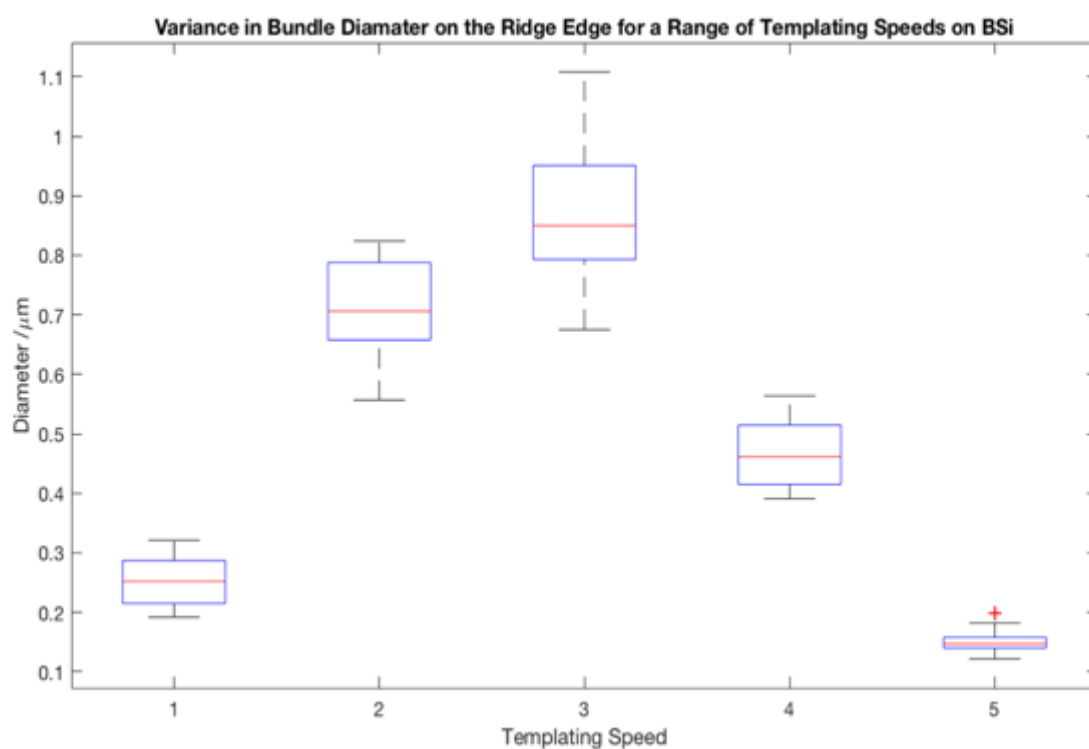


Figure 2.28 | Boxplot to demonstrate the effect of templating speed on bundle diameter during the EFD process on BSi. The EFD templating speeds of 14.9, 52.0, 74.3, 96.5 and 148.5 $\mu\text{m}.\text{min}^{-1}$ are represented by templating speeds 1, 2, 3, 4 and 5 respectively in the figure.

When comparing the bundle diameters on the ridge edge and that on the central point on the ridge, it was clear that at all templating speeds the bundle diameter was wider on the central point of the ridge (Figures 2.26 and 2.28). This was also clearly visible from the AFM images *via* naked eye (Figures 2.20 to 2.25).

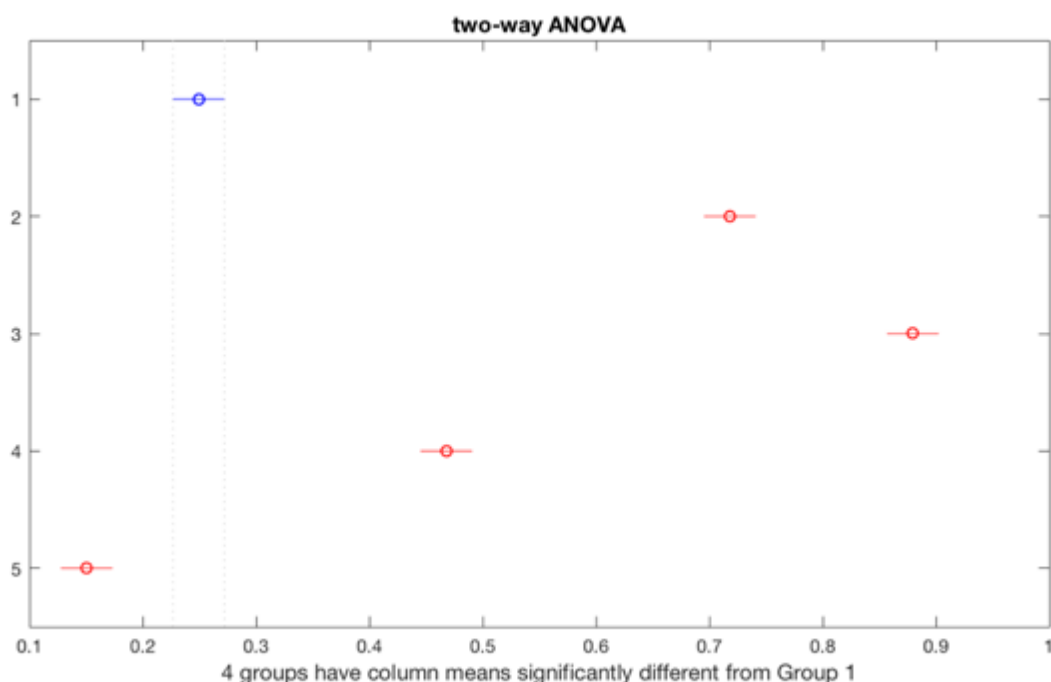


Figure 2.29 | Two-way ANOVA analysis for the bundle diameter taken from AFM imaging.

The two-way ANOVA for the samples conducted in MATLAB. The EFD templating speeds of 14.9, 52.0, 74.3, 96.5 and 148.5 $\mu\text{m}\cdot\text{min}^{-1}$ are represented by templating speeds 1, 2, 3, 4 and 5 respectively in the figure.

2.3.4.1.4 Phase-scan and FFT profiling of M13 EFD on BSi

The phase-scan profiles observe regions of different orientation or composition due to deflections of the cantilever from the surface. The phase shifts can therefore present strong contrasts between different domains within an image as observed above. The corresponding histograms highlight any clear preferences for specific angles of orientation. (Figures 2.31 and 2.32).

2D FFT was achieved through analysis of the AFM images in JPK Data Analysis software. The FFT function converts spatial information, contained within the z-direction, to a frequency domain. This allowed further understanding of the materials surface topography. When considering the spatial frequencies within the height-scan profiles achieved through AFM, it was decided to use Fast Fourier Transform (FFT)

characterisation of the topographical scans. Alongside FFT of the height-scan profiles each height-scan profile was subject to edge detection manipulations. The edge detection module within the JPK data analysis software allowed the generation of profiles that highlighted the edges in either the x-, y- or x- and y-directional plane. This extra manipulation of the height-scan profiles allowed the visualization of any additional behaviours observed by the different samples, in terms of directionality of M13 ordering within the ridges of the 1D array. The centre of the FFT images corresponds to the smallest spatial frequencies *i.e.* the largest distances are therefore observed within the image. The outer edges of the FFT image corresponds to the largest spatial frequencies, *i.e.* the smallest distances observed within the image (Figure 2.30).

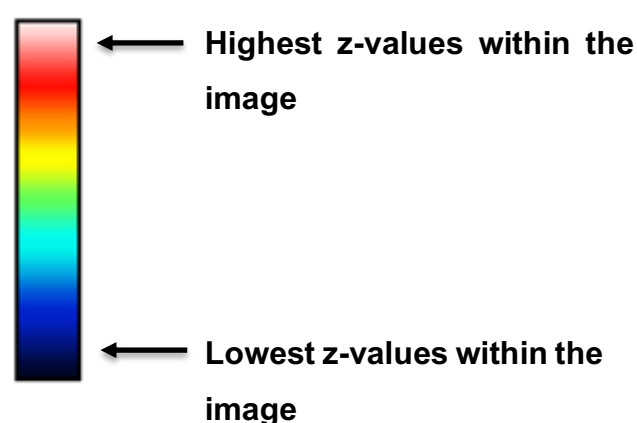


Figure 2.30 | Colormap key to indicate the colour representation of the FFT images used here for spatial frequency. The colormap goes from black; representation the lowest z-values within the FFT profile of an image, through the B-G-R spectrum, and finally to white; representing the highest z-values within the FFT profile of an image. The FFT profile therefore represents the distribution in occurrence of the range of spatial frequencies.

Observing the FFT manipulations set out in Figure 2.33 and 2.34, it can be seen that the three speeds of 14.9, 52.0 and 74.3 $\mu\text{m}.\text{min}^{-1}$ were distinctly different from those of 96.5 and 148.5 $\mu\text{m}.\text{min}^{-1}$, in that they represent much lower spatial frequencies, stipulated by their high density within the central point of the FFT profiles. The

templating speeds of 96.5 and 148.5 $\mu\text{m}.\text{min}^{-1}$, showed a spatial shift towards the outer regions of the FFT profile, indicative of larger spatial frequencies. The presence of the lower spatial frequencies for 96.5 and 148.5 $\mu\text{m}.\text{min}^{-1}$ suggests that the inter-bundle distance remains higher throughout the system. Whereas the larger spatial frequency associated with speeds of 14.9, 52.0 and 74.3 $\mu\text{m}.\text{min}^{-1}$, suggested that these speeds could produce a more intricate system of much smaller inter-bundle distances.

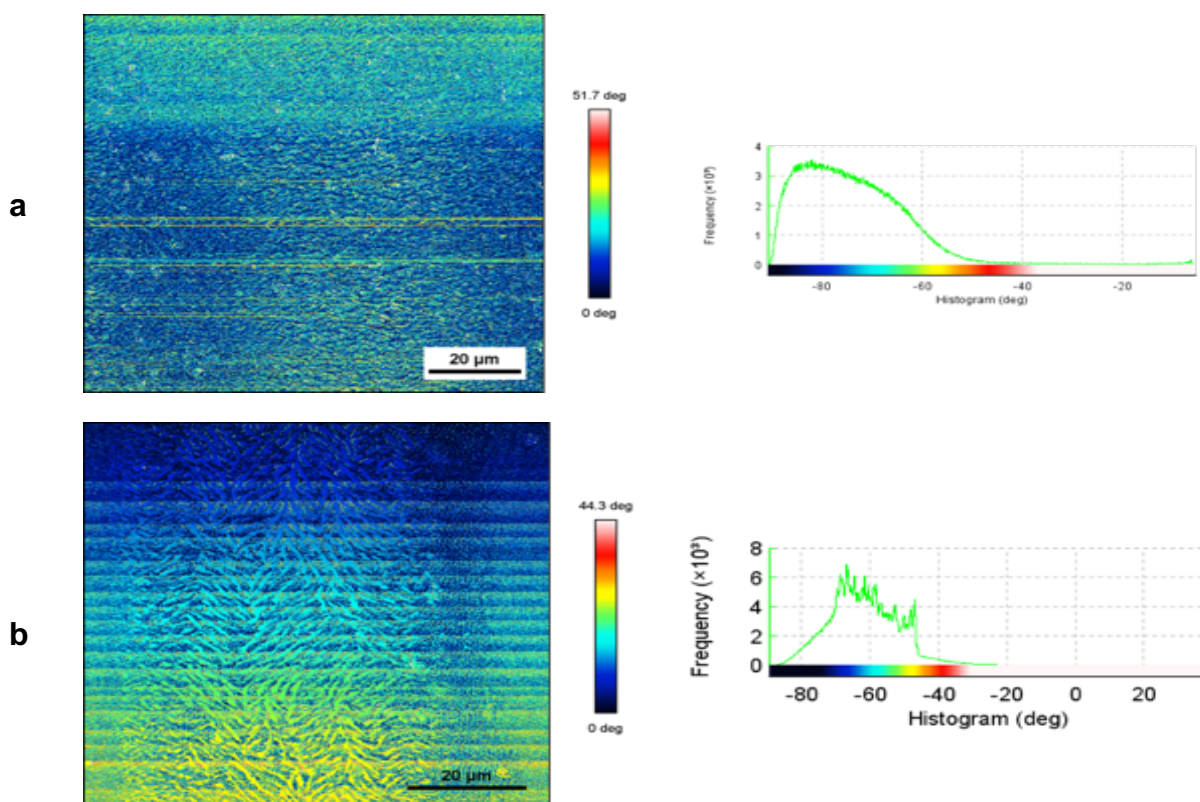


Figure 2.31 | Phase-scan profiles of M13 templated onto BSi at varying speeds and the corresponding histogram plots. a) M13 templated onto BSi at 14.9 $\mu\text{m}.\text{min}^{-1}$, b) M13 templated onto BSi at 52.0 $\mu\text{m}.\text{min}^{-1}$, c, M13 templated onto BSi at 74.3 $\mu\text{m}.\text{min}^{-1}$

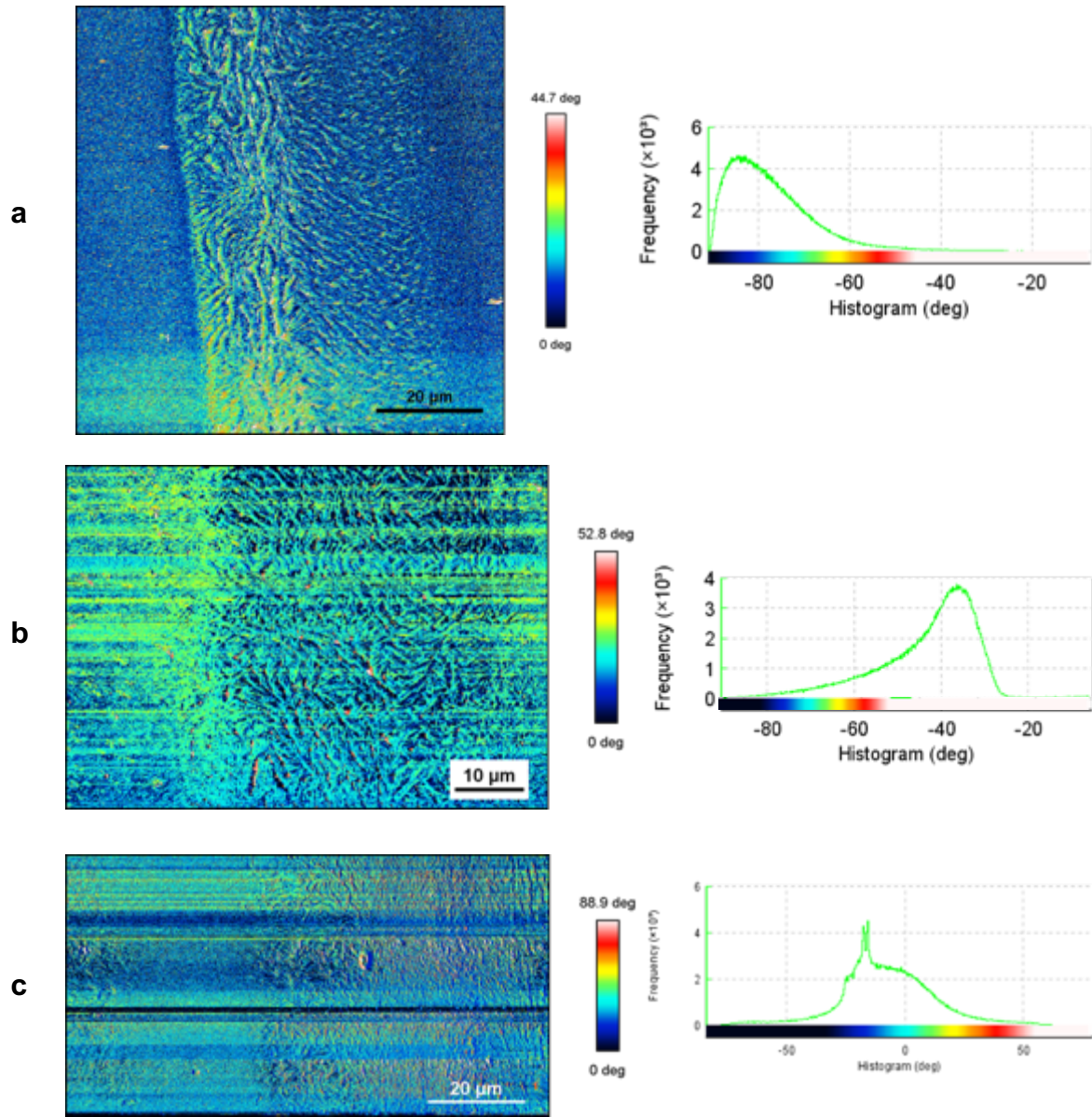


Figure 2.32 | Phase-scan profiles of M13 templated onto BSi at varying speeds and the corresponding histogram plots. a) M13 templated onto BSi at $74.3 \mu\text{m}\cdot\text{min}^{-1}$ b) M13 templated onto BSi at $96.5 \mu\text{m}\cdot\text{min}^{-1}$, c) M13 templated on BSi at $148.5 \mu\text{m}\cdot\text{min}^{-1}$.

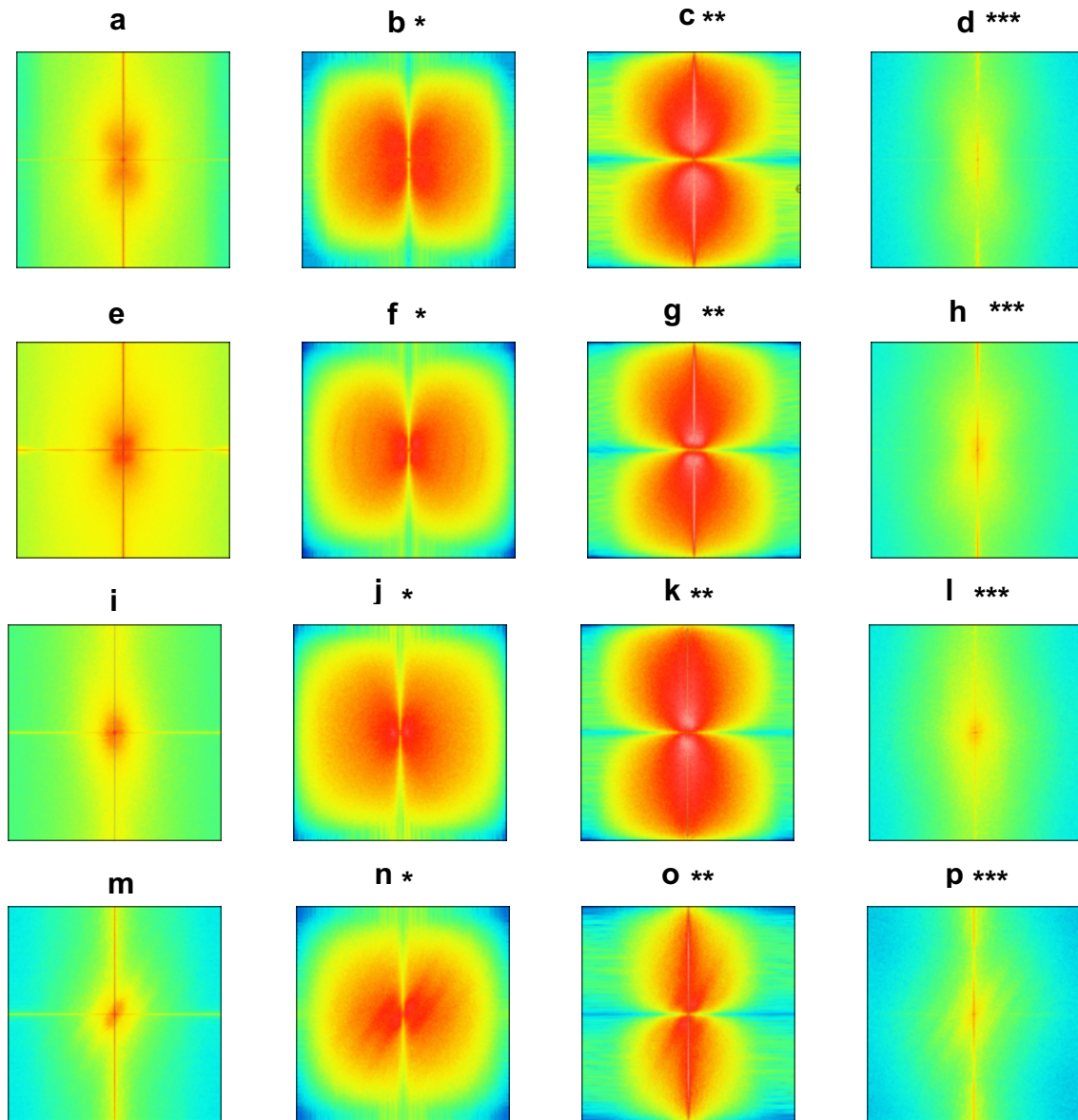


Figure 2.33 | FFT of height scan profiles of M13 templated onto BSi at varying speeds. Frequency domain processing, whereby the rate of cycling from lower to higher z-values and back represents the image's spatial frequency. **a-d)** represent M13 at $14.9 \mu\text{m}.\text{min}^{-1}$ **e-h)** represent M13 templated at $52.0 \mu\text{m}.\text{min}^{-1}$, **i-l)** represent M13 templated at $74.3 \mu\text{m}.\text{min}^{-1}$, **m-p)** represent M13 templated at $96.5 \mu\text{m}.\text{min}^{-1}$. * indicates an FFT of height-scan profile, ** indicates FFT of height-scan profile subjected to x-directional edge detection, *** indicates FFT of height-scan profile subjected to y-directional edge detection and *** indicates FFT of height-scan profile subjected to x- and y-directional edge detection.

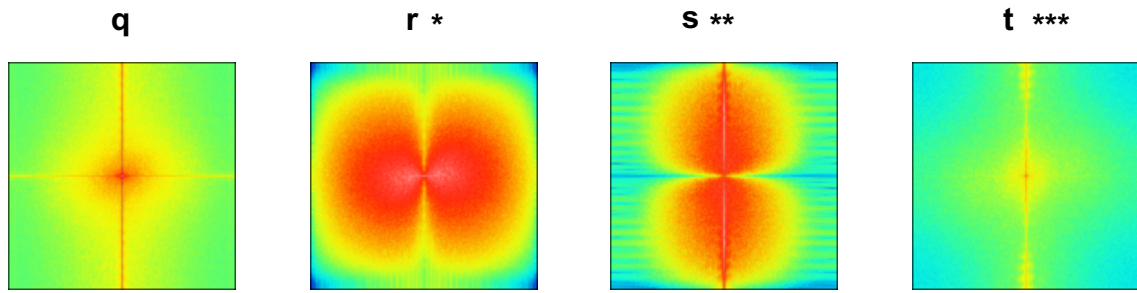


Figure 2.34 | FFT of height scan profiles of M13 templated onto BSi at varying speeds. Frequency domain processing, whereby the rate of cycling from lower to higher z-values and back represents the image's spatial frequency. **q-t**) represent M13 templated onto BSi at $148.5 \mu\text{m}.\text{min}^{-1}$, * indicates an FFT of height-scan profile, ** indicates FFT of height-scan profile subjected to x-directional edge detection, *** indicates FFT of height-scan profile subjected to y-directional edge detection and **** indicates FFT of height-scan profile subjected to x- and y-directional edge detection. 1

2.3.4.2 Analysis of M13 Evaporative Front Deposition on AuSi

2.3.4.2.1 imaging of M13 EFD on AuSi

Due to the ridge break down observed at higher templating speeds ($148.5 \mu\text{m}.\text{min}^{-1}$, Figure 2.20), and lack of ridge formation at lower templating speeds ($14.9 \mu\text{m}.\text{min}^{-1}$ Figure 2.16), when templating M13 onto BSi, it was decided to modify the speeds of templating onto the AuSi substrate. The templating speeds selected for AuSi were 52, 74.3, 96.5 and $111.4 \mu\text{m}.\text{min}^{-1}$. To observe the areas at each point of the ridge in more detail increased resolution height-scans were taken of these areas using AFM.

As with the BSi EFD process at $52.0 \mu\text{m}.\text{min}^{-1}$ (Figure 2.21), a single hierarchical layer was observed (Figure 2.35). There was clear discrete horizontal banding of M13 ridges and grooves arranged in a 1D array (Figure 2.35a). The increase in kinetic sliding

friction of the substrate surface leads to expectation that a decreasing templating speed would yield more defined structures as the increase in bond strength between Au and -NH_3 of the PVIII could afford a higher affinity for one another. It was also expected that at higher templating speeds M13 would have the ability to maintain the formation of the 1D array.

Increasing the templating speed to $74.3 \mu\text{m}\cdot\text{min}^{-1}$, brought about a different topography of the ridges of M13, whereby the ridge has a much higher dimensionality in the z-direction, indicated by the $1.46 \mu\text{m}$ max height within the height-scan profile (Figure 2.36b). Furthermore, a topographical difference at the outer region of the ridge was observed, whereby the top of the ridge (closest point to the micrometer) demonstrated isotropic ordering, whereas the base of the ridge (closest point the templating solution) demonstrated chiral ordering, *i.e.* ordering in two directions; x and y. The increase of templating speed from 52 to $74.3 \mu\text{m}\cdot\text{min}^{-1}$, indicated a distinct shift in ridge topography, from nematic to cholesteric *i.e.* from y- to x-, y-and z-plane directionality of the M13 bundles (Figures 2.35 and 2.36).

Increasing the templating speed further to $96.5 \mu\text{m}\cdot\text{min}^{-1}$ retained the 1D array formation of ridges and grooves, that exhibited 3D cholesteric ordering within the ridge portions (Figures 2.37). However, the increase of templating speed prevented increased volumes of M13 from being able to adhere to the AuSi substrate, affording a much lower z-directionality, indicated by a reduced ridge height in the height-scan profiles (Figure 2.37b and 2.37c).

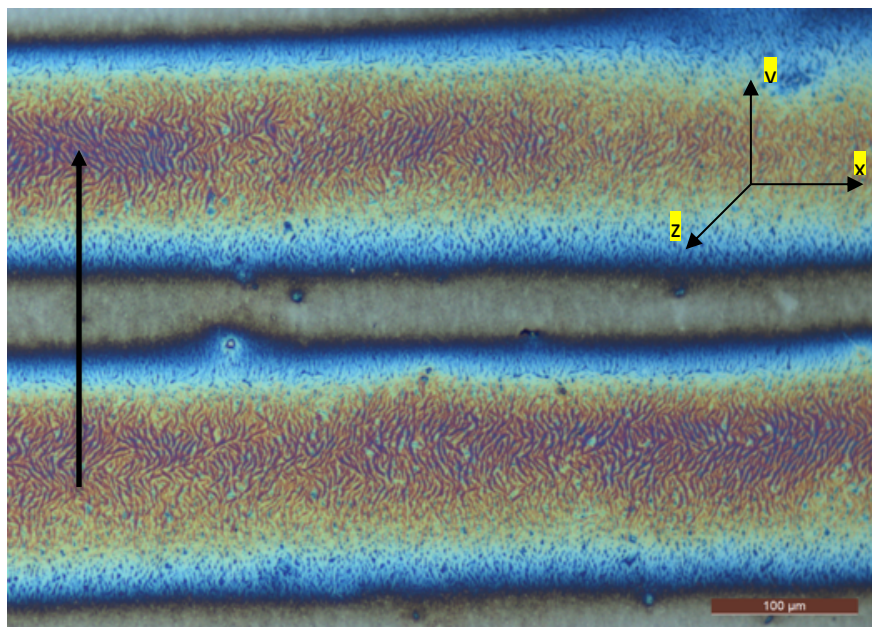
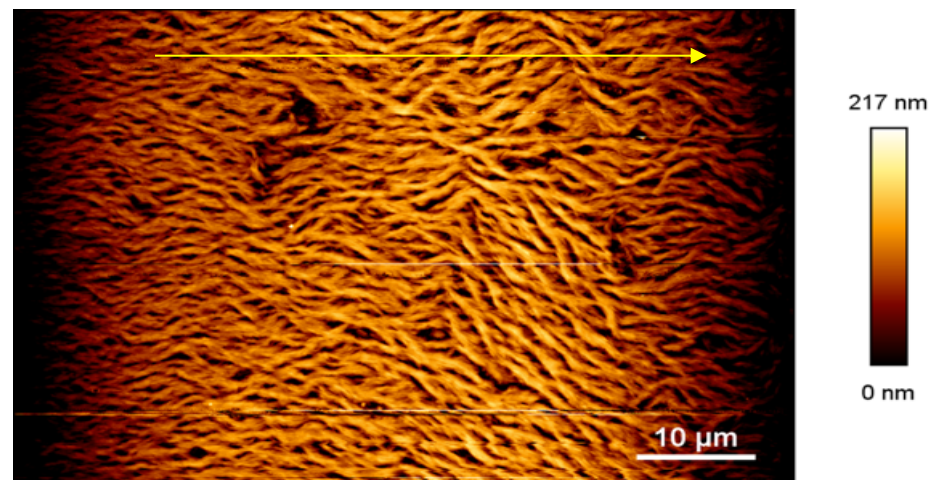
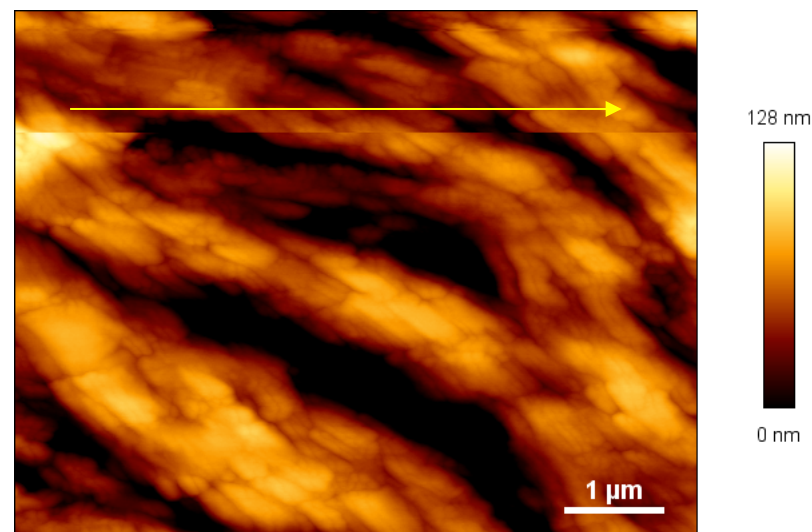
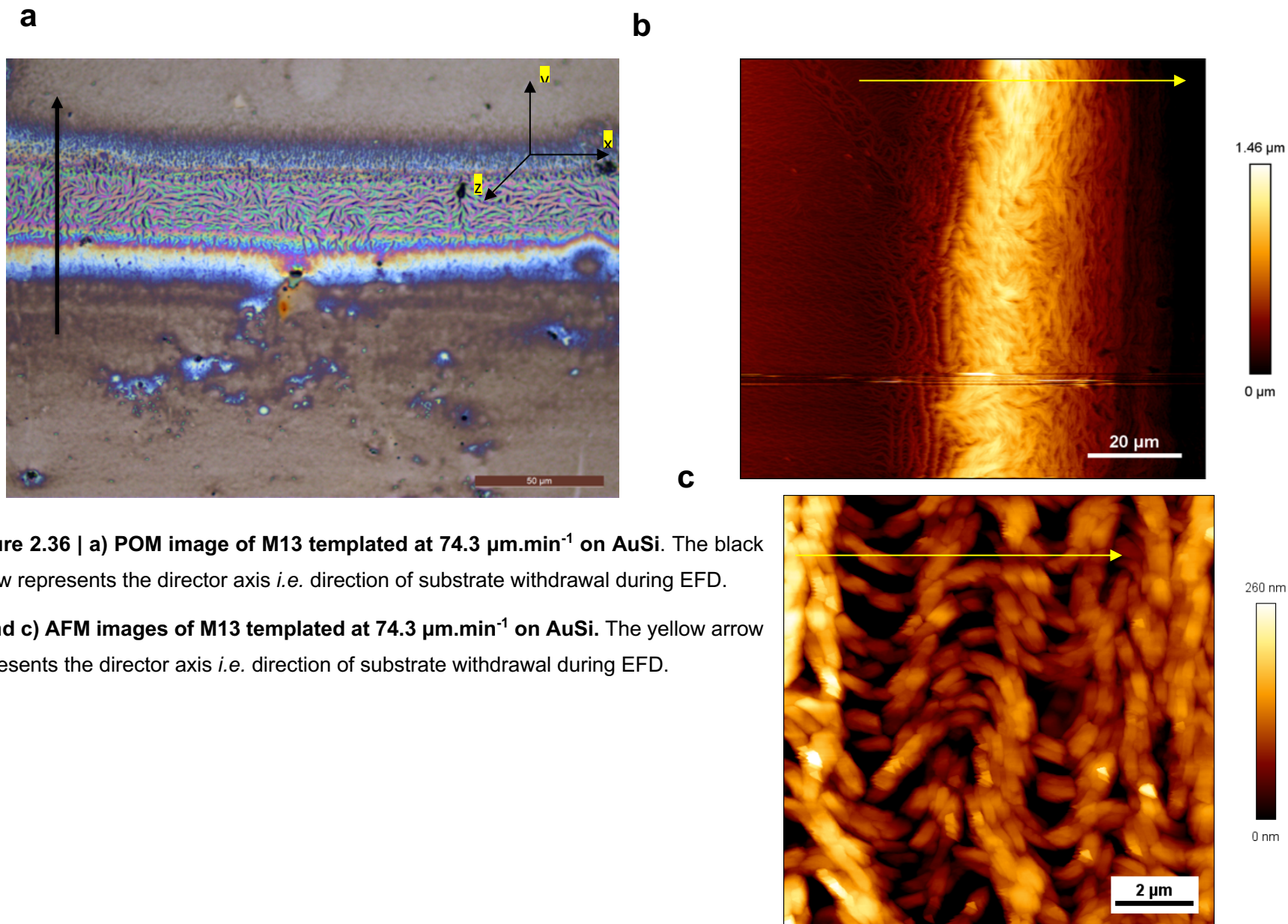
a**b****c**

Figure 2.35 | a) POM image of M13 templated at $52.0 \mu\text{m}.\text{min}^{-1}$ on AuSi. The oscillation of the dynamic contact line afforded a slip-stick motion on the substrate surface of the three-phase contact line and yielded distinct templated bands of M13 bundles perpendicular to the director axis in a 1D array.¹²³ The black arrow represents the director axis *i.e.* direction of substrate withdrawal during EFD

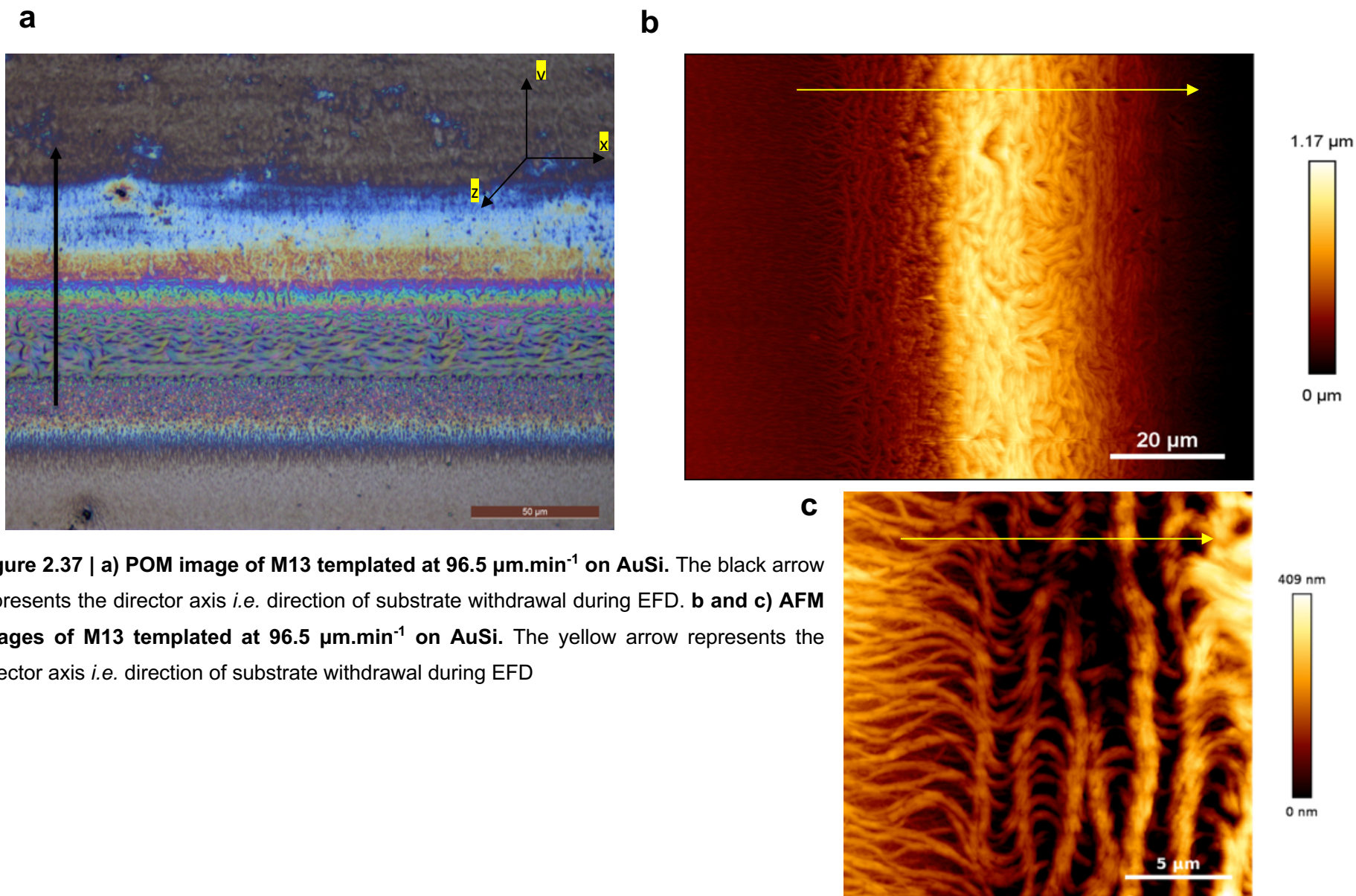
b and c) AFM images of M13 templated at $52.0 \mu\text{m}.\text{min}^{-1}$ on AuSi. The yellow arrow represents the director axis *i.e.* direction of substrate withdrawal during EFD.



When observing the AFM height image, it was interesting to note the area of which M13 fibres began to transition between nematic ordering in the same direction as the pulling mechanism, to at first a waved nematic order and finally to a chiral system (Figures 2.36c and 2.37c).

On increasing the templating speed to $111.4 \mu\text{m}.\text{min}^{-1}$ a contrasting picture was observed to that demonstrated by BSi (Figure 2.19), whereby M13 could produce a densely chiral structure within the central point of the ridge (Figure 2.38). Taking a higher resolution scan on the central point of the ridge (Figure 2.38c) gave a more in-depth analysis of the ability of M13 to bundle over itself within this region, to create densely packed bundles of M13 fibres. It was these fibres that ultimately created fine optical traps within each bundle to allow for NIM behaviour to be realised (Chapter 4).

It was clear from the 74.3 to $111.4 \mu\text{m}.\text{min}^{-1}$ templating speeds that the hierarchical ordering was not the same over the entirety of the ridge (Figures 2.35 to 2.38). However, the central region of the ridge demonstrated the highest percentage of the total ridge area, therefore it can be expected that this area has the highest significance on any optical activity witnessed in the following chapter. The ridge diameter was considered in further chapters, whereby the spot size of the laser or light beam was maintained to be of a larger diameter than the entirety of the widest ridge.



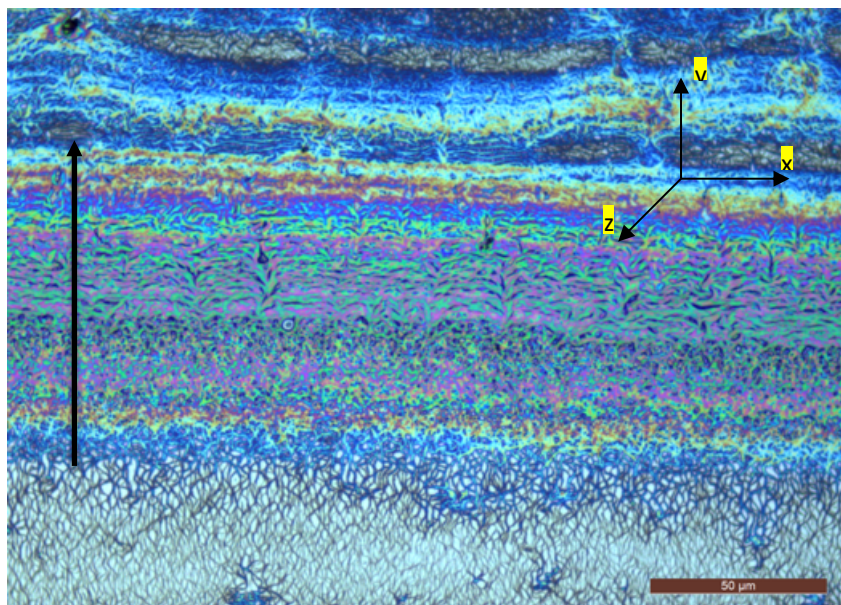
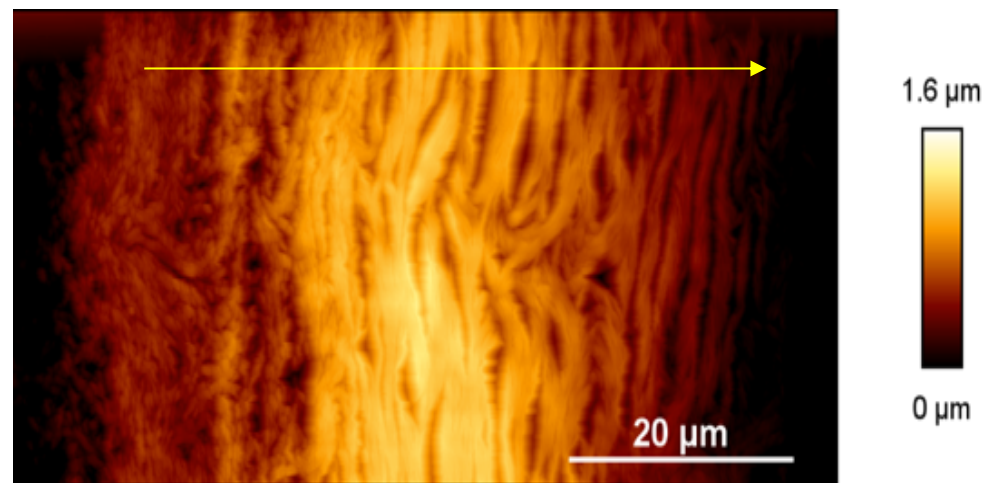
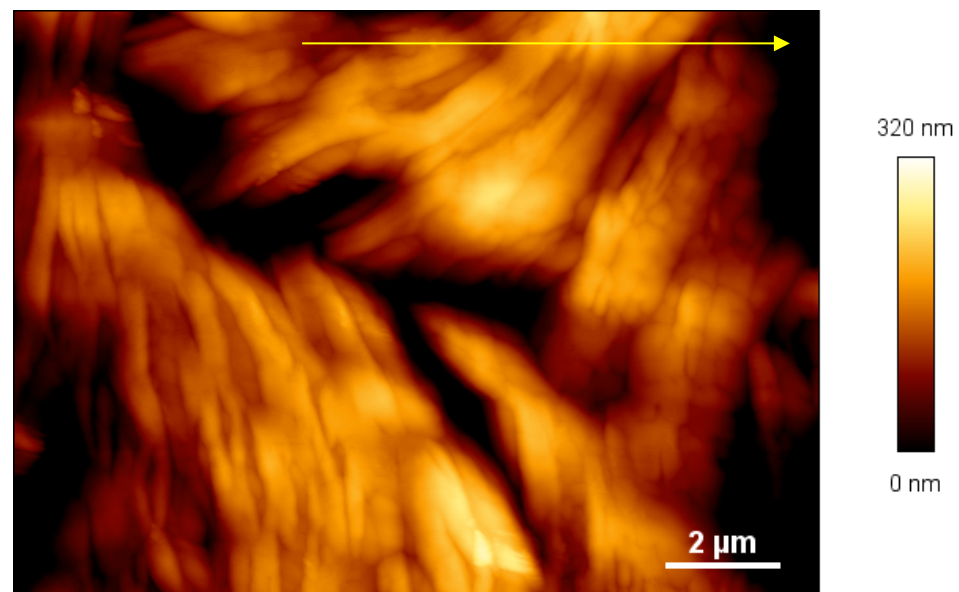
a**b****c**

Figure 2.38 | a) POM image of M13 templated at $111.4 \mu\text{m.min}^{-1}$ on AuSi. The black arrow represents the director axis *i.e.* direction of substrate withdrawal during EFD. **b and c) AFM images of M13 templated at $111.4 \mu\text{m.min}^{-1}$ on AuSi.** The yellow arrow represents the director axis *i.e.* direction of substrate withdrawal during EFD.

2.3.4.2.2 Analysis of ridge diameter vs. templating speed

The EFD templating speeds of 52.0, 74.3, 96.5 and 111.4 $\mu\text{m}\cdot\text{min}^{-1}$ are represented by templating speeds 1, 2, 3 and 4 respectively in the figures shown below. ANOVA two-way analysis was ran in MATLAB to determine whether there was both:

- 1. Significant difference between the ridge diameters of varying template speeds**
- 2. Significant difference between values obtained within each sample *i.e.* variance in the ridge diameters obtained for each templating speed**

It was expected that there should be significant difference regarding varying templating speeds. However, a significant difference posed within each sample would indicate that the templating method was un-reliable in producing reproducible 1D arrays of specified ridge diameter. For reference $P < 0.05$ was deemed significant and $P < 0.001$ was deemed highly significant. Within this section it was decided that only the AFM images would be used to collect data regarding the ridge diameter, and bundle diameters on both the central point of the ridge and the edge of the ridge.

Considering the boxplot (Figure 2.39) it was observed that an increase in templating speed was analogous to a decrease in ridge diameter. The highest templating onto AuSi was set at 111.4 $\mu\text{m}\cdot\text{min}^{-1}$ to eliminate the increase in ridge diameter past the critical point, whereby the turbulence within the templating solution surpasses the ability of the frictional adhesion of the substrate. Any templating speeds higher than that of the critical point therefore resulted in a disruption of the 1D array formation.

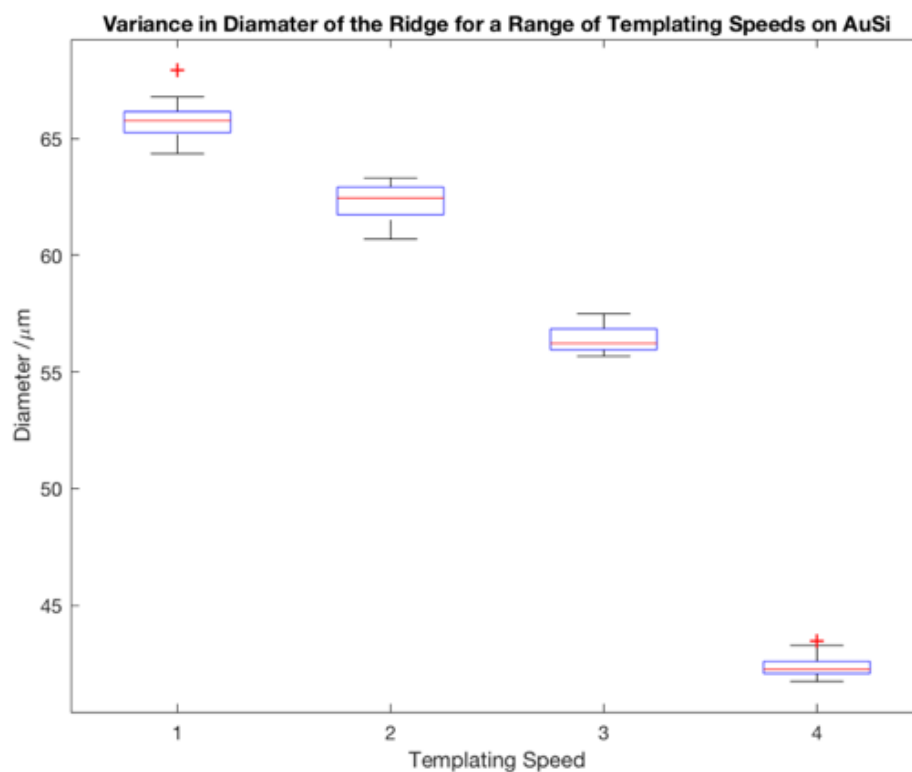


Figure 2.39 | Boxplot to demonstrate the effect of templating speed on ridge diameter during the EFD process on AuSi. The EFD templating speeds of 52.0, 74.3, 96.5 and 111.4 $\mu\text{m}\cdot\text{min}^{-1}$ are represented by templating speeds 1, 2, 3 and 4 respectively in the figure.

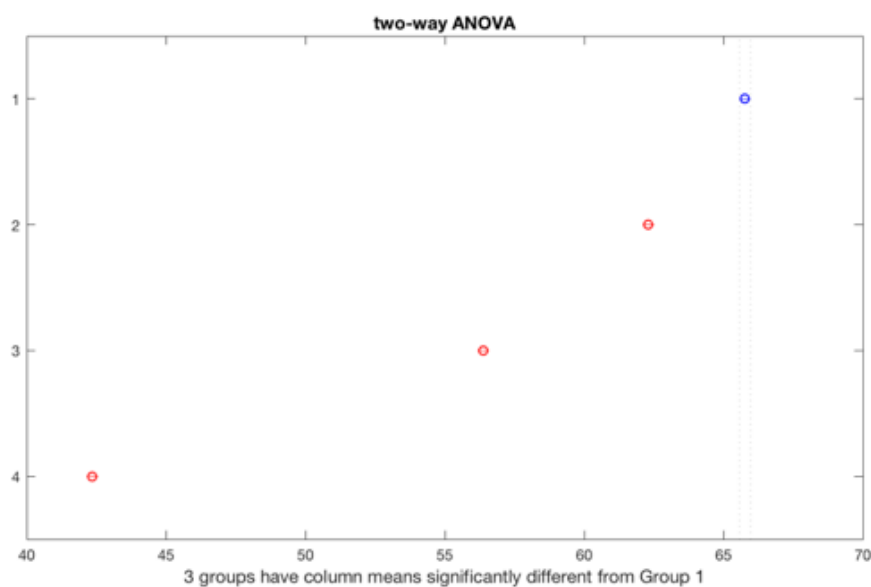


Figure 2.40 | Two-way ANOVA analysis for the ridge diameter taken from AFM imaging. The two-way ANOVA for the samples conducted in MATLAB. The EFD templating speeds of 52.0, 74.3, 96.5 and 111.4 $\mu\text{m}\cdot\text{min}^{-1}$ are represented by templating speeds 1, 2, 3 and 4 respectively in the figure.

The boxplot (Figure 2.39) highlighted there was a significant difference in ridge diameter over the range of templating speeds onto AuSi, this was highlighted by the lack of overlap between the boxes within the plot. Two-way ANOVA (Figure 2.40) was conducted to confirm the degree of significance to be $P < 0.001$ between all templating speeds. Templating speeds of 52.0 and 111.4 $\mu\text{m} \cdot \text{min}^{-1}$ showed between sample variance highlighted by the red crosses above the boxplots (Figure 2.41).

2.3.4.2.3 Analysis of bundle diameter on the central point of the ridge vs. templating speed

The boxplot (Figure 2.41) highlighted there was a significant difference in bundle diameter on the central point of the ridge over the range of templating speeds onto AuSi, this was highlighted by the lack of overlap between the boxes within the plot. Two-way ANOVA (Figure 2.42) was conducted to confirm the degree of significance to be $P < 0.001$ between all templating speeds.

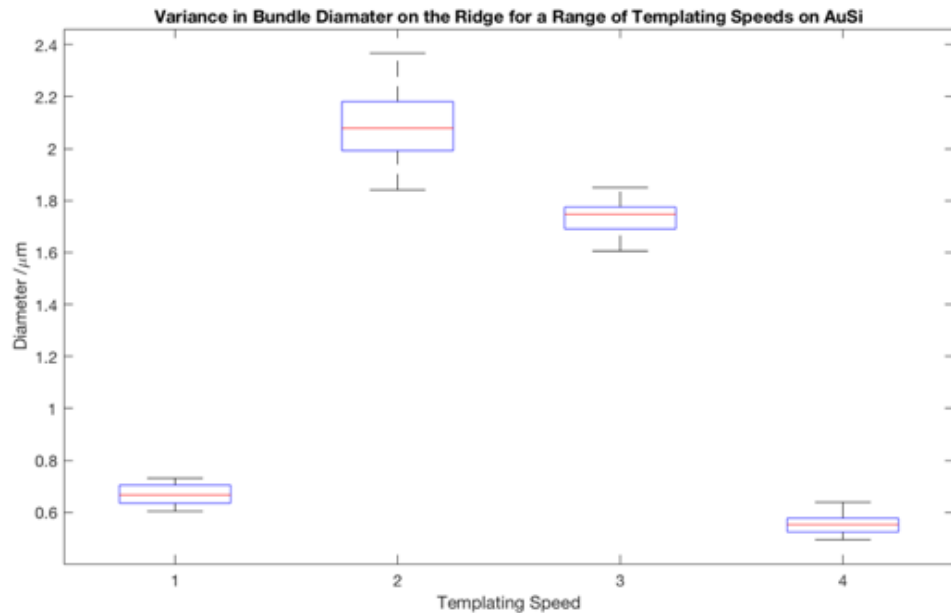


Figure 2.41 | Boxplot to demonstrate the effect of templating speed on bundle diameter during the EFD process on AuSi. The EFD templating speeds of 52.0, 74.3, 96.5 and 111.4 $\mu\text{m} \cdot \text{min}^{-1}$ are represented by templating speeds 1, 2, 3 and 4 respectively in the figure.

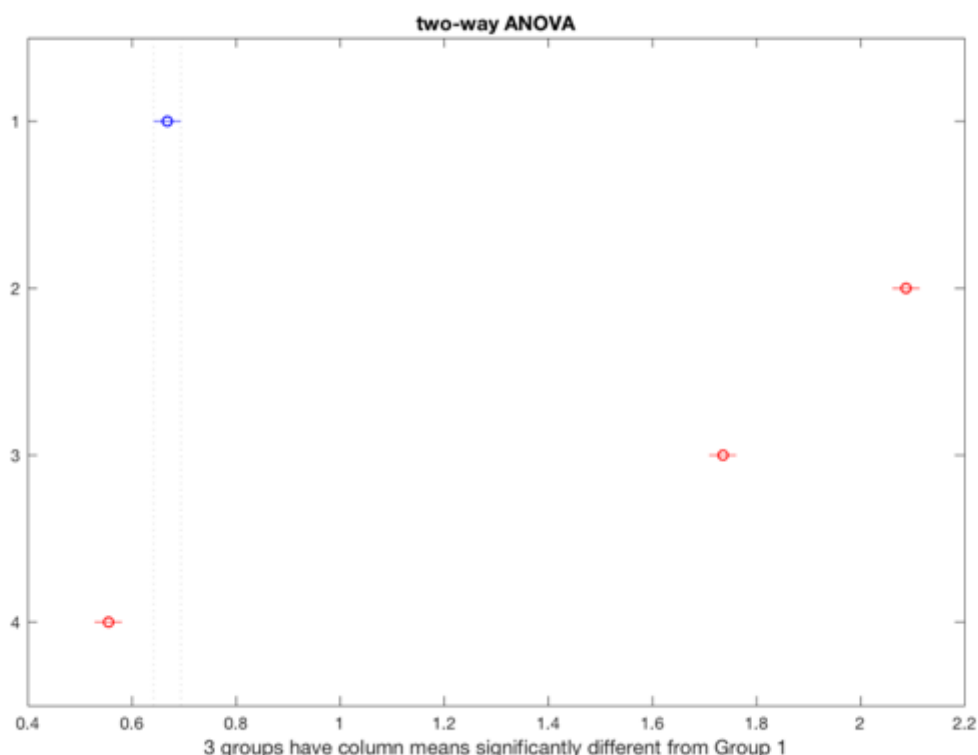


Figure 2.42 | Two-way ANOVA analysis for the bundle diameter taken from AFM imaging. The two-way ANOVA for the samples conducted in MATLAB. The EFD templating speeds of 52.0, 74.3, 96.5 and 111.4 $\mu\text{m}.\text{min}^{-1}$ are represented by templating speeds 1, 2, 3 and 4 respectively in the figure.

As the templating speed was increased from 52 to 74.3 $\mu\text{m}.\text{min}^{-1}$, the diameter of each bundle was increased by three (Figure 2.41). This could be attributed to the increased speed in drawing M13 to the surface of the 3-phase contact line. At 74.3 $\mu\text{m}.\text{min}^{-1}$, the time between each step of the micrometer to withdraw the substrate through the solution, was adequate to facilitate large numbers of M13 fibres to aggregate at the 3-phase contact line. This yielded maximum bundling at the 3-phase contact line of M13. Increasing the speed beyond 74.3 $\mu\text{m}.\text{min}^{-1}$, to 96.5 and 111.4 $\mu\text{m}.\text{min}^{-1}$ showed a decrease in bundle diameter. This could be due to a combination of both decreased volumes of M13 being drawn to the 3-phase contact line and the increased turbulence within the system to allow for tighter bundling of M13 phages within each bundle.

2.3.4.2.4 Analysis of bundle diameter on the outer ridge edge vs. templating speed

The boxplot (Figure 2.43) highlighted there was a significant difference in bundle diameter on the central point of the ridge over the range of templating speeds onto AuSi, aside from between 74.3 and 96.5 $\mu\text{m}.\text{min}^{-1}$ which showed no significant difference. Two-way ANOVA (Figure 2.44) was conducted to confirm the degree of significance to be $P < 0.001$ between all other templating speeds than 74.3 and 96.5 $\mu\text{m}.\text{min}^{-1}$ ($P > 0.05$).

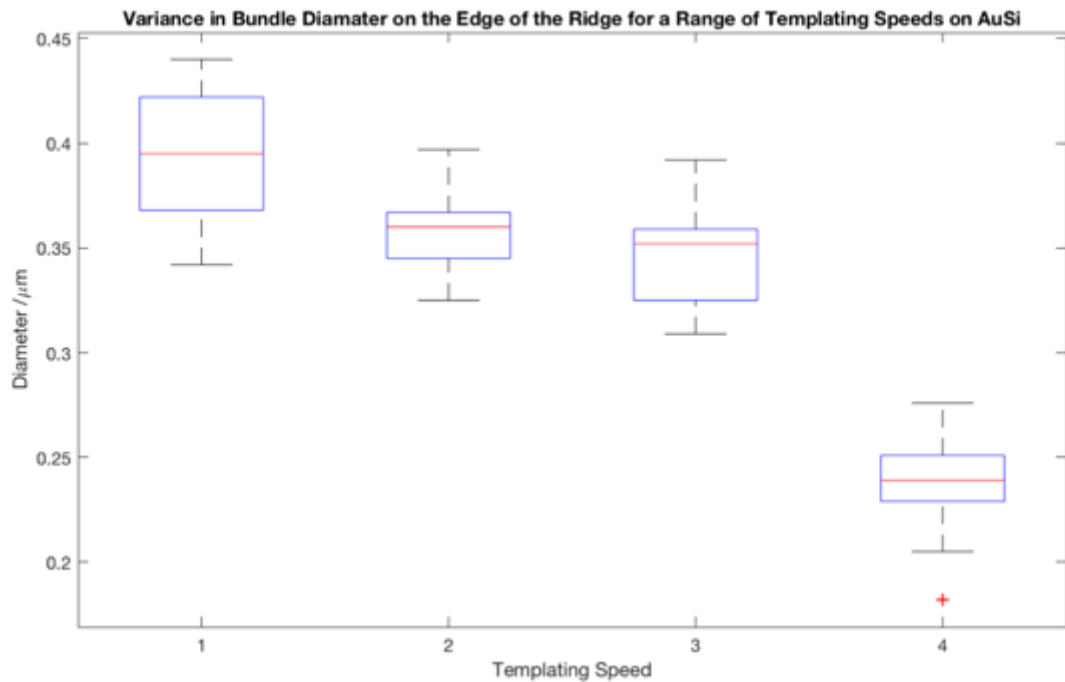


Figure 2.43 | Boxplot to demonstrate the effect of templating speed on bundle diameter during the EFD process on AuSi. The EFD templating speeds of 52.0, 74.3, 96.5 and 111.4 $\mu\text{m}.\text{min}^{-1}$ are represented by templating speeds 1, 2, 3 and 4 respectively in the figure

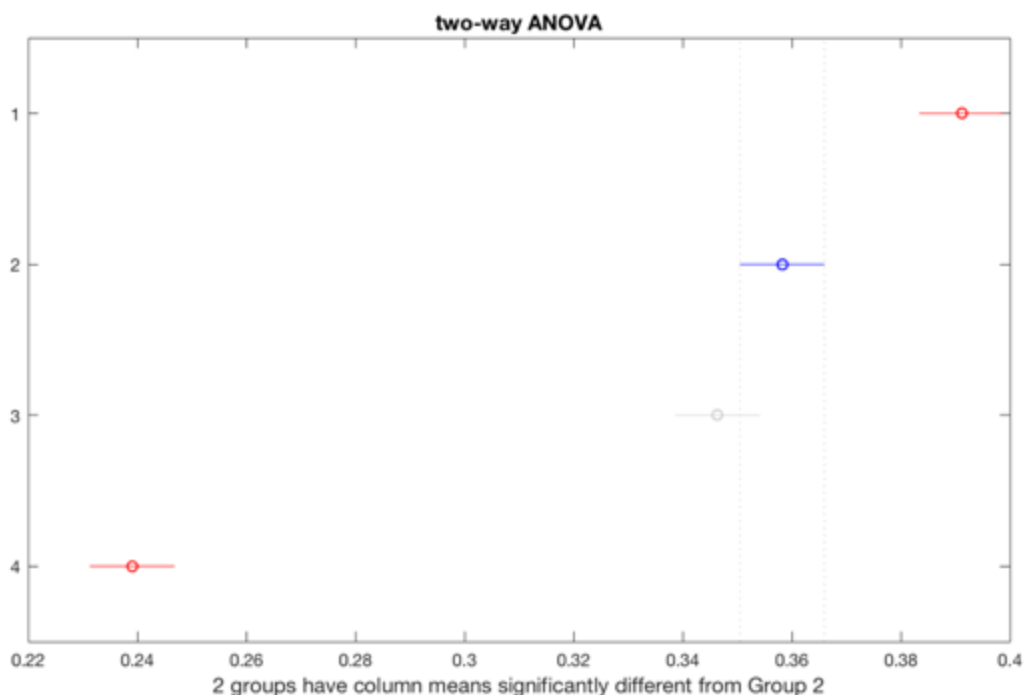


Figure 2.44 | Two-way ANOVA analysis for the bundle diameter taken from AFM imaging. The two-way ANOVA for the samples conducted in MATLAB. The EFD templating speeds of 52.0, 74.3, 96.5 and 111.4 $\mu\text{m}\cdot\text{min}^{-1}$ are represented by templating speeds 1, 2, 3 and 4 respectively in the figure.

2.3.4.2.5 Phase-scan and FFT profiling of M13 EFD on AuSi

AFM phase-scan profiles were analysed to confirm whether a preferential orientation of M13 was present at each templated speed. Histograms created from each phase-scan profile could highlight such a preference through a distinct peak in the data (Figure 2.45). For the consideration of the project a 90° or -90° phase shift would indicate templating of M13 bundles parallel to the director axis, *i.e.* direction of substrate withdrawal, whereas a 0° phase shift would indicate perpendicular templating of M13 bundles to the director axis.

As expected, the lower templating speed of $52.0 \mu\text{m}.\text{min}^{-1}$ (Figure 2.45a) showed a distinct preference for orientation *ca.* -90° indicating a nematic orientation within the ridges of the 1D array. An increase of templating speed to $74.3 \mu\text{m}.\text{min}^{-1}$ (Figure 2.45b) shifted the phase orientation to a more perpendicular value of *ca.* -20° , indicating the formation of a smectic or cholesteric phase ordering. Again, an increase of templating speed to $96.5 \mu\text{m}.\text{min}^{-1}$ (Figure 2.45c) marginally decreased the frequency of perpendicularly orientated M13 bundles, with a more preferential orientation to *ca.* -30° . This reduction in frequency of perpendicularly arranged bundles predicted that a templating speed between 74.3 and $96.5 \mu\text{m}.\text{min}^{-1}$ would be an optimal speed for the production of a 1D array with perpendicular M13 bundles to the templating speed. The final templating speed at $111.4 \mu\text{m}.\text{min}^{-1}$ (Figure 2.45d) represented an isotropic system within the ridges of the 1D arrays, whereby there was no distinct preference for any given orientation. This breakdown in successful formation of a hierarchical system within the ridges of the 1D array, was expected due to the turbulent flow of M13 within the M13 templating solution and lack of time for M13 to accumulate successfully at the three-phase contact point.

Observing the FFT manipulations set out in Figure 2.46, it was observed that two speeds; 52.0 and $111.4 \mu\text{m}.\text{min}^{-1}$, were distinctly different from those of 74.3 and $96.5 \mu\text{m}.\text{min}^{-1}$, in that they represented much lower spatial frequencies, stipulated by their high density within the central point of the FFT profiles. The templating speeds of 74.3 and $96.5 \mu\text{m}.\text{min}^{-1}$, however, showed a spatial shift towards the outer regions of the FFT profile, indicative of larger spatial frequencies.

The presence of the lower spatial frequencies for 52.0 and $111.4 \mu\text{m}.\text{min}^{-1}$ (Figure 2.46) suggested that the inter-bundle distance remained higher throughout the system. Whereas the larger spatial frequency associated with speeds of 74.3 and $96.5 \mu\text{m}.\text{min}^{-1}$, suggests that these speeds could produce a more intricate system of much smaller inter-bundle distances.

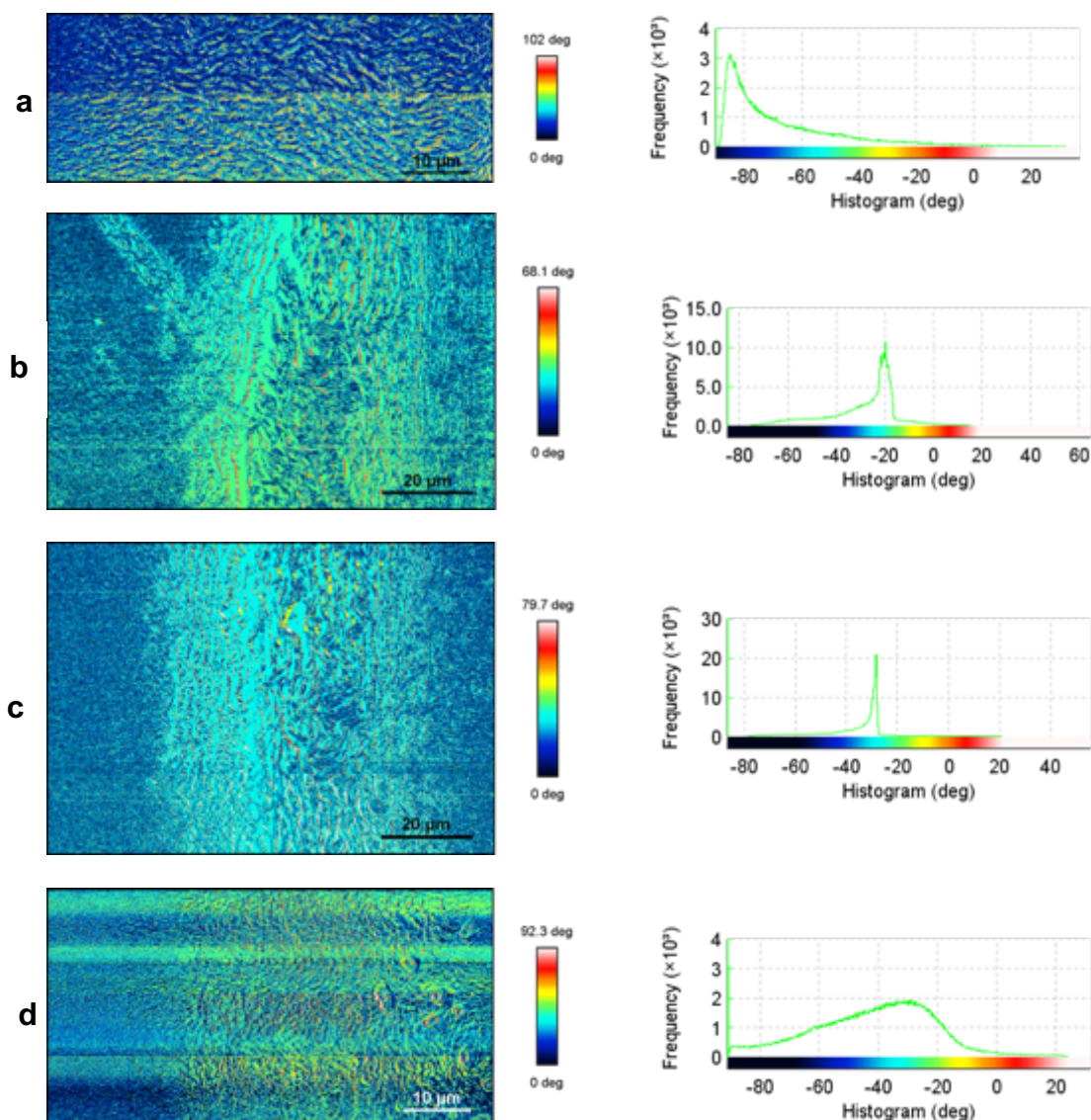


Figure 2.45 | Phase-scan profiles of M13 templated onto AuSi at varying speeds and the corresponding histogram plots. The phase-scan profiles observe regions of different orientation or composition due to deflections of the cantilever from the surface. The phase shifts could therefore present strong contrasts between different domains within an image as observed above. The corresponding histograms highlight any clear preferences for particular angles of orientation. **a)** M13 templated onto AuSi at $52.0 \mu\text{m}\cdot\text{min}^{-1}$, **b)** M13 templated onto AuSi at $74.3 \mu\text{m}\cdot\text{min}^{-1}$, **c)** M13 templated onto AuSi at $96.5 \mu\text{m}\cdot\text{min}^{-1}$ and **d)** M13 templated on AuSi at $111.4 \mu\text{m}\cdot\text{min}^{-1}$.

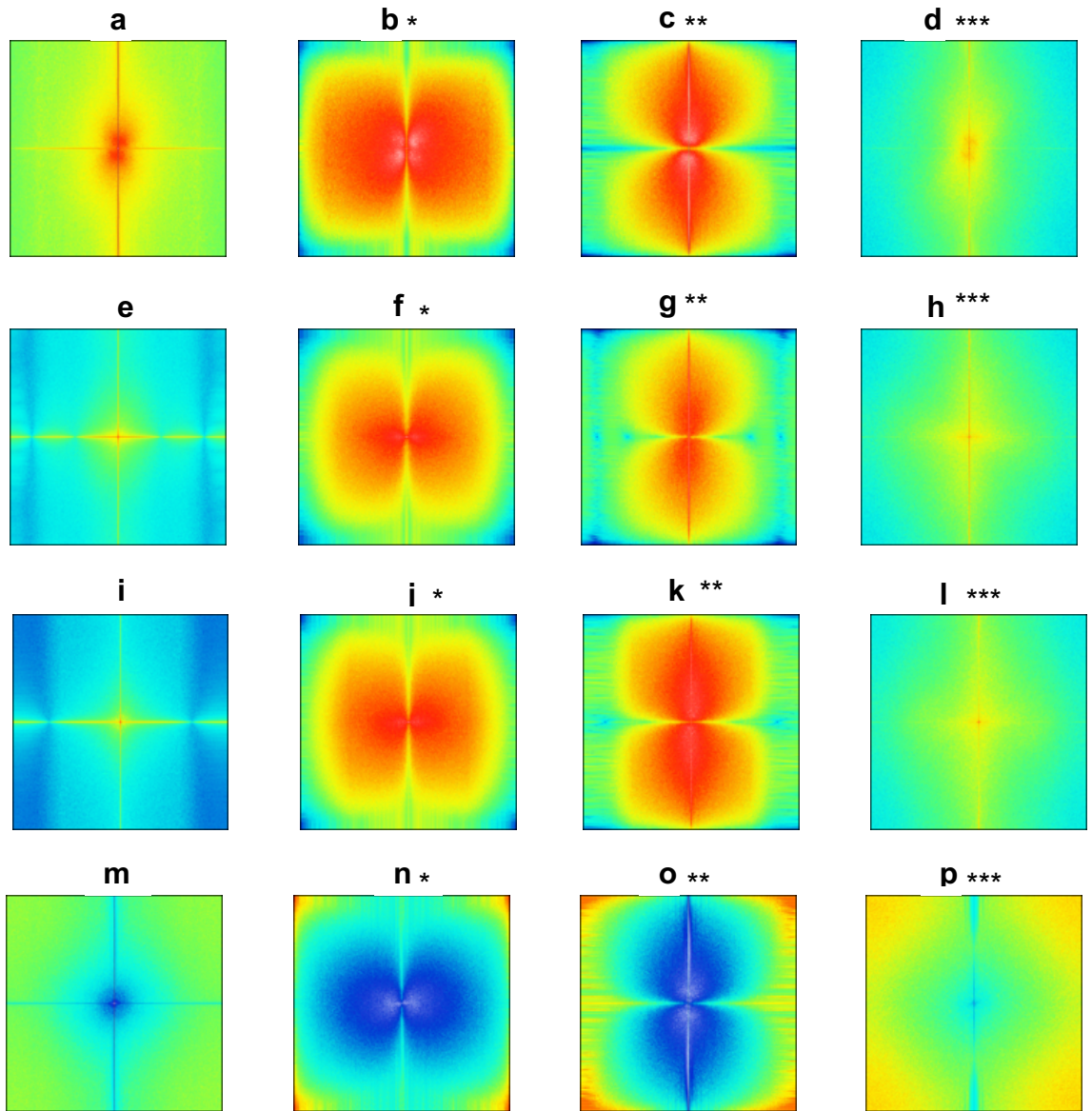


Figure 2.46 | FFT of height scan profiles of M13 templated onto AuSi at varying speeds. Frequency domain processing, whereby the rate of cycling from lower to higher z-values and back represents the image's spatial frequency. **a-d)** represent M13 at $52.0 \mu\text{m}.\text{min}^{-1}$ **e-h)** represent M13 templated at $74.3 \mu\text{m}.\text{min}^{-1}$, **i-l)** represent M13 templated at $96.5 \mu\text{m}.\text{min}^{-1}$, **m-p)** represent M13 templated at $111.4 \mu\text{m}.\text{min}^{-1}$. * indicates an FFT of height-scan profile, ** indicates FFT of height-scan profile subjected to x-directional edge detection, *** indicates FFT of height-scan profile subjected to y-directional edge detection and *** indicates FFT of height-scan profile subjected to x- and y-directional edge detection.

2.3.4.3 Analysis of M13 Evaporative Front Deposition on AuGMS

2.3.4.3.1 Atomic Force imaging of M13 Evaporative Front Deposition on AuGMS

Atomic imaging was carried out using AFM alone, due to the poorly reflective nature of the AuGMS substrate. AFM allowed visualisation of the nano and micro-scale architectures produced through templating M13 at varying speeds onto AuGMS.

Initial AFM scanning of M13 templated at $52.0 \mu\text{m}.\text{min}^{-1}$ highlighted the ability of producing a chiral structure on a glass (Figure 2.47). The edge of the ridge showed a nematic organisation of M13 with a shift in order towards a chiral system on the central region of the ridge. This can be seen by the ability of M13 to form thicker bundles at a perpendicular angle to that of the pulling direction (Figure 2.47). The slow templating speed of $52.0 \mu\text{m}.\text{min}^{-1}$, could be attributed to the inability of M13 to create one distinctive central region of chiral ordered M13. This was theorised as the high ridge height indicated that sufficient amounts of M13 were being brought to the three-phase contact line, yet the energy required to promote bundling at this point was not sufficient. The reduced energy was a function of the time between each 'step' of motor to pull the substrate upwards through the sample, the contact angle of the substrate and the ability of the Au layer on AuGMS to attract M13 to the three-phase contact line.

The increase in templating speed to $74.3 \mu\text{m}.\text{min}^{-1}$ (Figure 2.48), caused an anomalous AFM image to be collected. Here narrow bands of chiral ordering were observed at a perpendicular angle to that of the pulling speed. of *ca.* $5 \mu\text{m}$, much lower than that observed during any other sample generated *via* EFD of M13 on AuGMS, AuSi or BSi. Between the narrow ridges there was weak nematic

ordering of M13 in the same direction as the pulling direction. There was uncertainty as to why this anomalous result occurred.

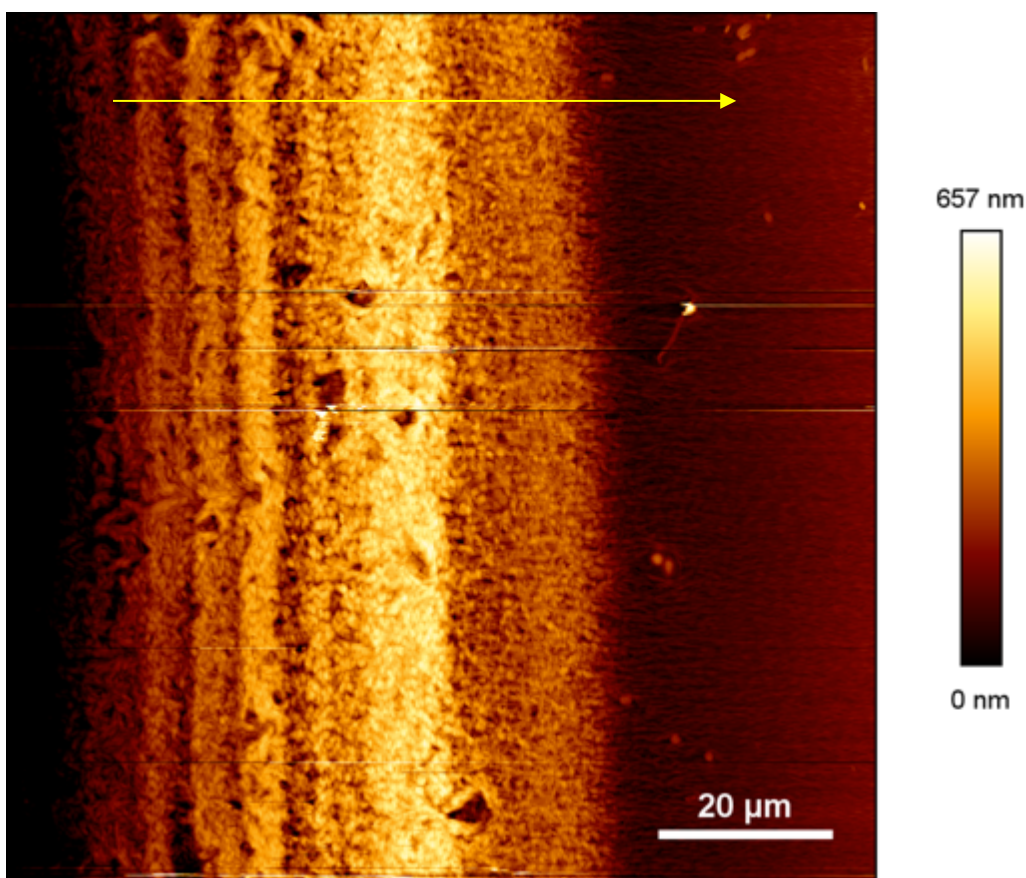


Figure 2.47 | AFM image of M13 templated at $52.0 \mu\text{m}.\text{min}^{-1}$ on AuGMS. The yellow arrow represents the director axis *i.e.* direction of substrate withdrawal during EFD.

Several factors could have influenced the architecture of this sample:

- Humidity of the room on templating, led to a change in evaporation of water from the 3-phase contact line, hence an altered topography of M13 on the AuGMS. As samples were constructed throughout the year a particularly humid day could have had effect on this sample.
- Inadequate coverage of the glass microscope slide with Au could have caused the Au layer to slip along the glass microscope slide as withdrawal was taking place. This would have prevented M13 from adhering to the AuGMS in a way to facilitate bundling of M13.

Therefore, sample was not considered in the conclusive results as it was deemed un-reproducible. However, it was included within this report, as it was acknowledged that a progression towards much narrower ridges e.g. 5 μm could be beneficial in creating an increased NIM effect (discussed later in Chapter 3).

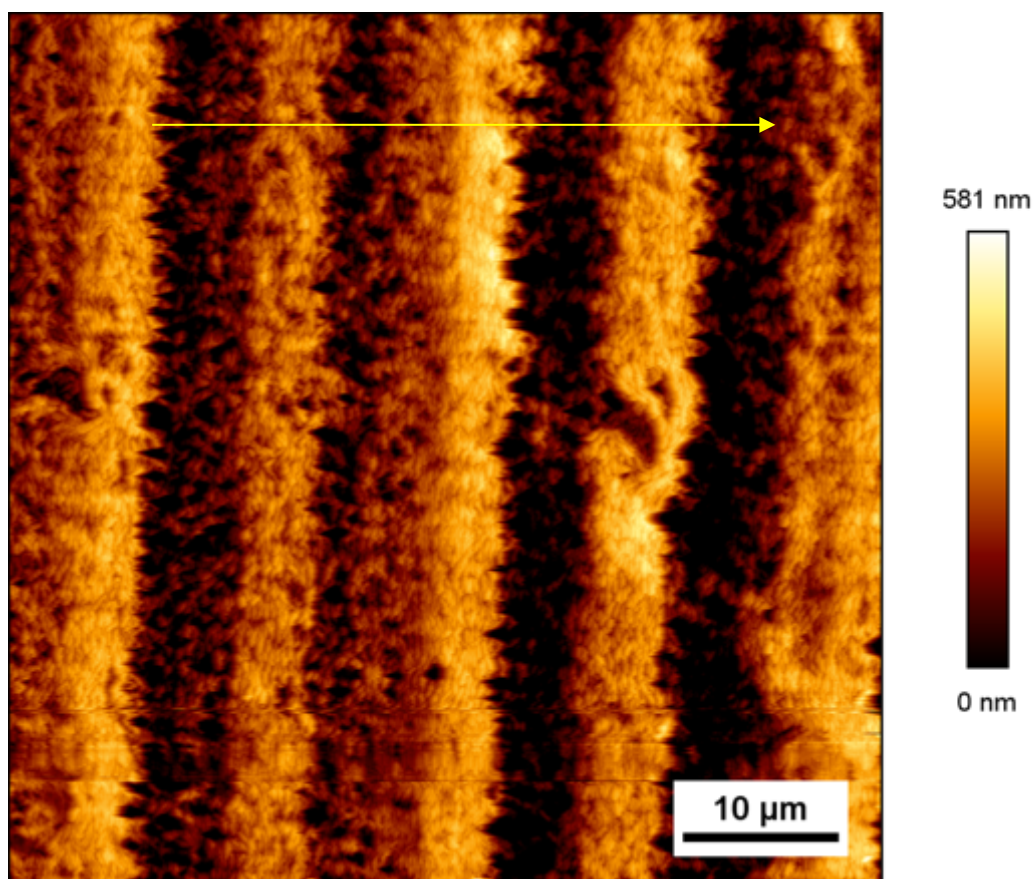


Figure 2.48 | AFM image of M13 templated at $74.3 \mu\text{m}.\text{min}^{-1}$ on AuGMS. The yellow arrow represents the director axis *i.e.* direction of substrate withdrawal during EFD.

A move towards higher templating speeds of $96.5 \mu\text{m}.\text{min}^{-1}$ (Figures 2.49 and 2.50), began to form ridges of M13 on AuGMS that were consistent with those observed on BSi and AuSi at this templating speed. The ridge edges showed a nematic organisation of M13 fibres in the direction of the pulling speed. Whilst the central chiral band of thicker M13 bundles was at an angle perpendicular to that of the pulling system. The increase in templating speed allowed for enough energy to be generated at the three-phase contact line to initiate bundling of M13

into a chiral organisation. The attraction between M13 and the Au layer was also enough to adhere M13 to the surface without excessive slipping of the three-phase contact line.

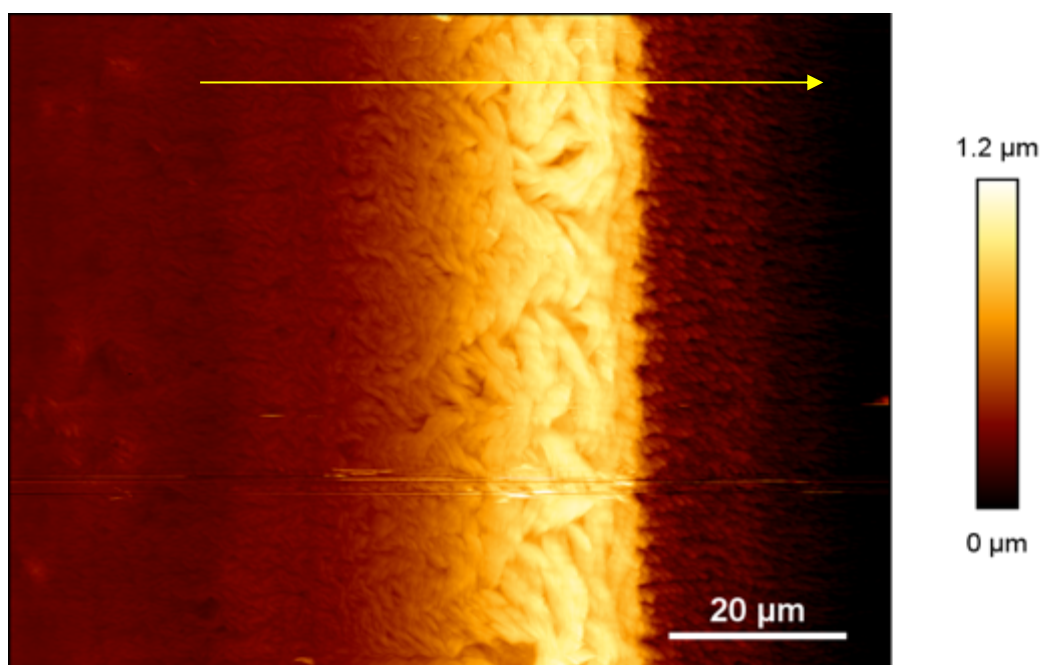


Figure 2.49 | AFM image of M13 templated at 96.5 $\mu\text{m}.\text{min}^{-1}$ on AuGMS. The yellow arrow represents the director axis *i.e.* direction of substrate withdrawal during EFD.

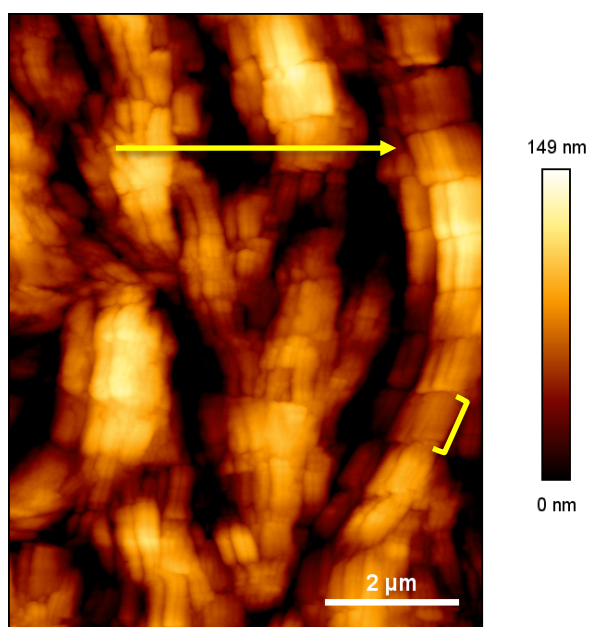


Figure 2.50 | AFM image of M13 templated at 96.5 $\mu\text{m}.\text{min}^{-1}$ on AuGMS – increased resolution The yellow arrow represents the director axis *i.e.* direction of substrate withdrawal during EFD.

A higher resolution AFM image taken on the ridge (Figure 2.50) allowed visualisation of the intricate bundling of M13 on the ridge. The length of one M13 fibre would equate to between 700-1000 nm, this was easily viewed within the higher resolution AFM height-profile (Figure 2.50). As each of the bundles bind to each other they rotate and form a chiral structure, rotating around 360°.

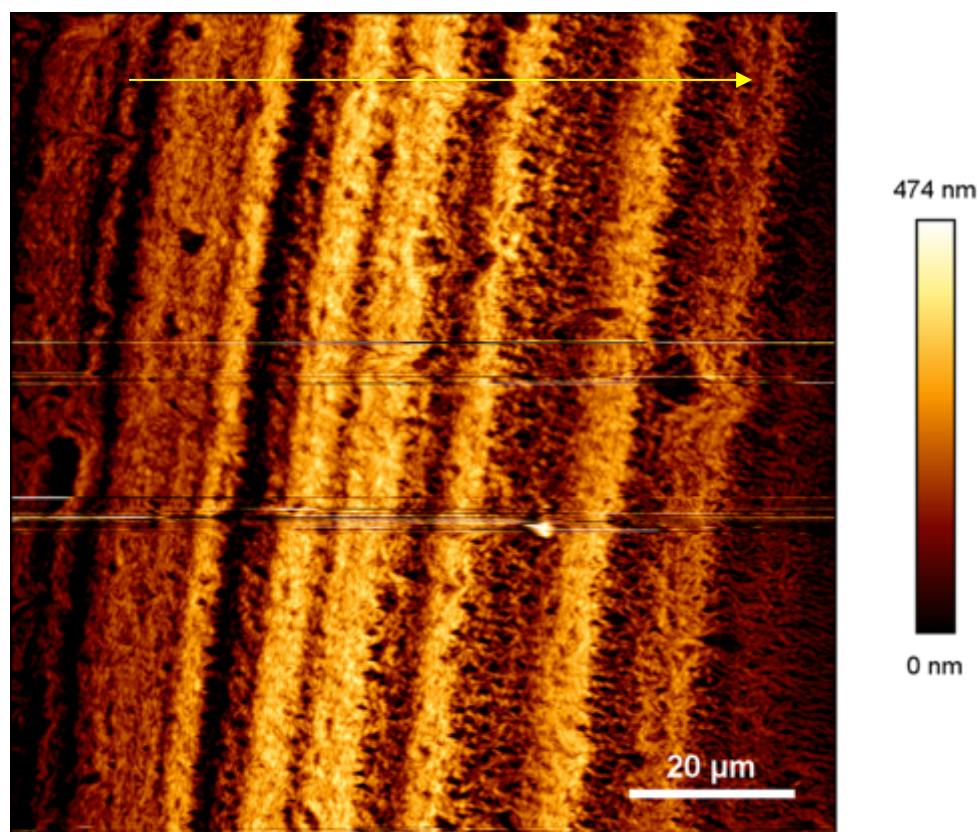


Figure 2.51 | AFM image of M13 templated at 111.4 $\mu\text{m}.\text{min}^{-1}$ on AuGMS. The yellow arrow represents the director axis *i.e.* direction of substrate withdrawal during EFD.

Increase of the templating speed to 111.4 $\mu\text{m}.\text{min}^{-1}$, however, resulted in a regression in the ability of M13 to form multiple narrow chiral bands (Figure 2.51) in the central portion of the ridge as with Figure 2.36. The architecture produced here was similar structure to that observed during lower templating speeds of 52.0 $\mu\text{m}.\text{min}^{-1}$ (Figure 2.47), indicating that a force was overcoming the ability of M13 to create adequate bundling of M13 within the ridge. One reason for this could be the lack of time between ‘steps’ of the motor pulling the substrate

upwards through the solution. The reduced time dissipates the ability of the Au coat on the AuGMS substrate to attract M13 to the three-phase contact line, reducing the bundling effect caused by mass migration of M13 to the three-phase contact line.

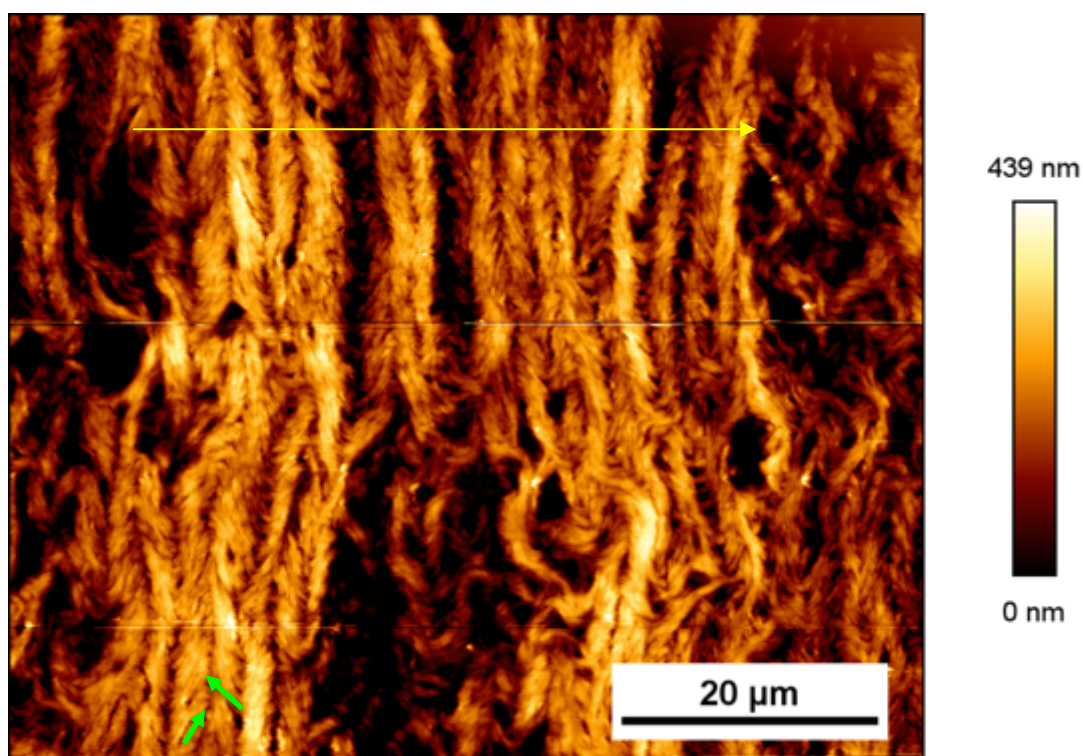


Figure 2.52 | AFM image of M13 templated at $148.5 \mu\text{m}.\text{min}^{-1}$ on AuGMS. The yellow arrow represents the director axis *i.e.* direction of substrate withdrawal during EFD

Further increase of the templating speed to $148.5 \mu\text{m}.\text{min}^{-1}$, produced an interesting result. Here, M13 begun to form herringbone ordering on AuGMS (Figure 2.52) similar to that observed by Chung *et. al.*³⁰ An increased resolution image of a small section of this image to better visualise this structure (Figure 2.53). During herringbone ordering two distinct phases are observed for the directionality of M13 these are highlighted on the image by green arrows (Figure 2.52). However, whilst there are regions where the herringbone organisation was observed, it was not consistent and there were many areas whereby M13 has begun to take on an isotropic appearance throughout the templating.

The herringbone chiral formation was the organisation observed by *Chung et al.* during their EFD process.³⁰

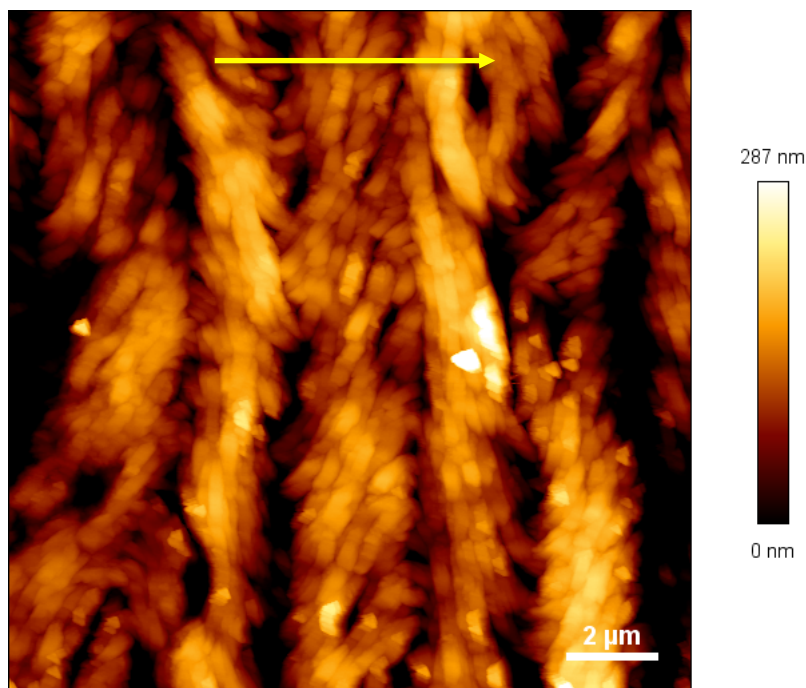


Figure 2.53 | AFM image of M13 templated at $148.5 \mu\text{m}.\text{min}^{-1}$ on AuGMS – increased resolution. The yellow arrow represents the director axis *i.e.* direction of substrate withdrawal during EFD.

2.3.4.3.2 Phase-scan and Fourier Force Transform profiling of M13 Evaporative Front Deposition on AuGMS

The phase-scan profiles observe regions of different orientation or composition due to deflections of the cantilever from the surface. The phase shifts can therefore present strong contrasts between different domains within an image as observed above. The corresponding histograms highlight any clear preferences for angles of orientation.

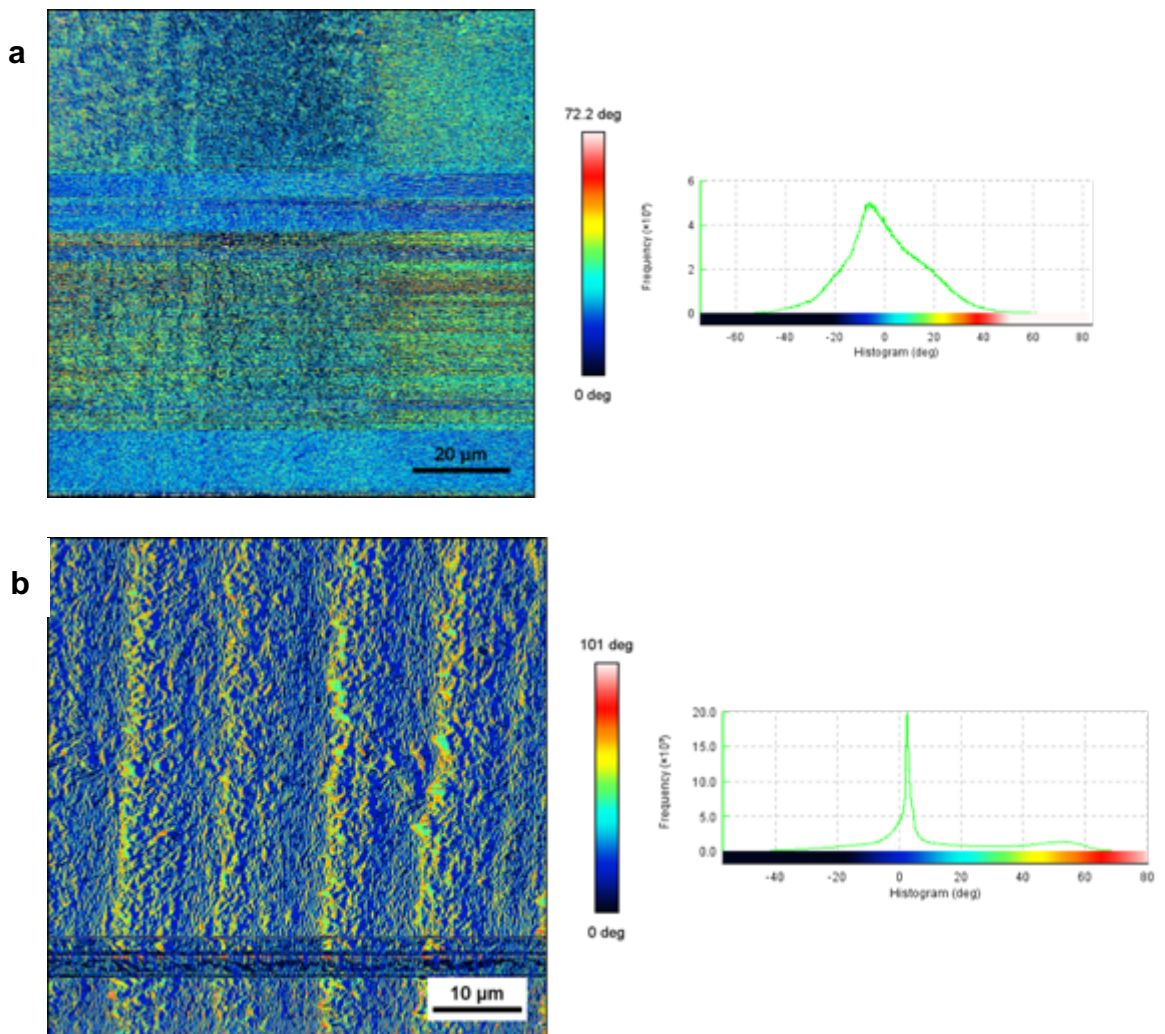


Figure 2.54 | Phase-scan profiles of M13 templated onto AuGMS at varying speeds and the corresponding histogram plots. a) M13 templated onto AuGMS at 52.0 $\mu\text{m}\cdot\text{min}^{-1}$, b) M13 templated onto AuGMS at 74.3 $\mu\text{m}\cdot\text{min}^{-1}$,

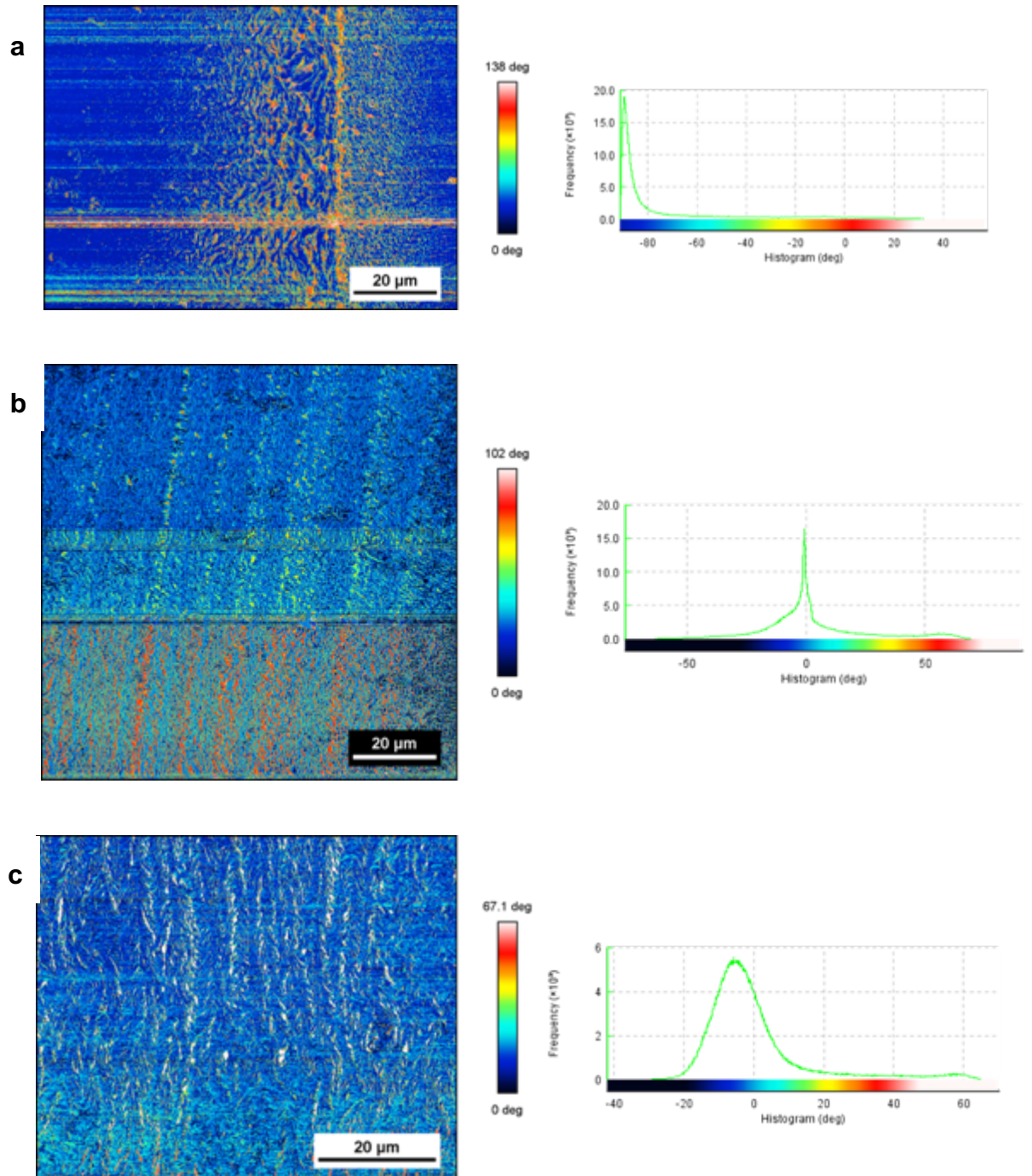


Figure 2.55 | Phase-scan profiles of M13 templated onto AuGMS at varying speeds and the corresponding histogram plots. a) M13 templated onto AuGMS at $96.5 \mu\text{m}\cdot\text{min}^{-1}$ b) M13 templated on AuGMS at $111.4 \mu\text{m}\cdot\text{min}^{-1}$ and c) M13 templated on AuGMS at $148.5 \mu\text{m}\cdot\text{min}^{-1}$

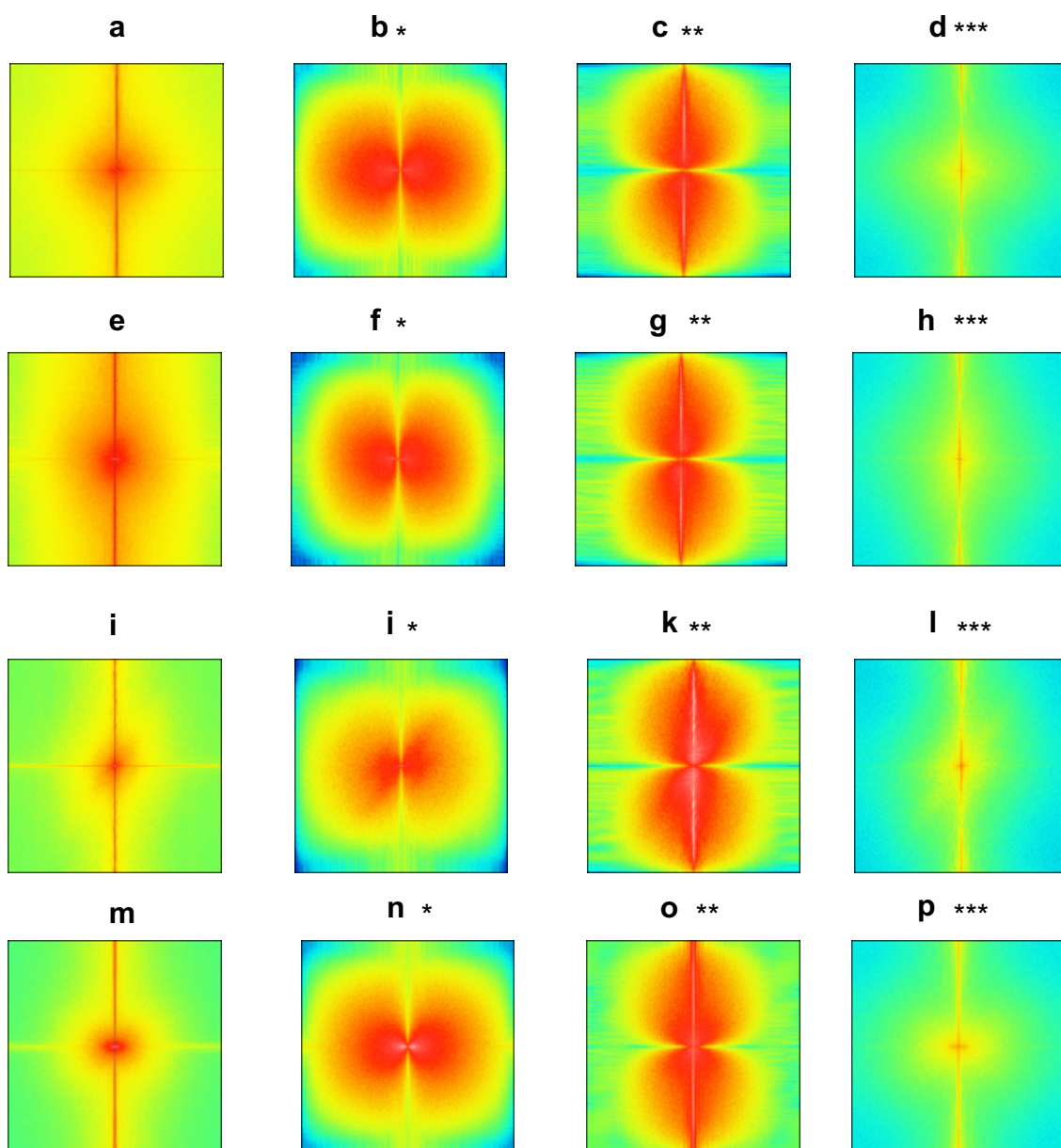


Figure 2.56 | FFT of height scan profiles of M13 templated onto AuGMS at varying speeds. Frequency domain processing, whereby the rate of cycling from lower to higher z -values and back represents the image's spatial frequency. **a-d)** represent M13 at $52.0 \mu\text{m}.\text{min}^{-1}$ **e-h)** represent M13 templated at $74.3 \mu\text{m}.\text{min}^{-1}$, **i-l)** represent M13 templated at $96.5 \mu\text{m}.\text{min}^{-1}$, **m-p)** represent M13 templated at $111.4 \mu\text{m}.\text{min}^{-1}$. * indicates an FFT of height-scan profile, ** indicates FFT of height-scan profile subjected to x-directional edge detection, *** indicates FFT of height-scan profile subjected to y-directional edge detection and *** indicates FFT of height-scan profile subjected to x- and y-directional edge detection.

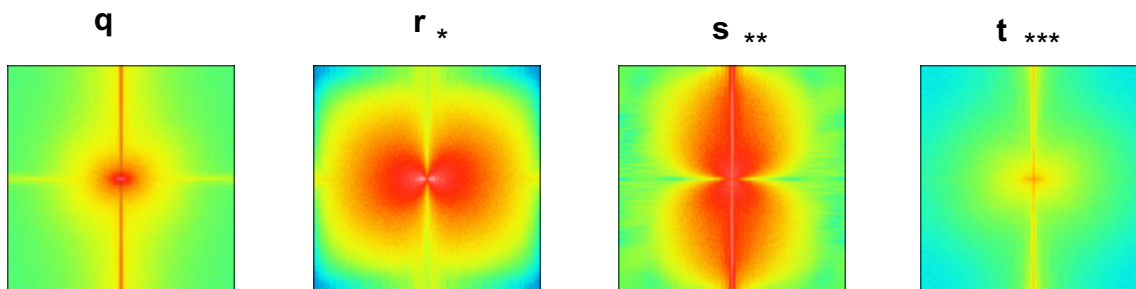


Figure 2.57 | FFT of height scan profiles of M13 templated onto AuGMS at varying speeds. Frequency domain processing, whereby the rate of cycling from lower to higher z-values and back represents the image's spatial frequency. **q-t)** represent M13 templated onto AuGMS at $148.5 \mu\text{m}.\text{min}^{-1}$, * indicates an FFT of height-scan profile, ** indicates FFT of height-scan profile subjected to x-directional edge detection, *** indicates FFT of height-scan profile subjected to y-directional edge detection and *** indicates FFT of height-scan profile subjected to x- and y-directional edge detection. 1

AFM phase-scan profiles were analysed to confirm whether a preferential orientation of M13 was present at each templated speed. Histograms created from each phase-scan profile could highlight such a preference through a distinct peak in the data (Figure 2.54 and 2.55). For the consideration of this project a 90° or -90° phase shift would indicate templating of M13 bundles parallel to the director axis, *i.e.* direction of substrate withdrawal, whereas a 0° phase shift would indicate perpendicular templating of M13 bundles to the director axis.

Two templating speeds of 52.0 and $148.5 \mu\text{m}.\text{min}^{-1}$, showed a diffuse peak within the phase shift profiles (Figures 2.54a and 2.55c).

Templating speeds of $52.0 \mu\text{m}.\text{min}^{-1}$, produced a centralised phase shift around 0° (Figure 2.54a), indicating a weak preference towards parallel templating of M13 to the director axis. The diffuse appearance of the peak indicates that there was a considerable range associated with the templating of M13 (-40 to $+40^\circ$).

Templating speeds of $148.5 \mu\text{m}.\text{min}^{-1}$ produced a centralised phase shift around -10° (Figure 2.55c), indicating a slight movement away from parallel templating of M13 in respect to the director axis. Again, the diffuse appearance of the peak

indicates there was a considerable range associated with the templating. Here, a diffuse peak was expected due to the herringbone formation produced by the EFD templating procedure. The range was considered to be -20 to $+15^\circ$, thus a slight preference towards a left-handed deviation from the parallel templating of M13 onto AuGMS.

Templating speeds of 74.3 and $111.4 \mu\text{m}\cdot\text{min}^{-1}$ produced sharp peaks around 0° indicated a preference to parallel templating of M13 to the director axis (Figures 2.54b and 2.55c). Templating at $96.5 \mu\text{m}\cdot\text{min}^{-1}$ again produced a sharp peak (Figure 2.55a), but this time at 90° indicating a preference of templating in the perpendicular direction to the director axis, which was expected due to the distinct ridge of M13 produced by the templating speed (Figure 2.49).

The presence of the lower spatial frequencies for 52.0 and $74.3 \mu\text{m}\cdot\text{min}^{-1}$ suggested that the inter-bundle distance remained higher throughout the system. Whereas the larger spatial frequency associated with speeds of 96.5 to $148.5 \mu\text{m}\cdot\text{min}^{-1}$, suggests that these speeds could produce a more intricate system of much smaller inter-bundle distances (Figure 2.57).

2.3.4.4 Analysis of Ridge Diameter

Initially the water within the PBS solution began to evaporate from the three-phase contact line, resulting in a decreased contact angle (C_A) of the meniscus.¹¹⁶ The non-volatile M13 fibres were transported to the edge of the meniscus *via* an upward flow driven by the water evaporation, this pinned the meniscus *i.e.* the contact line, to the surface. This was further aided by the increased surface tension created by the moving substrate, upwards out of the templating solution. When the C_A fell below the critical value (C_C), increased surface tension forces (γ) surpassed the frictional forces (fN), de-pinning the

contact line. This caused a jerking motion to a new position downwards from the initial contact line point, leaving behind a horizontal 'band' deposit of M13, observed as ridges and grooves on the substrate surface.^{38,39,109} This pinning and de-pinning motion occurs until one of three conditions was broken:

1. The micrometer used to mount the substrate reaches its limit of movement
2. The concentration of M13 within the solution was diminished to such a point that the contact line can no longer be pinned to the substrate
3. The solvent has evaporated from solution, leaving behind the non-volatile e.g. NaCl, constituents within the container

Whilst the kinetic sliding friction (Table 2.5) remained the same for AuGMS and AuSi, there was significant differences in their structural topography of the surface. The ridge and groove diameter for the two samples (Table 2.7 and 2.8) were both considered highly significantly different ($P < 0.001$), indicating that there were other physical parameters impacting the ordering of M13 at the three-phase contact line. One major impact that could be at play was the fluctuation in environmental conditions during templating. It was well known that factors such as humidity and temperature can have a significant impact on the drying of a meniscus. To rectify this, it would be advised for any future work to be conducted in a controlled environment to ensure that the temperature and humidity of the surroundings could be properly maintained. This was not a possibility due to equipment constraints during this project, therefore the air conditioning in the room was set at 17°C for the duration of the EFD process to ensure reproducibility of samples. However, as other people were using the laboratory this was not always guaranteed to be kept constant.

2.3.4.5 Analysis of Ridge Height

Height fluctuations were observed in the ridges of the 1D array even at a constant withdrawal speed of the substrate from solution due to the stick and slip motion periods. During the slow-motion period the concentration of M13 within the solution increases overtime as water evaporates from the PBS solution. This afforded a thicker horizontal 'band' of templated M13 as an increased volume of M13 fibres was dragged to the contact line. At sufficiently slow templating speeds, as used in the experiments here, the time allowed for M13 to accumulate at this point causes bundling of M13 to existing M13 nucleation sites. This in turn slowed down the deposition process further. The slow period therefore led to an increase in height of the templated band as more M13 was accumulated in a facile manner.

^{38,109}

Following on from the slow-motion period a faster more turbulent process followed. The fast period of motion led to a mass deposition of M13 at 3 phase contact line as the solution became sufficiently concentrated, due to solvent evaporation during the slow period. This mass deposition of M13 significantly and quickly decreased the concentration of M13 within the solution. In turn forming narrower, more concentrated bands of M13 bundles. A decrease in height of the deposited band was therefore observed, due to the fast moving meniscal front not allowing for the accumulation of M13 at the contact line in the same manner as the slow period.^{38,39,109}

Similarly to that of the analysis of ridge diameter, all samples tended to produce an increase in the height of the templated ridge up until around $96.5 \mu\text{m}.\text{min}^{-1}$, after which the height began to decrease once again. This can be explained by the above theory.

2.3.4.6 Analysis of Bundle Sizes

Observing of the AFM images it was clear that the larger bundle sizes could create finer pore sizes within the 3D structures of each of the ridges on the 1D arrays. This was evident due to the decreased spacing between the bundles highlighted (Figures 2.34, 2.34, 2.45, 2.56 and 2.47) by the FFT data. The finer pore sizes had the capability of slowing down the phase velocity of light through the material as the light wave had to modify its path through the material and out of the most peripheral pores (Figure 2.58).

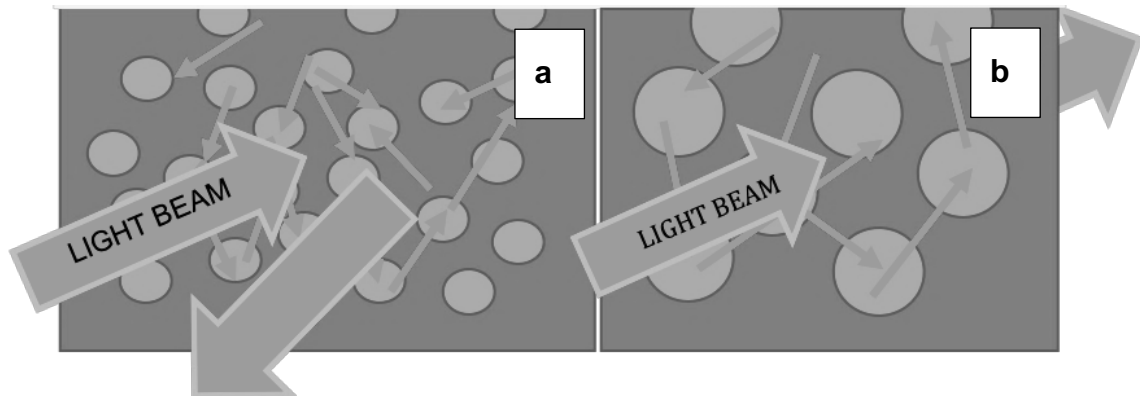


Figure 2.58 | Schematic displaying the effect of pore size on the incident light beam.
a) represents the light beam reaching a material in which finer pores are present within the sample. As the light infiltrates the material it becomes slowed by the optical traps created by the pores within the material to such an extent that a negative phase velocity was achieved.
b) represents the situation where, a larger pore size was present. The larger pore sizes are ineffective in slowing the light beam and thus it passes through the material.

In a standard material light propagation occurs at an inferior speed to the vacuum. The change in phase velocity of the light was manifested as refraction. The reduction in speed was quantified by the ratio of the vacuum speed and the phase velocity and referred to as the refractive index of the material. Slow light occurs when a propagating pulse was substantially slowed down by the interaction with the medium in which the propagation takes place. The slowing down of the light wave as in the 3D M13 architectures produced here, afforded a negative phase

velocity of the light wave as the propagation favours the backward flow of energy towards the substrate surface. This could be due to the rapidly changing refractive index over a small range of frequencies within each of the ridges. Larger pores would allow for quicker release of energy from the system, whereby the negative flow of energy would not be favourable for the system. As these larger pores are associated with narrower bundles on the ridge, it was expected that the optimal speed of templating would be $96.5 \mu\text{m}.\text{min}^{-1}$ for both BSi and AuGMS and $111.4 \mu\text{m}.\text{min}^{-1}$ for AuSi to yield the strongest degree of negative refraction and ultimately the lowest negative index of refraction for the material.

Through consideration of both the bundle diameter in the central portion of the ridge and that at the edges of the ridge it can be observed whether there are any relationship effects occurring between both the bundles diameters and templating speed, and also between the bundle diameters themselves. From the boxplot analysis of the bundle diameter on the central portion of the ridges and the edges of the ridges there was no clear relationship between these factors (Figures 2.26, 2.28, 2.41 and 2.43). There was, however, a distinct relationship between the templating speed and both bundle diameter on the central portion of the ridge and on the ridge edge (Figures, 2.26, 2.28, 2.41 and 2.43). The bundle diameter on the central portion of the ridge appeared to widen as the templating speed of EFD was increased from 52.0 to $74.3 \mu\text{m}.\text{min}^{-1}$, however after this point the diameter of the bundles begins to narrow again during $111.4 \mu\text{m}.\text{min}^{-1}$. This initial increase in bundle diameter could be attributed to the required energy of the system to achieve bundling of M13 atop of each other at the three-phase contact point, as previously described.

2.3.5 Compiled Data Tables for Each Substrate

For consolidation of data collected within Chapter 2, tables compiling data collected for each sample surface are supplied here.

Table 2.6 | Experimental data gained for M13 templated onto BSi at varying speeds.

The table here, highlights the effect of templating speed during the EFD process of M13 onto BSi. Phase alignment of the sample was realised through the phase-scan profile of the topographical surface using AFM in tapping-mode. The peak-to-valley roughness and RMS roughness squared were observed utilising the height-scan profile from AFM of the sample, alongside the ridge height and diameter.






Speed of templating / $\mu\text{m}.\text{min}^{-1}$	Phase Alignment	Peak-to-Valley Roughness	RMS Roughness Squared	Ridge Height / R_H	Ridge Diameter $\mu\text{m} / \Gamma$
14.9		463.7 nm	41.5 nm	183 nm	84 \pm 5
52.0		680.0 nm	91.8 nm	405 nm	62 \pm 1
74.3		619.5 nm	137.6 nm	606 nm	53 \pm 1.5
96.5		787.9 nm	136.7 nm	602 nm	43 \pm 2
148.5		1117.0 nm	81.5 nm	359 nm	70 \pm 1

Table 2.7 | Experimental data gained for M13 templated onto AuSi at varying speeds.

The table here, highlights the effect of templating speed during the EFD process of M13 onto AuSi. Phase alignment of the sample was realised through the phase-scan profile of the topographical surface using AFM in tapping-mode. The peak-to-valley roughness and RMS roughness squared were observed utilising the height-scan profile from AFM of the sample, alongside the ridge height and diameter.










Speed of templating / $\mu\text{m}.\text{min}^{-1}$	Phase Alignment	Peak-to-Valley Roughness	RMS Roughness Squared	Ridge Height / R_H	Ridge Diameter $\mu\text{m} / \Gamma$
52.0		0.691 μm	49.4 nm	0.22 μm	66 ± 2
74.3		1.644 μm	351.9 nm	1.46 μm	62 ± 1
96.5		1.264 μm	266.7 nm	1.17 μm	56 ± 1
111.4		1.763 μm	370.7 nm	1.6 μm	42 ± 1

Table 2.8 | Experimental data gained for M13 templated onto AuGMS at varying speeds. The table here, highlights the effect of templating speed during the EFD process of M13 onto AuGMS. Phase alignment of the sample was realised through the phase-scan profile of the topographical surface using AFM in tapping-mode. The peak-to-valley roughness and RMS roughness squared were observed utilising the height-scan profile from AFM of the sample, alongside the ridge height and diameter.

Speed of templating / $\mu\text{m}.\text{min}^{-1}$	Phase Alignment	Peak-to-Valley Roughness	RMS Roughness Squared	Ridge Height / R_H	Ridge Diameter $\mu\text{m} / \Gamma$
52.0		2.163 μm	149.3 nm	657 nm	66 ± 2
74.3		1.485 μm	107.6 nm	474 nm	5 ± 1
96.5		1.656 μm	272.2 nm	1200 nm	55 ± 2
111.4		0.535 μm	58.9 nm	259 nm	44 ± 2
148.5		1.884 μm	99.9 nm	439 nm	-

2.4 Conclusions

Moving forwards from initial templating of M13 several templating speeds were isolated that produced interesting 3D structures within the 1D arrays. These samples were chosen due to their ideal physical characteristics such as narrow inter-bundles distances, optically thin ridges and superior hierarchical levels. After highlighting the initial experimental requirements for templating onto BSi, exploration into templating M13 onto AuSi and AuGMS was explored to expand the capability and versatility of the fabricated 3D material. Due to laboratory constraints in analysing the material as a NIM, it was required the 3D structure to

be templated onto an optically transparent material *e.g.* glass, this proved to be difficult due to the physical properties of glass not being particularly suitable for the EFD templating process, hence it was chosen to use AuGMS, which was capable of being optically transparent, whilst also retaining a similar 3D ridged structure of M13 to that templated on BSi and AuSi.

CHAPTER 3 M13: A CHIRAL ROUTE TO NEGATIVE REFRACTION

Nature has adapted tremendously throughout extreme conditions posed by the environment to display exotic characteristics.^{9,126,127} Current mimicry of these extraordinary adaptations nature has provided has probed the development of smart devices that not only mimic the properties posed in nature, but also surpass them through novel fabrication methods.

When considering bulk 3D MM two main conditions need to be met. The first being that the optical resonators, in the case of this project the bundles of M13, within the ridges, must be arranged in 3 dimensions of space. Secondly, the optical resonators must be of a dimension that was smaller than the wavelength of the perturbing light beam.^{85,92,95,128} Whilst satisfying these conditions does not definitively produce MM; they are a significant indicator as to the possibility of engineering MM.

At present there was a significant gap in the research where nature's building blocks have not been explored to synthesise MM. The EFD methodology developed previously (Chapter 2.1) allowed the self-assembly of M13 bacteriophage 3D structures atop of inorganic substrates. The architected structures displayed the precursor structural foundations to yield MM; such as optical cavities and a consistent arrangement of 1D arrays (Chapter 2.3).

Recently it was proposed that a negative index of refraction could be achieved through a chiral route and since chiral metamaterials have attracted more and more attention. Whilst displaying negative indices of refraction, chiral metamaterials can pose interesting properties such as giant optical activity and circular dichroism, which can expand their uses for optical activities.^{82,129,133,179} A

chiral metamaterial lacks any symmetry, so that there is cross-coupling between the electric and the magnetic fields at the resonance. Consequently the degeneracy of the two circularly polarised waves; right handed circularly polarised light (RCP) and left handed circularly polarised light (LCP), is broken and so display different refractive indices.^{119,127,130}

This project focuses on creating hybrid inorganic/organic chiral 3D MM with sub-wavelength optical cavities that could interact with and perturb light to demonstrate NIM behaviour at VIS to mid-infrared range (MIR) wavelengths of light. It was expected that these tuneable-engineered structures could demonstrate extraordinary capabilities for use in a broad range of applications, from perfect-lenses to defence systems.

In this chapter the practical and computational efforts will be explored where possible to determine any novel abilities of the structure's architecture in Chapter 2. As already highlighted in Chapter 1, a distinctly high or low circular dichroism (ΔCD) and therefore anisotropic factor (g) could lead to the production of a NIM and therefore negative phase velocity. Further ΔCD and (g) to have a relationship with any negative refraction observed for the sample materials.

3.1 The Chiroptical Response

Chirality was a phenomenon observed widely in nature in a magnitude of scales, ranging from microscopic DNA to macroscopic seashells.^{40,131,132} Yet it was Louis Pasteur that made the initial breakthrough in connecting chirality and optical activity in 1848 during an experiment on tartaric acid crystals.¹²⁶ In its simplest form chirality was a characteristic of an object or molecule in which its mirror image cannot be superimposed on oneself.

Whetten and *Schaff* discovered that a differential shift in circular dichroism (CD) towards LCP and RCP (Figure 3.1, Eqn. 1.2) *i.e.* chirality, could be observed for biological molecules within the electromagnetic spectrum.¹³⁴ This has since prompted researchers to use nature as a mimic for not only traditional engineering solutions but also in the nanoscale for advanced functional materials. Similarly the response of helical structures to an electromagnetic field was associated with the effect of Δ CD.^{135,136}

Theoretically it has been proposed that Δ CD can also be achieved in the visible wavelengths through the collective plasmon excitation in chiral assemblies of metal nanoparticle (NP).^{83,134,137,138} This was predicted due to the helical display of AuNP on the helical biomolecule. Coupled plasmon waves that propagate along the helical path, could lead to increased absorption by those NP, due to the collective plasmon-plasmon interactions within the nanohelices.¹³⁹ The optical response resulted from such a material has been shown to generate giant circular dichroism in the visible spectrum.¹³⁹ Hence the absorption of CPL was predicted to be strongest in the vicinity of the metal NP surface plasmon resonance (SPR) band (Figure 3.1).^{27,45,139}

It was predicted that through modulating the mechanical (templating speed) and chemical (M13 and NP concentration) parameters of the EFD process a hierarchical hybrid M13-NP 3D structure could be achieved. The NP were expected to be arranged in close proximity within the open nano-pores that were created by the intertwining bundles of M13.^{140–142} This close proximity of the NP was expected to further enhance the Δ CD signal within the vicinity of the SPR band.^{140–142}

Chirality can be extrinsic, wherein chiroptical activity was observed on tilting of a sample in respect to the incident light beam, or intrinsic in which chiroptical activity was witnessed as a function of the wavelength of light used as the incident beam.¹²⁸ Whilst Δ CD was generally measured in solution, here the traditional

methodology has been adapted to build an 'in-house' rig that was suitable for observing ΔCD for bulk substrates as in a molecular system. Taking the principles of CD *i.e.* the ability to characterise the differential absorption of left-handed circularly polarised light and right-handed circularly polarised light as a function of wavelength, a system was created to fit the principles laid out by conventional CD detection systems. This was discussed further in Section 3.4.3.^{119,128,143,144}

The (g) , (Eqn. 1.3) could then be calculated to observe the significance of the observed ΔCD values in a quantitative manner. The ΔCD spectra were normalized by their corresponding extinction to yield arbitrary values. A variation in (g) was indicative of a change in the physical orientation of the sample.^{126,128,145}

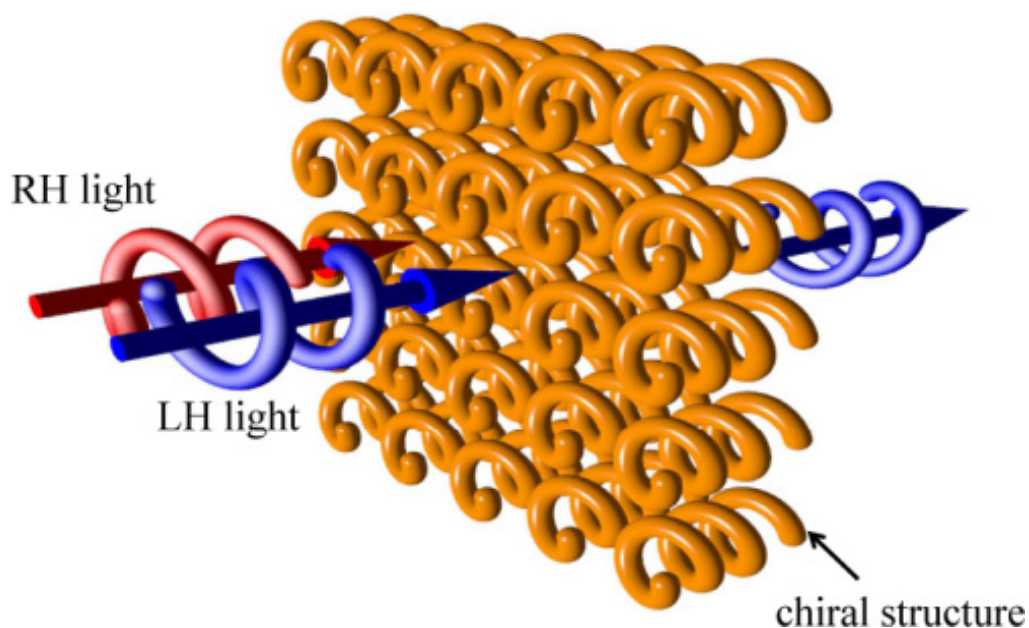


Figure 3.1 | Interaction of CPL with an inherently chiral structure. Here, the schematic for the interaction was shown for both left and right-handed circularly polarised light with an inherently chiral structure that contains right-handed helices. As the right-handed CPL was of same handedness as the chiral structure the RCP light was absorbed through the structure, whereas the LCP of opposite handedness to the helices within the chiral structure was free to move through the structure was transmitted through the backside of the material. Thus, only an LCP signal would be detected emitting on the backside of the material.

3.2 Negative Index Materials (NIM)

Schuster first discussed negative refraction in 1909 in the book 'An Introduction to the Theory of Optics', where the field of MM was painted with a significantly pessimistic view. In particular it was detailed that to achieve a NIM would be absurd due to the physical demands of the system, in that the thickness of such a material would need to be much smaller than the wavelength of light used to promote a NIM effect (Figure 3.2).¹⁴⁶ Since 1909 many efforts to disprove this theory have shown fruitful results, however, these examples are in the majority concerned with long wavelengths of light such as microwaves. One such example was that presented by *Li et al.* where double negativity of the MM (*i.e.* $n_{\text{eff}} < 0$) was achieved in the acoustic microwave region of the electromagnetic spectrum.¹⁴⁷ Double negativity refers to a material that can exhibit a negative value for both permittivity and permeability simultaneously.

Snell's Law demonstrates the relationship between the angles of incidence and refraction in respect to light waves travelling through a boundary between two different media. (Eqn. 3.1)

$$n_1 \sin \theta_1 = n_2 \sin \theta_2 \quad (\text{Eqn. 3.1})$$

However, when considering a non-continuous film such as the templated 1D array of hierarchical bands it was not possible to use Snell's Law (Eqn.3.1) to determine the refractive index. Instead a variation on Snell's Law (Eqn.3.2) deduced by *Yu et al.* to theoretically predict the $\theta_{t,\perp}$ value based on the periodicity *i.e.* dimension of the ridge width, the wavelength (λ_0) and angle of the incident light beam was used.^{71,72,148,149} The height profile of the templated material was not taken into consideration during the calculations as the value of the phase shift ($d\Phi/dx$) would be negligible given the height of the 3D structures upon the sample surface.

n_{sub} = refractive index of substrate

θ_i = angle of incident light beam

λ_0 = wavelength of incident light beam

Γ = the periodicity of the ridges *i.e.* the diameter of the ridges within the sample

$$\theta_{t,\perp} = \arcsin[n_{\text{sub}} \sin(\theta_i) - (\lambda_0/\Gamma)] \quad (\text{Eqn. 3.2})^{72}$$

Taking this consideration further, calculations following practical calculations of $\theta_{t,\perp}$ and n will also omit the height of the 1D array.

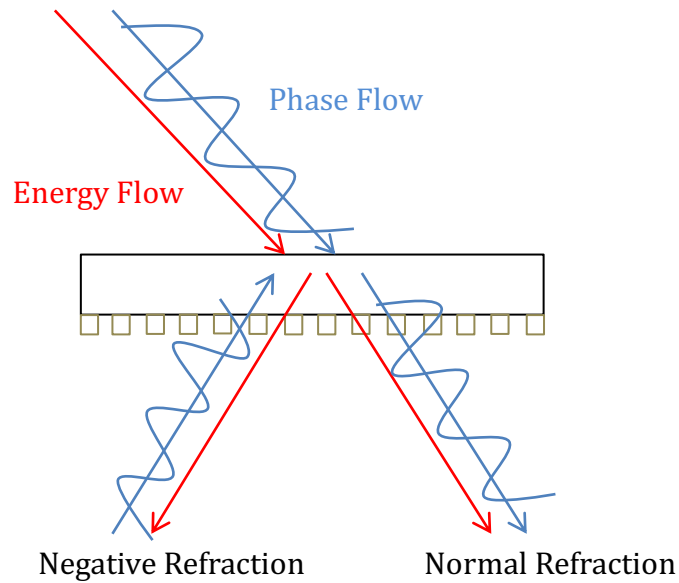


Figure 3.2 | Schematic representation of negative phase velocity leading to negative refraction. As the light wave travels through the substrate and subsequently the MM the propagation of light perturbing the MM becomes trapped in the optical cavities within the ridges of the 1D array, led to the phase velocity to slow. Sufficient optical trapping by the cavities allowed for the phase velocity to be slowed to such an extent that the phase velocity changes direction, flowing backwards into the MM towards the substrate. The release of the energy from the system was then of an anomalous direction to that observed by an

ordinary material, in that it was on the same side of the normal to the incoming light wave to the MM.

3.3 Reflectance and Transmittance of Linear Light

When considering anisotropic media whereby the molecular components are displaying disorder in the system, non-local effects begin to affect the SPR band, yielding angle dependent colour change. A similar effect was witnessed in the *Papilio blumei* butterfly. Structural colour witnessed in nature are considered to originate from five fundamental optical processes and their contributions:

- **Thin film interference**
- **Multilayer interference**
- **Diffraction grating effect**
- **Photonic crystals**
- **Light scattering**

It was n't until 1917 when Rayleigh proposed the multilayer interference principal that physical interpretation of structural colour could be achieved. Since then it has been widely accepted that structural colour was due to interference in some manner.

When a plane wave of light approaches the surface of the material the reflected beams from the two interfaces n_A and n_B interfere with each other (Figure 3.3). The interference differs depending on whether $n_A < n_B$. In the case of the structure M13 was templated atop of a gold-coated silicon wafer, where the refractive index of the 3D structure was predicted to be lower than that of both gold and silicon due to its lower characteristic SPR peak. Variations in reflectivity present in the visible spectrum as a shift in observed colour, *i.e.* a shift in the SPR peak. Holding

true the definition of reflection itself, it therefore follows that a change in SPR can be attributed to a change in refractive index.

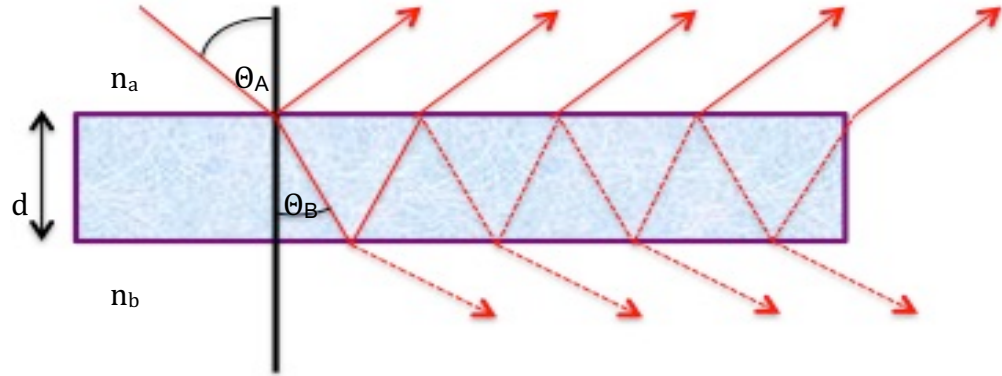


Figure 3.3 | Schematic representation of reflectivity and refractivity of light through a medium. Where n = refractive index of the medium, θ_a = reflection angle, θ_b = refraction angle and d = layer thickness.

The 3D nanoarchitecture of M13 was termed as a nonlinear multilayer as the thickness of the templated 3D structure \neq the thickness of gold thin layer or the silicon substrate ($d_A \neq d_B \neq d_C$). Despite the fabricated structure having a nonlinear multilayer structure, simple transfer matrix calculations of reflection still hold valid. This was true as the multilayer structure contains varying refractive indices of arbitrary value and thickness without periodicity. Upon the introduction of periodicity to the 3D nanoarchitecture the nanopores within the 3D structure yields an anti-reflective system irrespective of whether $n_A < n_B$. This occurs as the pores within the system have the capability to trap volumes of air much larger than that of a flat thin film. It was this trapped air that affords slowing of the light within the media.

3.4 Methodology

3.4.1 Linear Reflectance

An in-house rig (Figure 3.4), was set up to characterise the linear reflectance of the samples produced in Chapter 2. All measurements were taken within a dark room to eliminate any interference from daylight.

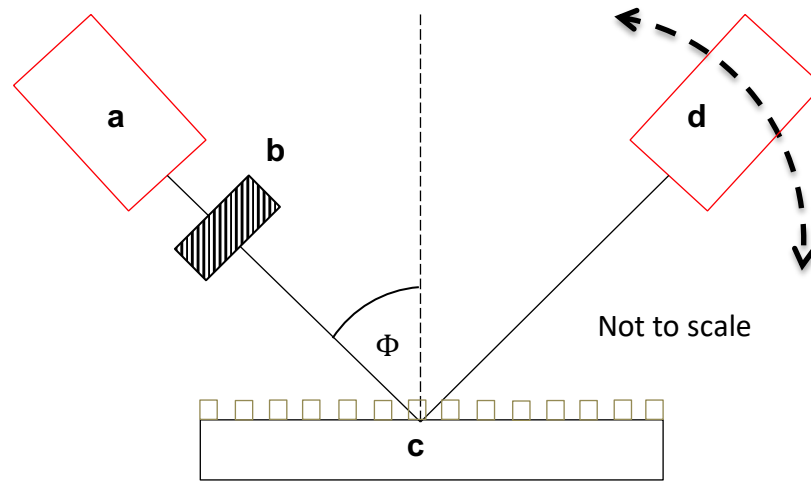


Figure 3.4 | Schematic representation for linear reflectance characterisation of 1D arrays of M13 templated via EFD onto BSi and AuSi. The substrate surface displaying the 1D array of M13 was fixed into a rotating head with the 1D array facing towards the laser source. The rotating head allowed for a movement of the sample through a 360° x-plane rotation, thus modifying the angle of Φ from the laser source to the 1D array. **a)** The laser beam of specified wavelength was emitted from a laser source, after which it passes through a **b)** linear polariser before reaching **c)** the 1D array templated onto the substrate surface. The 1D array then absorbs a certain portion of the incident light beam, the rest was reflected towards **d)** the detector, where an intensity value (I) was recorded as wattage. By placing the detector between the linear polariser and the 1D array and collecting the power of the incident light beam (I_0) this value can be used and the value of I to calculate the reflected portion of the incident beam. The same process was repeated for bare substrates to normalize the results, accounting for any inherent reflective properties of the substrate surface itself.

The rig consisted of a light emission source, of which the wavelength of incoming light could be manipulated. The freedom in being able to manipulate the wavelength of incoming light allowed analysis into the effectiveness of a range of wavelengths from 450 to 1100 nm in creating resonance peaks within the absorbance spectra. The samples were fixed onto a stage, whereby the angle of the sample to the incoming light beam could be manipulated, this allowed the consideration of the effect of Φ on the linear reflectance of the sample.

The laser emitting the light was fixed into position and directed through the central point of a linear polarised lens. The linearly polarised light was then able to interact with the templated side of samples produced from Chapter 2. Initially the light detection diode was placed in front of the sample to record the wattage of the incoming light, after which it was moved to the position at which the light was reflected off from the sample surface. The reflected portion of the light was then recorded as a power measurement. A simple equation to calculate percentage reflectance (%R, Eqn. 3.3) could then be applied, whereby the intensity of the reflected light (I) was divided by the intensity of the incoming light beam (I_0).

$$\%R = \frac{I}{I_0} \times 100 \quad \text{Eqn. 3.3}$$

The resulting %R value for each of the templated samples was then divided by the %R value of the blank substrate, this allowed normalization of all calculated %R values to the blank, giving the normalised reflection (NR). The blank was considered as the substrate for which each templated 1D array was produced upon. For example, if EFD of M13 was conducted onto an AuSi wafer, its corresponding blank would be an AuSi wafer.

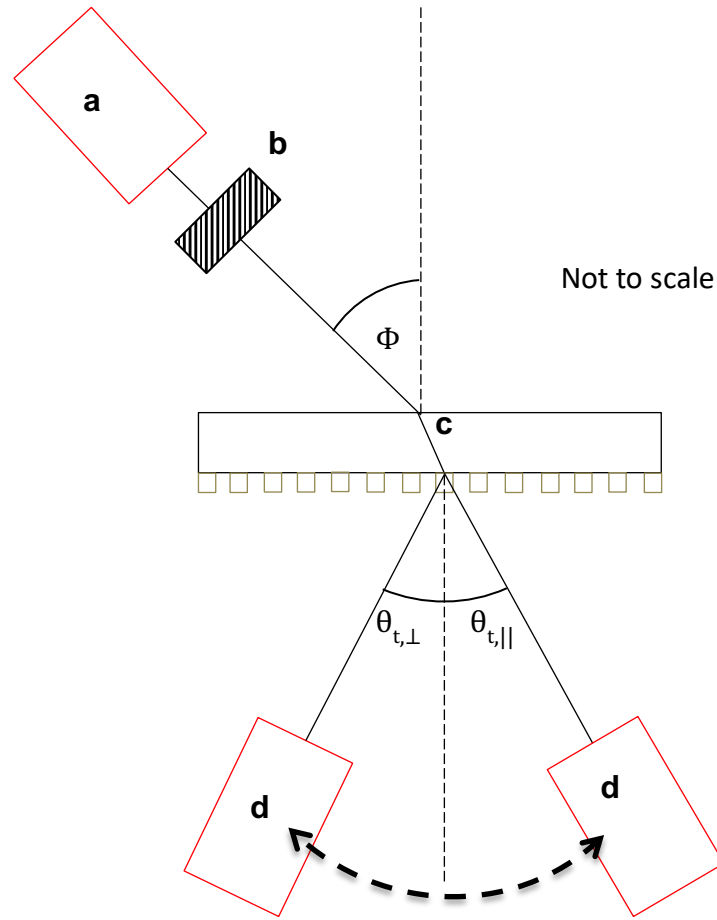


Figure 3.5 | Schematic representation for linear refraction characterisation of 1D arrays of M13 templated via EFD onto AuGMS. The substrate surface displaying the 1D array of M13 was fixed into a rotating head with the 1D array facing away from the laser source. The rotating head allowed for a movement of the sample through a 360° x-plane rotation, thus modifying the angle of Φ from the laser source to the 1D array. **a)** The laser beam of specified wavelength was emitted from a laser source, after which it passes through **b)** a linear polariser before reaching **c)** the substrate surface and finally the 1D array. The substrate material first absorbs a portion of the light beam whilst the rest is refracted through the material towards the 1D array. The 1D array then absorbs a certain portion of the incident light beam, the rest is refracted through the array towards **d)** the detector, where the intensity value (I) of the refracted ray was recorded as wattage. By placing the detector between the linear polariser and the substrate surface and collecting the power of the incident light beam (I_0) this value can be used and the value of I to calculate the reflected portion of the incident beam. The same process was repeated for bare substrates to normalize the results, thus accounting for any inherent reflective properties of the substrate surface itself.

For the case of measuring the ΔCD of M13 templated via EFD onto AuGMS the detector was moved to the transmitted position (Figure 3.5) of the light beam behind the templated material i.e. the templated structure was on the opposing side to that observed for %R. Therefore, instead of %R, percentage transmission (%T, Eqn. 3.4) was measured, whereby the same equation was utilised. The intensity of the transmitted light (I) was divided by the intensity of the incoming light beam (I_0).

$$\%T = \frac{I}{I_0} \quad \text{Eqn. 3.4}$$

Again the %T value for each of the templated samples was then divided by the %T value of AuGMS substrate, this allowed normalization of all calculated %T values to the blank.

3.4.2 Circular Dichroism (ΔCD) and Dissymmetry Factor (g)

An in-house rig (Figures 3.6 and 3.7), was set up to characterise the circular dichroism of the samples produced in Chapter 3. All measurements were taken within a dark room to eliminate any interference from daylight.

The rig consisted of a light emission source, of which the wavelength of incoming light could be manipulated. The freedom in being able to manipulate the wavelength of incoming light allowed the effectiveness of a range of wavelengths from 450 to 1100 nm to create ΔCD shifts to be mapped, indicating intrinsic chirality within the sample. The samples were fixed onto a stage, whereby the angle of the sample to the incoming light beam could be manipulated, this allowed the effects of Φ on the ΔCD of the sample to be considered. ΔCD as a result of Φ demonstrates its ability to achieve extrinsic chirality.

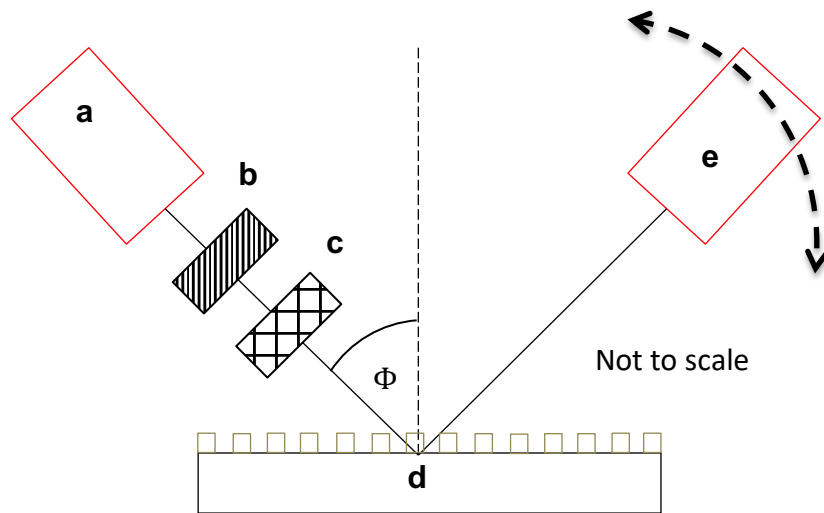


Figure 3.6 | Schematic representation for Δ CD and (g) characterisation of 1D arrays of M13 templated via EFD onto BSi and AuSi. The substrate surface displaying the 1D array of M13 was fixed into a rotating head with the 1D array facing towards the laser source. The rotating head allowed for a movement of the sample through a 360° x-plane rotation, thus modifying the angle of Φ from the laser source to the 1D array. **a)** The laser beam of specified wavelength was emitted from a laser source, after which it passes through **b)** a linear polariser and **c)** a circular polariser ($\lambda/4$) (fixed at either 45° or 135° to achieve LCP and RCP respectively) before reaching **d)** the 1D array templated onto the substrate surface. The 1D array then absorbs a certain portion of the incident light beam, the rest was reflected back towards **e)** the detector, where an intensity value (I) was recorded as wattage. By placing the detector between the linear polariser and the 1D array and collecting the power of the incident light beam (I_0) this value can be used and the value of I to calculate the reflected portion of the incident beam. The same process was repeated for bare substrates to normalize the results, thus accounting for any inherent reflective properties of the substrate surface itself. For all templated or bare substrate surfaces the effects of LCP and RCP were recorded.

The laser emitting the light was fixed into position and directed through the central point of a linear polarised lens followed by a circular polariser ($\lambda/4$). To observe the Δ CD effects, the circular polariser was adjusted to 45° and 135° to observe left and right-handed circularly polarised light effects respectively. The circularly polarised light was then able to interact with the templated side of samples produced from Chapter 3. Initially the light detection diode was placed in front of the sample to record the wattage of the incoming light, after which it was moved

to the position at which the light was reflected off from the sample surface. The reflected portion of the light was then recorded as wattage. A simple equation to calculate percentage reflectance (%R, Eqn. 3.3) could then be applied, where the intensity of the reflected light (I) was divided by the intensity of the incoming light beam (I_0).

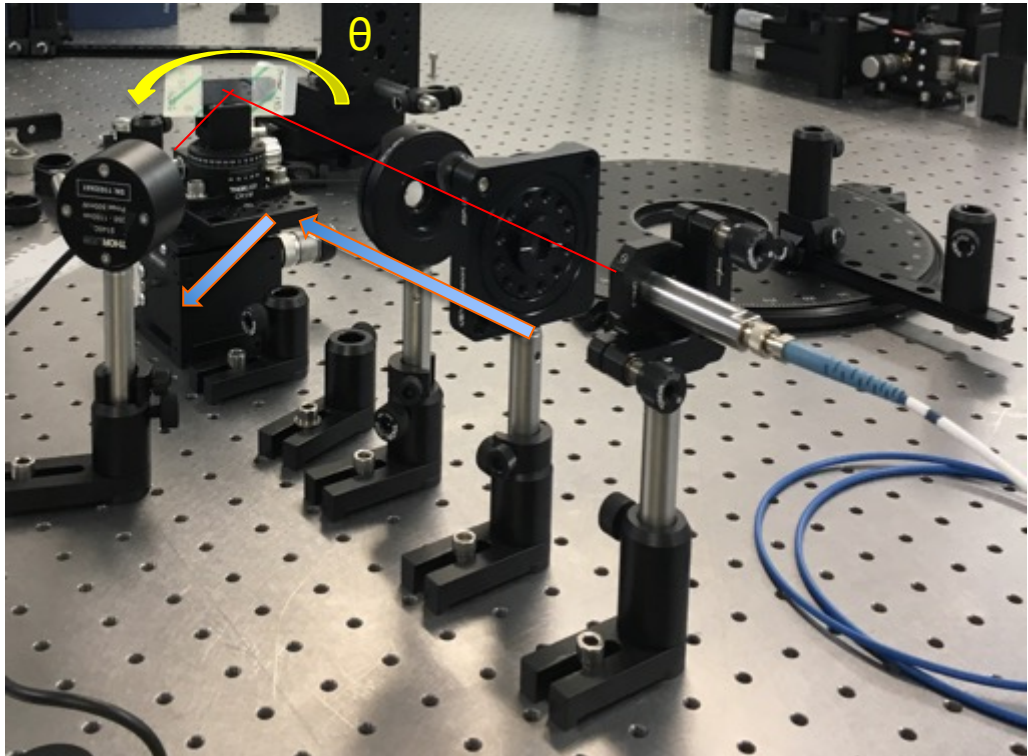


Figure 3.7 | Experimental rig set up for Δ CD and (g) characterisation of 1D arrays of M13 templated via EFD onto BSi and AuSi.

The resulting %R value for each of the templated samples was then divided by the %R value of the blank substrate, this allowed normalization of all calculated %R values to the blank. The blank was considered as the substrate for which each templated 1D array was produced upon. For example, if EFD of M13 was conducted onto an AuSi wafer, its corresponding blank would be an AuSi wafer. For each of the normalised %R values the achieved the values were then

subjected to Eqn.9, to calculate the anisotropic factor *i.e.* the significance of ΔCD effect, as a function of both Φ (extrinsic) and λ (intrinsic) chirality.

For the case of measuring the ΔCD of M13 templated via EFD onto AuGMS the detector was moved to the transmission position of the light beam behind the templated material *i.e.* the templated 1D array was on the opposing side to that observed for %R. Therefore, instead of %R, % transmission (%T, Eqn. 3.4) was measured, whereby the same equation was utilised. The intensity of the transmitted light (I) was divided by the intensity of the incoming light beam (I_0).

For each of the normalised %T values achieved the values were then subjected to Eqn.3.2, to calculate the dissymmetry factor *i.e.* the significance of ΔCD effects, as a function of both Φ (extrinsic) and λ (intrinsic) chirality.

3.4.3 Negative Refraction ($\theta_{t,\perp}$)

As the templated 1D arrays were optically thin it was not expected for there to be drastic angular change of the refracted light when using short wavelengths (600-1100 nm). If analysis of the NIM behaviour with the templated material on the frontside of the substrate material as had done for the chirality measurements, the refraction angle of the substrate material may have dampened the effects of any negative refraction. This was due to the ratio of thickness between the substrate surface and the height of the 3D structures. During the experiments it was practically restricted to observing NIM behaviour at shorter wavelengths; hence simulations were produced for longer wavelengths of light, whereby it was expected that longer wavelengths of light would move slower through the sample. This slow movement of the light waves through the sample would allow it to become optically trapped within the hierarchically arranged bundles of M13 to

such an effect that the phase flow could begin to propagate backwards, thus producing negative refraction.

As highlighted earlier in Section; 3.2, a modified Snell's Law equation (Eqn. 3.2) was utilised for phase discontinuity samples, to simulate the refraction angles expected for 1D arrays of M13, of ranging ridge dimensionality *i.e.* periodicity, on substrates BSi, AuSi, AuGMS and PtSi. Each of these substrates were analysed as a function of both Φ and λ . Initial simulations allowed insight into selecting optimum wavelengths and angles of incident light polarisations that could exhibit a NIM effect.

$$\theta_{t,\perp} = \arcsin[n_{sub}\sin(\theta_i) - (\lambda_0/\Gamma)] \quad \text{Eqn. 3.2}$$

To analyse negative refraction of the 3D structures the influence the templated material on the backside of the substrate material was observed. The samples were analysed in this manner due to the ability of being able to characterise the exact angle of incoming light prior to being deflected through the templated 1D arrays. Comparing the bare substrates (blanks) to those templated with the 1D arrays the interaction of the templated structure on the backside of the substrate surface could be excluded as the reason for any effect on the angle of refracted light. For the means of measuring negative refraction only the 1D arrays of M13 templated onto AuGMS were considered due to limitations within the laboratory not allowed observation into the effects produced by the samples templated atop of BSi or AuSi. This was due to lack of appropriate detector to observe the refracted light through the BSi or AuSi substrates. To measure the angular displacement of the refracted light beam as with %T (Eqn. 3.4) and given the reasoning highlighted in Section; 4.2, the templated side of the substrate was mounted in such a way that the light beam passed through the substrate before the 1D array of M13.

An iPhone 7 was placed in a mount behind the templated array at a distance of 7 cm from the backside of the substrate so a full view of the rig could be maintained. (Figure 3.8) By placing the detector between the linear polariser and the substrate surface and collecting the power of the incident light beam (I_0) this value can be used and the value of I to calculate the reflected portion of the incident beam. The same process was repeated for bare substrates to normalize the results, thus accounting for any inherent reflective properties of the substrate surface itself. For all templated or bare substrate surfaces the effects of LCP and RCP were recorded. The iPhone 7 was maintained in this position for the entirety of image collection. Initial image collection of the refracted light beam was taken using the blank AuGMS substrate (Au coated side nearest the iPhone). This initial position gave the positional normal for which the refracted light beam should be emitted at. Subsequently AuGMS samples templated with 1D arrays were analysed. For both the blank and templated samples of AuGMS the optical wavelength was kept at 700 nm, this was due to 700 nm being the highest wavelength of which the iPhone 7 could detect without problems.

Further it was decided to analyse a narrow range of angles of Φ ($0 - 5^\circ$), again due to the simulation predictions that larger angles of Φ would require much longer wavelength of light to generate a negative refractive index.

Standard trigonometric calculations can be utilised to predict AB (Figure 72) theoretically when two practical conditions are known:

- **The distance from the back of the substrate to the detector/camera.**
- **The $\theta_{t,\perp}$ value calculated from Eqn. 12.**

Similarly, if the following practical conditions are known the calculation for $\theta_{t,\perp}$ can be computed:

- **The distance from the back of the substrate to the detector/camera**
- **The distance of displacement of the laser**

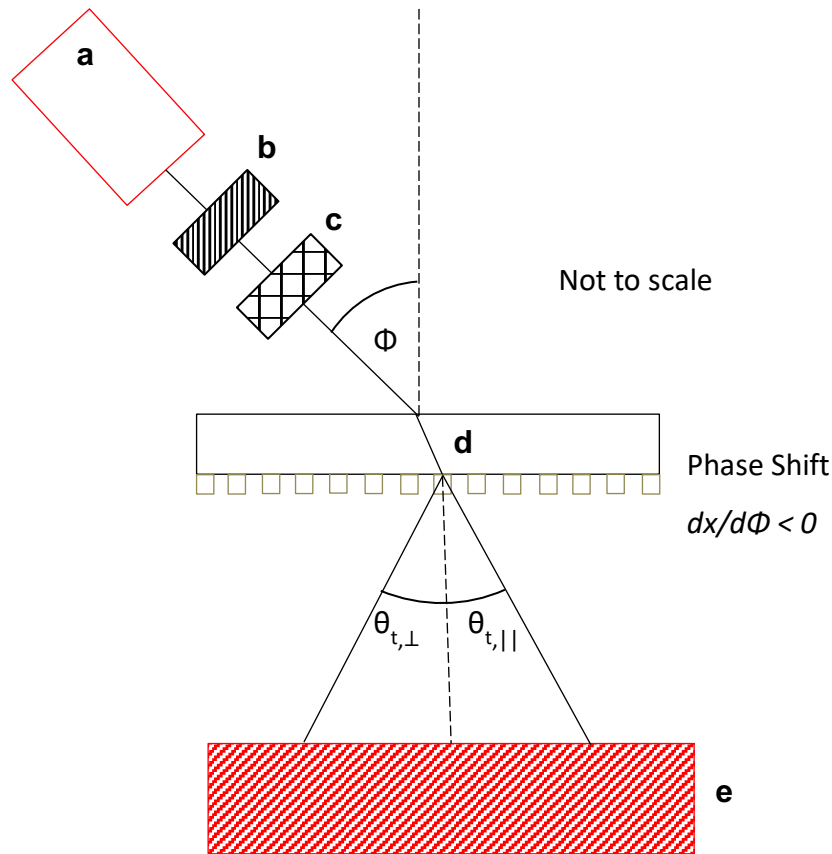


Figure 3.8 | Schematic representation for ΔCD , (g) and negative refraction characterisation of 1D arrays of M13 templated via EFD onto AuGMS. The substrate surface displaying the 1D array of M13 was fixed into a rotating head with the 1D array facing away from the laser source. The rotating head allowed for a movement of the sample through a 360° x-plane rotation, thus modifying the angle of Φ from the laser source to the 1D array. **a)** The laser beam of specified wavelength was emitted from a laser source, after which was passes through **b)** a linear polariser followed by **c)** a circular polariser ($\lambda/4$) (fixed at either 45° or 135° to achieve LCP and RCP respectively) before reaching **d)** the substrate surface and finally the 1D array. The substrate material first absorbs a portion of the light beam whilst the rest was refracted through the material towards the 1D array. The 1D array then absorbs a certain portion of the incident light beam, the rest was refracted through the array towards **d)** the detector (in this instance an iPhone 7), where the intensity value (I) of the refracted ray was recorded as wattage.

Practically it was decided to measure the displacement of the laser from its original position *i.e.* the point at which the laser was refracted through the bare substrate material e.g. AuGMS (Figures 3.8 and 3.9). This measurement of laser displacement allowed the use of simple trigonometric calculations using the \tan^{-1} function (Eqn. 3.5) to calculate the value of $\theta_{t,\perp}$. Eqn. 3.6 was derived from the original format of the tan equation that would be shown to achieve the value of AB (Figure 3.9). As the distance was maintained between the backside of the sample being examined and the detector, Eqn. 3.6 could be utilised for all calculations.

$$\tan(\theta_{t,\perp}) * 7 = AB \quad \text{Eqn.3.5}$$

$$\theta_{t,\perp} = \tan^{-1}\left(\frac{AB}{7}\right) \quad \text{Eqn. 3.6}$$

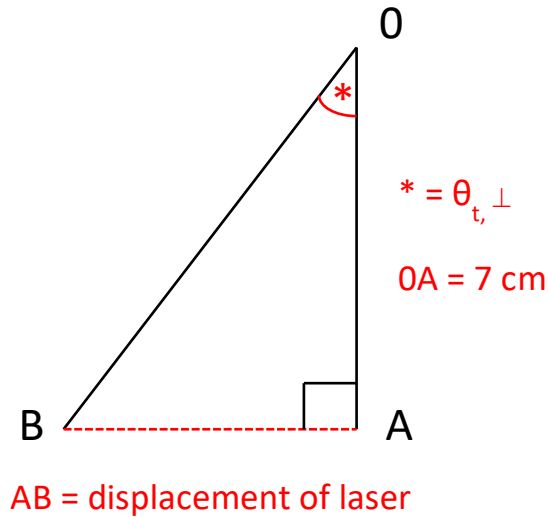


Figure 3.9 | Trigonometric calculation of the laser displacement of the refracted light beam. A simple trigonometric function can be utilised to calculate either AB or $\theta_{t,\perp}$ using the \tan or \tan^{-1} function (Eqn. 11 and 12 respectively).

The position of the refracted light beam through the bare substrate angle was taken as the 0 position. Subsequently any displacement of the light beam to the left of the 0 position, were taken to be negative and displacements that occurred to the right of the 0 position were taken to be positive values, due to the light being refracted in the normal direction (Figure 3.9)

3.4.4 *Mesh grids created using MATLAB*

To plot graphs with x-, y- and x-axis data MATLAB, mesh plot was utilised to visualise the data. The coding used to create the mesh plots is included in APPENDIX VI.

3.5 Problems Encountered During Phase II

Initially a rig to obtain refractive data about the produced hierarchical structures required construction due to the lack of commercially available products that were suitable to analyse the sample. Whilst a primitive rig to observe negative refraction and chirality using a macro-scale technique was successful, an automated rig system would provide much more finite control over the system, where a continuous change of both λ and Φ could be analysed. Further this would greatly reduce the time a user would need to spend readjusting the equipment and by removing the user interference with the system it was also able to reduce some degree of error associated with moving the laser by such small angles of Φ . Moving towards an autonomous rig design in this instance would have proved highly costly, with a lot of time required to engineer the system itself, hence it was suggested that this would be more beneficial in an industry setting where high throughput of samples would be required to be analysed in a short time frame.

To observe negative refraction using available lasers and equipment at the University of Birmingham or alliance universities within the DSTL cohort, analysis

was limited to relatively short wavelength lasers (450 – 1100 nm) and low-resolution CCD cameras with a small area for detection. Hence, an inverse design process to backwards engineer a rig was required using the available instruments and materials to generate a rig with the capability to realise negative refraction practically. Using high-throughput theory searches for previous models of measuring negative refraction, combined with the laws that govern the principle of negative refraction itself, it was possible able to develop a rig system that could practically visualise negative refraction in the visible wavelengths (450 – 750 nm).

3.6 Results and Discussion

3.6.1 Linear Reflectance

Utilising the observational change in linear reflectance *i.e.* the effects that linear polarised light (LPL) could portray on the system, it could be determined whether Φ , Γ and/or λ could effectively influence the SPR. As organic materials, such as M13, are termed to have a natural $n > 1$, it was expected that by templating 1D arrays atop of BSi wafers, which have an inherent $n > 1$ (for all concerned wavelengths of the investigations $\lambda_{600-1000 \text{ nm}}$), the normalized reflection (NR) would exhibit a value < 1 (Table 3.1). However, for those 1D arrays templated atop of AuSi an increase of NR would be expected, due to the n of AuSi remaining < 1 for all concerned wavelengths (Table 3.1).

Observing initial samples qualitatively by naked eye it was clear that the samples demonstrated strong nonlinear angle dependent colour change. From the top (90°) and side (5°) the colour of the samples appeared dark red whilst the range between these angles appeared as a blue colour. (Figure 3.10) However, it

became apparent that on altering the templating speed of M13 that colours portrayed by the sample changed.

Table 3.1 | The effect of wavelength of the incident light beam to the sample surface in generating a refractive index. The above table highlights the effect of the wavelength of the incident light beam on the refractive index of BSi and AuSi substrate surfaces prior to templating with M13 1D arrays. The fields marked * indicate the lattice band absorption and SPR band for BSi and AuSi respectively.¹⁵⁰

Wavelength of Incident Light (μm)	Refractive Index of BSi	Refractive Index of AuSi
0.50	4.2992	0.840
0.75	3.7348	0.160*
1.00	1.5344	0.224
1.50	1.5278	0.357
3.00	1.5000	1.170
5.00	1.5000	3.270
8.00	0.2500*	7.820
15.00	1.7500	21.000

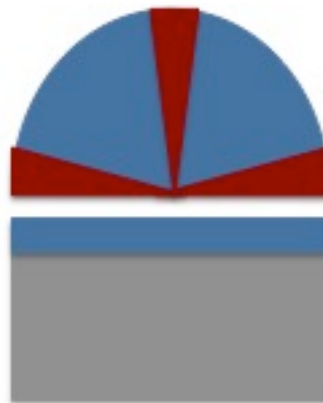


Figure 3.10 | Visual representation of the colour change observed by M13 1D arrays templated onto BSi ($\Gamma=55 \mu\text{m}$). The schematic above highlights the observational colour change of the sample surface under day light conditions. Here it can be seen that the sample shifts through the red and blue portions of the reflected spectrum.

3.6.1.1 Linear Reflection; A Function of Wavelength and Periodicity

Here, BSi 45, BSi 55 and BSi 65, represent samples produced *via* EFD of M13 templated onto BSi where the ridge diameters were 45, 55 and 65 μm respectively. Similarly, AuSi 45, AuSi 55 and AuSi 65, represent ridge diameters of 45, 55 and 65 μm respectively.

When observing Figure 3.11, BSi 65 demonstrated the highest normalized reflection (NR), having increased values compared to both the BSi 55 and BSi 45 data sets. This was not as expected, due to the increased area deposition of M13 on the surface initially probing a hypothesis that an increase in M13 coverage on the substrate would yield the largest reduction in NR of the sample. However, when considering the AFM height-profile scans of BSi templated with M13 1D arrays at $52.0 \mu\text{m}.\text{min}^{-1}$, to yield a Γ of 65 μm , the height of the ridge was relatively low (405 nm at z_{max}) with clear gaps between the M13 bundles within the ridge. As the gaps allow for light to reach the BSi substrate below the 1D arrays, this could account for the increase NR observed at $\Gamma=65 \mu\text{m}$ (Figure 74). Furthermore, the low height combined with the inferior hierarchical ordering of BSi 65 (chiral-smectic) to BSi 55 (cholesteric) and BSi 45 (cholesteric), could have influenced the NR value, as the incoming light waves succumb to less light trapping *i.e.* absorption within the ridges of the 1D array.

Through increasing the templating speed of the 1D arrays to $74.3 \mu\text{m}.\text{min}^{-1}$ on BSi (BSi 55) a 66% decrease in NR compared to bare BSi wafers was achieved over $\lambda_{600-1100 \text{ nm}}$ (Figure 3.11). This reduced reflectivity was as expected due to the increase of hierarchical ordering within the system, displaying cholesteric ordering. This increase of hierarchical layers provided an intricate structure of which increased the ability to trap light inside the small gaps within the ridge led to increased absorption of light at the surface. As more light was absorbed by the 3D ridges of M13, less light had the ability to pass through to the substrate surface

of BSi, and subsequently be reflected back towards the detector. As Si has an increased n over the wavelength range $\lambda_{600-1100\text{ nm}}$ light trapping via the 1D arrays was required to slow down the phase velocity of light as it propagated through the structures.

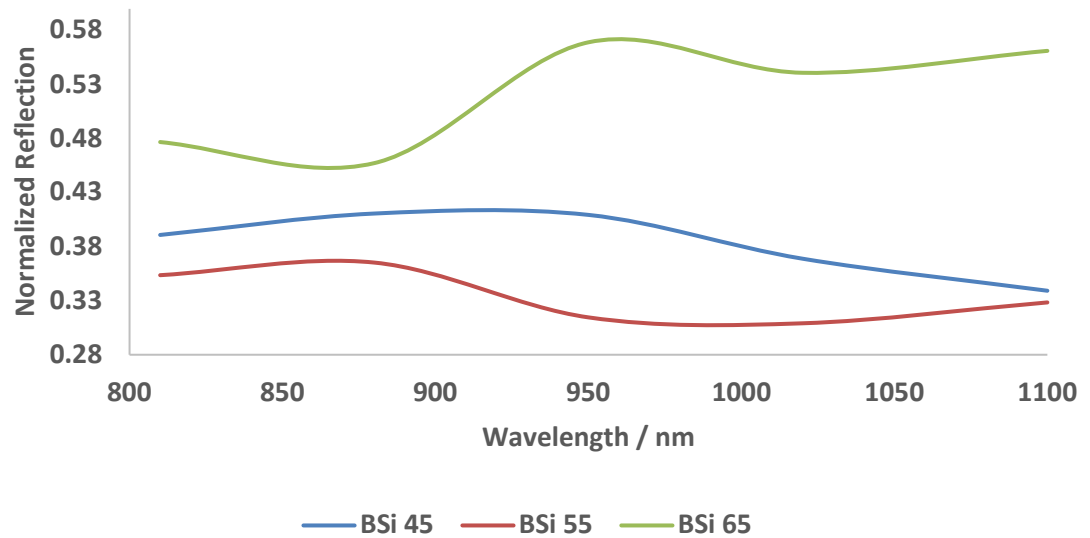


Figure 3.11 | Graphical representation of normalized reflection, as a function of wavelength and periodicity for M13 templated via EFD onto BSi wafers at varying templating speeds. The data above highlights the effects of varying the wavelength of incoming light on the reflectivity of the 1D arrays. The data shown here has been normalised with data collected for the bare BSi wafers to account for any reflective properties the substrate (BSi) would portray on the system. Each data set was labelled according to its periodicity of the ridge within the 1D array, e.g. BSi 45 would indicate a periodicity (ridge width) of 45 μm . Any value between 0 and 1 was indicative of a system that has weakened the reflective property of the bare BSi wafer.

For BSi 45, the 1D array produced from templating M13 at $96.5\text{ }\mu\text{m}\cdot\text{min}^{-1}$, an increase in NR from that of BSi 55 was demonstrated (Figure 3.11) as expected due to the increase of bare BSi wafer available between the ridges, capable of reflecting the incident LPL back towards the detector. As the diameter of the laser spot reaching the sample surface was $400\text{ }\mu\text{m}$, an averaging effect of the ridges and grooves within the region was measured during each analysis. For example, a Γ of $45\text{ }\mu\text{m}$ would contain *ca.* 5 ridges and 5 grooves. As the value of Γ

increases, the average number of ridges and grooves measured at each point would decrease, thus introducing some error into the system.

When observing the data sets for BSi together (Figure 3.11) a clear drop in NR was demonstrated at 870 nm for BSi 65, indicating a shift in resonance of the SPR, a further shallower peak appears again at 1020 nm. BSi 55, however shows a much broader and shallower peak at 970 nm to that observed at 870 nm for BSi 65. Furthermore, BSi 45 begins to show an SPR shift at around 1100 nm. Considering these data sets in tandem it was suggested that as the Γ decreases *i.e.* templating speed increases, a broader red-shifted SPR band will be observed.^{12,69,104,119}

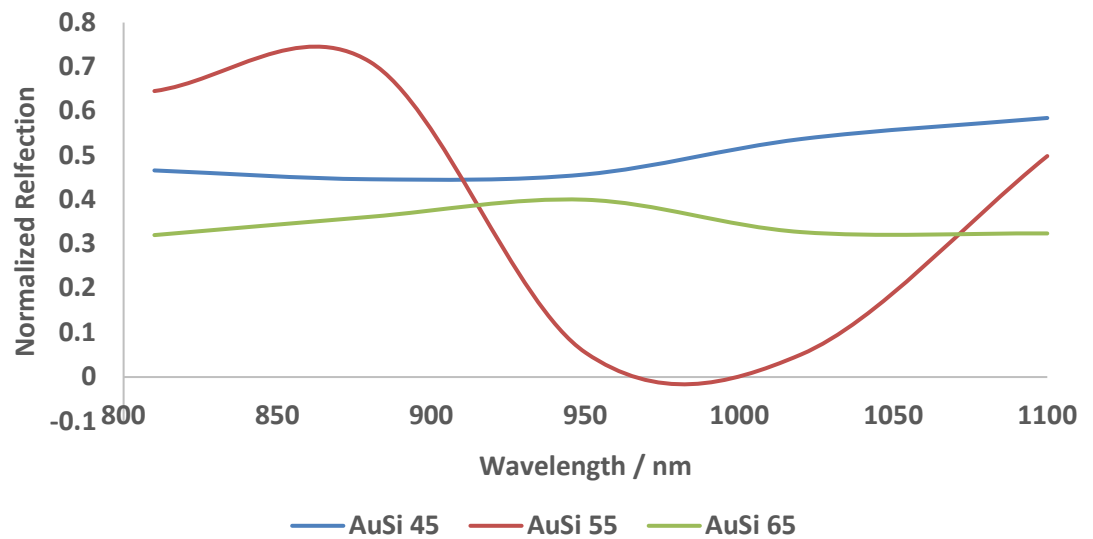


Figure 3.12 | Graphical representation of normalized reflection, as a function of wavelength and periodicity for M13 templated via EFD onto AuSi wafers at varying templating speeds. The data above highlights the effects of varying the wavelength of incoming light on the reflectivity of the 1D arrays. The data shown here has been normalised with data collected for the bare AuSi wafers to account for any reflective properties the substrate (AuSi) would portray on the system. Each data set was labelled according to its periodicity of the ridge within the 1D array, e.g. AuSi 45 would indicate a periodicity (ridge width) of 45 μm . Any value between 0 and 1 was indicative of a system that has weakened the reflective property of the bare AuSi wafer.

Due to the strong absorption band of Au at 540-620 nm, the observed λ range was moved from 600 – 1100 nm to 810 – 1100 nm to eliminate the strong absorption band associated with Au (Figure 3.12). M13 1D arrays were initially expected to produce NR values >1 when templated onto AuSi due to the increased n of M13 in comparison to the n values of AuSi over the λ range analysed. However, as can be seen from Figure 3.11 all data sets showed NR values <1 . It can be seen that AuSi 55 showed a distinct fluctuation from the expected values (Figure 3.12) that were expected to lie somewhere between the data plots for AuSi 45 and AuSi 65. At the lower end of the λ range (800 – 900 nm) only a 25% decrease in NR was observed compared to that of the bare AuSi wafer. However, as the λ of the incident light beam approached 975 nm a drastic resonance shift was observed, whereby the NR dropped by 95% from that of a bare AuSi wafer. Thus, only 5% of the incident light beam was reflected back towards the detector. As analysis progressed to more red-shifted longer wavelengths the reflective properties of the 1D array templated atop of AuSi began to remerge to ca. 50% at 1100 nm. Due to the effectiveness of the $\lambda_{850-1050\text{ nm}}$ to produce a strongly absorptive effect it was therefore hypothesised that an increase in ΔCD and (g) could be witnessed within this λ range and thus activity as a NIM.

3.6.1.2 Linear Reflection; A Function of Wavelength and Incident Angle

Here, BSiC 10, BSiC 20 and BSi 30, represent samples produced *via* EFD of M13 templated onto BSi 10, 20 and 30 represent the angle of Φ , the ridge diameters were kept to 55 μm . Similarly, AuC 10, AuSi 20 and AuSi 30, represent Φ of 10, 20 and 30 μm respectively.

When considering the data sets produced in Figures 3.13 and 3.14 by M13 1D arrays templated onto BSi and AuSi wafers samples of $\Gamma=55\text{ }\mu\text{m}$ were considered. This periodicity was selected due to it being the only periodicity that could be simultaneously achieved using the same templating speed of M13 onto both BSi and AuSi. This was a crucial factor as it was aimed to analyse both the effect of Φ and wavelength on the NR but also the effects of coating the substrate surface with Au prior to templating with M13 1D arrays.

From Figure 3.13 it can be seen that there was a general trend observed for all three angles of Φ (10, 20 and 30) that a red-shift towards longer wavelengths of light produced a decrease in NR. This could be attributed to the drop in refractive index of Si when moving from 500 – 1500 nm. BSiC 30 however, shows a distinct divergence from the decline observed from both BSiC 10 and BSiC 20 (Figure 76). Through naked eye analysis tilting of the BSiC substrate templated with 1D arrays of M13 ($\Gamma=55\text{ }\mu\text{m}$) a clear visual colour change could be observed. Shifting the angle of the substrate from horizontal towards the left and right demonstrated a shift from blue (horizontal position) to red (tilted position) indicating a shift in the SPR within the visible part of the electromagnetic spectrum at a range of 0-30 Φ . The strong reduction of NR at 700 nm for BSiC 30 (Figure 3.13) could be attributed to this visual change in colour at the sample surface.

The non-planar shape of M13 bundles caused disorder, leading to iridescence of the light wave within the hierarchical structure creating angle-dependent reflected colour. This can be confirmed *via* a strong resonance shift in the reflected light as a function of Φ *i.e.* the angle of incident linearized light to the sample surface. A highly porous structure produced through a lower rate of deposition where the inter-bundle distance was greatest yields anti-reflective structures. This was represented by a weak reflectance value *i.e.* high absorbance of the specified wavelength of light. This anti-reflective property was achieved, as the structure was able to trap large volumes of air intrinsically, creating bulk optical disorder.

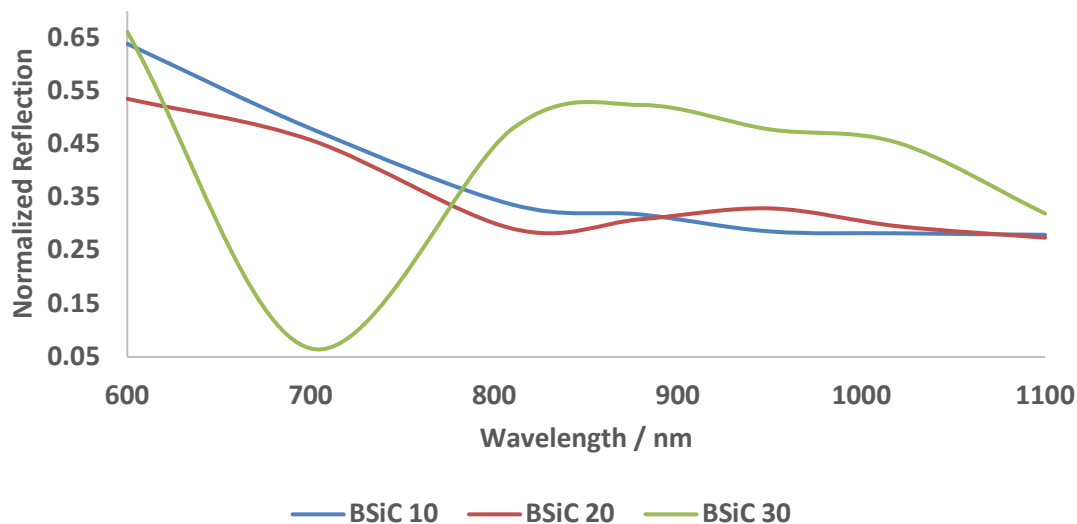


Figure 3.13 | Graphical representation of normalized reflection, as a function of wavelength and Φ for M13 templated via EFD onto BSi wafers at $74.3 \mu\text{m}.\text{min}^{-1}$. The data highlights the effects of varying both wavelength and phi of the incoming light on the reflectivity of the 1D arrays. The data shown here has been normalised with data collected for the BSi wafers to account for any reflective properties the substrate. Each data set was labelled according to its angle of phi to the incoming light beam, e.g. BSiC 10 would indicate a value of $10^\circ \Phi$. Any value between 0 and 1 was indicative of a system that has weakened the reflective property compared to that of the BSi wafer.

Examination of M13 1D arrays templated onto AuSi gave a much more varied visual colour spectrum when the sample was tilted from left to right over the horizontal plane, to demonstrate green, red and blue variations, mimicking that of oil iridescence. Following on from the hypothesis set out earlier in this section that organic M13, with a natural $n=1$, templated onto AuSi, of much lower n over the observed λ range (800 – 1100 nm), would increase the n of the sample and lead to an increase in NR when compared to bare AuSi wafers.

Figure 3.14 demonstrates that the hypothesis has held for AuC 10 and AuC 20, with both data sets maintaining $\text{NR}>1$ for all λ s. However, AuC 30 showed an

NR<1 at all λ s. Data points of NR>1 highlight the ability of the sample area (averaged ridges and grooves) to increase the reflectivity of the surface in comparison to bare AuSi wafers, whereas those points of NR<1 highlight the ability to dampen the reflectivity of the material and generate increased absorption. As see here (Figure 3.14), the initial tilting of the sample through to 20Φ creates a superior reflective surface to that of AuSi alone, however further titling switches the optical profile of the surface to an absorptive material. This ability of the material to switch between two opposing states through a trivial motion, such as tilting makes it very tuneable, with possibilities in many defence applications such as heat reflection systems and heat absorption systems.

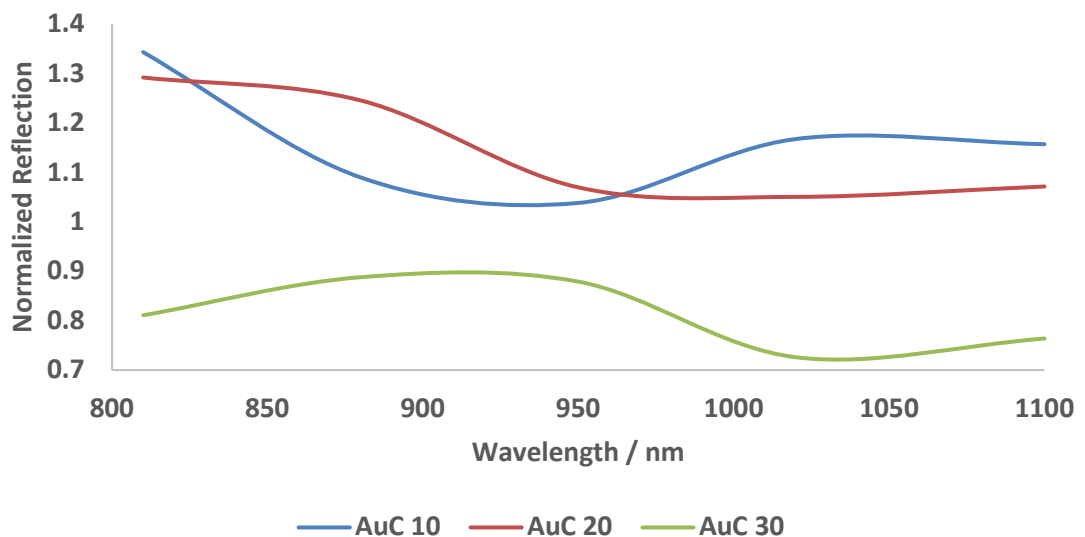


Figure 3.14 | Graphical representation of normalized reflection, as a function of wavelength and Φ for M13 templated via EFD onto AuSi wafers at $74.3 \mu\text{m}.\text{min}^{-1}$. The data above highlights the effects of varying both wavelength and Φ of the incoming light on the reflectivity of the 1D arrays. data shown here has been normalised with data collected for the AuSi wafers to account for any reflective properties the substrate. Each data set was labelled according to its angle of phi to the incoming light beam, e.g. AuC 10 would indicate a value of $10^\circ \Phi$. Any value between 0 and 1 was indicative of a system that has weakened the reflective property of the bare BSi wafer, whereas values >1 are indicative of a system that has increased reflectivity to that of the bare AuSi wafer.

3.6.2 Circular Dichroism and Degree of Anisotropy

For the purpose of this section the samples have been described as a function of their substrate surface followed either their Γ or the incident light angle of Φ . It was chosen to move from templating speed to Γ due to different substrates producing different Γ values at the same templating speed. As Γ was of more importance than the templating speed in the following sections and calculations, Γ was taken forward within the labelling of graphs.

ΔCD was the differential absorption of LCP and RCP as a function of λ . CD will be exhibited in absorption bands of any optically active molecule e.g. M13, due to its dextrorotary and levorotary components. For example if a material where to show a preference for RCP less light would be absorbed by the detector compared to LCP, due to the eigenmode of the medium showing right-handedness, which would absorb the RCP wave. Similarly, for a material that showed a preference for LCP less light would be absorbed by the detector compared to RCP, due to the eigenmode of the medium showing left-handedness, which would absorb the LCP wave.

Through calculation of ΔCD it can be observed whether there was preference over the entire media was favoured for RCP or LCP. A positive ΔCD would indicate affinity for RCP and a negative ΔCD would indicate LCP affinity. To achieve ΔCD , a degree of anisotropy must be present, hence any value of $\Delta CD \neq 0$ would indicate ΔCD as a value of 0 on the x-axis would indicate isotropy within the system.

3.6.2.1 Intrinsic Circular Dichroism and Degree of Anisotropy; A Function of Wavelength and Periodicity

Here, BSi 45, BSi 55 and BSi 65, represent samples produced *via* EFD of M13 templated onto BSi where the ridge diameters were 45, 55 and 65 μm respectively. Similarly, AuSi 45, AuSi 55 and AuSi 65, represent ridge diameters of 45, 55 and 65 μm respectively.

The ΔCD and (g) were observed as a function of Γ , at a set value of 10° , various substrate surfaces were examined (BSi, AuSi, and PtSi). The value of 10° was selected as this value afforded minimal stretching of the laser at the substrate surface.

λ_{osc} could be observed within the spectra collected for intrinsic chirality as a function of Γ and substrate surface. The λ_{osc} was taken as the range at which the data set passed through the $y=0$ axis at 3 consecutive points, creating the characteristic sinusoidal curve. The y axis represented the value of ΔCD and the x axis represented the value of λ . This could have been demonstrated to start from either a trough to reach a minima value or a peak to reach some maxima. When observing Figure 78, BSi 45 showed only one major peak at $600\text{ nm} = 50 (g)$, whereas AuSi 45 (Figure 3.15) showed a distinctive minima and maxima value at 800 and $880\text{ nm} = -20$ and $+30 (g)$ respectively indicating the ability of the addition of the Au layer to BSi, to enhance the chiral capability of templated 1D arrays on the substrate. For BSi 45 (Figure 3.15) and AuSi 45 (Figure 3.16) the data sets did not follow the same oscillation path (λ_{osc}) over the wavelength range. Taking the λ_{osc} pathway of BSi to be of original value, it was possible to compare how the addition of the Au layer to the substrate surface prior to templating with the 1D arrays affected the λ_{osc} , in terms of red/blue wavelength shifts in direction, and also narrowing or stretching of the λ_{osc} . BSi 45 (Figure 3.15) showed an λ_{osc} stretched over a 200 nm at both $700\text{-}900\text{ nm}$ and 780 to

980 nm, however from 880 – 1080nm a full $1\lambda_{osc}$ had not been achieved, indicating that stretching of the λ_{osc} may occur as a move towards NIR ranges of light occurred. AuSi 45 (Figure 3.16) showed only one complete λ_{osc} throughout the λ range observed, this spanned over 350 nm from 650 – 1000 nm. This stretching of λ_{osc} led to a $3/2\lambda_{osc}$.

As both BSi 45 (Figure 3.15) and AuSi 45 (Figure 3.16) both showed clear oscillation from the $y=0$ axis intrinsic chirality can be said to have been achieved as the value of (g) differed as a function of wavelength.

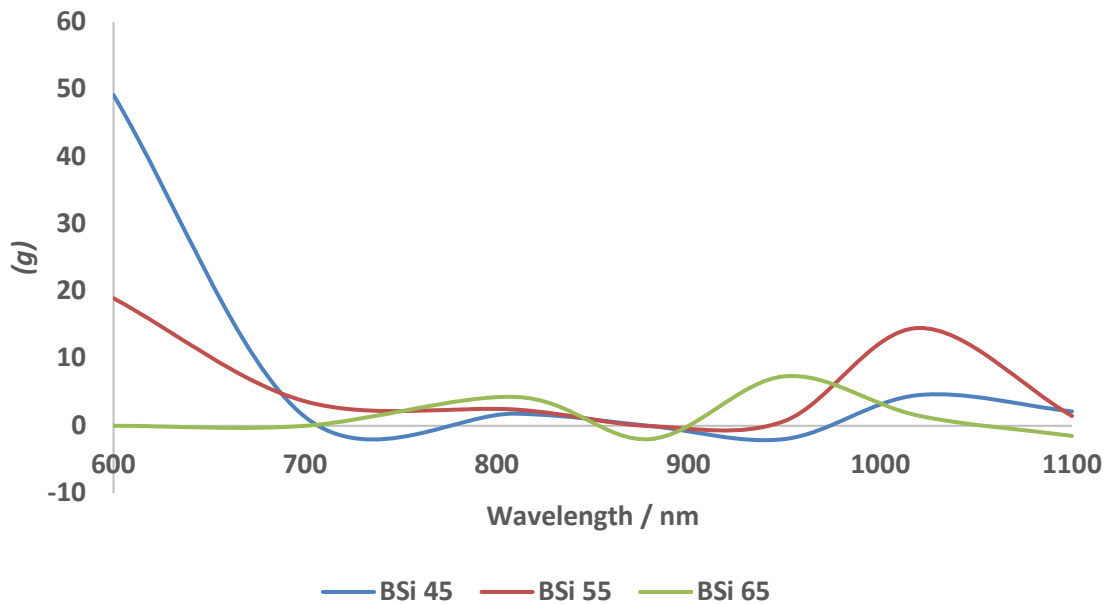


Figure 3.15 | Graphical representation of g , as a function of wavelength and periodicity for M13 templated via EFD onto BSi wafers at varying templating speeds. The data above highlights the effects of varying the wavelength of incoming light on the degree of (g) *i.e.* the anisotropic factor. The data shown here has been normalised with data collected for the bare BSi wafers to account for any reflective properties of the substrate (BSi) would portray on the system. Each data set was labelled according to its periodicity of the ridge within the 1D array, e.g. BSi 45 would indicate a periodicity (ridge width) of 45 μm . Any oscillation around the y -axis ($y=0$) was indicative of some degree of anisotropy. A (g) value above zero of was indicative of the 1D array having an affinity towards RCP for that particular wavelength, conversely a value for (g) below zero highlights an affinity towards LCP.

Intrinsic chirality highlights the ability of the medium to absorb the eigenmode of either RCP or LCP to produce intrinsic ΔCD . Consequently, the anisotropy factor, g , a quantity which expresses the strength of ΔCD was observed on a dramatic scale, with high values observed over the visible spectrum for M13 templated on both BSi and AuSi.

The majority of the BSi 55 (Figure 3.15) data set remained above the $y=0$ axis, indicating that the data set had a clear affinity for RCP, of which it was the only data set to demonstrate this property from both Figures 3.15 and 3.16. Due to this affinity for RCP there was no clear λ_{osc} value due to the lack of the data set passing through the $y=0$ axis. The BSi 55 (Figure 3.15) data set did however differ significantly ($P<0.001$) from that of the AuSi 55 data set (Figure 3.16) at all λ s observed. AuSi 55 (Figure 3.16) showed a distinct lack of oscillation through the $y=0$ axis over the entire λ range, which indicated that the addition of the Au layer to the substrate prior to templating with the 1D array produced a dampening effect on the ability of the 1D array to produce an intrinsically chiral signal. Further the lack of negative (g) value for BSi 55 and any value of (g) for AuSi 55 did not allow comment on the effectiveness of the Au layer to compress or stretch the λ_{osc} value over this λ range.

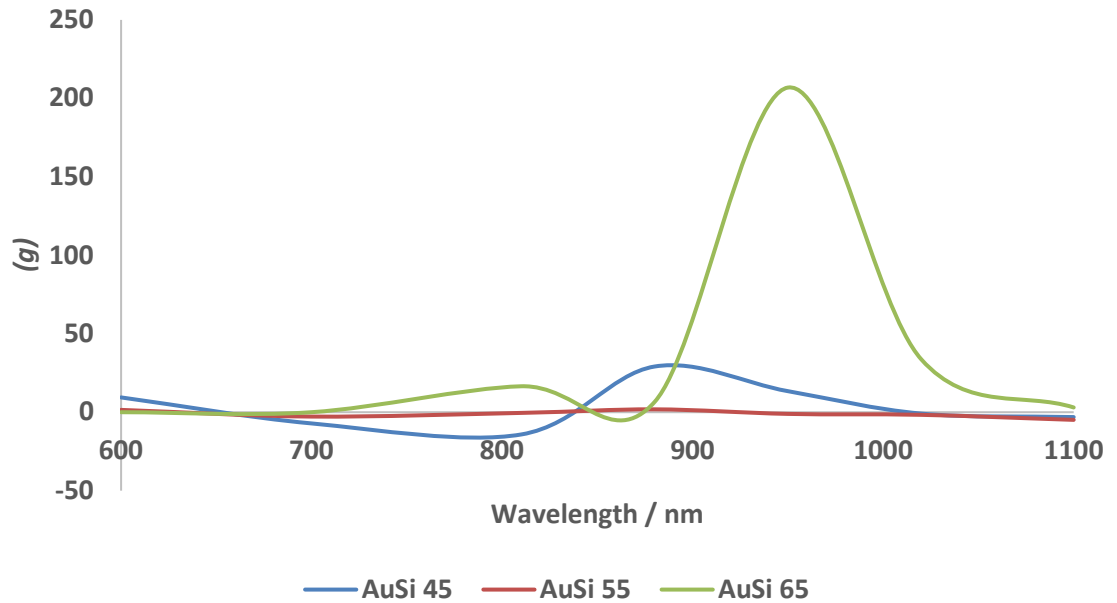


Figure 3.16 | Graphical representation of g , as a function of wavelength and periodicity for M13 templated via EFD onto AuSi wafers at varying templating speeds. The data above highlights the effects of varying the wavelength of incoming light on the degree of (g) i.e. the anisotropic factor. The data shown here has been normalised with data collected for the bare AuSi wafers to account for any reflective properties the substrate (BSi) and the subsequent coating of Au (AuSi) would portray on the system. Each data set was labelled according to its periodicity of the ridge within the 1D array, e.g. AuSi 45 would indicate a periodicity (ridge width) of 45 μm . Any oscillation around the y-axis ($y=0$) was indicative of some degree of anisotropy. A (g) value above zero of was indicative of the 1D array having an affinity towards RCP for that particular wavelength, conversely a value for (g) below zero highlights an affinity towards LCP.

Comparison of λ_{osc} (Figure 3.17) for BSi 65 and AuSi 65 highlighted a narrowing effect of λ_{osc} due to the application of the Au layer prior to templating with the 1D arrays. BSi 65 showed a λ_{osc} pathlength of 200 nm from 700 – 900 nm and again at the red-shifted λ s from 850 – 1050 nm. Whereas, for AuSi 65 λ_{osc} took a value of 180 nm reaching from 700 – 880 nm, which yielded a $9/10\lambda_{\text{osc}}$ narrowing. The decrease in templating speed used to create the wider Γ within the 1D arrays showed to move from a stretching of the λ_{osc} at the narrowest Γ of 45 μm through to no change at 55 μm and finally a λ_{osc} narrowing at 65 μm .

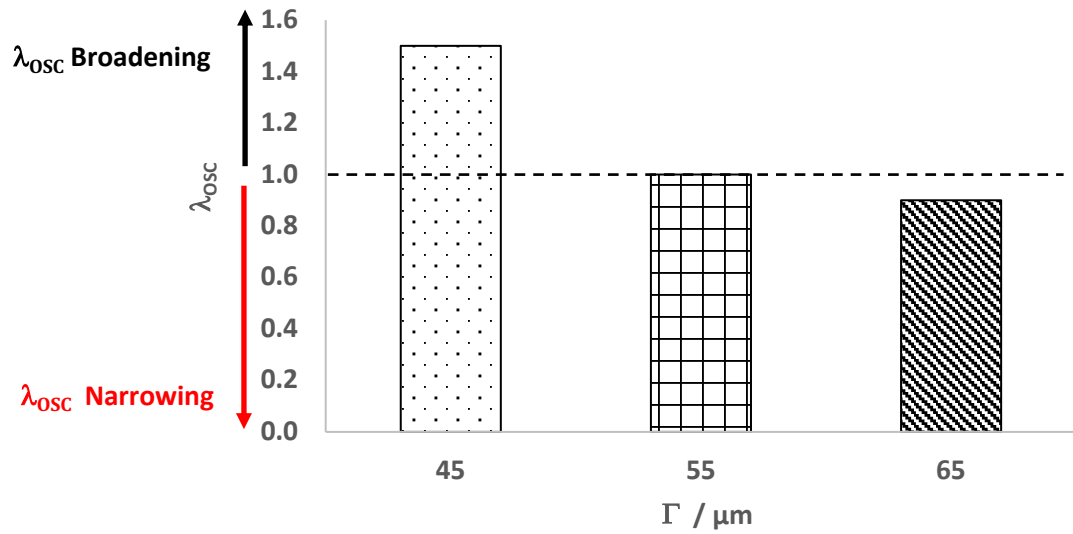


Figure 3.17 | Graphical representation of broadening and narrowing of λ_{osc} , as a function of periodicity (Γ) for M13 templated via EFD. The data above shows the influence of subjecting BSi to thin layer Au deposition on the λ_{osc} of the sample at varying Γ ; 45, 55 and 65 μm . The Γ correspond to 52, 74.3 and 96.5 $\mu\text{m} \cdot \text{min}^{-1}$ for 1D arrays templated on BSi and 14.9, 52 and 74.3 for AuSi, respectively.

3.6.2.2 Intrinsic-Extrinsic Circular Dichroism and Degree of Anisotropy; A Function of Wavelength and Incident Angle

Here, BSi 10, BSi 20 and BSi 30, represent samples produced *via* EFD of M13 templated onto BSi 10, 20 and 30 represent the angle of Φ , the ridge diameters were kept to 55 μm . Similarly, AuSi 10, AuSi 20 and AuSi 30, represent Φ of 10, 20 and 30 μm respectively.

When carrying out initial experiments a Φ range of $10 - 30^\circ$ was selected. This was due to:

- $<10^\circ$ would cause the reflected beam to be too close to modules within the intrinsic light beam pathway *i.e.* the circular polariser, for the detector to fit alongside the other modules.
- $>30^\circ$ caused the diameter of the laser spot on the sample to stretch over the surface to become more of an ellipsoid shape. It was found that this change in area covered would produce inaccurate results within the experimental design.

The ΔCD and (g) were observed as a function of Φ , for samples templated at $74.3 \mu\text{m}.\text{min}^{-1}$ onto BSi and AuSi. This templating speed was highlighted as the most effective at producing consistent, 1D arrays of M13 ridges and grooves on each substrate surface. The effects of incident light beam angle (Φ) to the 1D array at first was considered, separately from that of the previous analysis of templating speed at a defined angle of Φ , and then in a combined effect. As Φ was now introduced into the system, the move from measuring solely intrinsic chirality to a combined analysis of intrinsic-extrinsic chirality was made.

Through comparing the data sets of M13 templated onto BSi (Figure 3.18) and AuSi (Figure 3.19) at $74.3 \mu\text{m}.\text{min}^{-1}$ and $96.5 \mu\text{m}.\text{min}^{-1}$ respectively to generate Γ of $55 \mu\text{m}$ on both substrates, the effectiveness of solely altering the value of Φ could be observed. This was due to the removal of stretching or narrowing of the λ_{osc} observed at both Γ of 45 and $65 \mu\text{m}$. At $10^\circ \Phi$ the data sets for BSiC 10 (Figure 3.18) and AuC 10 (Figure 3.19) showed altered λ_{osc} pathways. The BSiC 10 λ_{osc} (Figure 3.18) ranged by 200 nm from $690\text{--}890 \text{ nm}$ increasing to 250 nm at the red-shifted range of $800 - 1050 \text{ nm}$. AuC 10 (Figure 3.19) produced a λ_{osc} of 240nm from $600 - 840 \text{ nm}$ followed by 200 nm from $740 - 840 \text{ nm}$ and finally 160 nm from $840 - 1000 \text{ nm}$. The patterns of λ_{osc} for BSiC 10 and AuC 10 therefore differed as they become red-shifted to longer λ of light, yielding

$10/12\lambda_{\text{OSC}}$, $1/2\lambda_{\text{OSC}}$, and $25/16\lambda_{\text{OSC}}$ for the 600-840 nm, 740-840 nm and 840-1000 nm ranges respectively.

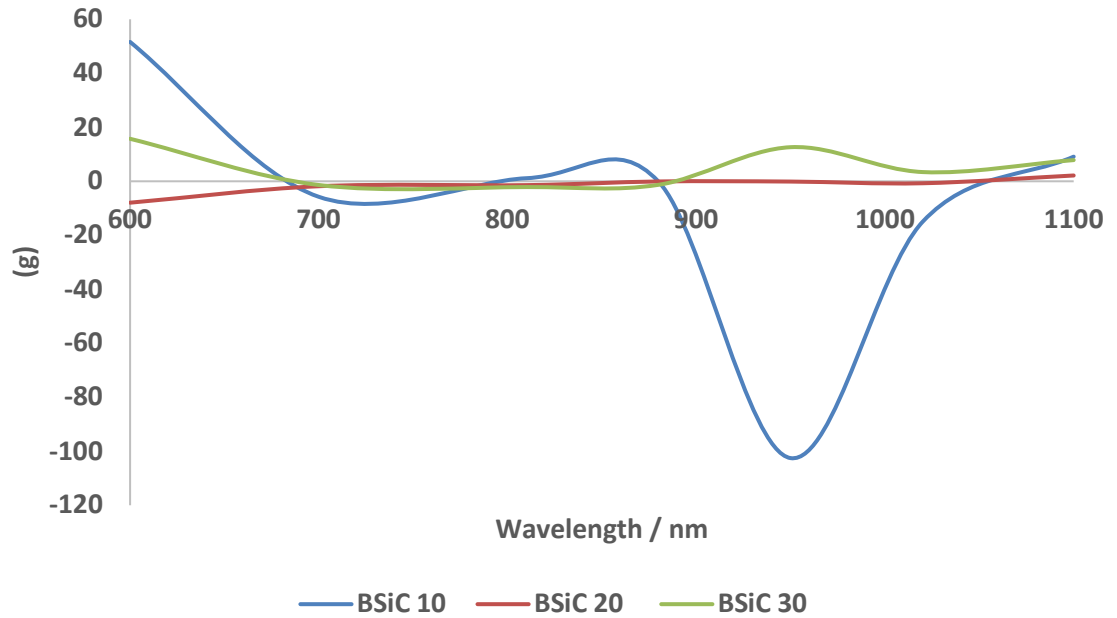


Figure 3.18 | Graphical representation of g , as a function of wavelength and Φ for M13 templated via EFD onto BSi wafers at $74.3 \mu\text{m}.\text{min}^{-1}$. The data above highlights the effects of varying both wavelength and phi on the degree of (g) *i.e.* the anisotropic factor. The data shown here has been normalised with data collected for the BSi wafers to account for any reflective properties of the substrate. Each data set was labelled according to its angle of Φ to the incoming light beam, e.g. BSiC 10 would indicate a value of $10^\circ \Phi$. Any oscillation around the x-axis ($x=0$) was indicative of some degree of anisotropy. A (g) value above zero of was indicative of the 1D array having an affinity towards RCP for that particular wavelength, conversely a value for (g) below zero highlights an affinity towards LCP.

The addition of Au to the BSi substrate prior to templating with the 1D arrays therefore yielded narrowing λ_{OSC} over the entire λ range that was considered for the analysis. As the λ_{OSC} path for both BSiC 10 and AuC 10 oscillated from the $y=0$ axis for the λ range 600-1100 nm the 1D array can be said to produce intrinsic chirality when subjected to templating on both substrates over $\lambda_{600-1100 \text{ nm}}$. In particular the BSiC 10 signals generated at 600 nm and 950 nm (+50 and -100

(*g*) respectively) were particularly strong, indicating a clear affinity for RCP and LCP respectively at these λ s. AuC 10 also showed two particularly strong intrinsically chiral signals at 800 and 880 nm (-45 and +70 (*g*) respectively) indicating a clear affinity for LCP and RCP respectively at these λ s.

At 20 Φ both the BSiC 20 (Figure 3.18) and AuC 20 (Figure 3.19) showed minimal oscillation from the $y=0$ axis, indicating only marginal intrinsic chirality within the 1D arrays templated on both substrate surfaces. BSiC 20 (Figure 3.18) only demonstrates a weak chiral signal -8 (*g*) at 600 nm, with the rest of the data set falling around the $y=0$ axis showing affinity predominantly for LCP at the 600 nm point. AuC 20 (Figure 3.19) conversely showed an affinity for RCP with its only weak chiral signal appearing at 880 nm +11 (*g*). Due to neither BSiC 20 nor AuC 20 creating a clear λ_{osc} path the effectiveness of the Au layer to create λ_{osc} stretching or narrowing could be commented on over the λ range observed.

At 30 Φ produced a non-sinusoidal curve for BSiC 30 (Figure 3.18) with no 3 points consecutively passing through the $y=0$ axis. Instead the points within the data set remained almost consistently above the $y=0$ axis indicating an affinity towards RCP. This was especially visible at 600 and 950 nm where values of (*g*) reached weak values of +15 and +13 respectively. AuC 30 (Figure 3.19) did however, produce a λ_{osc} sinusoidal curve spanning 420 nm from 600-1020 nm. Again, as BSiC 30 (Figure 3.18) did not produce a sinusoidal curve it was not possible to decipher any λ_{osc} narrowing or stretching that the Au layer produced. However, it was clear that for the $\lambda_{600-1100\text{ nm}}$ the BSi and AuSi substrates allowed the 1D arrays to produce intrinsically chiral signals as both BSiC 30 and AuC 30 produced fluctuation from the $y=0$ axis. In particular AuC 30 generated a strong intrinsically chiral signal at 950 nm +345 (*g*), indicating a clear affinity for RCP at this λ (Figure 3.19).

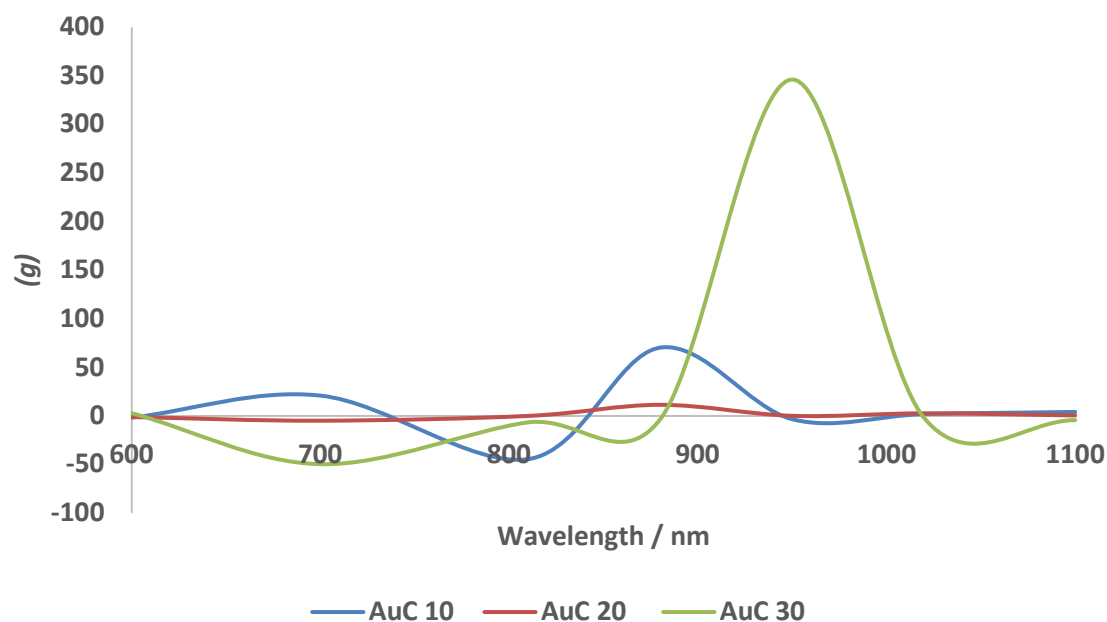


Figure 3.19 | Graphical representation of g , as a function of wavelength and Φ for M13 templated via EFD onto AuSi wafers at $96.5 \mu\text{m}.\text{min}^{-1}$. The data above highlights the effects of varying both wavelength and phi on the degree of (g) *i.e.* the anisotropic factor. The data shown here has been normalised with data collected for the bare AuSi wafers to account for any reflective properties the substrate (BSi) and the subsequent coating of Au (AuSi) would portray on the system. Each data set was labelled according to its angle of Φ to the incoming light beam, e.g. AuC 10 would indicate a value of 10° phi. Any oscillation around the x-axis ($x=0$) was indicative of a degree of anisotropy. A (g) value above zero of was indicative of the 1D array having an affinity towards RCP for that particular wavelength, conversely a value for (g) below zero highlights an affinity towards LCP.

As all data sets for 1D arrays templated atop of both BSi and AuSi produced varying spectra when subjected to varying angles of incident light to the sample surface it can be concluded that extrinsic chirality was produced by the samples. However, at $20^\circ \Phi$ the effectiveness of the 1D arrays templated onto both BSi and AuSi to demonstrate intrinsic chirality was greatly reduced. When observing the intrinsic chirality of the BSi alone, prior to templating with the 1D arrays, the wafers alone showed between 2 – 5x higher (g) values for the $20^\circ \Phi$ than the 10° and $30^\circ \Phi$, though of 2-3 orders of magnitude smaller than that of the templated

samples at 10 and 30 Φ . This indicated that the BSi wafer contained some inherent chirality at 20 Φ . As the (*g*) value of the BSi at 20 Φ approached *the* (*g*) value that the templated 1D arrays displayed at 20 Φ , the data set normalizes to values within close proximity of the *y*=0 axis. The bare AuSi substrate however, only displayed (*g*) values 2x higher at 20 Φ than 10 and 30 Φ . This indicated that the extrinsic-intrinsic chirality of the untemplated BSi wafers at 20 Φ for $\lambda_{600-1100}$ nm had been dampened by the addition of Au to the substrate surface.

3.6.3 Negative Index Material activity

To analyse the NIM functionality of the fabricated surfaces simulations were produced and experimental data was collected for all samples. A broad range of incident light wavelength ranges (0.5 – 15 μ m) were tested for the theoretical predictions, however, due to instrumental constraints only a narrow range of incident light wavelengths (0.5 – 1.5 μ m) could be analysed. A graph to highlight the region by which NIM activity would be realised in a practical sense was provided (Figure 3.20).

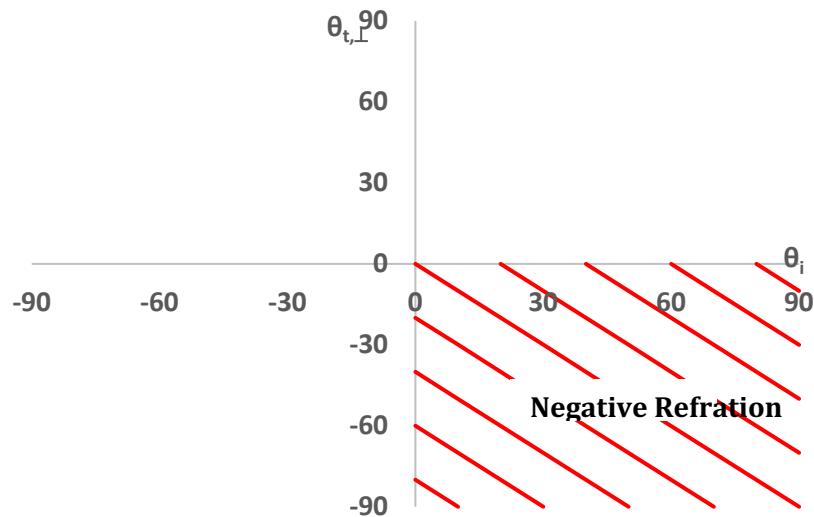


Figure 3.20 | Representation of $\theta_{t,\perp}$ and θ_i values able to produce negative refraction.

The graphical representation above shows the range of combinations of $\theta_{t,\perp}$ and θ_i that have the ability to produce negative refraction angles. This range is shaded on the graph. Given a negative angle of refraction a negative index material will follow.

3.6.3.1 Theoretical Models for Negative Index Material Activity in the Visible to Mid-Infrared Range

Utilising the figure of merit (FOM) function early predictions could be made (Figure 3.21) to identify the potential ranges of λ_0 with the ability to demonstrate NIM activity at given templating speeds. The variance in templating speeds has previously been shown (in Chapter 3) to have direct influence on the ridge width diameter *i.e.* the periodicity, Γ . FOM can thus be used as a predictor of NIM due to the activity of FOM as a multiplier within the equation for negative refraction (Eqn. 3.2).

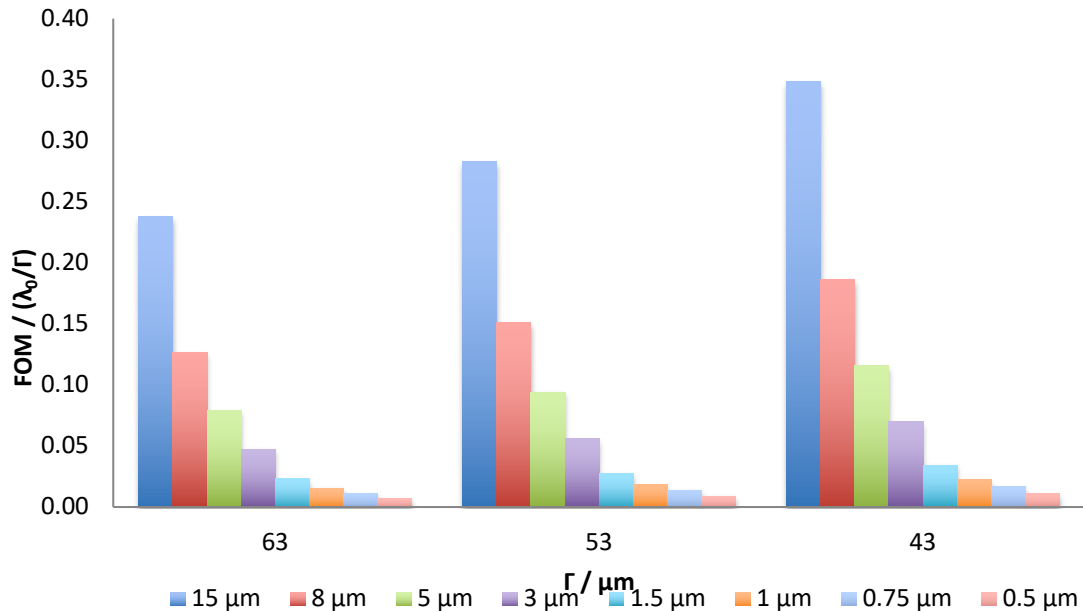


Figure 3.21 | Graphical simulation for FOM as a function of λ and Γ . The data sets shown here highlight the variance in values of FOM by 1D arrays of M13 templated atop of BSi at a range of templating speeds. The periodicity Γ of the sample represents the diameter of the ridges within the 1D arrays. Each Γ was subjected to analysis at a range of wavelengths from 15-0.5 μm indicated by the key above the data plot. As previously highlighted (Chapter 2) the ridge diameter decreases with increasing templating speeds of the EFD process. Therefore, it could be said that as the templating speed increases the value of the FOM increases also. This was shown by the increasing value of FOM from Γ of 63 to 43 μm at all wavelengths examined. Due to the significance of the FOM value in Eqn. 3.2, it can be used as a primitive indicator as to the ability of the 1D array to produce a negative refraction angle at varying wavelengths.

As the λ_0 blue shifts to lower wavelengths the $\lambda_0:\Gamma$ decreased to afford lower values for FOM. As the FOM value was directly incorporated into the theoretical calculations of the refracted angle of light $\theta_{t,\perp}$, and subsequently the refractive index, the templated structure was affected by a change in FOM. In particular it was noted that the decrease of FOM reduced the range of λ_0 angles (Φ) that produced a negative $\theta_{t,\perp}$. Therefore, an increased value of FOM would be indicative of a larger range of Φ capable of producing a NIM. As the FOM value only considers the λ_0 and Γ values it was independent of the substrate for which the ridges have been templated on top of. Therefore, it was still needed to compute the fully modified Snell's Law for phase discontinuity samples to obtain accurate indications of the ability of the sample to produce a negative $\theta_{t,\perp}$ and subsequently a NIM.

M13 acts as an optical resonator where its hierarchical structure presents areas of different reflective capability. The amplified light becomes trapped within the air cavity pores of the 3D structure, enhancing the stimulated emission as the phase velocity slowed and began to propagate backwards. The light was then emitted through the least reflective areas. As a principle a decrease in reflectivity was regarded as being due to a decrease in refractive index from high to low, thus the light was emitted from the areas of lowest refractive index.

3.6.3.1.1 Silicon Wafer Substrate

When considering Si as a substrate it must be noted that crystalline Si $\langle 111 \rangle$ has high reflectivity in the visible and NIR range (400 nm – 4 μ m), hence its absorptivity was low, and n was high. During MIR wavelengths (5-37 μ m) Si

exhibits strong optical absorption arising from the lattice absorption bands in this range. Therefore, a sharp decline in the n of the substrate below the critical value of 1 becomes crucial in the production of negative values of $\theta_{t,\perp}$ and subsequently n . Further the strong absorption allowed for a broad range of θ_i values to demonstrate NIM activity (Figures 3.22).

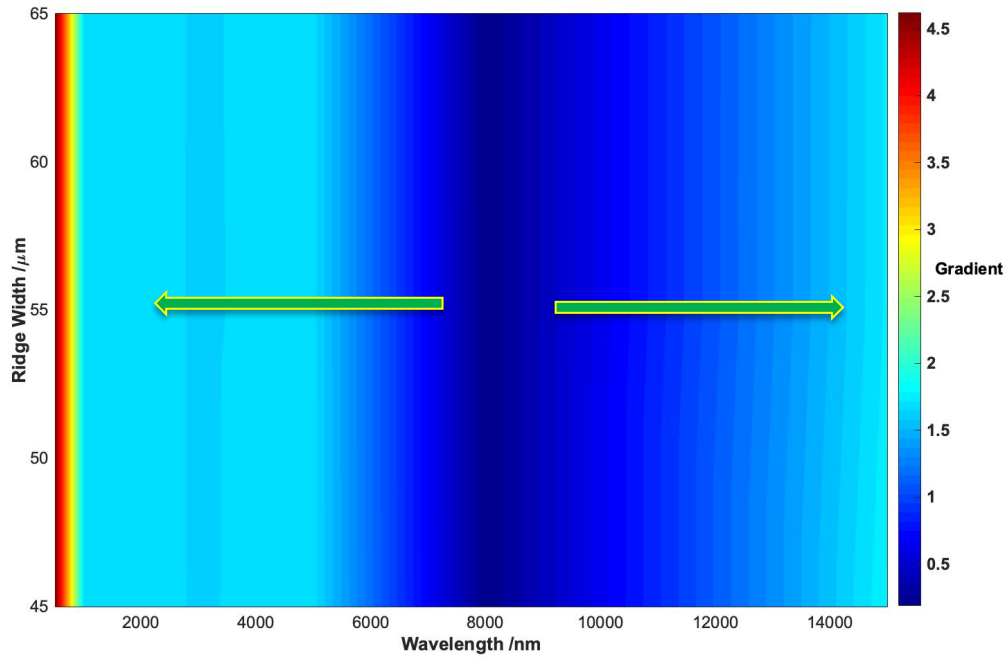


Figure 3.22 | Simulation of the gradient value as a function of Γ and λ_0 , for M13 templated onto BSi. Gradients were taken from the graphical projections of refractive index as a function of Φ , λ_0 and Γ . Lower gradients running through the lower right quadrant of Figure 3.20 are associated with a higher range of Φ that led to negative refractive indices.

The arrow represents movement away from the wavelengths that produced the largest range of negative refractive index, the lower the gradient the larger the range of negative refractive index, due to the curve passing through the lower right quadrant of Figure 3.20.

3.6.3.1.2 Au Coated Substrates

The incident light beam first passes through the substrate before being refracted through the thin Au layer, and subsequently the discontinuous templated array of M13 ridges. Due to the very thin layer of Au (10 nm) deposited on the surface of the substrates (Si wafer or glass), it was deemed negligible in altering the angle of the incident light beam. Using the constructed optical set up it was not possible to determine the angle of refraction through a silicon wafer. Therefore, a silica fused glass substrate was used analysed practically to confirm that coating the surface with an ultra-thin layer of Au did not affect the refracted angle of the incident light beam. Using this model and literature analysis into the effects of ultra-thin Au coatings on silicon wafers the values of θ_t were considered to be the identical to that of the incident beam refracted from a BSi wafer.

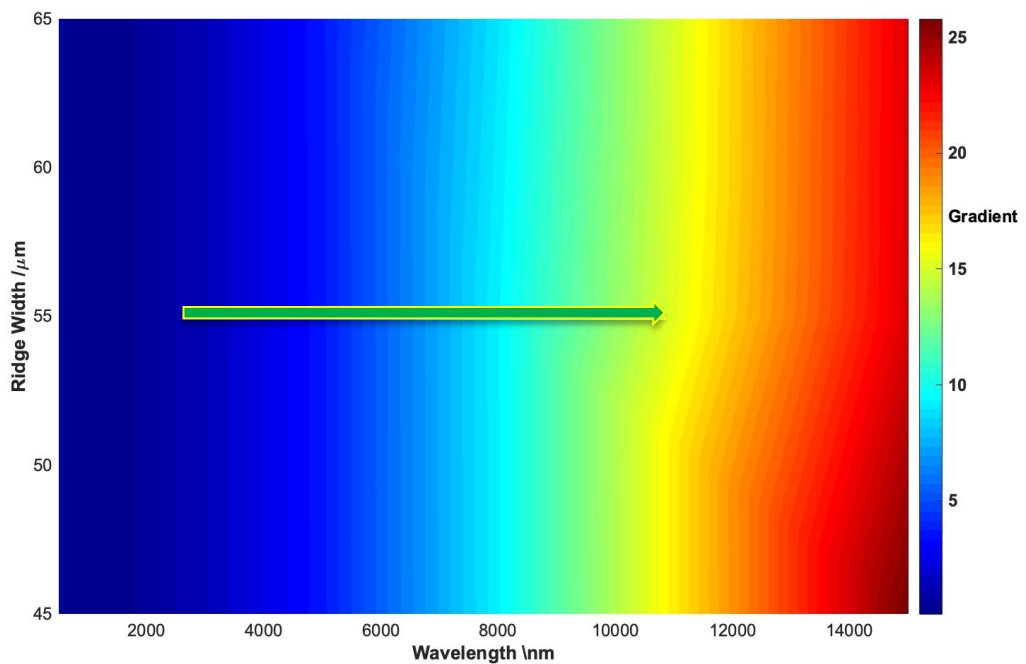


Figure 3.23 | Simulation of the gradient value as a function of Γ and λ_0 for M13 templated onto AuSi. Gradients were taken from the graphical projections of refractive index as a function of Φ , λ_0 and Γ . Lower gradients running through the lower right quadrant of Figure 3.20 are associated with a higher range of Φ that led to negative refractive indices.

The arrow represents movement away from the wavelengths that produced the largest range of negative refractive index, the lower the gradient the larger than range of negative refractive index, due to the curve passing through the lower right quadrant of Figure 3.20.

When considering Au as a substrate it must be noted Au exhibits strong optical absorption at 536 nm, from its' surface plasmon resonance band. Therefore, a sharp decline in the n of the substrate below the critical value of 1 becomes crucial in the production of negative values of $\theta_{t,\perp}$ and subsequently n . Further, the strong absorption allowed for a narrow range of θ_i values to demonstrate NIM activity (Figures 3.23).

3.6.3.2 MATLAB Simulations of Negative Index Material Behaviour for 1D Arrays of M13 onto BSi, AuSi and PtSi

PtSi had been analysed here for its' activity to generate NIM behaviour as it represents a material that shows no optical absorption between the visible to MIR range. Further, in the previous chapter (Chapter 2), whilst exploring methods of imaging of the samples, SEM was highlighted as a potential tool. However, SEM was subsequently discounted, which led to several samples having been coated with Pt for SEM analysis. Therefore, it was decided to assess these samples for intrinsic and extrinsic chiral activity alongside that of BSi and AuSi.

When considering the M13 3D hierarchical structure on BSi this system would be most effective in the MIR range (Figure 3.24). This was observed due to the large lattice band absorption of Si in the 5000 – 9000 nm region. The availability of the material to absorb increased volumes of light within this region allowed for optical %transmittance of the light through the material. This absorbed light then slows down as it was refracted through the templated 1D array due to the optical trapping achieved by the hierarchically bundled M13 fibres, ultimately being

refracted back through the material rather than in the normal direction. This then negatively refracted light exits the NIM at an anomalous angle to what would be observed from the BSi wafer. As expected BSi will reflect most of the light <5000 nm and >18000 nm and so the percentage transmittance was greatly reduced, impacting on the availability of the of 1D array to act as a NIM. Due to the strength of the lattice band absorption reaching its maximum at ca. 8000 nm the widest ranges of incident angles of which NIM can be observed oscillates around this region to produce a highly effective NIM model. The availability of this NIM model to produce a broad band range of wavelengths of light in which NIM can be readily achieved at a sufficient range of incident angles of incoming light makes it a viable option for scaling up as a defence application e.g. as a laser avoidance system or as an optical cloaking device.

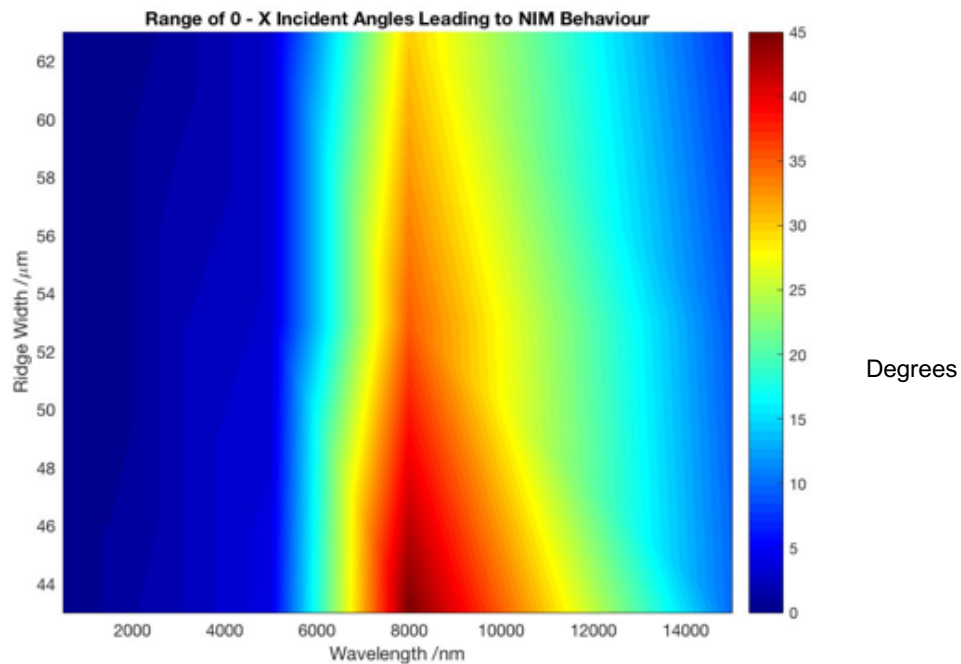


Figure 3.24 | MATLAB simulation observing the intrinsic and extrinsic chirality of the 1D arrays of varying ridge diameter (Γ) for M13 templated onto BSi. Here, the MATLAB mesh plot allowed the visualisation of both the occurrence of extrinsic and intrinsic chirality within the system, through the variance in λ and Φ respectively. The points within the mesh grid highlight ranges of Φ at a particular λ that will lead to the observance of NIM behaviour. This simulation represents M13 templated using EFD on BSi to achieve ridge diameters of 65, 55 and 45 μm .

On the AuSi substrate a different effect of the 1D array was observed. Au masks the strong lattice band absorption of Si due to the strong reflectance properties of the Au coating. Au itself only contains a weak SPR band absorption ca. 400-1100 nm (Figure 3.25 and 3.26). This weak and narrow absorption band allowed for sufficient light to be transmitted through the substrate material to the 1D array, however due to the short wavelengths of light being absorbed by the material only minimal amounts of light are available to be perturbed by the hierarchically bundles M13 fibres in the 1D array. This presents a very narrow band for which NIM behaviour can be observed and restricts the effectiveness over broad angle ranges of incident light, like those observed on the BSi model. However, the importance of being able to generate NIM behaviour at visible wavelengths as observed with the AuSi model should be highlighted as this remains an area, in which at present there are extremely limited practical demonstrations of NIM at these wavelengths.

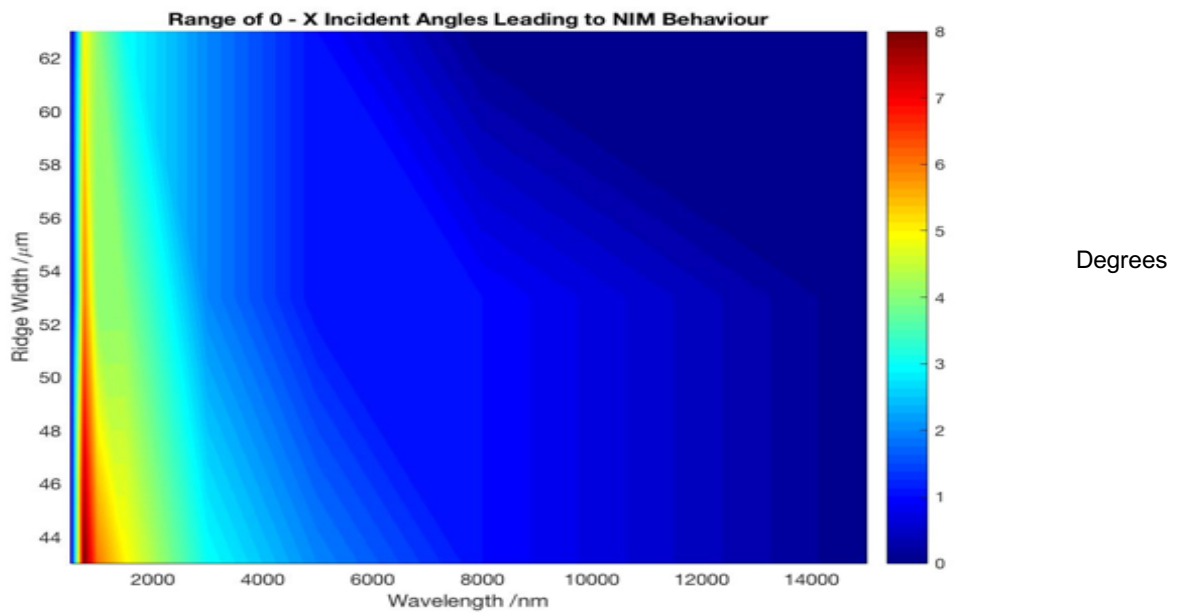


Figure 3.25 | MATLAB simulation observing the intrinsic and extrinsic chirality of the 1D arrays of varying ridge diameter (Γ) for M13 templated onto AuSi. Here, the MATLAB mesh plot allowed the visualization of both the occurrence of extrinsic and intrinsic chirality within the system, through the variance in λ and Φ respectively. The points within the mesh grid highlight ranges of Φ at a particular λ that will lead to the observance of NIM behaviour.

When considering the simulated effects of the 1D array templated onto both BSi and AuSi (Figures 3.24 and 3.25), it was clear that the absorption qualities of the substrates was having a significant effect on the capability of the 1D array to achieve negative refraction angles, and thus NIM behaviour. Therefore, it was decided to explore a final coating of Pt onto a BSi wafer (PtSi) to conduct the EFD process in the templating of M13. Pt not known for its light absorption properties, has no distinct SPR peak in the visible range, nor lattice band absorptions in the NIR to MIR ranges that were examined. As expected, when running the MATLAB simulation for 1D arrays of varying ridge diameter, the PtSi substrate only showed NIM behaviour in a range of $<1^\circ \Phi$ at the λ range of ca. 1800-15000 nm (Figure 3.27). This indicates that the PtSi model would not be a suitable option to produce a MM that could be used in the real world.

This simulation represents M13 templated using EFD on AuSi to achieve a 1D array of ridge diameters of 45, 55 and 65 μm .

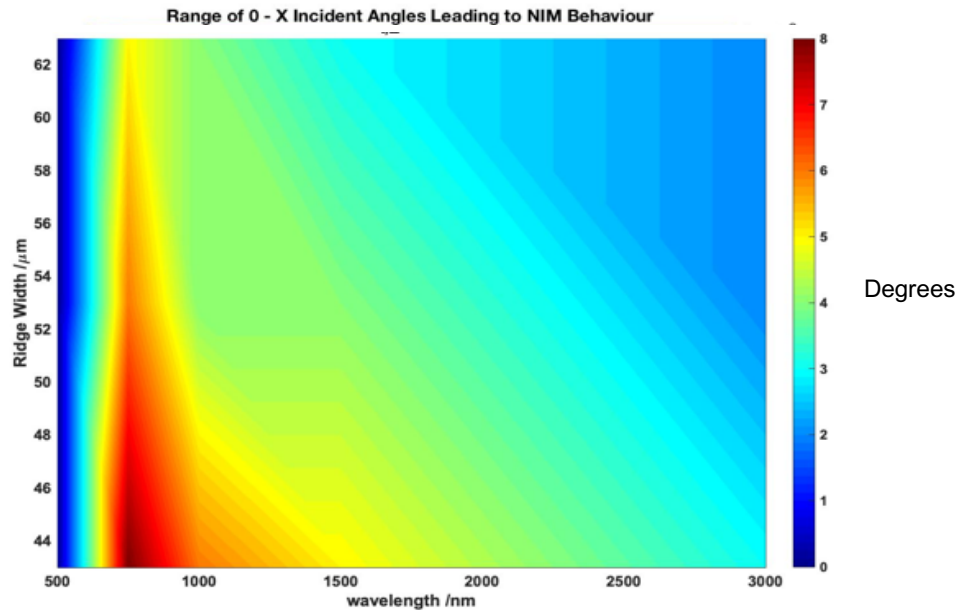


Figure 3.26 | MATLAB simulation observing the intrinsic and extrinsic chirality of the 1D arrays of varying ridge diameter (Γ) for M13 templated onto AuSi at a reduced range of wavelengths. Here, the MATLAB mesh plot allowed the visualization of both the occurrence of extrinsic and intrinsic chirality within the system, through the variance in λ and Φ respectively. The points within the mesh grid highlight ranges of Φ at a particular λ that will lead to the observance of NIM behaviour. This simulation represents M13 templated using EFD on AuSi to achieve a 1D array of ridge diameters of 45, 55 and 65 μm .

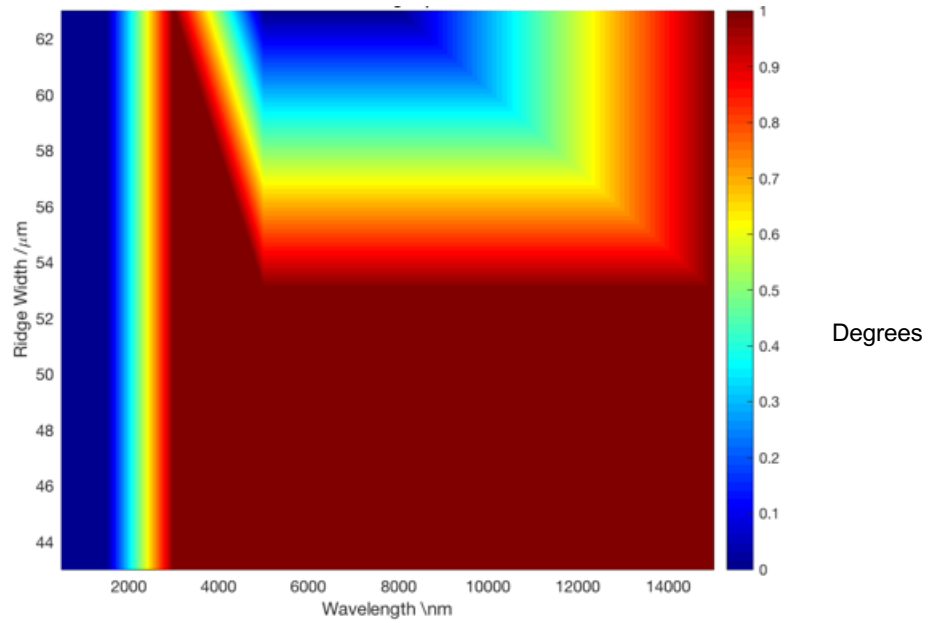


Figure 3.27 | MATLAB simulation observing the intrinsic and extrinsic chirality of the 1D arrays of varying ridge diameter (Γ) for M13 templated onto PtSi. Here, the MATLAB mesh plot allowed the visualization of both the occurrence of extrinsic and intrinsic chirality within the system, through the variance in λ and Φ respectively. The points within the mesh grid highlight ranges of Φ at a particular λ that will lead to the observance of NIM behaviour. This simulation represents M13 templated using EFD on PtSi to achieve a 1D array of ridge diameters of 42, 55 and 65 μm .

3.6.3.3 MATLAB Simulation and Practical Demonstration of Negative Index Material Behaviour for 1D Arrays of M13 onto AuGMS

Following on from the theoretical calculations made above a practical analysis was carried out on the templated samples with the same values of Γ . However, due to equipment constraints a λ_0 range of 450 – 1100 nm was used. Using the wavelength range available good accordance of the theoretical and practical values for $\theta_{t,\perp}$, were observed, therefore it would be expected that the predicted values by the above model would hold true for the red-shifted values of λ_0 .

As mentioned earlier within this section, due to equipment constraints it was only able to visualize the NIM behaviour of the M13 1D arrays templated onto AuGMS. It was decided that the λ of 700 nm for the characterisation due to the availability of using a simple camera to visualize NIM behaviour at this wavelength. Further the longer λ of light allowed the maximum displacement of the refracted beam to observe the NIM behaviour.

Initially a MATLAB simulation was produced for the system to determine the optimal ranges Φ of which NIM behaviour would be expected. The simulation (Figure 3.26) highlighted values $<5^\circ$ Φ to show greatest NIM activity. Hence, it was decided to explore this region for the practical analysis. It was clear from the practical data collected for the EFD on M13 onto the AuGMS substrate that the ridge width, as expected, did portray an effect on the ability of the 1D array to exhibit NIM behaviour. When considering AFM images from Chapter 3 of the sample it was clear that the narrower ridge widths produced by increased templating speed (up until $96.5 \mu\text{m}^{-1}$) produced more consistent ridges and grooves within the sample, highlighted by the decreased standard deviation value for these samples. The increased hierarchical layers at increased templating speeds also present a more intricate system of 3D arranged bundles within each ridge of the 1D array.

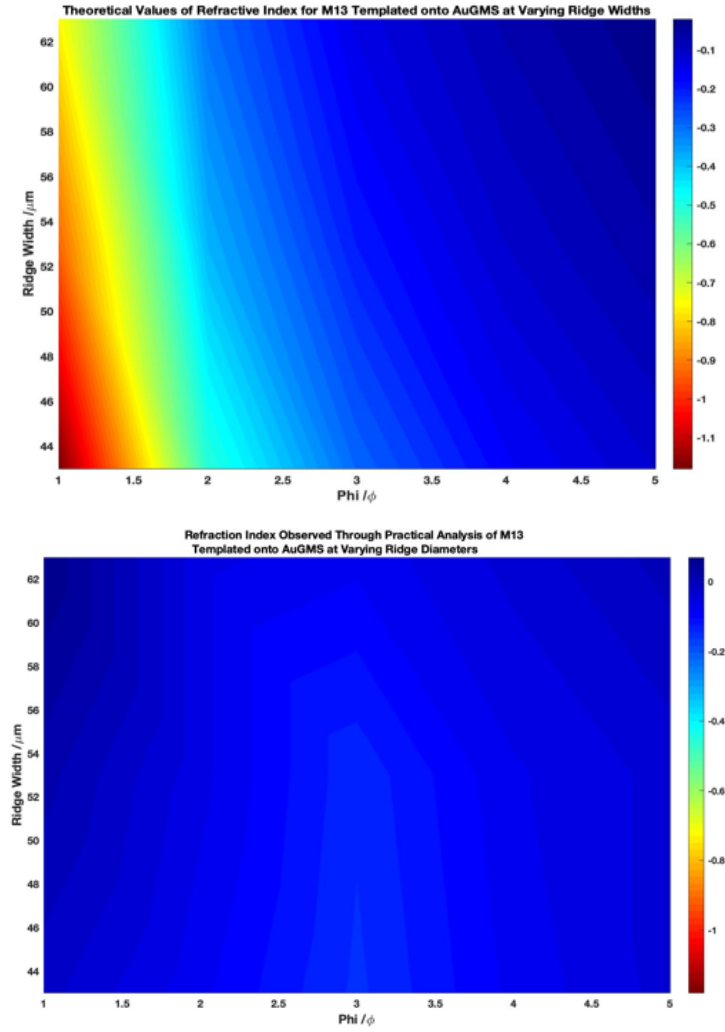


Figure 3.28 | MATLAB plot using a, simulated and b, practical data to observe how small angles of Φ impacted the refractive index of the 1D arrays, of varying ridge diameter (Γ) for M13 templated onto AuGMS. Here, the MATLAB mesh plot allowed visualization of the effect of Φ at a particular λ (700 nm) to achieve changing refraction angles. The points within the mesh grid highlight the refraction angles observed from the 1D arrays at varying values of Φ using a $\lambda=700$ nm incident light beam. Those of negative value indicated NIM behaviour. This computation of practical data represents M13 templated using EFD on AuGMS to achieve a 1D array of ridges and grooves at templating speeds of 52.0, 96.5 and 111.4, which correspond to ridge diameters of 42, 56 and 66 μm .

These hierarchically arranged bundles could create optical cavities within the ridge, whereby the incoming λ of light can be trapped and slowed down as it

moves through the 3D structure. The slowing of the incoming light can be reduced to such an extent that whilst the propagation direction remains constant there is a negative phase velocity. It was these negative polarisations of the light waves that exhibit the NIM effect, demonstrating a negative refraction angle as observed in the material (Figures 3.28, 3.29, 3.30 and 3.31).

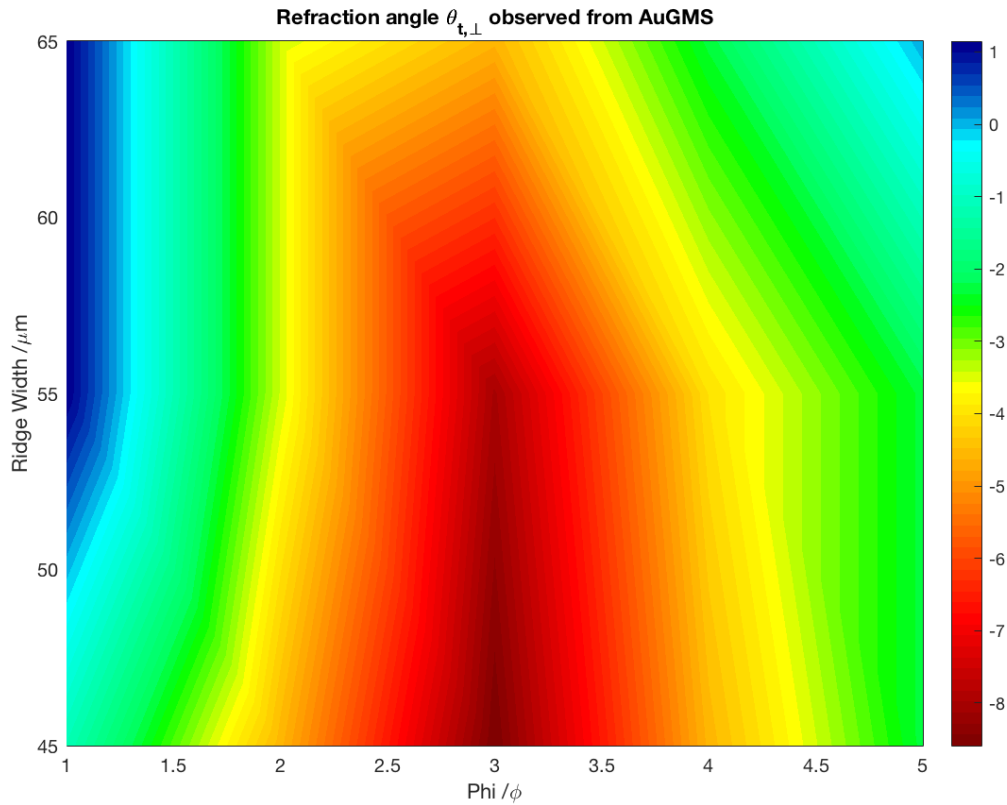


Figure 3.29 | MATLAB plot using practical data to observe how small angles of Φ impacted the refractive angle of the 1D arrays, of varying ridge diameter (Γ) for M13 templated onto AuGMS. Here, the MATLAB mesh plot allowed the visualization of the effect of Φ at a particular λ (700 nm) to achieve changing refraction angles. The points within the mesh grid highlight the refraction angles observed from the 1D arrays at varying values of Φ using a $\lambda=700$ nm incident light beam. Those of negative value templated using EFD on AuGMS to achieve a 1D array of ridge diameters of 42, 56 and 66 μm .

When using a comparative scale for n as in Figure 3.28, the data sets show little comparison, as the n observed for M13 templated onto AuGMS practically was of an order of magnitude smaller than that of the theorized values (Figure 3.28).

A secondary plot was constructed for each data set to contain a reduced n scale bar to better visualise and compare the data sets obtained for the theoretical and the practical work.

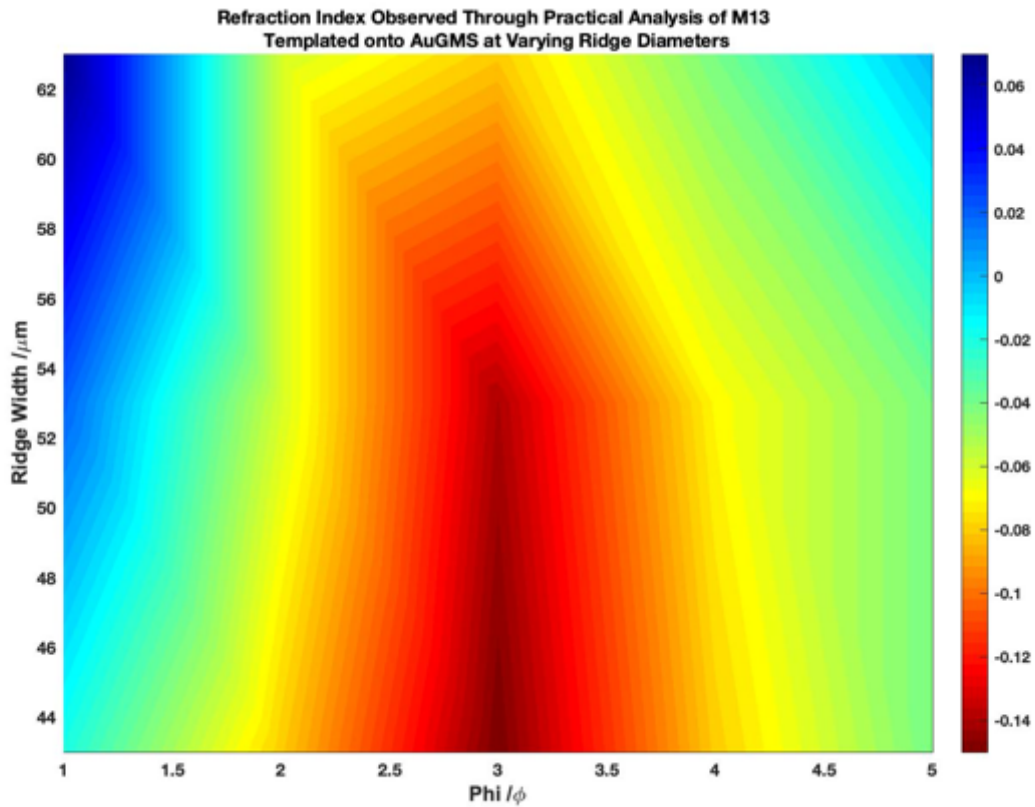


Figure 3.30 | MATLAB plot using a, practical data to observe how small angles of Φ impacted the refractive index of the 1D arrays, of varying ridge diameter (Γ) for M13 templated onto AuGMS. Here, the MATLAB mesh plot allowed the visualization of the effect of Φ at a particular λ (700 nm) to achieve changing refraction angles. The points within the mesh grid highlight the refractive index observed from the 1D arrays at varying values of Φ using a $\lambda=700$ nm incident light beam. Those of negative value indicated NIM behaviour. This computation of practical data represents M13 templated using EFD on AuGMS to achieve a 1D array ridge diameters of 42, 56 and 66 μm .

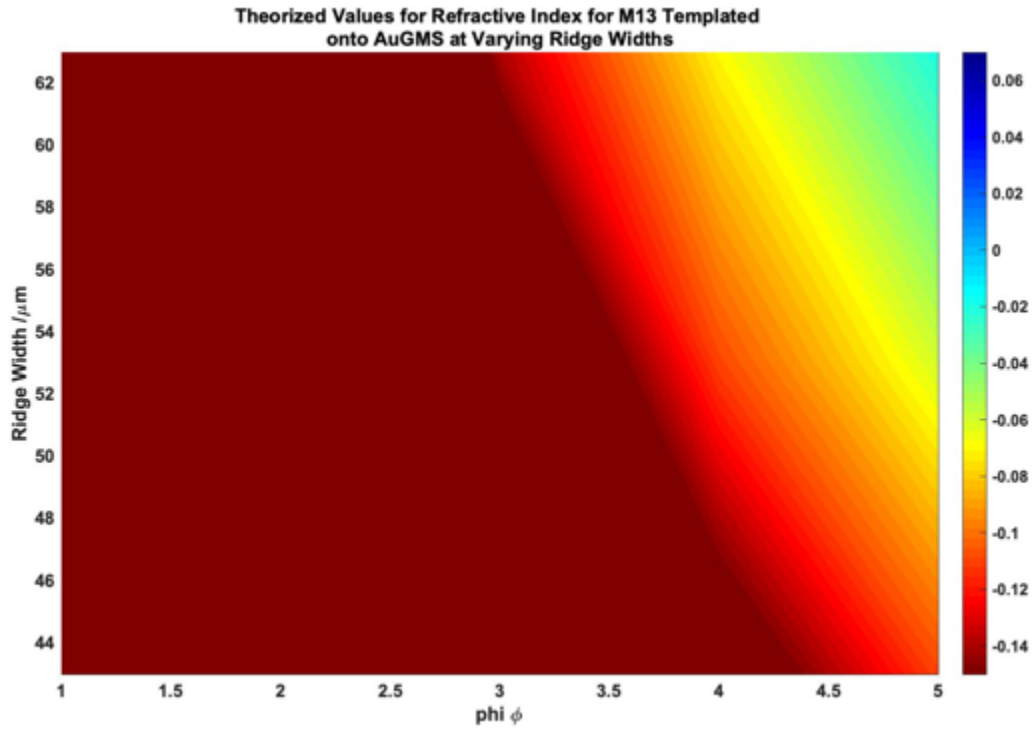


Figure 3.31 | MATLAB plot using theoretical data to observe how small angles of Φ impacted the refractive index of the 1D arrays, of varying ridge diameter (Γ) for M13 templated onto AuGMS. Here, the MATLAB mesh plot allowed the visualization of the effect of Φ at a particular λ (700 nm) to achieve changing refraction angles. The points within the mesh grid highlight the refractive index observed from the 1D arrays at varying values of Φ using a $\lambda=700$ nm incident light beam. Those of negative value indicated NIM behaviour. This computation of practical data represents M13 templated using EFD on AuGMS to achieve a 1D array ridge diameters of 42, 56 and 66 μm .

When reducing the scale of the n , it was clear that whilst the n of M13 templated onto AuGMS was *ca.* 10x smaller than that predicted theoretically, a NIM effect was still able to be observed at $1.5^\circ < \Phi < 5^\circ$ for ridge widths of 45 and 55 μm . An increased ridge diameter to 65 μm however, reduced the window in which NIM activity was observed to $1.7^\circ < \Phi < 4.7^\circ$. Thus, the slower templating speed was less effective at creating a NIM effect (Figures 3.29 and 3.20).

One clear difference between the theorised (Figure 2.31) and practical data (Figure 2.30) was that the practical demonstration appeared to show an optimal window of $2.75^\circ < \Phi < 3.25^\circ$ for the observation of a NIM effect. Within this band an n of ca. -0.14 was visualised for both the 45 and 55 μm ridge widths. Comparatively the theorised MATLAB projection shows that the optimal window begins around $4.4^\circ \Phi$ projecting all the way down to $1^\circ \Phi$, hence a much wider window was observed. Further the projection also would indicate that a wider ridge width of 65 μm should also be capable of producing a NIM effect at around $3^\circ \Phi$, again projecting down to $1^\circ \Phi$.

The disparity between the projection and the practical data could be attributed to a number of problems, not limited to that the smaller the value of Φ being observed in the laboratory, the higher error that could be associated with both the targeting of the light beam to the surface for characterisation, and also the recording of the delta-shift of the light beam itself once it have passed through the ridged structure and substrate.

3.7 Conclusions

When considering modifications that could provide further information regarding the LPL and CPL interaction with the ridges of the 1D arrays, it was highlighted that whilst a spot of 400 μm in diameter from the laser emission source, was useful in creating an average of the interaction with both ridges and grooves, it did not allow a conclusive analysis of the ridges and grooves independently. Through utilisation of smaller diameter laser spots, it was confirmed that the groove portion of the 1D arrays were in fact impacting the NR, ΔCD and (g) values obtained for the samples. However, to use a laser spot with a narrower diameter many modifications to the rig system would need to be considered. In particular a microscope system would need to be incorporated into the system to allow for pinpointing of the laser source on the ridge or groove. Further as the

reflected/refracted light ray would be much narrower in diameter and undetectable via the naked eye a much wider diode detector would need to be sourced to be sure that the ray was reaching the detector adequately.

The theoretical values for FOM are directly influenced by Γ , whereby a lower Γ gives a higher value for FOM. Therefore, if one were to desire a NIM in the visible λ range *i.e.* smaller values of λ , smaller values of Γ would need to be produced to demonstrate a sufficiently high FOM. However, practically achieving reproducible and suitably hierarchical structured ridges, using the set-up, at the high speeds needed to create such small Γ was not feasible. A possible solution to allow the methodology to realise NIM structures in the visible spectrum at broad ranges of Φ , would be to manipulate the environment in which the templating was conducted. More control of conditions such as temperature and humidity, which have been proven to have profound effect on the evaporation rate of the three-phase contact line, would be a suitable recommendation. Due to equipment constraints the evaluation of temperature and humidity variance on the methodology of evaporative front deposition was not possible.

Another possibility to increase the effectiveness of the ridges would be to fabricate a methodology whereby the ridges were of greater height. The greater height of the ridges would allow for increased optical trapping to occur within the ridge to amplify the ability of the ridge to induce negative phase velocities at a higher magnitude. One methodology that could be explored would be to use a prefabricated architecture to guide to assembly of M13 into trenches as the EFD process was carried out. Again, this was a problem beyond the scope of the research here due to limited resources and time available to complete the research.

The addition of a circular polariser to a POM-SPEC setup could allow for a non-discrete spectrum for each sample from $\lambda=250-1500$ nm (the limitations of the

POM-SPEC). This additional characterization would be a more precise analysis of ΔCD for each 1D array, than what was achieved using the 'in-house' set up (detailed in Chapter 4). However, it would not be suitable to measure extrinsic chirality of the system *i.e.* a function of Φ , therefore it would still be required to calculate this data through the in-house rig.

On comparison of the two templating speeds 74.3 and 14.85 $\mu\text{m}.\text{min}^{-1}$, it was the higher templating speed that demonstrated NIM behaviour, whilst the 14.85 $\mu\text{m}.\text{min}^{-1}$ demonstrated a low but positive refractive index (PIM). Earlier analysis in Chapter 2 depicted the two distinct hierarchical levels created by the higher templating speed, such that it was possible to deduct from the negative refraction analysis that it was the uppermost hierarchical layer that caused the shift from PIM to NIM. This could be suggested due to the inability of a singular layer of nematically ordered M13 bundles in creating a NIM effect as observed during the 14.85 $\mu\text{m}.\text{min}^{-1}$ templating speed.

CHAPTER 4 M13: Further Applications of the 3D Scaffold

M13 bacteriophage presents an interesting option as a scaffold due to the ability of the filamentous fibres to self-assemble into various ordered structures with well-defined shapes, which can lead to novel materials for a wide range of functional applications, including energy generation, biosensors, semiconductors and tissue-regenerating materials.

There is a particular interest growing around the chemical modification of M13, as although genetic engineering approaches have been widely used to design novel bionanomaterials, they are restricted to small peptides of <20 amino acids in length. There are four main motives for the move towards chemical modifications of M13 for novel applications:

- **Genetically programmable biomaterials cannot incorporate that vast chemical diversity of natural or synthetic compounds**
- **Excessive mutations plaguing genetic engineering diminishes the packaging, replication and assembly efficiency of M13**
- **Chemical modifications provide the opportunity to incorporate synthetic functional groups in site specific and quantitative manners**
- **Chemical modifications are relatively inexpensive and require environmentally friendly synthesis processes that are easily scalable to industry**

Upon initial characterisation of the 3D scaffold achieved through EFD of M13, it was noted that an increased surface area created by the intertwining of phage bundles over the substrate material presented further applications for the 3D scaffold to display functional nanomaterials (Chapter 2). The high loading capacity per unit area of the 3D scaffold, compared to that shown by the bare substrate, presented an exciting opportunity to exploit this material for the

detection of metal ions.^{151–153} It was therefore chosen to explore the possibility of heavy metal detection using the phage-based systems for lead (Pb^{2+}) through the incorporation of gold nanoparticles (AuNP) into the 3D scaffold.^{154,155}

The premise here was not to provide a quantitative analysis of the ability of M13 scaffolds decorated with nanomaterials to detect heavy metals. Further, the specificity of AuNP bound to M13 for the detection of Pb^{2+} in the presence of other ions was not explored.

Instead preliminary experiments and calculations will be shown that highlight the capability of the scaffold to 'load' the nanomaterials onto its exterior surface and be subsequently subjected to the EFD process to create a multi-layered scaffold for nanomaterial attachment. It was important to highlight at this stage the aim was to showcase how the M13 3D scaffold can be exploited for its increased surface area compared to that of a bare substrate.

4.1 Heavy Metal Detection Systems

Heavy metal ions, such as Pb^{2+} , are considered to be among the most toxic pollutants in the environment.^{156,157} Not only was Pb^{2+} detrimental to human and environmental health, but also the widespread of Pb^{2+} use in everyday items, such as mobile phones, renders it a significant danger. Heavy metal ions are also non-biodegradable and hence they can accumulate in the environment to toxic levels.^{158,159}

Colourimetric detectors are widely used in environmental, food and safety analysis, as well as molecular diagnostic tools, such as pregnancy testing.^{160–163} Naked-eye colourimetric sensors have many advantages over other more developed methods such as inductive coupled plasma optical emission spectroscopy (ICP-OES) and mass spectrometry (MS). In that, they require little

to no training to use and they are extremely portable and generally inexpensive to produce at a high yield using green chemistries.¹⁶² Colorimetric sensors, however, are plagued by low sensitivity with false positives a common occurrence.¹⁶⁴ This has promoted a plethora of research groups to research into ways to increase the sensitivity of colourimetric devices *via* an array of methods, such as the utilization of smartphones to achieve the point of care testing of blood samples.¹⁶³

. Accumulation of Pb^{2+} in the body was therefore especially dangerous in children, whereby high levels of Pb^{2+} consumption can lead to irreversible brain damage and retard both mental and physical developments.¹⁵⁶ In the case of existing Pb^{2+} detection systems traditional methodology such as atomic absorption spectrometry (AAS), inductive coupled plasma mass spectrometry (ICP-MS) and inductive coupled plasma atomic emission spectrometry (ICP-AES) have been successful in pico-molar concentration detection of Pb^{2+} . However, these analysis methods all require complicated sample preparation and complex instrumentation that was not available to be provided outside of the laboratory. Therefore it was critical that developments begin to be made towards constructing simple rapid detection systems that can be used on-site.^{165–167} Recent advances have surrounded the modification of AuNP with specific Pb^{2+} agents. In particular, a lot of work has considered the binding of AuNPs to wild-type M13 ssDNA to generate a stimuli-responsive material at the nanoscale.¹⁶⁸ AuNPs are known for their extraordinary tuneable properties that enable very broad-spectrum detection systems.^{169–172}

Chen et al. proposed a simple detection method that combined glutamine rich-ssDNA with AuNPs to afford a detection system that actively displaces the M13 from the AuNPs surface, binding to the Pb^{2+} instead.¹⁶⁷ Freeing of the AuNPs allowed for aggregation of AuNPs and hence a distinct colour change from red to blue in solution.¹⁶⁷ Whilst this was a valid method of detection when the precursor solutions have recently been made the longevity of the solutions would be

questionable in terms of stability outside of refrigeration systems. Whilst M13 ssDNA was stable over a wide range of temperatures it was known to precipitate out of solution quite readily, if this were to occur the bound AuNPs would be free to aggregate within the solution affording a colour change from red to blue, and therefore would no longer be suitable to detect Pb^{2+} .

Moving from a solution to solid-state detection system, a significant loss of sensitivity was expected.¹⁶³ This was primarily down to the limited surface area available to the nanomaterials. It is expected that the increased surface area provided by the EFD process, to 'hold' AuNP-GA within the 3D scaffold via electrostatic interaction until contact was made with a Pb^{2+} containing solution, would allow for a progression from a liquid to a substrate based detection system with a comparable limit of detection values.¹⁶⁹

Binding of AuNP-GA to M13 was achieved *via* initially exposing cysteine molecules on the exterior of the M13 protein coat *via* a deacetylation reaction, to facilitate an interaction between M13 and AuNP-GA. Once bound to M13, the EFD process was utilised, as in Chapter 3, to afford coating of M13-AuNP on BSi and AuSi.

4.2 Methodology and Results

4.2.1 Materials and Reagents

Sodium citrate (Na_3Ct) and chloroauric acid ($\text{HAuCl}_4 \cdot 3\text{H}_2\text{O}$) were purchased from Merck and Sigma-Aldrich Company. Deionised water was used throughout experiments. Phosphate buffered saline – pellets (PBS) were purchased from Sigma-Aldrich Company and made up according to the specification, the PBS was further autoclaved to prevent contamination to M13 stock solutions. Lead nitrate ($\text{Pb}(\text{NO}_3)_2$) was purchased from Merck and used as provided unless otherwise stated.

4.2.2 Instruments

Heating and magnetic stirring during experiments were conducted on a Camlab MS-H280-Pro Magnetic Hotplate Stirrer. UV-Vis absorption spectra were recorded using UV-VIS (Cary 6000i UV-Vis-NIR combined with Cary WinUV software). Dynamic Light Scattering (DLS) was carried out using a Zetasizer NanoS DLS Instrument, operating with Zetasizer version 7.10 software. was used to analysis particle size and distribution within the samples.

4.2.3 Synthesis of AuNP

AuNPs were synthesised *via* a citrate reduction method, resulting in slightly negative AuNPs, whereby the slight negative charge prevents aggregation of the NP.¹⁷³ AuNPs produced using this method display a characteristic red colour, owing to the surface plasmon resonance (SPR) peak at around 540 nm.^{167,173}

Na₃Ct (2.2 mM, 150 mL) was heated in a 250 mL Erlenmeyer flask (150°C, 15 min, vigorous stirring at 350 rpm) until boiling. HAuCl₄ (25 mM, 1 mL) was then added. A visible colour change was observed after boiling (10 min) from yellow to a ruby red colour (Figure 96), indicating the successful synthesis of AuNP (*ca.* 10 nm, *ca.* 3×10^{12} NPs/mL).¹⁷³

The surface of AuNPs are coated with negatively charged citrate ions and so do not aggregate within the ddH₂O solution.¹⁷³ However, to ensure degradation of AuNP did not occur due to light interaction within the laboratory, the AuNPs solution was placed in an amber glass bottle and kept at 5°C.¹⁷³

The SPR peak was observed via UV-Vis analysis at a wavelength range of 200 – 1100 nm to confirm successful AuNPs synthesis. Subsequently, the size of the AuNPs produced were characterised using DLS. The standard “aunp sizes.sop” produced and distributed by Malvern Instruments Ltd was used, whereby the

chamber was set at 25 °C. The sample methodology included the material (AuNP) refractive index of 0.47 with absorption of 1, and the dispersant (ddH₂O) refractive index of 1.330 combined with its viscosity 0.8872 cP.

4.2.4 Synthesis of AuNP-GA

Gallic acid (GA) was used to reduce Au to create gallic acid capped NPs. The hydroxyl (-OH) group, provided by the phenyl group on gallic acid, acted as the reducing agent (Figure 94). The carboxyl (-COOH) group acted as a stabilizer for the solution to prevent aggregation of the resulting AuNPs (Figure 4.1).¹⁵⁵ Based on previously published literature, molarity values for successful reduction of Au by GA indicated a range of concentrations of constituent materials for optimal reduction parameters, a range of concentrations were trialled for both HAuCl₄ and GA, after which the optimal concentrations were obtained (APPENDIX VII).

A solution of HAuCl₄ (500 µM, 100 mL) was reduced to AuNPs by addition GA (42.3 µM GA, 100 mL). The solution was then left to react for 5 min before it was filtered using a 0.2 µm filter head into an amber glass bottle for storage and further use.^{155,174}

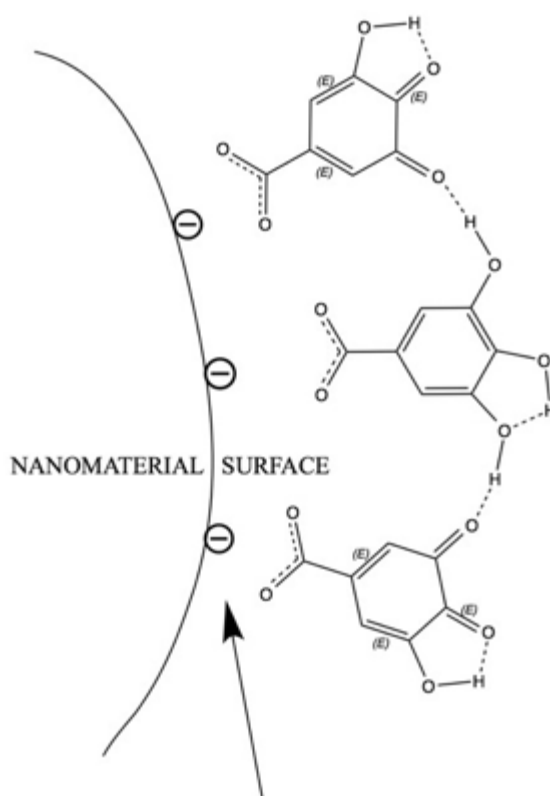


Figure 4.1 | Surface attraction between GA and the nanomaterial surface. The hydroxyl (-OH) group, provided by the phenyl group on gallic acid, acted as the reducing agent. The carboxyl (-COOH) group acted as a stabilizer for the solution to prevent aggregation of the resulting AuNP-GAs.

4.2.5 Synthesis of M13-AuNP and Mechanism of Action Towards Pb^{2+}

The ssDNA property of M13 was what allowed for the direct adsorption onto AuNP. The nitrogenous rich exterior PVIII protein has a high affinity to Au; this electrostatic interaction prevents the aggregation of AuNPs.¹⁵¹ If a molecule containing dsDNA was used, this type interaction would be impossible as the double-stranded phosphate backbone repels the negatively charged AuNPs due to electrostatic interaction. However, in the presence of Pb^{2+} the random helical structure of M13 dissipates into a rigid G-quartet that reduces the exposure of the nitrogenous exterior whilst also increasing the surface charge density. This change in conformational structure prevents the adsorption onto the AuNP surface *via* electrostatic binding. No longer stabilised by M13, AuNPs are again

free to aggregate.¹⁶⁷ The schematic for the mechanism of action proposed by *Chen et al.* was shown in Figure 4.2, whereby a salt (NaCl) was added to further induce stabilisation of the solution. In the methodology this stage was omitted as M13 was dispersed in a PBS solution prior to the addition to AuNP-GAs, the -COOH group on the AuNP-GAs also acts a stabiliser in the solution.

To remove unbound AuNP-GAs from the solution a modified PEG precipitation was used to draw the M13 (bound to AuNP-GA) out of the solution.

M13 (0.1 mg/mL, 1 mL in PBS) was added to a 2 mL Eppendorf Tube, AuNP-GA (0.5 mM, 1 mL) were added to the solution. PEG (6000 KDa, 100 μ L) was added to the solution and the tube was left on ice for 1 h. After 1 h the tube was centrifuged at 10 000 RCF for 15 min. The pellet was removed and dispersed in 1000 μ L of PBS. This was then centrifuged again (15 min, 12 000 rpm). UV-Vis confirmed that the supernatant did not contain AuNPs *via* the absence of a peak at λ_{564} nm. The final pellet was then dispersed in 1000 μ L PBS. UV-Vis was used to confirm whether both the M13 peak at *ca.* 269 nm and the AuNP-GA peak at *ca.* 536 nm remained in the M13-AuNP produced

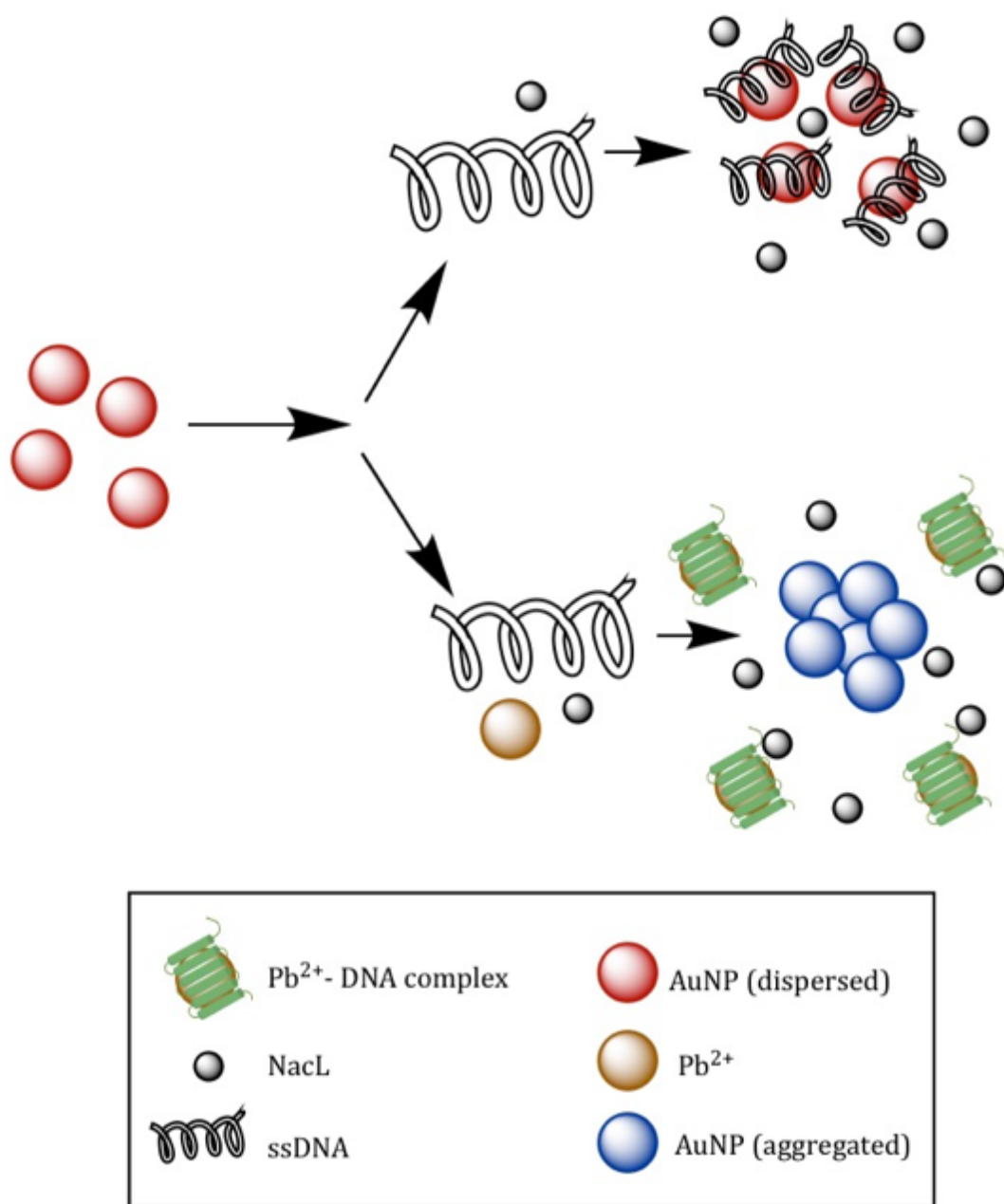


Figure 4.2 | Schematic of the phage-based detection system for Pb^{2+} . In solution AuNPs can be added to M13, whereby they will not aggregate in the presence of NaCl. However, on addition of Pb^{2+} into the solution, Pb^{2+} dissipates the nitrogenous exterior of M13, removing its ability to bind electrostatically to AuNPs. AuNPs now free in solution have the ability to aggregate to form Au^0 .¹⁶⁷

4.3 Results and Discussion

4.3.1 Synthesis of AuNPs

AuNP were synthesised (Table 4.1) to confirm the formation of AuNP-GA, whereby a slight redshift and peak broadening was observed from the AuNP SPR peak of 536 nm to 543 nm. This method of characterising GA conjugation to AuNP agrees with work by *Moreno-Alvarex et al.*, which showed the UV-Vis absorption of gallic acid stabilised AuNP shifted to a broader band.^{174,175}

Table 4.1 | Characterisation data for synthesised AuNP. Sample colour changed observed from Figure 4.3. SPR peak observed from Figure 4.4. Average particle size (Z-average size) was observed from Figure 4.5.

Sample and Concentration	AuNPs were dispersed in ddH ₂ O (1.7829 mol/L)
Colour Change Observation	Pale yellow to ruby red (Figure 4.3)
SPR Peak	534 nm (Figure 4.4)
Z-Average Size	8 d.nm (Figure 4.5)

The UV-Vis spectra in Figure 4.6 demonstrates the peak obtained for the formation of M13-AuNP, and subsequently M13, AuNP and AuNP-GA. The dampening of the AuNP-GA and M13 peaks in the M13-AuNP spectrum was due to the lower concentration of each of these molecules in the solution required for templating during the EFD process.

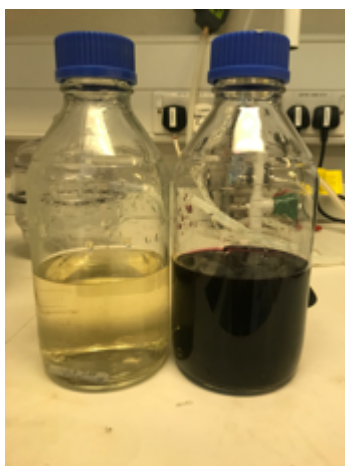


Figure 4.3 | Observational colour change during successful AuNP synthesis. The initial colour of the solution resulting from the addition of HauCl_4 to Na_3Ct was pale yellow. Upon boiling the mixture for 10 min under vigorous stirring a ruby red colour was observed indicating the successful reduction of Au^{3+} to Au^+ and subsequently a disproportionation to Au^0 . The Na_3Ct then acts as a capping agent towards AuNPs stabilizing the NPs within solution.

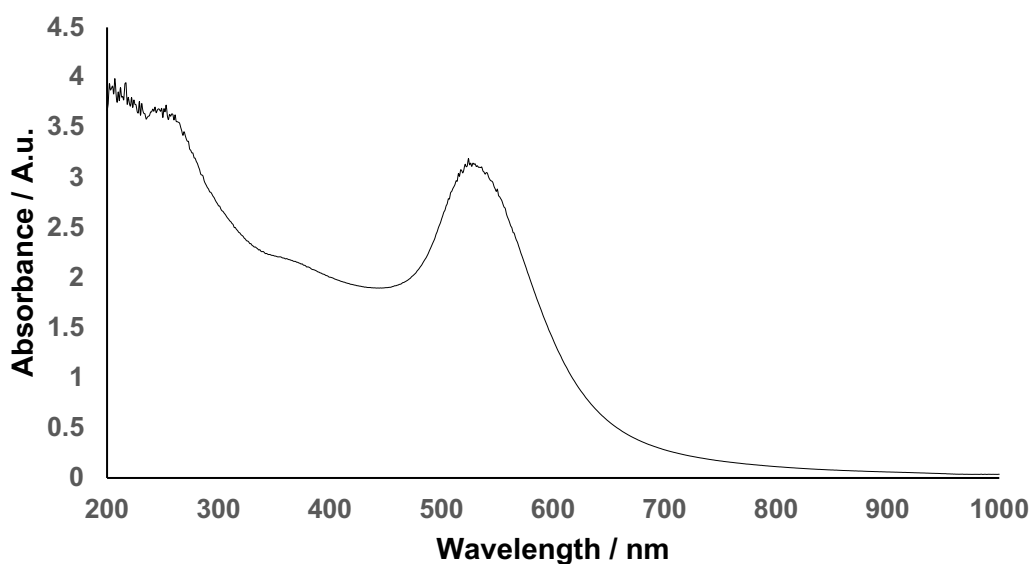


Figure 4.4 | Absorbance of prepared AuNP. AuNP prepared in ddH₂O (1.78 mol/L).

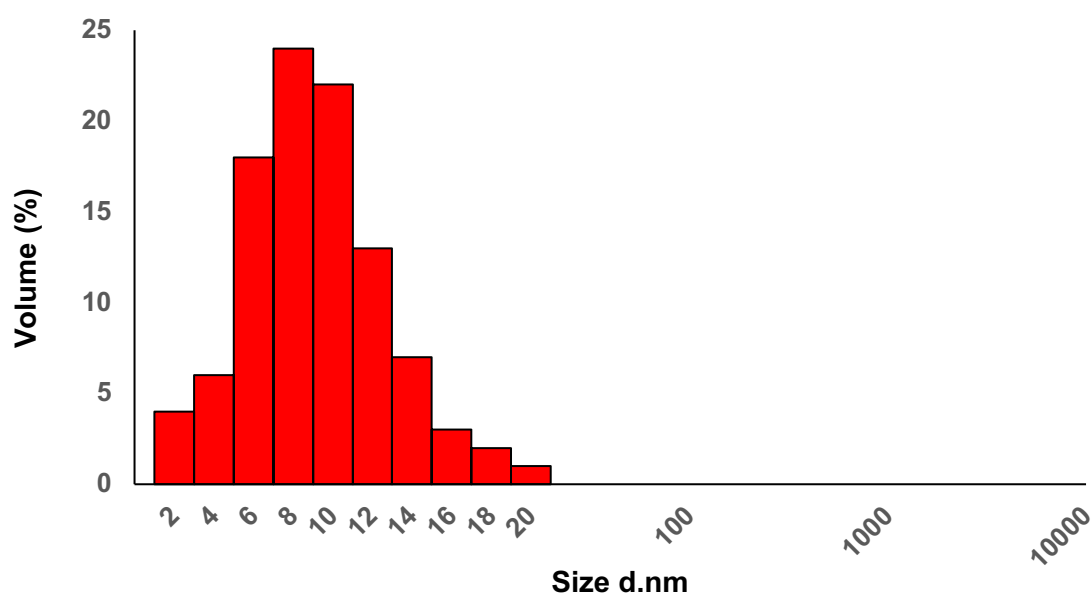


Figure 4.5 | DLS size distribution by volume. AuNP-GA (1.78 mol/L) diluted in ddH₂O at 0.5 mg/mL and filtered using a 0.2 μ m filter (Camlab 1173446 Syringe Filter, polytetrafluoroethylene, non-sterile 0.2 μ m).

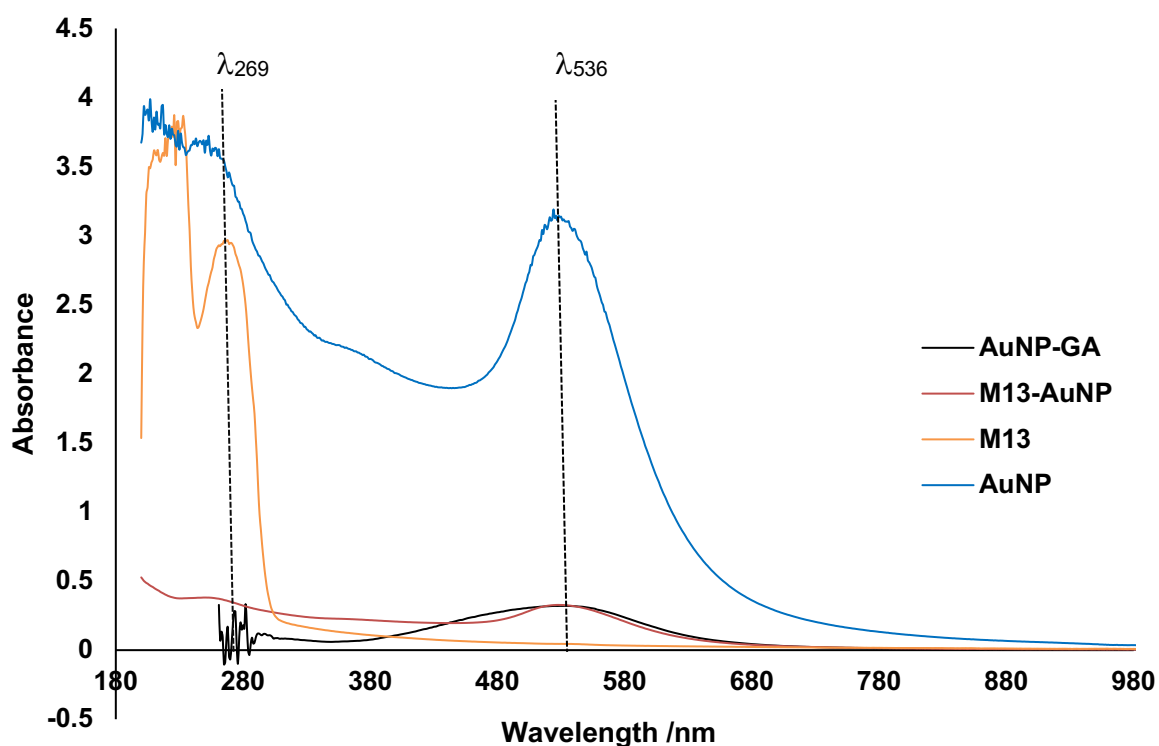


Figure 4.6 | UV-Vis spectra for the formation of M13-AuNP. The characteristic λ peaks associated with M13 (λ_{269} nm) and AuNP (λ_{536} nm) are indicated on the spectra.

4.3.2 Evaporative Front Deposition of Active Material bound M13

To achieve 3D assemblies of M13 embedded with AuNPs, M13 was first conjugated to AuNPs-GA prior to the EFC process (M13-AuNPs). The withdrawal speed of $111.4 \mu\text{m min}^{-1}$ was selected to take forward in templating of AuNPs and M13-AuNPs onto BSi or AuSi substrates. This templating speed was chosen due to the ability of this templating speed to achieve reliable and consistent ridge diameters observed in Chapter 3. Both BSi and AuSi substrates were explored as the affinity between AuNP-GAs and the AuSi was expected be increased (Table 1.1). Therefore, some difference in the way the templated M13 would interact with the surface may be altered.

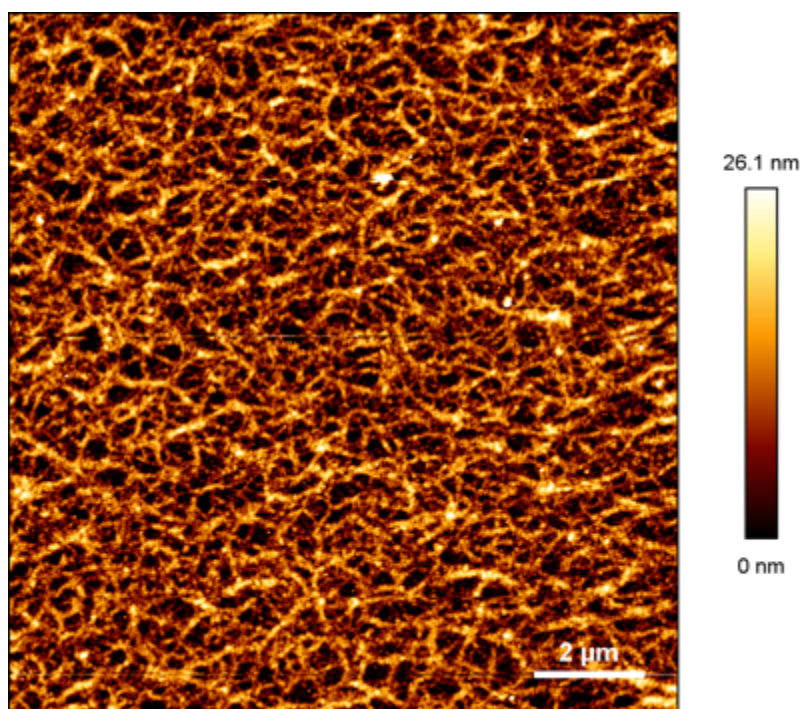


Figure 4.7 | AFM image of M13-AuNP onto BSi. M13-AuNP templated onto BSi at $111.4 \mu\text{m min}^{-1}$.

Initially EFD was conducted with a solution of AuNPs to confirm no inherent ability of AuNPs to form ridges on the substrate during EFD (APPENDIX VIII).

From Figure 4.7 and 4.8 it can be seen that the presence of AuNPs decorated along the exterior of M13 (M13-AuNP) has greatly impacted the ability of M13 to produce the chiral hierarchical ridges observed in Chapter 2. Instead, the fibres of M13-AuNP have displayed isotropic disorder when templated onto BSi (Figure 4.7) and weak nematic ordering when organised onto AuSi (Figure 4.8).

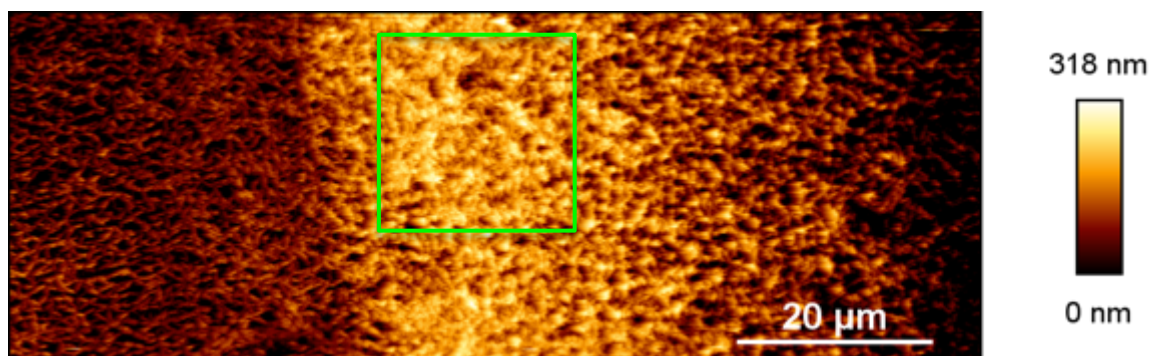


Figure 4.8 | AFM image of M13-AuNP templated onto AuSi via EFD. M13-AuNP templated onto AuSi at $111.4 \mu\text{m min}^{-1}$. The highlighted box represents a $40 \mu\text{m}^2$ region of the ridge.

The presence of a ridge when M13-AuNP was templated onto AuSi opposed to BSi could be attributed to the increased affinity between the AuNPs on the surface of M13 and the Au coating on the surface of the Si wafer. This affinity was increased due to the S-S interaction compared with the Si-S interaction as highlighted in (Table 1.1).

4.3.3 Projections of M13-AuNP loading of the substrate

Here the projections by which, M13-AuNP conjugates, could be loaded onto a defined area of BSi or AuSi, when compared to AuNP are highlighted. To account for the variance in size of M13-AuNP, two projections have been made (Figures 4.9 and 4.10) to highlight the smallest and largest possible area for the M13-

AuNP conjugates. This has been done, as overlaying error bars would not be suitable to the difference in values stated on the y-axis for Figures 4.9 and 4.10.

4.3.3.1 Projections using average AuNP-GA size

Whilst ridges of the chiral hierarchical structures were not able to be fabricated by M13-AuNPs on either substrate of BSi or AuSi, multiple layers of isotropic M13-AuNPs fibres on the substrate present enough opportunity to increase the concentration of AuNPs per unit area when compared with AuNP templated onto BSi alone. It was theorised the number of AuNPs per an example area of $40\ \mu\text{m}^2$, using data obtained about the dimensionality of AuNPs (8 d.nm) and literature data regarding the dimensionality of a single M13 strand (6 d.nm \times 800 nm). The calculations relating to Figures 4.7 and 4.8, can be found in APPENDIX IX. BSi was projected to have 2 isotropic layers due to the height value obtained from the AFM analysis (Figure 4.7) and height of the hybrid M13-AuNPs (22 nm). The full height shown on the AFM was subjective due to the inability of the tip of radius 5 nm to create an accurate distance from the height of the M13-AuNP scaffold to the substrate, further blunting of the tips after successive use reduces the effectivity of the tip to probe the sample.¹⁷⁶ Thus, it was projected that 2 isotropic layers are present. AuSi was projected to have around 15 nematic/isotropic layers within the highlighted area on the ridge (Figure 4.10). This was again calculated by dividing the z-height obtained from AFM analysis by the height of the M13-AuNPs hybrid (22 nm).

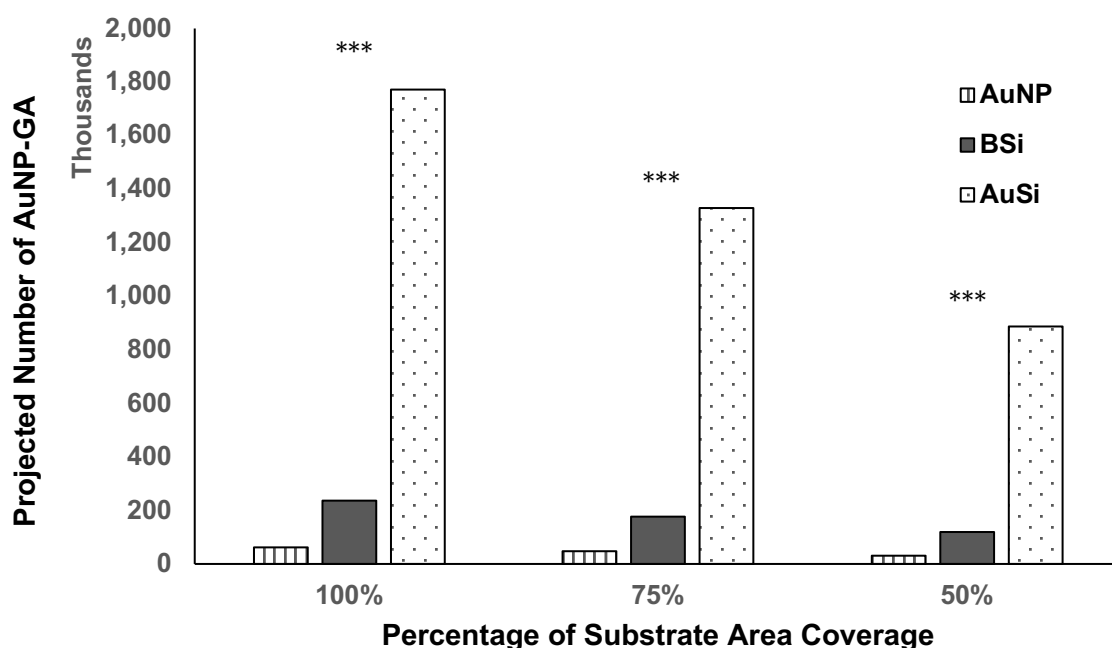


Figure 4.9 | Projection for the number of AuNP-GA per area. The projection covers 3 concepts: AuNPs; AuNP-GAs alone templated via EFD onto an AuSi wafer, BSi; M13-AuNP templated via EFD onto a BSi wafer and AuSi; M13-AuNP templated via EFD onto an AuSi wafer. Calculations in APPENDIX IX.

It can be seen from Figure 4.9 that through conjugating AuNPs to the surface of M13 a significant increase of the number of AuNPs per unit area of the substrate, using M13 as a scaffold to display the nanomaterials was created. Even when only 50% coverage of the 40 μm^2 substrate with M13-AuNP was considered compared to 100% coverage of AuNP-GAs the number of AuNP-GA present was increased by 89% for BSi and 1318% for AuSi.

When comparing like for like coverages e.g. both at 50%, which was much more likely in a practical sense, an increase of 278% in AuNP-GAs per 40 μm^2 on BSi was observed and 2736% on AuSi.

This particularly highlights the effectivity of templating M13-AuNP onto an AuSi substrate to yield maximum loading of the substrate with AuNP-GAs.

4.3.3.2 Projections using maximum AuNP-GA size

Following on from the projections made using the average diameter of the produced AuNP-GA (8 d.nm), projections were made using the maximum diameter of AuNP-GA produced (30 d.nm).

BSi was projected to have 1 isotropic layer due to the height value obtained from the AFM analysis (Figure 4.7) and height of the hybrid M13-AuNPs (66 nm). AuSi was projected to have around 5 nematic/isotropic layers within the highlighted area on the ridge (Figure 4.8). This was again calculated by dividing the z-height obtained from AFM analysis by the height of the M13-AuNPs hybrid (66 nm).

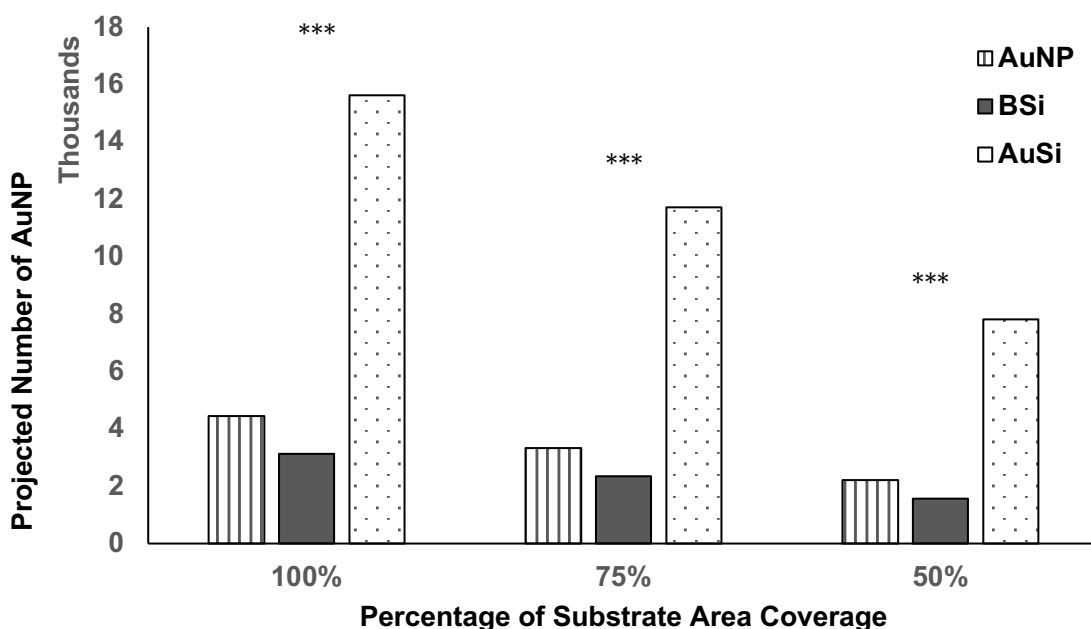


Figure 4.10 | Projection for the number of AuNP-GA per area. The projection covers 3 concepts: AuNP; AuNP alone templated via EFD onto an AuSi wafer, BSi; M13-AuNP templated via EFD onto a BSi wafer and AuSi; M13-AuNP templated via EFD onto an AuSi wafer. *** indicates $P < 0.01$ significance between data sets. Calculations in APPENDIX IX.

It can be seen from Figure 104 that through conjugating AuNP-GAs to the surface of M13 a significant increase of the number of AuNP-GAs per unit area of the

substrate was created using M13 as a scaffold to display the nanomaterials. However, unlike the projections made in Figure 4.9, when comparing 50% coverage with M13-AuNP templated onto BSi with AuNP-GA alone, with 100% coverage, a slight decrease (-5.47%) in AuNP-GA numbers were produced.(Figure 4.10) M13-AuNP templated onto AuSi, however, did still show 323% increase in AuNP-GA per 40 μm^2 .(Figure 4.11)

When comparing like for like coverages e.g. both at 50%, which was much more likely in a practical sense, an increase of 89% in AuNP-GAs per 40 μm^2 on BSi was observed and 845% on AuSi, when using M13 as a scaffold. (Figure 4.11)

Through using the maximum diameter of AuNP-GA within the sample (Figure 4.5), it has been demonstrated that even at a larger diameter such as 30 d.nm the M13 scaffold provides an excellent scaffold for increasing the number of AuNP-GA per unit area. This was especially prevalent when templating M13-AuNP onto AuSi.

4.4 Conclusions

Here the ability of M13 to display a functional nanomaterial along its exterior capsid has been shown. It is therefore expected that M13, therefore, has the capacity to act as a scaffold for many other functional materials that can exploit the cysteine (-SH) functional groups on the capsid. Further still modification of the functional groups displayed on the exterior of M13 would allow for the scope of material able to be bound to M13 to be even broader.

Using the EFD methodology it has been shown that even when bound to functional materials such as AuNP-GA, that have been previously shown to have detection capabilities towards Pb^{2+} by *Chen et al.*, exploitation of the intrinsic ability of M13 to self-assemble can be used at the 3-phase contact line to produce

a 3D scaffold that can essentially 'hold' the functional material within it. The nanoscale dimensionality of M13 makes it a superior scaffold to commercially available scaffolds with the ability to increase AuNP-GA loading of a surface by 178% on a BSi wafer and 1336% on an AuSi wafer. Through the mass loading capability of the functional material, it was expected that the limit of detection observed through liquid detection systems as observed by *Chen et al.*, could be realised on a substrate level. This would be a great progression from the work produced by *Chen et al.*, as the substrates could be stored without the need for a fridge thus making them accessible in many more environments. However, much more extensive research would need to be carried out to confirm the viability of the M13-AuNP architectures in successfully detecting Pb^{2+} from samples. This would also need to consider longitudinal storage evaluation *i.e.* degradation during heat, humidity and light exposure.

Whilst it is evident that this work remains primitive, it is hoped that a progression towards biological scaffolds could hold the key to better substrate detection systems that present a more economically and environmentally friendly substitution to those currently available.

CHAPTER 5 CONCLUDING REMARKS AND GOING FORWARD

M13 over the past two decades has presented itself as one of most powerful candidates for use in a range of novel research areas to include fluorescence, SPR, bio sensing and optics. The versatility of M13 was attributed to its nontoxic and well-defined shape that has superiority in the field of self-assembly and specific binding abilities. In addition, the ability of M13 to withstand adverse conditions such as elevated temperature and acidic/basic conditions in combination with its biocompatibility and genetic engineering, make it a robust building block for a diverse range of applications. It was this accumulation of properties and characteristics that predict the exploitation of M13 bacteriophage to continue to expand and be developed in an ever-growing breadth of fields. Throughout the research presented here the surface has only just been scratched into the abilities of M13 to be used in bio-optics for metamaterial behaviour and activity as sensing systems.

Although chirality has been around for some time now academically speaking, the translation of the principles of chirality from the molecular scale to 2D and 3D architectures has only recently began to gain traction.^{126,177} Manifestation of structural and/or surface 2D and 3D chirality was driven by supramolecular chemistry, whereby molecules are held together by non-covalent intermolecular interactions. This allowed the structures to possess no inversion symmetry elements, rendering them capable in displaying enantiomeric forms.

M13 self-assembly was a soft supramolecular interaction at the metal surface, which drives the structure to become chiral. At the surface molecular self-assembly was driven by the subtle balances between molecule-surface and molecule-molecule interactions. Appropriate choices of substrate surface and molecule can mediate these forces. This can lead, as in the case, to achieve special categories of assembly, whereby chiral structures can be achieved to

display non-superimposable mirror forms. Through utilising inherently chiral M13 molecules sufficient complexity has been introduced into the system, such that all inverse symmetry elements are eradicated. Chirality was instigated from complexity and in order to understand its induction and propagation at surfaces, the full range of rigorous surface science techniques would be needed to explore the structures produced here in further detail.^{9,19,30,40,177,178}

Through intelligently designing the structure type and the parameters of the units *i.e.* ridges in the case, metamaterials present exotic properties that cannot be found in natural materials *i.e.* negative refractive index. The periodic nature of the 1D arrays that have been produced of ridges and grooves gave rise to giant interaction of the electromagnetic wave to the artificial structures. Further through modulation of the 1D array dimensions *i.e.* Γ and height of the ridges, extraordinary electromagnetic functions were observed such as high-efficiency absorption chirality. Using nanoscale starting materials such as M13 bacteriophage as the building blocks for the scaffold, it was able to greatly reduce the height of the 3D ridges to consistently maintain between 2000 – 100 nm height of the ridges and 20 – 80 μm Γ on both AuSi and BSi templating substrates. TThrough the use of a chiral starting material such as M13, the produced bundles, intertwined with one another in hierarchical structures proved chiral themselves. The strong coupling between the electric and magnetic fields within the structures allowed for a chirality of much larger proportion in comparison to natural chiral materials, again contributing to the ability to fabricate a material that exhibited negative refractive index. Negative refractive index was a phenomenon that has been proved mathematically by Pendry and Monzen and at long microwave wavelengths in other literature experimentally. More recent examples have been demonstrated towards the visible sector of the spectrum it has shown that the rapid development in this area has proved fruitful. However, now that theoretical and practical examples of negative refraction have been readily achieved, the move towards a translational period must be achieved. Through scalable and green driven technologies to achieve extraordinary materials progress can begin

to be made from the laboratory bench to real world applications.
5,9,13,66,85,91,92,177,179,180

Our system yielded a highly organised periodic array with the ability to propagate over large areas on the surface. The ridges of M13 formed a 1D array of ridges of M13 bundled together via electrostatic interaction, these bundles were electrochemically bound by ionic bonds through the PVIII NH_3 groups to the BSi/AuSi surfaces via the free electron pair on the N atom. The 1D arrays were propagated across large length scales with macroscopic surface organisation of which it was non-superimposable to its mirror image, and hence was termed chiral. M13 acted to organise on the surface as an adsorbate into chiral arrangements that broke the symmetry of Si $\langle 111 \rangle$.

One approach not considered here that could enhance the structure further was a multilayer structure, by which subsequent 1D arrays could be arranged atop of each other at varying angular configurations. This additional templating technique could be the route towards a 3D array of M13 ridges to create a fully 3D MM, as at current it is the 1D ridges that contain 3D assemblies.

Using ΔCD and (g) the dependence of concentration and pathlength within the system was eliminated. ΔCD spectra are extremely sensitive to structural changes; therefore, an observed difference can suggest that two different structures were produced, dependent on the substrate. A verification of this point was confirmed via AFM in the case of the structures showed a discrepancy of height within AuSi deposited 1D arrays being *ca.* double the height of those templated on BSi. The discrepancy between the same templating speed to construct arrays of different Γ , depending on the substrate being templated on top of. This was indeed highlighted by Tables 2.6 and 2.7 whereby all templating speeds aside from $74.3 \mu\text{m} \cdot \text{min}^{-1}$, produced some degree of significance between the two data sets for AuSi and BSi.^{3,88,92,181,182}

To further characterise the 3D structures for use in defence applications in which a period of brief magnetism could be utilised e.g. weaponry, it would be beneficial to consider the effects of magnetic ΔCD and g . This could be explored by introducing a magnetic field in a parallel position to the incident polarised light wave. This methodology would require a specialised detection system with capabilities further into the Infra-red wavelength range. Through observing the magnetic ΔCD , any degree of paramagnetism produced within the 3D architectures can be observed, whereby an intrinsic magnetic field can be produced within the material.¹⁸³ Due to the successfulness of the material to achieve large ΔCD and (g) values towards the Infra-red wavelengths it was expected that this could be a useful venture for future works.

It now at the discretion of DSTL as to which of the areas of the SynBio primary cohort (2011) they feel most promising to develop into real world applications for use in the defence sector.

References

1. Wen, A.M., Podgornik, R., Strangi, G., and Steinmetz, N.F. (2015). Photonics and plasmonics go viral: self-assembly of hierarchical metamaterials. *Rend. Lincei* 26, 129–141.
2. Zheludev, N.I., and Kivshar, Y.S. (2012). From metamaterials to metadevices. *Nat. Mater.* 11, 917–924.
3. Baev, A., Prasad, P.N., Gren, H., Samo, M., and Wegener, M. (2015). Metaphotonics: An emerging field with opportunities and challenges. *Phys. Rep.* 594, 1–60.
4. Andrea, A., and Nader, E. (2008). Plasmonic and metamaterial cloaking: physical mechanisms and potentials. *J. Opt. A Pure Appl. Opt.* 10, 93002.
5. Kivshar, Y.S. (2015). Metamaterials, metasurfaces, and metadevices. *Aust. Phys.* 52, 47–50.
6. Pendry, J.B., Schurig, D., and Smith, D.R. (2006). Controlling electromagnetic fields. *Science* (80-.). 312, 1780–1782.
7. Research, G.V. (2017). Metamaterial Market Analysis, By Product (Electromagnetic, Terahertz, Photonic, Tunable, Frequency Selective Surface, Non-linear), By Application, End-use, And Segment Forecasts, 2018 - 2025.
8. Tran, K.T.M., and Nguyen, T.D. (2017). Lithography-based methods to manufacture biomaterials at small scales. *J. Sci. Adv. Mater. Devices* 2, 1–14.
9. Zhi Liu, a Jing Qiao, a Z.N. and Q.W. (2017). Natural supramolecular building blocks: from virus coat proteins to viral nanoparticles. *Science* (80-.). 1, 1–7.
10. Chung, S.W., Ginger, D.S., Morales, M.W., Zhang, Z., Chandrasekhar, V., Ratner, M.A., and Mirkin, C.A. (2005). Top-down meets bottom-up: Dip-pen

nanolithography and DNA-directed assembly of nanoscale electrical circuits. *Small* 1, 64–69.

11. Liu, Y., Zhang, W., Zhu, Y., Luo, Y., Xu, Y., Brown, A., Culver, J.N., Lundgren, C.A., Xu, K., Wang, Y., *et al.* (2013). Architecturing hierarchical function layers on self-assembled viral templates as 3D nano-array electrodes for integrated Li-ion microbatteries. *Nano Lett.* 13, 293–300.
12. Kolle, M., Salgard-Cunha, P.M., Scherer, M.R.J., Huang, F., Vukusic, P., Mahajan, S., Baumberg, J.J., and Steiner, U. (2010). Mimicking the colourful wing scale structure of the *Papilio blumei* butterfly. *Nat. Nanotechnol.* 5, 511–5. A
13. Chern, R.L., and Chang, P.H. (2013). Negative refraction and backward wave in chiral mediums: Illustrations of Gaussian beams. *J. Appl. Phys.* 113.
14. Lee, S.W., Wood, B.M., and Belcher, A.M. (2003). Chiral smectic C structures of virus-based films. *Langmuir* 19, 1592–1598.
15. Warner, C.M., Barker, N., Lee, S.-W., and Perkins, E.J. (2014). M13 bacteriophage production for large-scale applications. *Bioprocess Biosyst. Eng.* 37, 2067–2072.
16. Chung, W.J., Lee, D.Y., and Yoo, S.Y. (2014). Chemical modulation of m13 bacteriophage and its functional opportunities for nanomedicine. *Int. J. Nanomedicine* 9, 5825–5836.
17. Mackenzie, A. What is design in synthetic biology? From techniques to reflexive meta-materials. Available at: <http://scholar.google.com/scholar?hl=en&btnG=Search&q=intitle:What+is+design+in+synthetic+biology?+From+techniques+to+reflexive+meta-materials#0>. [Accessed October 4, 2019].
18. Rong, J., Niu, Z., Lee, L.A., and Wang, Q. (2011). Self-assembly of viral particles. *Curr. Opin. Colloid Interface Sci.* 16, 441–450.
19. Liu, Z., Qiao, J., Niu, Z., and Wang, Q. (2012). Natural supramolecular building blocks: from virus coat proteins to viral nanoparticles. *Chem. Soc.*

Rev. 41, 6178–94.

20. Goodman, R.P. (2005). Rapid Chiral Assembly of Rigid DNA Building Blocks for Molecular Nanofabrication. *Science* (80-.). 310, 1661–1665.
21. Moon, J.-S., Kim, C., Kim, W.-G., Han, J., Sohn, J.-R., and Oh, J.-W. (2015). Recent progress of M13 virus-based chemical and biological sensing. *Toxicol. Environ. Health Sci.* 7, 251–261.
22. Flynn, C.E., Lee, S.W., Peelle, B.R., and Belcher, A.M. (2003). Viruses as vehicles for growth, organization and assembly of materials. *Acta Mater.* 51, 5867–5880.
23. Chung, W.-J., Merzlyak, A., and Lee, S.-W. (2010). Fabrication of engineered M13 bacteriophages into liquid crystalline films and fibers for directional growth and encapsulation of fibroblasts. *Soft Matter* 6, 4454.
24. S.D.Branston (2009). M13 and the implications for its' large -scale bio-processing. Available at: discovery.ucl.ac.uk/19306/1/19306.pdf.
25. Douglas, S.M., Dietz, H., Liedl, T., Högberg, B., Graf, F., and Shih, W.M. (2009). Self-assembly of DNA into nanoscale three-dimensional shapes. *Nature* 459, 414.
26. Seeman, N.C., and Lukeman, P.S. (2004). Nucleic acid nanostructures: bottom-up control of geometry on the nanoscale. *Reports Prog. Phys.* 68, 237–270.
27. Wang, D., Capehart, S.L., Pal, S., Liu, M., Zhang, L., Schuck, P.J., Liu, Y., Yan, H., Francis, M.B., and De Yoreo, J.J. (2014). Hierarchical assembly of plasmonic nanostructures using virus capsid scaffolds on DNA origami templates. *ACS Nano* 8, 7896–7904.
28. Liu, M., Amro, N.A., Chow, C.S., and Liu, G.Y. (2002). Production of Nanostructures of DNA on Surfaces. *Nano Lett.* 2, 863–867.
29. Giakos, G.C. (2007). Novel Biomolecular NanoPhotonic Devices , Sensors , Photonic Nanocrystals and Biochips : Advances in Medical Diagnostics , Environmental and Defense. 1–6.

30. Chung, W.-J., Oh, J.-W., Kwak, K., Lee, B.Y., Meyer, J., Wang, E., Hexemer, A., and Lee, S.-W. (2011). Biomimetic self-templating supramolecular structures. *Nature* 478, 364–368.
31. G.Lamas (1962). *Morpho menelaus didius*. Available at: http://www.butterfliesofamerica.com/L/ih/morpho0973_i.htm [Accessed October 4, 2019].
32. Gaillot, D.P., Deparis, O., Welch, V., Wagner, B.K., Vigneron, J.P., and Summers, C.J. (2008). Composite organic-inorganic butterfly scales: Production of photonic structures with atomic layer deposition. *Phys. Rev. E - Stat. Nonlinear, Soft Matter Phys.* 78, 1–6.
33. Turner, M.D., Schröder-Turk, G.E., and Gu, M. (2011). Fabrication and characterization of three-dimensional biomimetic chiral composites. *Opt. Express* 19, 10001.
34. Pris, A.D., Utturkar, Y., Surman, C., Morris, W.G., Vert, A., Zalyubovskiy, S., Deng, T., Ghiradella, H.T., and Potyrailo, R. a. (2012). Towards high-speed imaging of infrared photons with bio-inspired nanoarchitectures. *Nat. Photonics* 6, 564–564.
35. Purdy, K.R., and Fraden, S. (2004). Isotropic-cholesteric phase transition of filamentous virus suspensions as a function of rod length and charge. *Phys. Rev. E - Stat. Nonlinear, Soft Matter Phys.* 70, 1–8.
36. Dogic, Z., and Fraden, S. (2000). Cholesteric phase in virus suspensions. *Langmuir* 16, 7820–7824.
37. Wolkers, W.F., Haris, P.I., Pistorius, A.M.A., Chapman, D., and Hemminga, M.A. (1995). Ft-Ir Spectroscopy of the Major Coat Protein of M13 and Pf1 in the Phage and Reconstituted into Phospholipid Systems. *Biochemistry* 34, 7825–7833.
38. Li, B., Han, W., Byun, M., Zhu, L., Zou, Q., and Lin, Z. (2013). Macroscopic highly aligned DNA nanowires created by controlled evaporative self-assembly. *ACS Nano* 7, 4326–4333.
39. Kwon, S.W., Byun, M., Yoon, D.H., Park, J.-H., Kim, W.-K., Lin, Z., and

- Yang, W.S. (2011). Simple route to ridge optical waveguide fabricated via controlled evaporative self-assembly. *J. Mater. Chem.* *21*, 5230–5233.
40. Zhang, S. (2003). Fabrication of novel biomaterials through molecular self-assembly. *Nat. Biotechnol.* *21*, 1171–1178.
 41. Wink, T., van Zuilen, S.J., Bult, A., and van Benkom, W.P. (1997). Self-assembled monolayers for biosensors. *Analyst* *122*, 43R-50R.
 42. Schweikart, A., Horn, A., Böker, A., and Fery, A. (2010). Controlled wrinkling as a novel method for the fabrication of patterned surfaces. *Adv. Polym. Sci.* *227*, 75–99.
 43. Hyun, D.C., Park, M., and Jeong, U. (2016). Micropatterning by controlled liquid instabilities and its applications. *J. Mater. Chem. C* *4*, 10411–10429.
 44. Courchesne, N.M.D., Klug, M.T., Chen, P.Y., Kooi, S.E., Yun, D.S., Hong, N., Fang, N.X., Belcher, A.M., and Hammond, P.T. (2014). Assembly of a bacteriophage-based template for the organization of materials into nanoporous networks. *Adv. Mater.* *26*, 3398–3404.
 45. Scibilia, S., Lentini, G., Fazio, E., Franco, D., Neri, F., Mezzasalma, A.M., and Guglielmino, S.P.P. (2016). Self-assembly of silver nanoparticles and bacteriophage. *Sens. Bio-Sensing Res.* *7*, 146–152.
 46. Avery, K.N., Schaak, J.E., and Schaak, R.E. (2009). M13 Bacteriophage as a biological scaffold for magnetically-recoverable metal nanowire catalysts: Combining specific and nonspecific interactions to design multifunctional nanocomposites. *Chem. Mater.* *21*, 2176–2178.
 47. Liu, J., and Lu, Y. (2003). A colorimetric lead biosensor using DNAzyme-directed assembly of gold nanoparticles. *J. Am. Chem. Soc.* *125*, 6642–6643.
 48. Sharma, J., Chhabra, R., Andersen, C.S., Gothelf, K. V., Yan, H., and Liu, Y. (2008). Toward reliable gold nanoparticle patterning on self-assembled DNA nanoscaffold. *J. Am. Chem. Soc.* *130*, 7820–7821.

49. Jin, Z., Sun, W., Ke, Y., Shih, C.-J., Paulus, G.L.C., Hua Wang, Q., Mu, B., Yin, P., and Strano, M.S. (2013). Metallized DNA nanolithography for encoding and transferring spatial information for graphene patterning. *Nat. Commun.* *4*, 1663.
50. Nam, Y.S., Magyar, A.P., Lee, D., Kim, J.-W., Yun, D.S., Park, H., Pollom, T.S., Weitz, D. a, and Belcher, A.M. (2010). Biologically templated photocatalytic nanostructures for sustained light-driven water oxidation. *Nat. Nanotechnol.* *5*, 340–344.
51. Koch, S., Wolf, H., Danapel, C., and Feller, K.A. (2000). Optical flow-cell multichannel immunosensor for the detection of biological warfare agents. *Biosens. Bioelectron.* *14*, 779–784.
52. Bardhan, N.M., Ghosh, D., and Belcher, A.M. (2014). M13 Virus based detection of bacterial infections in living hosts. *J. Biophotonics* *7*, 617–623.
53. Nam, K.T., Wartena, R., Yoo, P.J., Liao, F.W., Lee, Y.J., Chiang, Y.-M., Hammond, P.T., and Belcher, A.M. (2008). Stamped microbattery electrodes based on self-assembled M13 viruses. *Proc. Natl. Acad. Sci. U. S. A.* *105*, 17227–31.
54. Soler-Illia, G.J.D.A.A., Sanchez, C., Lebeau, B., and Patarin, J. (2002). Chemical strategies to design textured materials: From microporous and mesoporous oxides to nanonetworks and hierarchical structures. *Chem. Rev.* *102*, 4093–4138.
55. Mills, A., Burns, L., O'Rourke, C., and Madsen, H. (2016). Rapid, simple method for determining the porosity of mesoporous TiO₂ films using a quartz crystal microbalance (QCM). *Sol. Energy Mater. Sol. Cells* *144*, 78–83.
56. Khoo, I.C. (2009). Nonlinear optics of liquid crystalline materials. *Phys. Rep.* *471*, 221–267.
57. Sun, C.Q. (2007). Size dependence of nanostructures: Impact of bond order deficiency. *Prog. Solid State Chem.* *35*, 1–159.
58. Storm, A.J., Chen, J.H., Ling, X.S., Zandbergen, H.W., and Dekker, C.

- (2003). Fabrication of solid-state nanopores with single-nanometre precision. *Nat. Mater.* 2, 537–540.
59. Oskam, G., Long, J.G., Natarajan, a, and Searson, P.C. (1999). Electrochemical deposition of metals onto silicon. *J. Phys. D. Appl. Phys.* 31, 1927–1949.
 60. P??rez-Juste, J., Liz-Marz??n, L.M., Carnie, S., Chan, D.Y.C., and Mulvaney, P. (2004). Electric-field-directed growth of gold nanorods in aqueous surfactant solutions. *Adv. Funct. Mater.* 14, 571–579.
 61. Chen, P.-Y., Dang, X., Klug, M.T., Courchesne, N.-M.D., Qi, J., Hyder, M.N., Belcher, A.M., and Hammond, P.T. (2015). M13 Virus-Enabled Synthesis of Titanium Dioxide Nanowires for Tunable Mesoporous Semiconducting Networks. *Chem. Mater.* 27, 1531–1540.
 62. Nanoparticles, D.A., Li, Z., Chung, S., Nam, J., Ginger, D.S., and Mirkin, C.A. (2003). Living Template for the Hierarchical Assembly of Gold Nanoparticles. *Angew. Chem. Int. Ed. Engl.* 115, 2408–2411.
 63. Mooney, J.M. (1988). Infrared optical absorption of thin PtSi films between 1 and 6 μm . *J. Appl. Phys.* 64, 4664–4667.
 64. Pieranski, P.O. and P. (2005). *Nematic and Cholesteric Liquid Crystals* (CRC Press).
 65. Fraden, S. (1995). Phase Transitions in Colloidal Suspensions of Virus Particles. *Obs. Predict. Simul. Phase Transitions Complex Fluids* 460, 113–164.
 66. Fang, A., Koschny, T., and Soukoulis, C.M. (2009). Optical anisotropic metamaterials: Negative refraction and focusing. *Phys. Rev. B - Condens. Matter Mater. Phys.* 79, 1–7.
 67. Stebe, K.J., Lewandowski, E.P., and Ghosh, M. (2009). Oriented assembly of metamaterials. *Science* (80-.). 325, 159–160.
 68. Weillie Zhou, Z.L.W. (2011). *Three-Dimensional Nanoarchitectures* (Springer New York).

69. Jorgensen, M.R., and Bartl, M.H. (2011). Biotemplating routes to three-dimensional photonic crystals. *J. Mater. Chem.* *21*, 10583.
70. Charlton, M.D.B., Roberts, S.W., and Parker, G.J. (1997). Guided mode analysis, and fabrication of a 2-dimensional visible photonic band structure confined within a planar semiconductor waveguide. *Mater. Sci. Eng. B* *49*, 155–165.
71. Huang, L., Chen, X., Mühlenbernd, H., Li, G., Bai, B., Tan, Q., Jin, G., Zentgraf, T., and Zhang, S. (2012). Dispersionless phase discontinuities for controlling light propagation. *Nano Lett.* *12*, 5750–5755.
72. Yu, N., Genevet, P., Kats, M. a, Aieta, F., Tetienne, J.-P., Capasso, F., and Gaburro, Z. (2011). Light Propagation with Phase Discontinuities Reflection and Refraction. *Science* (80-.). *334*, 333–337.
73. Wang, W., Zhang, W., Fang, X., Huang, Y., Liu, Q., Gu, J., and Zhang, D. (2014). Demonstration of higher colour response with ambient refractive index in *Papilio blumei* as compared to *Morpho rhetenor*. *Sci. Rep.* *4*, 1–8.
74. Bilotti, F., Tricarico, S., and Vegni, L. (2010). Plasmonic metamaterial cloaking at optical frequencies. *IEEE Trans. Nanotechnol.* *9*, 55–61.
75. Schurig, D., Mock, J.J., Justice, B.J., Cummer, S. a, Pendry, J.B., Starr, a F., and Smith, D.R. (2006). Metamaterial electromagnetic cloak at microwave frequencies. *Science* (80-.). *314*, 977–980.
76. Zhang, Y., and Mascarenhas, A. (2007). Negative Refraction of Electromagnetic and Electronic Waves in Uniform Media BT - Physics of Negative Refraction and Negative Index Materials: Optical and Electronic Aspects and Diversified Approaches. In, C. M. Krowne and Y. Zhang, eds. (Berlin, Heidelberg: Springer Berlin Heidelberg), pp. 1–18.
77. Al??, A., and Engheta, N. (2008). Multifrequency optical invisibility cloak with layered plasmonic shells. *Phys. Rev. Lett.* *100*, 1–4.
78. Schittny, R., Niemeyer, A., Mayer, F., Naber, A., Kadic, M., and Wegener, M. (2016). Invisibility cloaking in light-scattering media. *Laser Photonics Rev.* *10*, 382–408.

79. Gordon, P.G. (2013). Thin Film Precursors, Properties and Applications: Chemical Vapour Deposition and Atomic Layer Deposition of Group 4, 11 and 13 Elements and Their Oxides. 1–173.
80. Wang, W., Zhang, W., Fang, X., Huang, Y., Liu, Q., Gu, J., and Zhang, D. (2014). Demonstration of higher colour response with ambient refractive index in *Papilio blumei* as compared to *Morpho rhetenor*. *Sci. Rep.* 4, 5591.
81. Saba, M., Thiel, M., Turner, M.D., Hyde, S.T., Gu, M., Grosse-Brauckmann, K., Neshev, D.N., Mecke, K., and Schröder-Turk, G.E. (2011). Circular dichroism in biological photonic crystals and cubic chiral nets. *Phys. Rev. Lett.* 106, 1–4.
82. Chen, S., Zeuner, F., Weismann, M., Reineke, B., Li, G., Valev, V.K., Cheah, K.W., Panoiu, N.C., Zentgraf, T., and Zhang, S. (2016). Giant Nonlinear Optical Activity of Achiral Origin in Planar Metasurfaces with Quadratic and Cubic Nonlinearities. *Adv. Mater.* 28, 2992–2999.
83. Chen, S., Zeuner, F., Weismann, M., Reineke, B., Li, G., Valev, V.K., Cheah, K.W., Panoiu, N.C., Zentgraf, T., Zhang, S., *et al.* (2012). Visible transmission response of nanoscale complementary metamaterials for sensing applications. *Biochemistry* 6, 171–90.
84. Wang, P., Yu, S.-J., Govorov, A.O., and Ouyang, M. (2017). Cooperative expression of atomic chirality in inorganic nanostructures. *Nat. Commun.* 8, 14312.
85. Pile, D. (2009). Metamaterials: Chirality-assisted negative index. *Nat. Photonics* 3, 133.
86. Bustamante, C., Bryant, Z., and Smith, S.B. (2003). Ten years of tension: single-molecule DNA mechanics. *Nature* 421, 423–427.
87. Hoffman, A.J., Sridhar, A., Braun, P.X., Alekseyev, L., Howard, S.S., Franz, K.J., Cheng, L., Choa, F. Sen, Sivco, D.L., Podolskiy, V.A., *et al.* (2009). Midinfrared semiconductor optical metamaterials. *J. Appl. Phys.* 105, 1–7.
88. Liu, N., Fu, L.W., Guo, H.C., Kaiser, S., Schweizer, H., and Giessen, H. (2008). Three-dimensional metamaterials at optical frequencies. *Conf.*

89. Zajíček, R., Oppl, L., and Vrba, J. (2008). Broadband measurement of complex permittivity using reflection method and coaxial probes. *Radioengineering* 17, 14–19.
90. Zhang, S., Park, Y., Li, J., Lu, X., Zhang, W., Zhang, X., Genov, D.A., Wang, Y., Liu, M., Zhang, X., *et al.* (2006). Demonstration of metal-dielectric negative-index metamaterials with improved performance at optical frequencies. *Phys. Rev. Lett.* 23, 1–4.
91. Zhang, S., Park, Y., Li, J., Lu, X., Zhang, W., and Zhang, X. (2009). Negative Refractive Index in Chiral Metamaterials. *023901*, 1–4.
92. Liu, N., Guo, H., Fu, L., Kaiser, S., Schweizer, H., and Giessen, H. (2008). Three-dimensional photonic metamaterials at optical frequencies. *Nat. Mater.* 7, 31–37.
93. Gartstein, V.M.A. and Y.N. (2006). Spatial dispersion and negative refraction of light. *Physics-Uspekhi* 49, 1029.
94. Withayachumnankul, W., and Abbott, D. (2009). Metamaterials in the terahertz regime. *IEEE Photonics J.* 1, 99–118.
95. Zhang, S., Fan, W., Panoiu, N.C., Malloy, K.J., Osgood, R.M., and Brueck, S.R. (2006). Optical negative-index bulk metamaterials consisting of 2D perforated metal-dielectric stacks. *Opt. Express* 14, 6778–6787.
96. Hatakeyama, Y., Morita, T., Takahashi, S., Onishi, K., and Nishikawa, K. (2011). Synthesis of Gold Nanoparticles in Liquid Polyethylene Glycol by Sputter Deposition and Temperature Effects on their Size and Shape. *J. Phys. Chem. C* 115, 3279–3285.
97. Tomley, F.M. (1996). M13 Phage Growth and Single-Stranded DNA Preparation. In *Basic DNA and RNA Protocols*, A. J. Harwood, ed. (Totowa, NJ: Humana Press), pp. 359–362.
98. Cárdenas, M., Barauskas, J., Schullén, K., Brennan, J.L., Brust, M., and Nylander, T. (2006). Thiol-specific and nonspecific interactions between

DNA and gold nanoparticles. *Langmuir* 22, 3294–3299.

99. Seibel, E.M., Schoop, L.M., Xie, W., Gibson, Q.D., Webb, J.B., Fuccillo, M.K., Krizan, J.W., and Cava, R.J. (2015). Gold-gold bonding: The key to stabilizing the 19-electron ternary phases LnAuSb ($\text{Ln} = \text{La-Nd}$ and Sm). *J. Am. Chem. Soc.* 137, 1282–1289.
100. Nayfeh, M.H., and Mitas, L. (2008). CHAPTER ONE - SILICON NANOPARTICLES: NEW PHOTONIC AND ELECTRONIC MATERIAL AT THE TRANSITION BETWEEN SOLID AND MOLECULE. In, V. B. T.-N. Kumar, ed. (Amsterdam: Elsevier), pp. 1–78.
101. Ye, J.Y., Umemura, K., Ishikawa, M., and Kuroda, R. (2000). Atomic Force Microscopy of DNA Molecules Stretched by Spin-Coating Technique. *Anal. Biochem.* 281, 21–25.
102. Merzlyak, A., Indrakanti, S., Lee, S., Di, V., Berkeley, L., and Nanoscience, B. (2009). Genetically Engineered Nanofiber-Like Viruses For Tissue Regenerating Materials 2009.
103. Huang, L., Wind, S.J., and O'Brien, S.P. (2003). Controlled Growth of Single-Walled Carbon Nanotubes from an Ordered Mesoporous Silica Template. *Nano Lett.* 3, 299–303.
104. Huang, Y., Duan, X., Wei, Q., and Lieber, C.M. (2001). Directed Assembly of One-Dimensional Nanostructures into Functional Networks. *Science* (80-.). 291, 630 LP – 633.
105. Lay, M.D., Novak, J.P., and Snow, E.S. (2004). Simple Route to Large-Scale Ordered Arrays of Liquid-Deposited Carbon Nanotubes. *Nano Lett.* 4, 603–606.
106. Pretzl, M., Schweikart, A., Hanske, C., Chiche, A., Zettl, U., Horn, A., Böker, A., and Fery, A. (2008). A lithography-free pathway for chemical microstructuring of macromolecules from aqueous solution based on wrinkling. *Langmuir* 24, 12748–12753.
107. Huck, W.T.S., Bowden, N., Onck, P., Pardoën, T., Hutchinson, J.W., and Whitesides, G.M. (2000). Ordering of spontaneously formed buckles on

planar surfaces. *Langmuir* *16*, 3497–3501.

108. Merzlyak, A., Indrakanti, S., and Lee, S.W. (2009). Genetically engineered nanofiber-like viruses for tissue regenerating materials. *Nano Lett.* *9*, 846–852.
109. Alberts, E., Warner, C., Barnes, E., Pilkievicz, K., Perkins, E., and Poda, A. (2018). Genetically tunable M13 phage films utilizing evaporating droplets. *Colloids Surfaces B Biointerfaces* *161*, 210–218.
110. Shahidzadeh, N., Schut, M.F.L., Desarnaud, J., Prat, M., and Bonn, D. (2015). Salt stains from evaporating droplets. *Sci. Rep.* *5*, 10335.
111. Tarasevich, Y.Y., Vodolazskaya, I. V, and Bondarenko, O.P. (2013). Modeling of spatial–temporal distribution of the components in the drying sessile droplet of biological fluid. *Colloids Surfaces A Physicochem. Eng. Asp.* *432*, 99–103.
112. Nguyen, T.A.H., Hampton, M.A., and Nguyen, A. V (2013). Evaporation of Nanoparticle Droplets on Smooth Hydrophobic Surfaces: The Inner Coffee Ring Deposits. *J. Phys. Chem. C* *117*, 4707–4716.
113. Wender, H., de Oliveira, L.F., Feil, A.F., Lissner, E., Migowski, P., Meneghetti, M.R., Teixeira, S.R., and Dupont, J. (2010). Synthesis of gold nanoparticles in a biocompatible fluid from sputtering deposition onto castor oil. *Chem. Commun.* *46*, 7019–7021.
114. Kahraman, M., Zamaleeva, A.I., Fakhrullin, R.F., and Culha, M. (2009). Layer-by-layer coating of bacteria with noble metal nanoparticles for surface-enhanced Raman scattering. *Anal. Bioanal. Chem.* *395*, 2559.
115. Lee, J.H., Kang, W.S., Choi, B.S., Choi, S.W., and Kim, J.H. (2008). Fabrication of carbon nanotube AFM probes using the Langmuir-Blodgett technique. *Ultramicroscopy* *108*, 1163–1167.
116. Byun, M., Laskowski, R.L., He, M., Qiu, F., Jeffries-El, M., and Lin, Z. (2009). Controlled evaporative self-assembly of hierarchically structured regioregular conjugated polymers. *Soft Matter* *5*, 1583–1586.

117. Joo, Y., Brady, G.J., Arnold, M.S., and Gopalan, P. (2014). Dose-Controlled, Floating Evaporative Self-assembly and Alignment of Semiconducting Carbon Nanotubes from Organic Solvents. *Langmuir* 30, 3460–3466.
118. Wang, M., Zhao, X., Ohkohchi, M., and Ando, Y. (1996). Carbon Nanotubes Grown on the Surface of Cathode Deposit by Arc Discharge. *Fuller. Sci. Technol.* 4, 1027–1039.
119. Vignolini, S., Yufa, N.A., Cunha, P.S., Guldin, S., Rushkin, I., Stefik, M., Hur, K., Wiesner, U., Baumberg, J.J., and Steiner, U. (2012). A 3D optical metamaterial made by self-assembly. *Adv. Mater.* 24, 23–27.
120. Oh, J.-W., Chung, W.-J., Heo, K., Jin, H.-E., Lee, B.Y., Wang, E., Zueger, C., Wong, W., Meyer, J., Kim, C., *et al.* (2014). Biomimetic virus-based colourimetric sensors. *Nat. Commun.* 5, 3043.
121. Persson, B.N.J., and Volokitin, A.I. (2006). Rubber friction on smooth surfaces. *Eur. Phys. J. E* 21, 69–80.
122. Russell, P; Batchelor, D. (2001). SEM and AFM: Complementary Techniques for Surface Investigations. *Microsc. Anal.*
123. Lenhert, S., Gleiche, M., Fuchs, H., and Chi, L. (2005). Mechanism of regular pattern formation in reactive dewetting. *ChemPhysChem* 6, 2495–2498.
124. The wear of metals under unlubricated conditions (1956). *Proc. R. Soc. London. Ser. A. Math. Phys. Sci.* 236, 397 LP – 410.
125. Lim, S.C., and Ashby, M.F. (1987). Overview no. 55 Wear-Mechanism maps. *Acta Metall.* 35, 1–24.
126. Joseph, G. (2007). The discovery of biological enantioselectivity: Louis Pasteur and the fermentation of tartaric acid, 1857—A review and analysis 150 yr later. *Chirality* 20, 5–19.
127. Tang, Y., and Cohen, A.E. (2010). Optical Chirality and Its Interaction with Matter. *Phys. Rev. Lett.* 104, 163901.

128. Ben-Moshe, A., Maoz, B.M., Govorov, A.O., and Markovich, G. (2013). Chirality and chiroptical effects in inorganic nanocrystal systems with plasmon and exciton resonances. *Chem. Soc. Rev.* **42**, 7028–7041.
129. Wiltshire, M.C.K., Pendry, J.B., and Hajnal, J. V. (2009). Chiral Swiss rolls show a negative refractive index. *J. Phys. Condens. Matter* **21**.
130. Li, Z., Alici, K.B., Caglayan, H., Kafesaki, M., Soukoulis, C.M., and Ozbay, E. (2012). Composite chiral metamaterials with negative refractive index and high values of the figure of merit. *Opt. Express* **20**, 6146–6156.
131. Cornelissen, J.J.L.M., Rowan, A.E., Nolte, R.J.M., and Sommerdijk, N.A.J.M. (2001). Chiral Architectures from Macromolecular Building Blocks. *Chem. Rev.* **101**, 4039–4070.
132. Oda, R., Huc, I., Schmutz, M., Candau, S.J., and MacKintosh, F.C. (1999). Tuning bilayer twist using chiral counterions. *Nature* **399**, 566.
133. Belardini, A., Centini, M., Leahu, G., Hooper, D.C., Li Voti, R., Fazio, E., Haus, J.W., Sarangan, A., Valev, V.K., and Sibilia, C. (2016). Chiral light intrinsically couples to extrinsic/pseudo-chiral metasurfaces made of tilted gold nanowires. *Sci. Rep.* **6**, 1–9.
134. Shemer, G., Krichevski, O., Markovich, G., Molotsky, T., Lubitz, I., and Kotlyar, A.B. (2006). Chirality of silver nanoparticles synthesized on DNA. *J. Am. Chem. Soc.* **128**, 11006–11007.
135. Zhao, W. (2012). Helical Ordering in Chiral Block Copolymers.
136. Worley, C.G., Linton, R.W., Samulski, E.T., Hill, C., and Carolina, N. (1995). Electric-Field-Enhanced Self-Assembly of α -Helical Polypeptides. 3805–3810.
137. Hentschel, M., Wu, L., Schäferling, M., Bai, P., Li, E.P., and Giessen, H. (2012). Optical properties of chiral three-dimensional plasmonic oligomers at the onset of charge-transfer plasmons. *ACS Nano* **6**, 10355–10365.
138. Ladik, A. V., Geiger, F.M., and Walter, S.R. (2010). Immobilization of DNA onto Gold and Dehybridization of Surface-Bound DNA on Glass.

Nanoscape 7, 19–23.

139. Kuzyk, A., Liedl, T., Schreiber, R., Fan, Z., Pardatscher, G., Roller, E.-M., Högele, A., Simmel, F.C., and Govorov, A.O. (2012). DNA-based self-assembly of chiral plasmonic nanostructures with tailored optical response. *Nature* 483, 311–314.
140. Conde, J., Dias, J.T., Grazú, V., Moros, M., Baptista, P. V, and de la Fuente, J.M. (2014). Revisiting 30 years of biofunctionalization and surface chemistry of inorganic nanoparticles for nanomedicine. *Front. Chem.* 2, 48.
141. Pedersen D.B., D.E.J.. (2005). Surface Plasmon Resonance Spectroscopy of Gold Nanoparticle- Coated Substrates. *Surf. Plasmon Reson. Spectrosc. Gold Nanoparticle- Coat. Substrates*, 1–3.
142. Niikura, K., Nagakawa, K., Ohtake, N., Suzuki, T., Matsuo, Y., Sawa, H., and Ijro, K. (2009). Gold nanoparticle arrangement on viral particles through carbohydrate recognition: A non-cross-linking approach to optical virus detection. *Bioconjug. Chem.* 20, 1848–1852.
143. Schattschneider, P., Rubino, S., and Hébert, C. (2007). Circular Dichroism in the Transmission Electron Microscope. *Encycl. Mater. Sci. Technol.*, 1–11.
144. Wang, H., Li, Z., Zhang, H., Wang, P., and Wen, S. (2015). Giant local circular dichroism within an asymmetric plasmonic nanoparticle trimer. *Sci. Rep.* 5, 8207.
145. Wakabayashi, M., Yokojima, S., Fukaminato, T., Shiino, K., Irie, M., and Nakamura, S. (2014). Anisotropic Dissymmetry Factor, g : Theoretical Investigation on Single Molecule Chiroptical Spectroscopy. *J. Phys. Chem. A* 118, 5046–5057.
146. A.Schuster (1909). *An Introduction to the Theory of Optics* (Provided by the SAO/NASA Astrophysics Data System).
147. Li, J., and Chan, C.T. (2004). Double-negative acoustic metamaterial. *Phys. Rev. E - Stat. Physics, Plasmas, Fluids, Relat. Interdiscip. Top.* 70, 4.

148. Aieta, F., Genevet, P., Yu, N., Kats, M.A., Gaburro, Z., and Capasso, F. (2012). Out-of-plane reflection and refraction of light by anisotropic optical antenna metasurfaces with phase discontinuities. *Nano Lett.* *12*, 1702–1706.
149. Huang, L., Chen, X., Mühlenbernd, H., Zhang, H., Chen, S., Bai, B., Tan, Q., Jin, G., Cheah, K.-W., Qiu, C.-W., *et al.* (2013). Three-dimensional optical holography using a plasmonic metasurface. *Nat. Commun.* *4*, 2808.
150. Moses, A.J., and Command, I. (1970). Refractive index of optical materials in the infrared region. *Electron. Properties Inf. Cent.*, 250.
151. Blaik, R.A., Lan, E., Huang, Y., and Dunn, B. (2016). Gold-Coated M13 Bacteriophage as a Template for Glucose Oxidase Biofuel Cells with Direct Electron Transfer. *ACS Nano* *10*, 324–332.
152. Suthiwangcharoen, N., Li, T., Li, K., Thompson, P., You, S., and Wang, Q. (2011). M13 bacteriophage-polymer nanoassemblies as drug delivery vehicles. *Nano Res.* *4*, 483–493.
153. Zan, X., Feng, S., Balizan, E., Lin, Y., and Wang, Q. (2013). Facile method for large scale alignment of one dimensional nanoparticles and control over myoblast orientation and differentiation. *ACS Nano* *7*, 8385–8396.
154. Guan, J., Jiang, L., Zhao, L., Li, J., and Yang, W. (2008). pH-dependent response of citrate capped Au nanoparticle to Pb²⁺ ion. *Colloids Surfaces A Physicochem. Eng. Asp.* *325*, 194–197.
155. Yoosaf, K., Ipe, B.I., Suresh, C.H., and Thomas, K.G. (2007). In Situ Synthesis of Metal Nanoparticles and Selective Naked-Eye Detection of Lead Ions from Aqueous Media. *J. Phys. Chem. C* *111*, 12839–12847.
156. Goyer, R.A. (1990). Lead toxicity: from overt to subclinical to subtle health effects. *Environ. Health Perspect.* *86*, 177–181.
157. Carocci A., Catalano A., Lauria G., Sinicropi M.S., G.G. (2016). Lead Toxicity, Antioxidant Defense and Environment. (Reviews of Environmental Contamination and Toxicology).

158. Chansuvarn, W., and Imyim, A. (2012). Visual and colorimetric detection of mercury(II) ion using gold nanoparticles stabilized with a dithia-diaza ligand. *Microchim. Acta* 176, 57–64.
159. Dankovich, T.A., and Gray, D.G. (2011). Bactericidal paper impregnated with silver nanoparticles for emergency water disinfection. *COLLSYMP*-513.
160. Liu, B., Xu, H., Zhao, H., Liu, W., Zhao, L., and Li, Y. (2017). Preparation and characterization of intelligent starch/PVA films for simultaneous colorimetric indication and antimicrobial activity for food packaging applications. *Carbohydr. Polym.* 157, 842–849.
161. COHEN, S.L. (1966). A Method for the Rapid Colorimetric Assay of Total Estrins in Pregnancy Urine¹. *J. Clin. Endocrinol. Metab.* 26, 994–1004.
162. Luckham, R.E., and Brennan, J.D. (2010). Bioactive paper dipstick sensors for acetylcholinesterase inhibitors based on sol-gel/enzyme/gold nanoparticle composites. *Analyst* 135, 2028–2035.
163. Chen, W., Fang, X., Li, H., Cao, H., and Kong, J. (2016). A Simple Paper-Based Colorimetric Device for Rapid Mercury(II) Assay. *Sci. Rep.* 6, 31948.
164. Huang, C.-C., and Chang, H.-T. (2007). Parameters for selective colorimetric sensing of mercury(ii) in aqueous solutions using mercaptopropionic acid-modified gold nanoparticles. *Chem. Commun.*, 1215–1217.
165. Bermejo-Barrera, P., Nancy, M.A., Cristina, D.L., and Adela, B.B. (2003). Use of Amberlite XAD-2 Loaded with 1-(2-Pyridylazo)-2-naphthol as a Preconcentration System for River Water Prior to Determination of Cu²⁺, Cd²⁺ and Pb²⁺ by Flame Atomic Absorption Spectroscopy. *Microchim. Acta* 142, 101–108.
166. Kim, H.N., Ren, W.X., Kim, J.S., and Yoon, J. (2012). Fluorescent and colorimetric sensors for detection of lead, cadmium, and mercury ions. *Chem. Soc. Rev.* 41, 3210–3244.
167. Chen, P., Zhang, R., Jiang, Q., Xiong, X., and Deng, S. (2015). Colorimetric

Detection of Lead Ion Based on Gold Nanoparticles and Lead-Stabilized G-Quartet Formation. *J. Biomed. Sci. Eng.* 8, 451–457.

168. Deka, J., Mojumdar, A., Parisse, P., Onesti, S., and Casalis, L. (2017). DNA-conjugated gold nanoparticles based colorimetric assay to assess helicase activity: a novel route to screen potential helicase inhibitors. *Sci. Rep.* 7, 44358.
169. Huang, C.C., and Chang, H.T. (2006). Selective gold-nanoparticle-based “turn-on” fluorescent sensors for detection of mercury(II) in aqueous solution. *Anal. Chem.* 78, 8332–8338.
170. Sun, J., Guo, L., Bao, Y., and Xie, J. (2011). A simple, label-free AuNPs-based colorimetric ultrasensitive detection of nerve agents and highly toxic organophosphate pesticide. *Biosens. Bioelectron.* 28, 152–157.
171. Li, X.X., Cao, C., Han, S.J., and Sim, S.J. (2009). Detection of pathogen based on the catalytic growth of gold nanocrystals. *Water Res.* 43, 1425–1431.
172. Li, F., Chen, H., Zhang, Y., Chen, Z., Zhang, Z.P., Zhang, X.E., and Wang, Q. (2012). Three-dimensional gold nanoparticle clusters with tunable cores templated by a viral protein scaffold. *Small* 8, 3832–3838.
173. Bastús, N.G., Comenge, J., and Puentes, V. (2011). Kinetically controlled seeded growth synthesis of citrate-stabilized gold nanoparticles of up to 200 nm: Size focusing versus ostwald ripening. *Langmuir* 27, 11098–11105.
174. Rattanata, N., Klaynongsruang, S., Leelayuwat, C., Limpai boon, T., Lulitanond, A., Boonsiri, P., Chio-Srichan, S., Soontaranon, S., Rugmai, S., and Daduang, J. (2016). Gallic acid conjugated with gold nanoparticles: Antibacterial activity and mechanism of action on foodborne pathogens. *Int. J. Nanomedicine* 11, 3347–3356.
175. A. Moreno-Álvarez, S., Martínez-Castañón, G.-A., Nino, N., F. Reyes-Macías, J., Patiño-Marín, N., Loyola-Rodriguez, J., and Ruiz, F. (2010). Preparation and bactericide activity of gallic acid stabilized gold

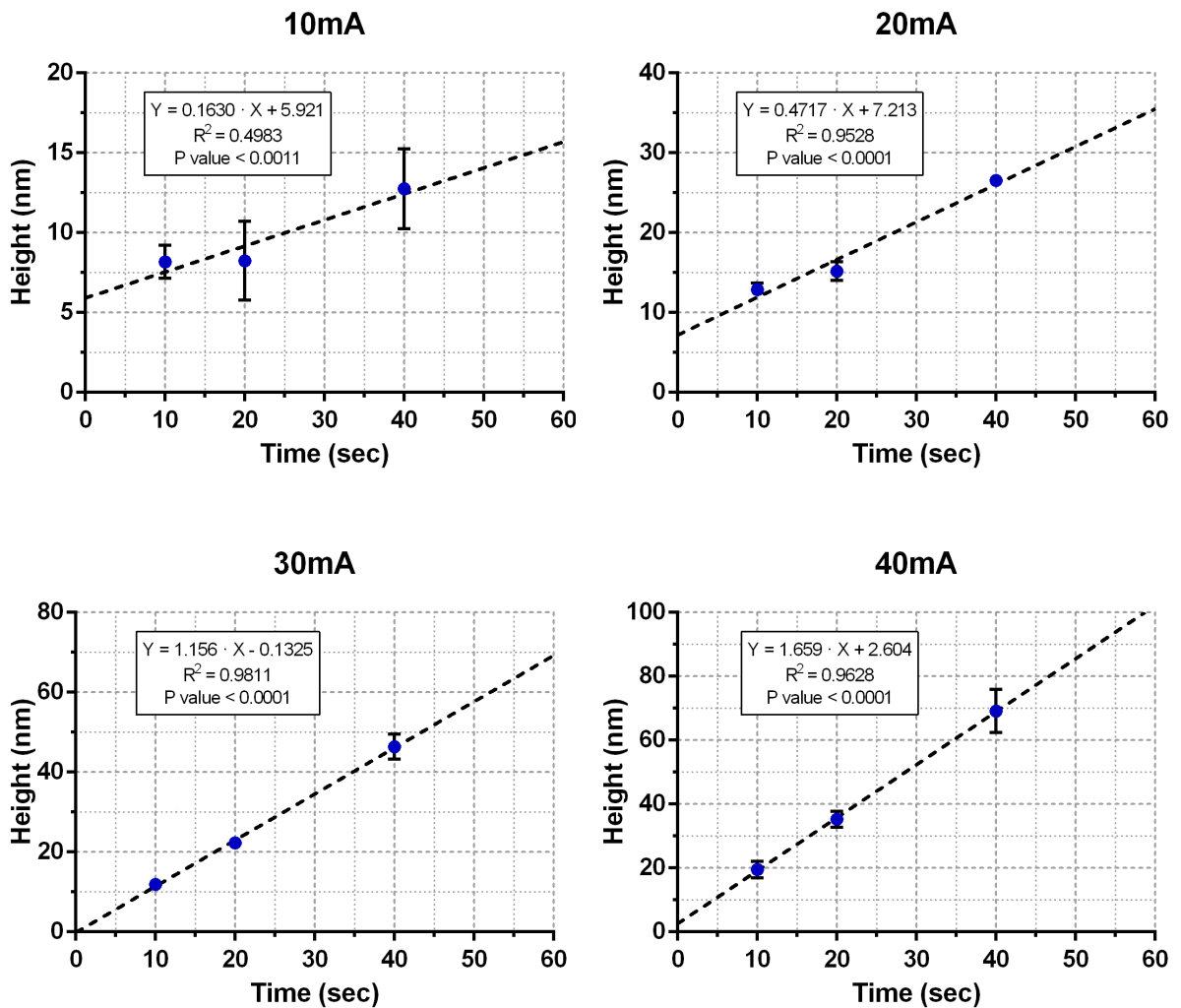
nanoparticles.

176. Last, J.A., Russell, P., Nealey, P.F., and Murphy, C.J. (2010). The applications of atomic force microscopy to vision science. *Invest. Ophthalmol. Vis. Sci.* 51, 6083–6094.
177. Humblot, V., Barlow, S.M., and Raval, R. (2004). Two-dimensional organisational chirality through supramolecular assembly of molecules at metal surfaces. *Prog. Surf. Sci.* 76, 1–19.
178. Scolaro, L.M., Castriciano, M.A., Romeo, A., Micali, N., Angelini, N., Lo Passo, C., and Felici, F. (2006). Supramolecular binding of cationic porphyrins on a filamentous bacteriophage template: Toward a noncovalent antenna system. *J. Am. Chem. Soc.* 128, 7446–7447.
179. Ma, X., Pu, M., Li, X., Guo, Y., Gao, P., and Luo, X. (2017). Meta-Chirality: Fundamentals, Construction and Applications. *Nanomaterials* 7, 116.
180. Hildreth, O.J., Fedorov, A.G., and Wong, C.P. (2012). 3D spirals with controlled chirality fabricated using metal-assisted chemical etching of silicon. *ACS Nano* 6, 10004–10012.
181. McPeak, K.M., Van Engers, C.D., Blome, M., Park, J.H., Burger, S., Gosálvez, M.A., Faridi, A., Ries, Y.R., Sahu, A., and Norris, D.J. (2014). Complex chiral colloids and surfaces via high-index off-cut silicon. *Nano Lett.* 14, 2934–2940.
182. Wang, Z., Cheng, F., Winsor, T., and Liu, Y. (2016). Optical chiral metamaterials: A review of the fundamentals, fabrication methods and applications. *Nanotechnology* 27.
183. Stephens, P.J. (1970). Theory of Magnetic Circular Dichroism. *J. Chem. Phys.* 52, 3489–3516.

APPENDICES

APPENDIX: I

Atomic Force Microscopy was carried out to determine the thickness of gold deposited using a sputter coating technique. The height-scan profiles were collated as a function of both amplitude and time.



APPENDIX:II

Calculations for withdrawal feed rate are shown here :

Step angle of stepper motor: 1.8°

$$\frac{360^\circ}{1.8^\circ} = 200 \text{ steps per rotation}$$

360° represented a $500 \mu\text{m}$ withdrawal distance, therefore a full $1000 \mu\text{m}$ withdrawal distance would be 2 full 360° rotations of the micrometer

Frequency of steps per second was inputted into the Gerbot GUI e.g.

$$1 F = \frac{1}{1} = 1 \text{ sec}$$

For a frequency of 1 F to travel $1000 \mu\text{m}$:

$$403.95 \text{ sec per mm} = 0.40395 \text{ sec per } \mu\text{m}$$

To convert to μm travelled per minute:

$$\frac{60 \text{ sec}}{0.40395 \text{ sec}} = 148.533 \mu\text{m per min}$$

Conversion table for calculated withdrawal feed rates as an F value for input into the Gerbot GUI.

Frequency (F)	Withdrawal Feed Rate ($\mu\text{m}.\text{min}^{-1}$)
1.000	148.533
0.750	111.400
0.500	74.267
0.400	59.413
0.300	44.560
0.250	37.133
0.125	18.567

APPENDIX III

Below details the code used in MATLAB to generate two-way ANOVA images used in chapter 2.

Two-way ANOVA code

```
clear
    clear all
        load AAP.mat
        AAP

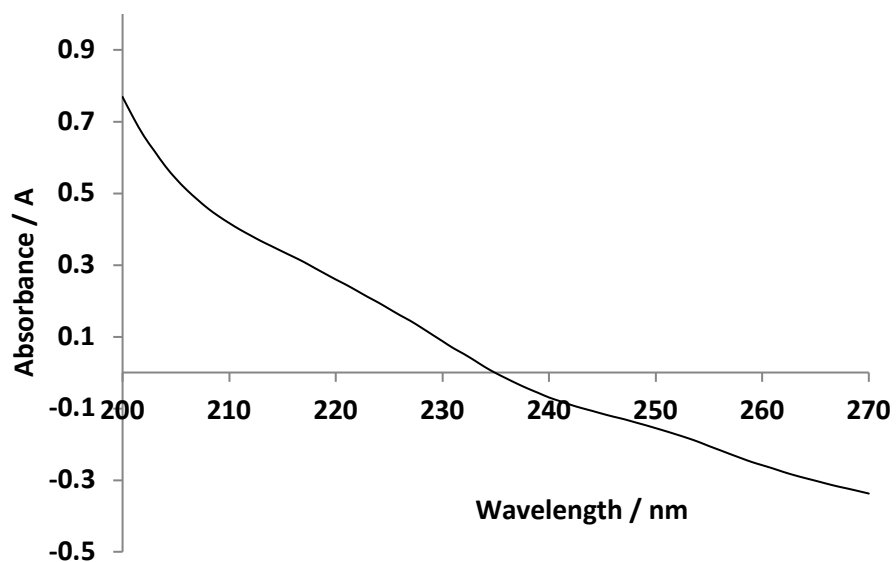
        [~,~,stats] = anova2(AAP,3,'off');
        stats

        %Next input returns stats on column
        c = multcompare(stats)

        %Next input returns stats on row
        c = multcompare(stats,'estimate','row')
end
```

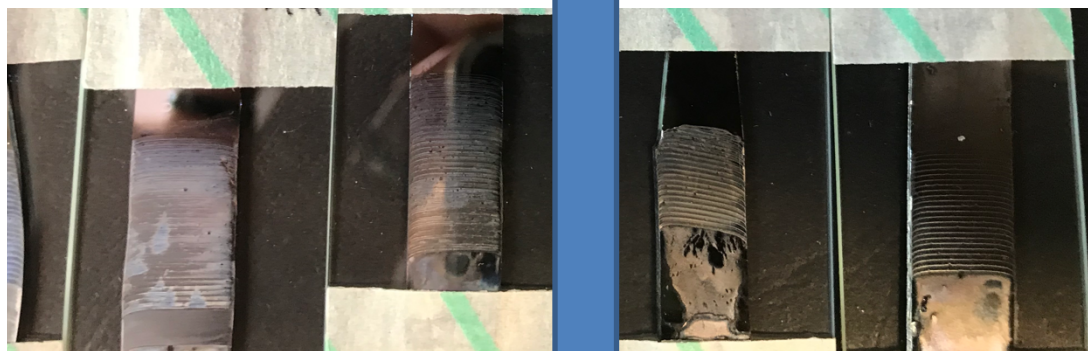

APPENDIX III

A typical absorbance spectra observed during CD analysis of an M13 phage solution is provided below.



APPENDIX: IV

Below highlights samples produced prior to and after the bunge cord system was implemented in Section 2.3.4 during the evaporative front deposition process.



Samples produced prior to the bungee cord system being developed at 3 mg.mL^{-1}

Samples produced after the bungee cord system was developed at 1 mg.mL^{-1}

APPENDIX: IV

Here, scanning electron microscope (SEM) are provided. Images were collected after evaporative front deposition (EFD) of M13 bacteriophage onto bare silicon wafers (BSi) at varying templating speeds. Increased resolution of particular areas of interest are included.

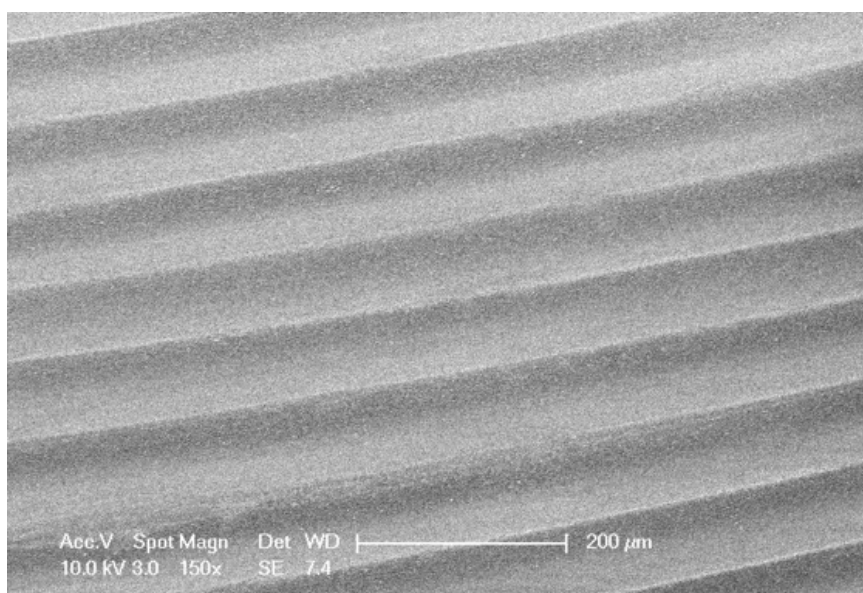


Image 1: SEM image taken at 150× magnification of M13 templated onto BSi at 96.5 $\mu\text{m}.\text{min}^{-1}$.

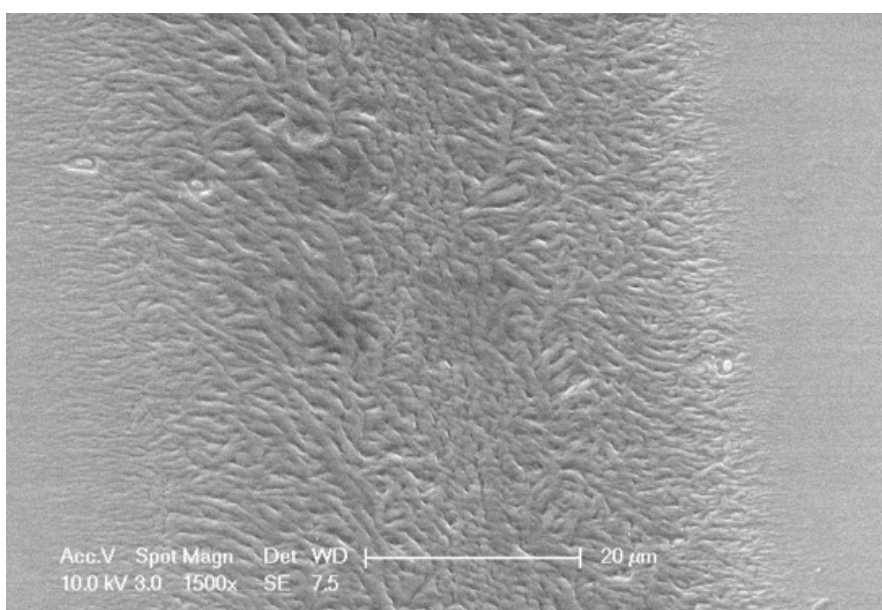


Image 2: SEM image taken at 1500 \times magnification of M13 templated onto BSi at 96.5 $\mu\text{m}.\text{min}^{-1}$, the image was taken from one of the ridges within the 1D array.

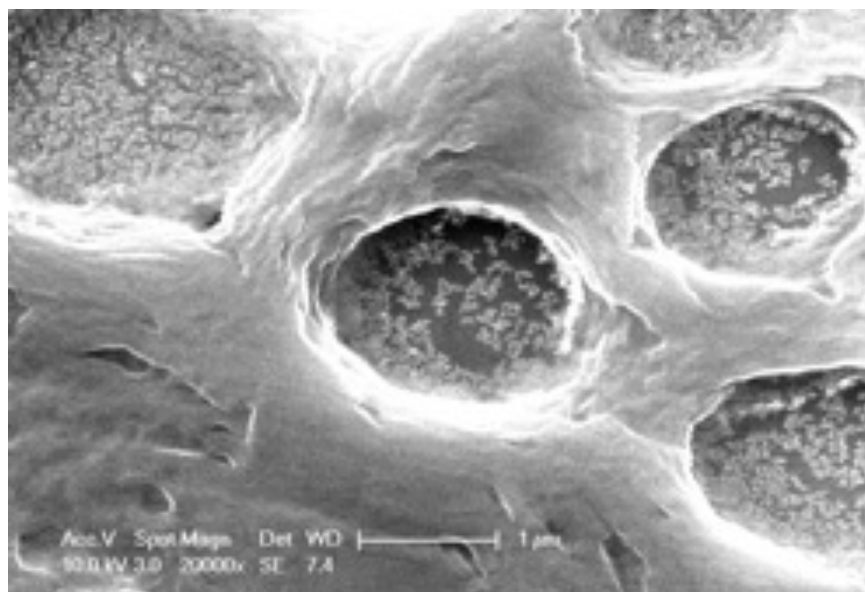


Image 3: SEM image taken at 20,000 \times magnification of M13 templated onto BSi at 96.5 $\mu\text{m}.\text{min}^{-1}$, this image highlights areas of the ridge that lacked complete bundling of M13. This produced 'holes' in the ridge evident here.

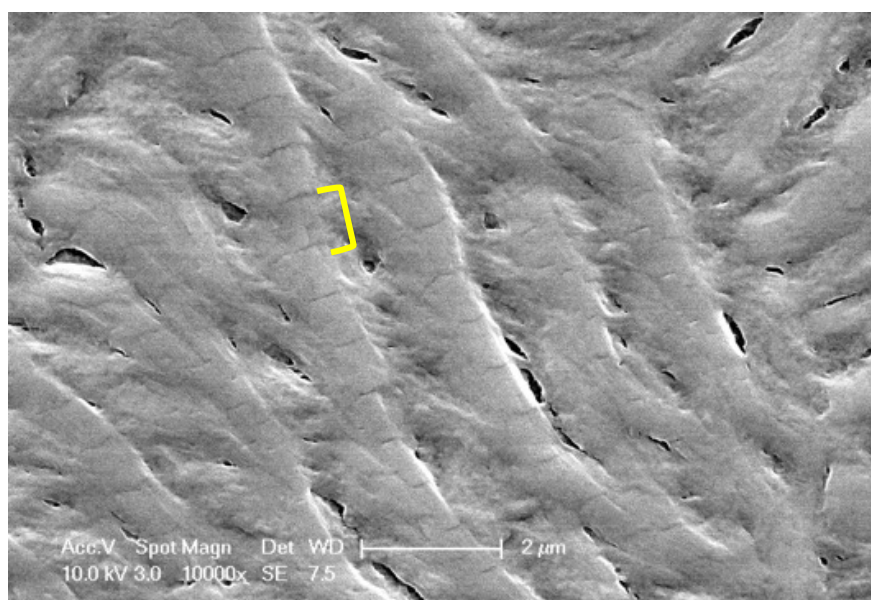


Image 4: SEM image taken at 10,000 \times magnification of M13 templated onto BSi at 96.5 $\mu\text{m}.\text{min}^{-1}$, this image was taken on the ridge. Here it is possible to see the individual bundles that bind together end to end. This is shown by the yellow

bracket on the image and is consistent with the 700 – 1000 nm length of M13 bacteriophage.

APPENDIX: VI

Below details the code used in MATLAB to generate the mesh plots used in chapter 3.

```
clear
    clear all
        load Silicon.mat

        %Defining data sets
        NR = data.refl;
        wl = data.wavelength;
        sd = data.speed;

        %Creating mesh grid graph
        [XX,YY] = meshgrid(wl,sd);

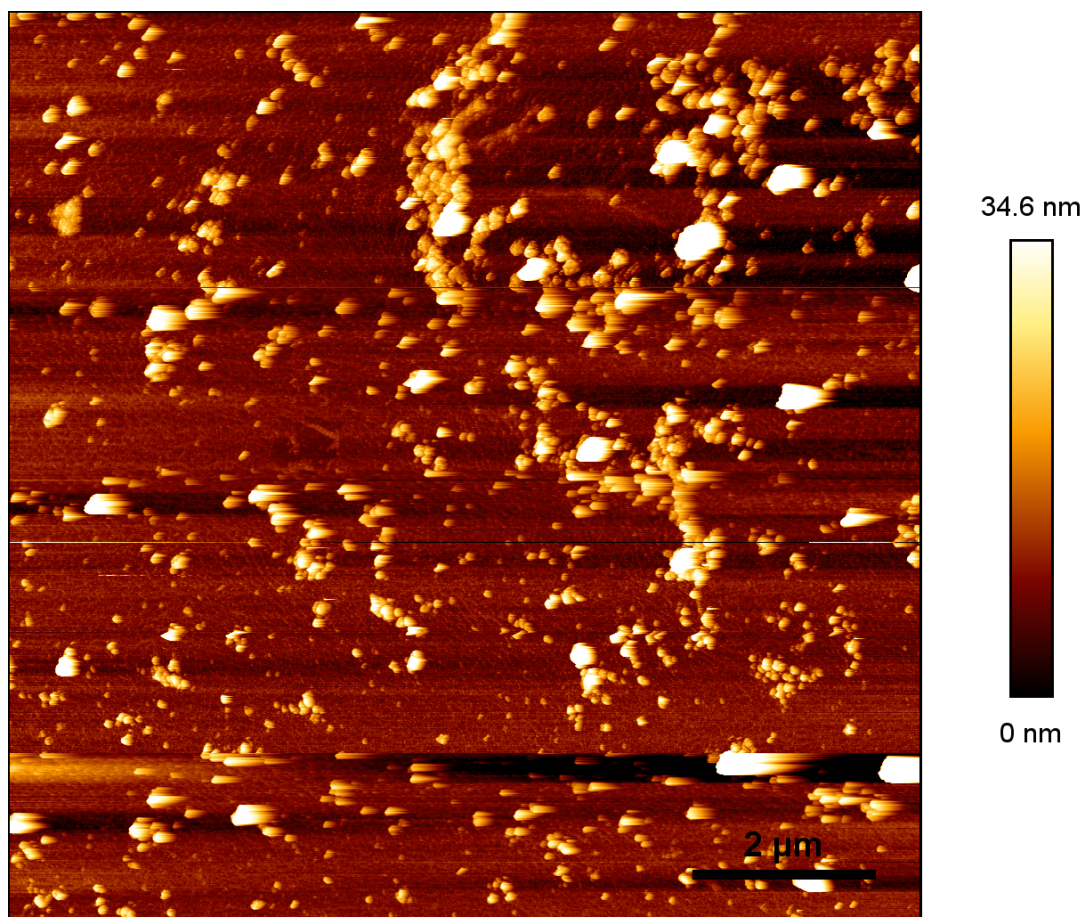
        %Defining figure parameters for the mesh grid graph
        figure(1)
        pcolor(XX,YY,NR)
        shading interp
        colormap jet
        xlabel('Wavelength /nm')
        ylabel('Ridge Width /μm')
        title('Range of 0 - X Incident Angles Leading to NIM
Behaviour')
        colorbar
    end
end
```

Below details the molarity concentrations explored to produce AuNP-GA.

X

APPENDIX: VIII

Below is an AFM height-scan profile taken after carrying out EFD with gold nanoparticles (AuNP) dissolved in PBS. EFD was carried out at $111.4 \mu\text{m min}^{-1}$.



APPENDIX: IX

Below indicated the calculations used in Chapter 4 to project the number of AuNP-GA per unit area.

Data used for minimum diameter of AuNP

Surface Area of M13	11366 nm ²
Flattened Surface Area of M13	4800 nm ²
Flattened Surface Area of AuNP	64 nm ²
Substrate Area	4,000,000 nm ²
AuNP per Substrate Area	62500
AuNP per M13	178
M13 per Substrate Area	833
Flattened Surface Area of M13-AuNP	6012 nm ²
M13-AuNP per Substrate Area	665

Data used for maximum diameter of AuNP

Surface Area of M13	11366 nm ²
Flattened Surface Area of M13	4800 nm ²
Flattened Surface Area of AuNP	900 nm ²
Substrate Area	4,000,000 nm ²
AuNP per Substrate Area	4444
AuNP per M13	13
M13 per Substrate Area	833
Flattened Surface Area of M13-AuNP	16166 nm ²
M13-AuNP per Substrate Area	247